Technical Report Documentation Page

1. Report No. ABC-UTC-2016-C1-FIU04 ABC-UTC-2016-C1-UW01	2. Government Accession No.	3. Recipient's Catalog No.	
4. Title and Subtitle **Innovative Foundation Alternative for High-Speed Rail Application**		5. Report Date April 22, 2021	
		6. Performing Organization Code	
7. Author(s) Andrew Stephenson, Michelle Chang, Priya Tripathi (orcid.org/0000-0003-1743-3219), Seung Jae Lee (orcid.org/0000-0002-2180-3502), John Stanton, Mohamed Moustafa (orcid.org/0000-0002-1006-7685), and Marc Eberhard (orcid.org/0000-0001-6752-3736)		8. Performing Organization Report No. ABC-UTC-2016-C1-FIU04 ABC-UTC-2016-C1-UW01	
9. Performing Organization Name and Address Department of Civil and Environmental Engineering Florida International University 10555 West Flagler Street, EC 3680 Miami, FL 33174		10. Work Unit No. (TRAIS)	
		11. Contract or Grant No. 69A3551747121	
12. Sponsoring Organization Name and Address Accelerated Bridge Construction University Transportation Center Florida International University 10555 W. Flagler Street, EC 3680 Miami, FL 33174	US Department of Transportation Office of the Assistant Secretary for Research and Technology And Federal Highway Administration 1200 New Jersey Avenue, SE Washington, DC 201590	13. Type of Report and Period Covered Final (04/15/18 – 05/31/21)	
		14. Sponsoring Agency Code	
15. Supplementary Notes Visit www.abc-utc.fiu.edu for other ABC reports.			

16. Abstract

High-speed railway provides a fast and robust travel choice that enhances transport of people and goods, which may act as the national economy's main artery. Compared to conventional railways, HSR has more stringent structural and geotechnical requirements to minimize deformations and avoid excessive vibrations. Bridges are a key component of the HSR infrastructure because it can avoid the interruption of existing roadways and the occupation of land. Several foreign countries including Japan and China have developed a standard design for the HSR infrastructure which stands as a great design reference for future projects within the United States. The main goal of this study is to compile and synthesize the existing and ongoing efforts for HSR bridge systems and understand the approaches to provide potential solutions to new design and construction. As a part of this effort, extensive literature review was performed to compile the modeling techniques for various HSR systems and identify common practices. A prototype HSR system model was developed for study. Due to the lack of a complete design guideline for a full HSR model, a train system, train-track system, and soil properties from separate studies are combined under the assumption that they are compatible. Static and dynamic analyses are demonstrated for a variety of train loading scenarios, and the data is used to analyze the behavior of the HSR superstructure. The analysis showcases some of the capabilities associated with the developed numerical model.

17. Key Words High-speed railway bridge		18. Distribution Statement No restrictions.	
19. Security Classification (of this report) Unclassified.	20. Security Classification (of this page) Unclassified.	21. No. of Pages 232	22. Price

Form DOT F 1700.7 (8-72)   Reproduction of completed page authorized

(this page is intentionally left blank)

Innovative Foundation Alternative for High-Speed Rail Application

Final Report

May 2021

Principal Investigator: Seung Jae Lee

Department of Civil and Environmental Engineering

Florida International University

Authors

Andrew Stephenson, Micelle Chang, Priya Tripathi,

Seung Jae Lee, John Stanton, Mohamed Moustafa, and Marc Eberhard

DISCLAIMER

ACKNOWLEDGMENTS

TABLE OF CONTENTS

LIST OF FIGURES

LIST OF TABLES

NOMENCLATURE

ABC	Accelerated Bridge Construction
BART	Bay Area Rapid Transit
BDS	Bridge Design Specifications
BNSF	Burlington Northern Santa Fe
CAHSR	California High-Speed Rail Authority
CHSTP	California High-Speed Train Project
CIDH	Cast-In Drilled-Hole
CIP	Cast-In Place
CISS	Cast-in Steel-Shell
CP	Construction Package
CRB	California Rail Builders
CRTS	China Railway Track Network
CSDC	Caltrans Seismic Design Criteria
CWR	Continuous Welded Rail
FRA	Federal Railroad Administration
HDPE	High Density Polyethylene
MLTRP	Medium- To Long-Term Railway Plan
FYP	Five-Year Railway Planning Plans
PDL	Passenger Dedicated Line
CWR	Continuous Welded Rail
IRCT	Institute Of Railway Comprehensive Technology Of Japan
CRTS	China Railway Track System
CWR	Continuous Welded Rail
CRH	China Railway High-Speed
CFST	Concrete Filled Steel Tubes
SCC	Self-Compacting Concrete
SR	State Route
DOT	Department Of Transportation
HSLM	High Speed Load Model
HSR	High-Speed Rail
HST	High-Speed Train
LRFD	Load and Resistance Factor Design
MCE	Maximum Considered Earthquake
MSS	Movable Scaffolding System
OBE	Operating Basis Earthquake
PDL	Passenger Dedicated Lines
TCR	Texas Central Railway
THSR	Taiwan High Speed Rail
UIC	International Union of Railways

1. INTRODUCTION

High-speed railway (HSR) provides a fast and robust travel choice that enhances transport of people and goods, which may act as the national economy's main artery. Compared to conventional railways, HSR has more stringent structural and geotechnical requirements to minimize deformations and avoid excessive vibrations. Bridges are a key component of the HSR infrastructure because it can avoid the interruption of existing roadways and the occupation of land. Several foreign countries including Japan and China have developed a standard design for the HSR infrastructure which stands as a great design reference for future projects within the United States.

The inherent characteristics of HSR raise new problems beyond those found in typical highway construction. For example, HSR bridge design requires good understanding of many complex issues including vertical/lateral deflections and rotational deformations, complex train-track interactions and vibrations caused by the high speed of trains, etc. These issues need to be robustly considered in the design of HSR bridge systems and comprehensive numerical approaches on the bridge structure modeling are needed. Good understanding of the sensitivity of a bridge span vertical deflections and rotational deformations, as well as train-track-bridge dynamic interactions and coupling vibrations are of great importance when designing HSR bridges. Compared with a conventional railway bridge, the design of HSR bridges require a higher service limit to minimize deformations and avoid excessive vibrations or resonance due to the crossing of trains to improve the riding comfort for passengers.

With the requirements for deflections, rotations, and natural frequencies of bridge spans, comprehensive understanding of the HSR dynamic interactions among train-track-bridge structures is a topic of great importance. Accordingly, national and international research studies have focused on dynamic interaction through sophisticated structural models. Upgrading of existing bridges is of particular concern, e.g., HSR bridge superstructures require high stiffness and are likely to be heavy, so upgrading of the existing structure for HSR will apply significant surcharge on the bridge foundation, for which a retrofit solution also needs to be developed; the stiff, heavy components will induce seismic forces that are much higher than in highway bridges, so the ABC solutions developed for highway bridges will have to be reworked to satisfy the more stringent requirements in seismic areas; Construction issues also have to be optimized regarding how this upgrade can be best accommodated in a short time without causing high costs and traffic disruptions.

A main goal of this study is to compile and synthesize the existing and ongoing efforts for HSR bridge systems and understand the approaches to provide potential solutions to new design and construction. As a part of this effort, extensive literature review was performed to compile the modeling techniques for various HSR systems and identify common practices. A prototype HSR system model was developed and a follow through of the steps taken to create a detailed model in OpenSees was documented and discussed sequentially. Due to the lack of a complete design guideline for a full HSR model, a train system, train-track system, and soil properties from separate studies are combined under the assumption that they are compatible. Static and dynamic analyses are demonstrated for a variety of train loading scenarios, and the data is used to analyze

the behavior of the HSR superstructure. The analysis aims to showcase some of the capabilities associated with the developed numerical model.

Literature published from national and international sources are reviewed and compiled to demonstrate and how the individual components within a train system, track system, or bridge system have been modeled in previous studies and the similarities and differences regarding the numerical modeling techniques. Doing so, the reader can gain insight on how to model different types of train, track, and bridge systems and apply this knowledge to the formulation of their own HSR system model. Selected prototype train-track-bridge system is modeled to demonstrate the application of the modeling techniques highlighted in the literatures. The modeling procedures for each component of the HSR model in-place followed the methods presented in their respective studies. Any information that was not stated in the reference study is assumed using knowledge gained from the literature search. A step-by-step guide of the process of formulating the model and analysis parameters from start to finish are documented, accompanied by snapshots from the OpenSees model in-place for demonstration.

2. CURRENT HIGH-SPEED RAIL BRIDGE SYSTEMS

2.1. INTRODUCTION
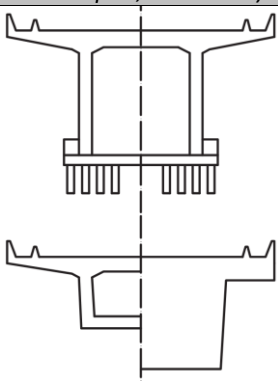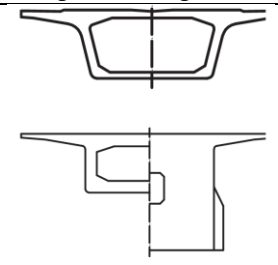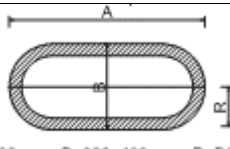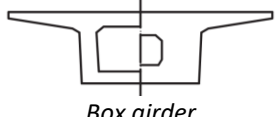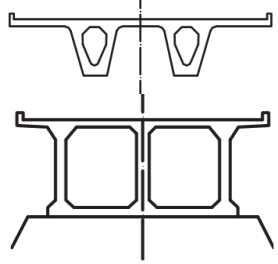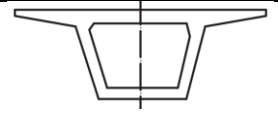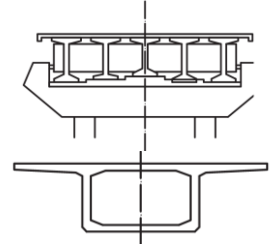
A transportation solution that has always been considered for the past few decades is the high-speed rail (HSR). The successful commercial operation of the Japanese Shinkansen, (bullet train) in 1964 marked the beginning of a new era for HSR and the development of HSR spread throughout the world. Plans for HSR in the United States date back to the High-Speed Ground Transportation Act of 1965 (Public Law 89-220, 79 Stat. 893) which was the first attempt by the U.S. Congress to foster the growth of HSR. Although the United States was one of the world's first countries to have a high-speed rail service in place with the Metroliner operating between Washington, D.C., and New York City in 1969, the trend did not spread through the rest of the country. Various state and federal HSR propositions followed but full implementation of an inter-state HSR has never been accomplished. The closest the United States currently has to an HSR system is the Acela, formerly known as Acela Express. The Acela is a high-speed service along the Northeast Corridor in the Northeastern United States operated by Amtrak and replaced the aging Metroliner. The Acela provides a route from Washington, D.C. to Boston with 16 intermediate stops which makes the service inter-state, but the top speeds of 240 km/h limit the service to be categorized as a higher-speed rail (HSR). Higher-speed rail is the jargon used to describe inter-city passenger rail services that have top speeds higher than conventional rail but are not high enough to be considered high-speed rail services. Typically, an inter-city rail service must have a minimum speed of 250 km/h to be considered as a high-speed rail service.

There is a wide range of HSR superstructure types around the world from 30 m box girder bridges to over 1000 m suspension bridges. Early designs used simply-supported, deep, post-tensioned concrete box girders (Kang et al. 2018), but since then many other types have emerged (Yan et al. 2015). Table 2.1 provides a partial list of different bridge types for reference, sorted by the length of span. While there is a good spectrum of superstructure types, each country tends to use a typical structural design in order to facilitate faster production. The selection of a common structural system also influences the construction procedures. The most common superstructure type for HSR is a simply supported prestressed concrete beam. Some features of simply supported beam bridges from six countries are listed in Table 2.2. Current HSR superstructures from Japan, China, Europe, and the United States are discussed in more detail in the following sections.

Table 2.1 Partial list of international HSR bridges

Name	City/Locality	Country	Year	Main Span (m)	Materials	Type
WuFengShan Bridge	Zhenjiang	China	2020	1092	multiple	Suspension
TianXingZhou Bridge	Wuhan	China	2009	504	multiple	Cable Stay
Almonte Viaduct	Alcantara	Spain	2016	384	Concrete	Arch
DaShengGuan Bridge	Nanjing	China	2010	336	Steel	Arch
Sannai-Maruyama Bridge	Aomori	Japan	2008	150	Concrete	Extradosed
Leuven HSR Bridge	Leuven	Belgium	2002	117	Steel	Arch
Avignon Viaducts	Avignon	France	1999	100	Concrete	Haunched box girders
Meuse Viaduct	Lacroix-sur-Meuse	France	2005	52	Composite	Haunched twin girders
Archidona Viaduct	Archidona	Spain	2012	50	Composite	Haunched twin girders

Table 2.2 Features of simply-supported HSR bridges from six countries (Yan et al. 2015)

Country	Typical Cross-Sections (L: at mid-span; R: at ends)	Standard Span(s)	Typical Pier and Foundation	Construction Method(s)
Japan	*T-girder, box girder*	24.2, 29.2, 34.2, 39.2, and 44.2 m	Rectangular or circular pier Pile group or spread footing	Precast Cantilever Cast-in-place
China	*Box girder (2 types)*	32 m	A=800 cm B=300~480 cm R=B/2 *Round-ended pier with pile group*	Precast Cantilever
France	*Box girder*	≤ 25 m	Rectangular or circular pier Pile group or spread footing	Precast Cantilever Cast-in-place
Italy	*Box girder*	24, 33.6, 43.2, and 55.0 m	Rectangular pier Single pile	Cantilever Cast-in-place Launching
Germany	*Box girder*	25, 44, and 58 m	Rectangular pier Single pile or pile group	Cast-in-place Launching
Spain	*I-girder or box girder*	26.6 m	Rectangular pier Single pile or pile group	Cantilever

2.2. *JAPAN*

Japan is the birthplace of HSR and developed the Shinkansen (colloquially known as the bullet train) in time for the 1964 Olympic Games. The embarkment of this national project heavily influenced the landscape, national economy and mobility of people between Tokyo and Osaka, two major metropolitan cities in Japan. Over 50 years later, the Shinkansen railway network continues to expand; the construction of new Shinkansen lines has been progressing under the Nationwide Shinkansen Railways Construction Act and currently spans a total of 3,040 km (1,890 miles). The extension of the Tohoku Shinkansen to the Northern part of Japan was completed in December 2010, and the extension of the Kyushu Shinkansen to the southern part of Japan was completed in March 2011. The inauguration of these new lines completed the connection of all regions from north to south by high-speed rail and considerably increased mobility within Japan (Figure 2.1). Additional extensions such as the Kyushu Shinkansen Nagasaki-route scheduled for 2022 and the Linear Chuo Shinkansen's service between Shinagawa and Nagoya scheduled for 2027 demonstrate the continuous extension of Shinkansen transportation in Japan.
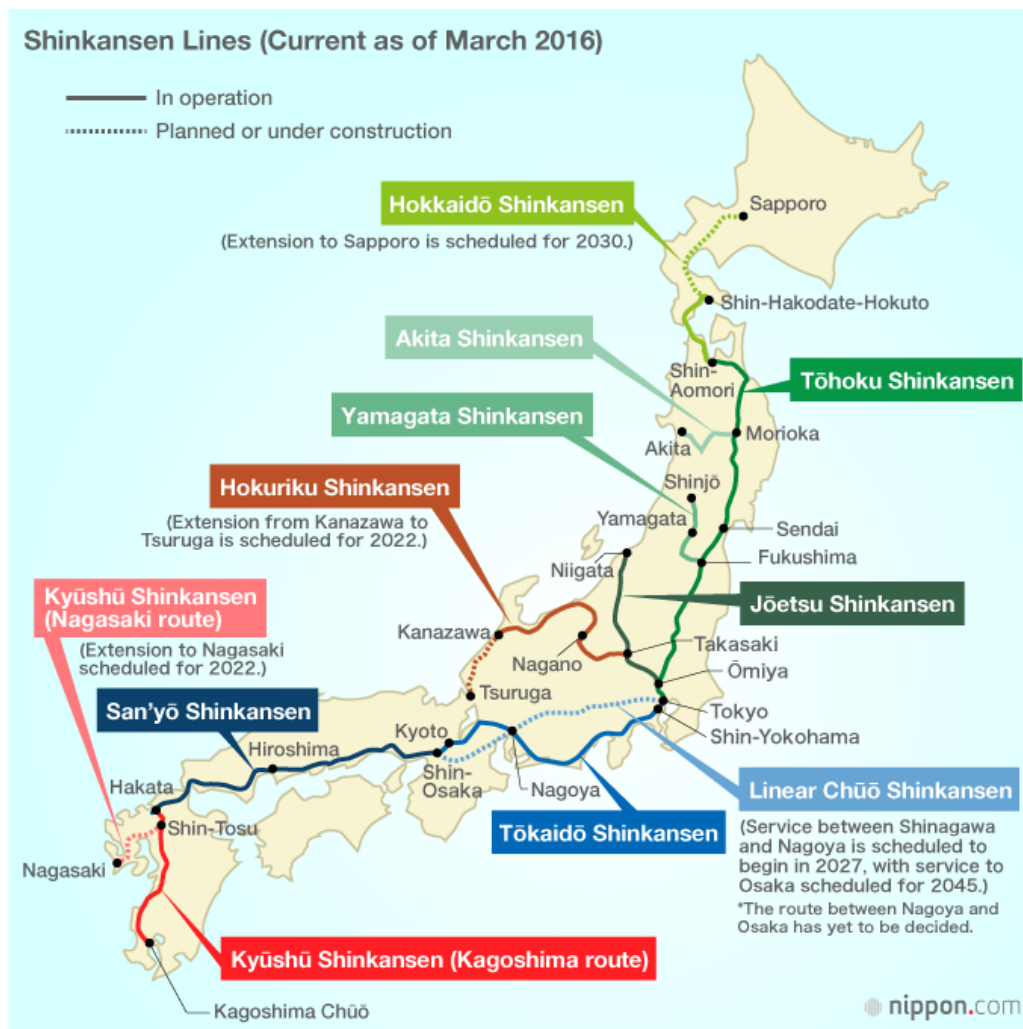
Figure 2.1. Shinkansen network in Japan (Takuma 2019)

The Japanese archipelago is located in a highly seismic region due convergence of the oceanic and continental plates. Therefore, Shinkansen structures have faced several destructive earthquakes, including the 1995 Hyogoken-Nanbu (Kobe) earthquake which caused eight bridges to collapse (Table 2.3). Through damage analyses of road and railway structures after the Kobe earthquake, Japanese seismic design procedures and specifications were significantly revised (Nishimura 2004) and existing bridges were also retrofitted per revision of the standards. Many of HSR bridges in the Kobe earthquake occurred due to shear failure of the columns, so common retrofits included steel jacketing of reinforced concrete columns. The retrofits were observed to be effective in following earthquakes, including the 2011 Great East Japan earthquake (Akiyama et al. 2014). Although the recorded magnitude of 9.0 is the largest in Japan's recorded earthquake observation history, no major damage was reported for structures that had been given the post-1995 seismic retrofit (Abé and Shimamura 2014).

Table 2.3. Seismic damage to Shinkansen HSR line from recent major earthquakes (Source: Damage Statistics from Mizuno and Nozawa (2011))

Earthquake	1995 Kobe	2004 Chūetsu	2011 Tōhoku	
Date	January 17	October 23	March 11[a]	April 7[b]
Time	5:46 JST	17:56 JST	14:46 JST	N/A
Magnitude	7.3	6.8	9.0	7.1
Total deaths	6,434	68	19,238	4
Total infrastructure losses (JPY)	9.9 trillion	1.7 trillion	16.9 trillion	
Damaged routes and lengths (km)	Sanyo (83)	Jōetsu (65)	Tōhoku (536)	
Derailments	0	1	0	0
Related casualties	0	0	0	0
Collapsed bridges	8	0	0	0
Bridge unseating events	72	1	2	7
Damaged viaduct columns	708	47	~100	~20
Damaged tunnels	4	4	0	0
Damaged electric-power poles	43	61	~540	~270
Damaged electric transformers	3	1	~10	~10
Days to operation recovery	82	67	49	

Note: JPY = Japanese yen; JST = Japan Standard Time.
[a]Main shock event.
[b]Major aftershock event.

As a feature of high-speed rail infrastructure design, it is important to not only support heavy trains, but to also provide sufficient rigidity for the structure as needed to strictly control the quantity of deflection. The deflection must be controlled within a limit to maintain the safety and stability of the running train and accordingly, the Railway Technology Standards have designated a performance-oriented design for railway structures. Per this standard, the running safety and comfort of the trains are to be checked at the same level as the serviceability of the structures. The severe restrictions on high-speed rail bridge deformations affect the surrounding conditions of its construction site with the requirement of larger curve radius and a less steep gradient by the limited flexibility of high-speed train routes (Minami and Shimizu 2011). These inherent characteristics of high-speed rail bridges pose the designers with the contradicting conditions of minimal deformation and longer spans, simultaneously.

2.2.1. REQUIRED PERFORMANCE CHARACTERISTICS FOR HSR BRIDGES

The Railway Technology Standards requires the performance characteristics of HSR bridges to be satisfied in the following three categories: safety, serviceability, and repairability. Each category has respective performance indexes as shown in Table 2.4, where the required performance categories are shown with criteria to satisfy the performance items and check indices. The items of performance include running safety and comfort items that are unique to high-speed rail bridges as well as rupture, fatigue, and damage that are common to all structures.

Table 2.4. Required performance for HSR bridges. (Tamai and Shimizu 2011)

Required performance	Items of performance	Check indexes
Safety	Rupture	Member force at ultimate limit state
	Fatigue	Variable stress of reinforcement
	Running safety	Wheel levitation, Axle load *Displacement, Deflection*
	Public safety	Durability of concrete
Serviceability	Comfort	Body acceleration *Displacement, Deflection*
	Appearance	Crack width
Recoverability	Damage	Member force under over-load Member load or deflection under seismic load

Indirect check index for conventional method

*Running safety and comfort should be evaluated through altering axle loads or vibration accelerations, and a trial run, but as noted (see *) in the table, bridge displacements and deflections should be checked during the design phase. Displacement and deformation limits are set as the ratio to the span length. As the span lengths increase, the limits also increase, and can even exceed 100 mm in some cases but which is doubtful as an acceptable index. Additionally, the interactions between the train and track system make the realistic calculation of displacement and deformation difficult without considering dynamics of the train load.*

Therefore, the Railway Technical Research Institute in Japan has developed the dynamic analysis code for solving such issues. Sophisticated models including the train-structure system are modeled by multiple degrees of freedom and allow for the simulation of the trial run necessary to evaluate the running safety and comfort. The model can also output the magnitude of wheel-levitation which causes derailment and the train body acceleration which affects the riding comfort of passengers. These values are used to check the performance indices.

For the displacement and deflection limit check of the HSR bridges, the initial track irregularity precondition that may occur before the passing of trains must be minimized since the track slab is directly connected to the structure. The initial track irregularity may be caused by temperature

and shrinkage and creep of the track slabs and are time- and season-related phenomena. While irregularity with such effects has been known for a long time, the recent implementation of longer spans have caused increased irregularity and negatively affect running safety and comfort. Checking the running safety and comfort without considering the time- and season-related irregularity is possible with the model created but is not recommended for reliability of the high-speed rail operations.

2.2.2. SANNAI-MARUYAMA BRIDGE

2.2.2.1. STRUCTURE OF SANNAI-MARUYAMA BRIDGE

The Sannai-Maruyama Bridge on the Tohoku Shinkansen extension was completed in 2008 and has one of the largest spans among HSR structures in Japan (Figure 2.2). The bridge consists of two 150 m main spans and two 75 m end spans over a highway, river, and reservoir near the famous Sannai-Maruyama archeological site from the Jomon period. Due to these crossings, falsework and scaffolding were not permitted; therefore, a prestressed concrete girder and the balanced cantilever construction method were considered as a potential solution. Nevertheless, a deep prestressed concrete girder was determined to be aesthetically unpleasing and seismically unfavorable due to its internal tendons making the girder too thick and heavy at the pier. An extradosed bridge was proposed as the final solution, which allowed use of the balanced cantilever construction method while also permitting a shallower girder. Double pylons were used but are not connected to each other by a cross beam to eliminate ice falling on the train (Figure 2.3).

Figure 2.2. Sannai Maruyama Bridge in Aomori, Japan (Zenitaka 2010)
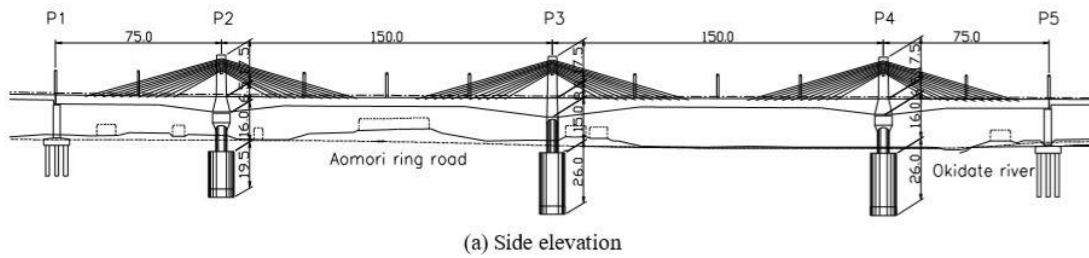
(a) Side elevation
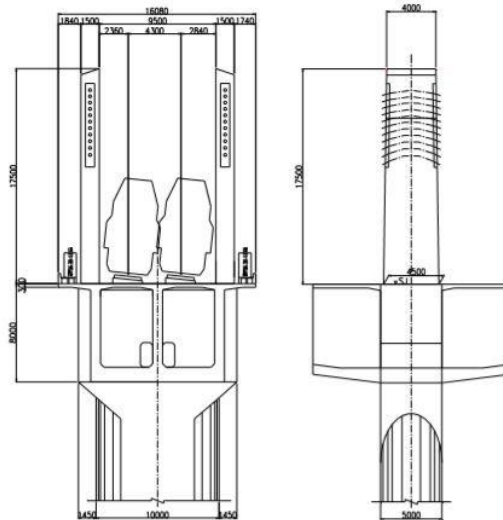
(b) P3 Pier and pylon

Figure 2.3. Elevation of Sannai-Maruyama Bridge: (a) Side elevation; (b) Section (L) and elevation (R) of the central double-pylon pier (dimensions are in mm) (Akiyama et al. 2014)

2.2.2.2. METHODS FOR CONTROLLING INITIAL DEFORMATION

The design of the Sannai-Maruyama Bridge applied measures for reducing time- and season-related deformation.

2.2.2.2.1 SLIDING ELASTIC BEARING

The effect of thermal deformations can be seen in Figure 2.4 for a continuous rigid frame, which is a common design for long spanned bridges in recent years due to the high seismic performance and low maintenance costs. Expansion and contraction of the bridge spans are transferred to the piers and cause the top of the piers to rotate and the girder to displace vertically if rigidly connected (Figure 2.4a). For the Sannai-Maruyama bridge, sliding elastic bearings were installed on four piers except the center pier, which works as the stationary point of the bridge, to reduce the displacements caused by the expansion and contraction. The bearings on P2 and P4 (Figure 2.4b) are arranged in two lines transverse to the bridge length due to the weight of the superstructure and reduce the clear span of the girder and deflection due to the train loads. The layout of the bearings on the piers is shown in Figure 2.5, and this measure effectively reduced the vertical displacements of the girder.
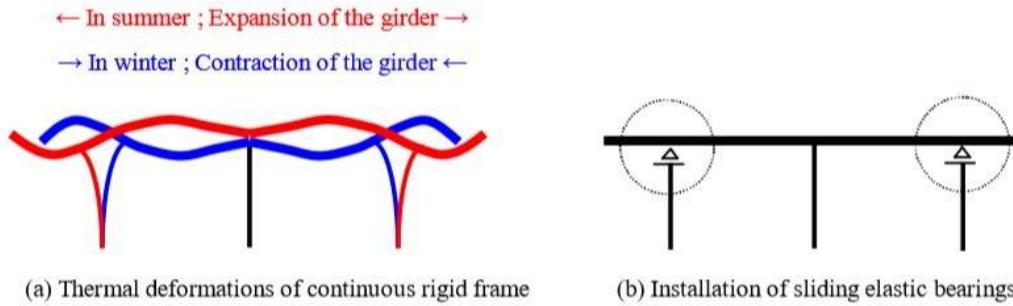
Figure 2.4. Thermal deformations of continuous rigid frame bridges (Minami and Shimizu 2011)
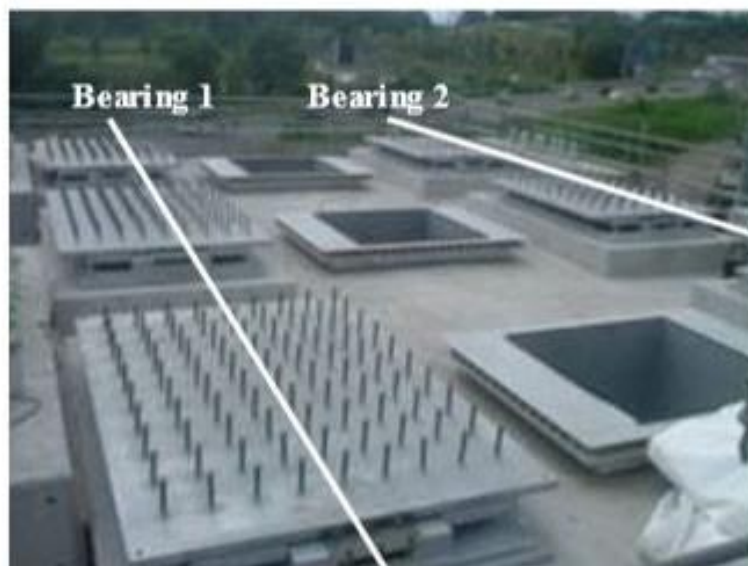
Figure 2.5. Sliding elastic bearings aligned in two lines (Minami and Shimizu 2011)

2.2.2.2.2 LOWER PYLON

With the elegant structural form of an extradosed bridge designed with a shallow deck and long pylons, the long stay cables exposed under direct sunlight may cause substantial deflections of the deck. The design of Sannai-Maruyama bridge therefore was considered to incorporate a lower pylon, shorter stay cables, and a deeper girder to secure stiffness against the train loads which reduces thermal displacements of the cables and girder and making this a suitable for high-speed railway bridges (Figure 2.6).
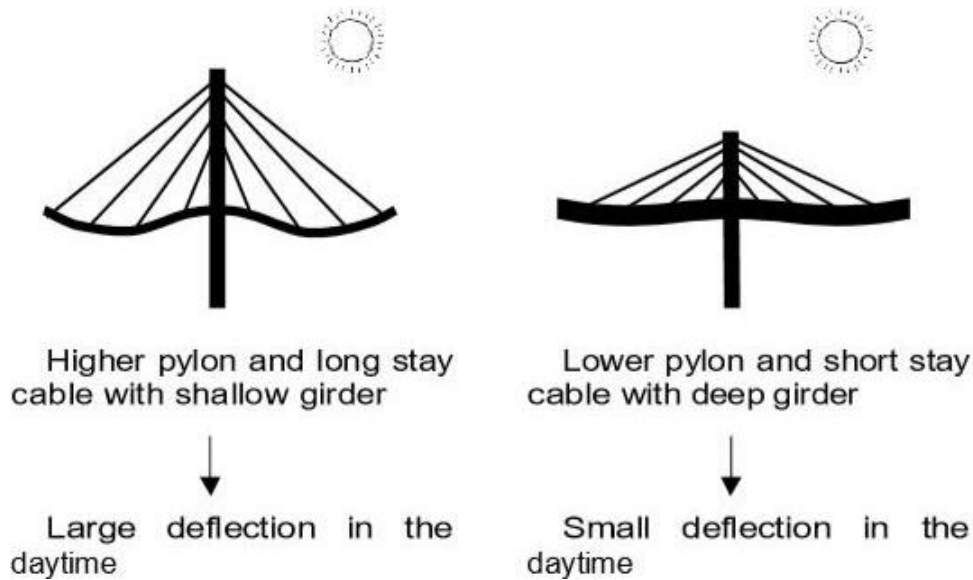
Figure 2.6. Deflection in higher and lower pylons (Minami and Shimizu 2011)

2.2.2.2.3 *INSULATION OF STAY CABLE FROM SUNSHINE*

In addition to the shorter pylons, the stay cables of Sannai-Maruyama bridge utilized a thermal insulation system to help control the change in length of the cable due to increase of temperature. A three-layered cable protection system comprising epoxy coated strands encased in high density polyethylene (HDPE) tube filled with cement grout was used as the thermal insulator (Figure 2.7) instead of a prefabricated cable system with resin filler that is increasingly adopted in recent years due to its insufficient thermal insulation. The light gray color for the epoxy coating also helps to reduce the heating up of the stay surface.
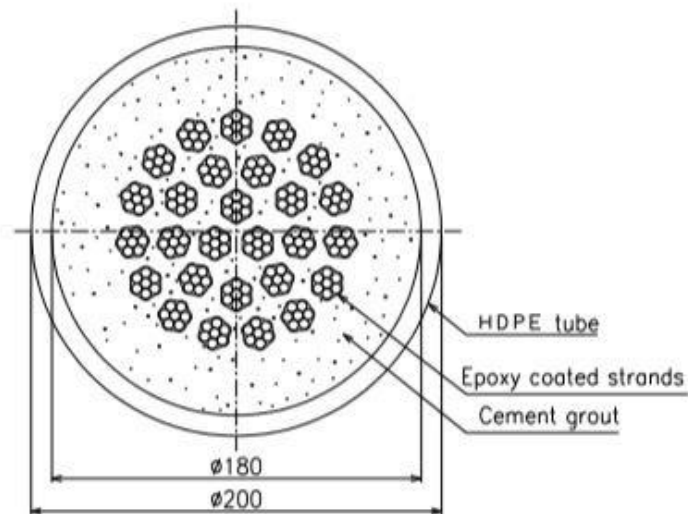
Figure 2.7. Stay cable system with thermal insulation (Tamai and Shimizu 2011)

2.2.3. MATSUBARA BRIDGE

2.2.3.1. KYUSHU SHINKANSEN

The Kyushu Shinkansen line consists of around 250 km of high-speed railway running through the Kyushu Island in Japan. Beginning operations in 2004, the Kyushu Shinkansen line was constructed from the southern part which is in a mountainous area presenting difficult conditions for construction. The line is isolated from the existing Tokaido-Sanyo Shinkansen line which connects Tokyo with Kyushu Island, and the new Kyushu Shinkansen opened in March 2011 connects the existing line with a 121 km extension (Figure 2.8). Through this extension, Fukuoka, the largest city in Kyushu Island, and Kagoshima, the largest city in the south of Kyushu Island, can be travelled in less than one-and-a-half hours, and a through service with the Tokaido-Shinkansen has become available. The mountainous terrain of the southern part of Kyushu Island led to 69% of the line being underground and in contrast, the northern part was built mainly in urbanized areas. The northern HSR infrastructure consists of 77.44 km of bridges and only 2.71 km are consisted of steel-type bridges (two arch, one truss, others with composite girder), which are used when the surrounding conditions are very tough.
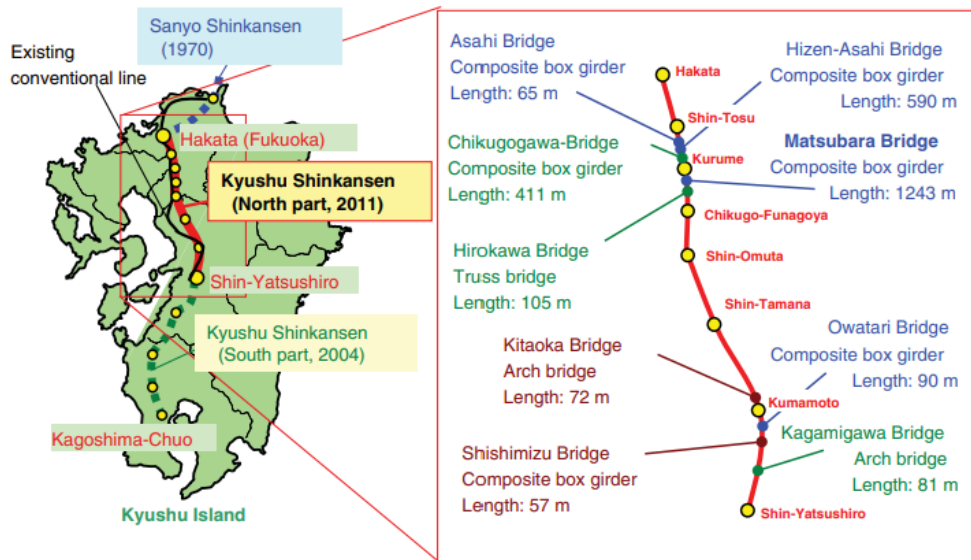
Figure 2.8. Matsubara Bridge in Fukuoka, Japan (Minami and Shimizu 2011)

Matsubara Bridge is located in the city of Kurume, a highly industrialized city with a population above 300,000 and an area of approximately 200 km² (Minami and Shimizu 2011). The Kyushu Shinkansen line approaches the densely populated downtown Kurume, which required parts of the structure to be constructed above existing in-service railway lines that saw more than 340 trains running each day. Moreover, the erection of the main girders and the cross beams of the frame piers had to be assembled and installed within the confined space of overcrowded buildings with proximity to existing tracks. Furthermore, the erection work above existing tracks were limited to 200 min per each night of work and extending working time was prohibited. Working above existing tracks also meant that any mistakes or accidents would severely affect the operation of the existing tracks. With the constraints, scheduling and management were critical.

State-of-the-art bridging methods were utilized to construct the Matsubara Bridge on the Kyushu Shinkansen extension, due to its severe conditions at the construction site. The Matsubara Bridge is located in the city of Kurume, Japan, a highly industrialized city with a population of more than 300,000. A photo of the bridge and the surrounding infrastructure is shown in Figure 2.9. Construction of the Matsubara Bridge was the most difficult among the new Kyushu Shinkansen bridges because of the space and time constraints.

The structure consists of a simple box girder, four three-span continuous box girders, and two four-span continuous box girders. The simple girder has a single-box structure with a web height of 3.5 m and a length of 85 m for overpassing the broad road. The continuous girders have a double-parallel-box structure with a web height of 2.8 m and a length of 60 m. The substructure consists of 16 steel rigid frame piers spanning 25 m for the section overpassing existing tracks and 6 reinforced concrete piers for the other sections.

Figure 2.9. Matsubara Bridge in Fukuoka, Japan (Minami and Shimizu 2011)

2.2.3.3. STATE-OF-THE-ART BRIDGING METHOD

Erection of the main girders and the cross beams of the frame piers proved to be difficult due to the overcrowded buildings and proximity of existing rail tracks. Erection work above the existing lines were also limited to 200 minutes in each night's work. Due to these constraints, a steel bridge was selected and innovative erection methods such as the balancing rotation method and launching method were utilized since there was not enough space for cranes.

2.2.3.3.1 BALANCING ROTATION METHOD FOR CROSS BEAM OF PORTAL FRAME

For the balancing rotation method, the crossbeams were assembled parallel to the existing tracks and were rotated on the columns by using rotation devices and counterweights, as shown in Figure 2.10. Cross beams were supported by pivot shoes after the rotation. The small device made rotation possible in the narrow space in combination with clevis jacks, which gave supplied force

in the direction of rotation by the reaction of hydro-clamp devices. The method was newly developed for this construction and was later patented by the Japan Railway Construction, Transport, and Technology Agency. The construction site was divided into two (595 m and 648 m), and superstructures were assembled on both sides and pushed towards the center using launching devices.
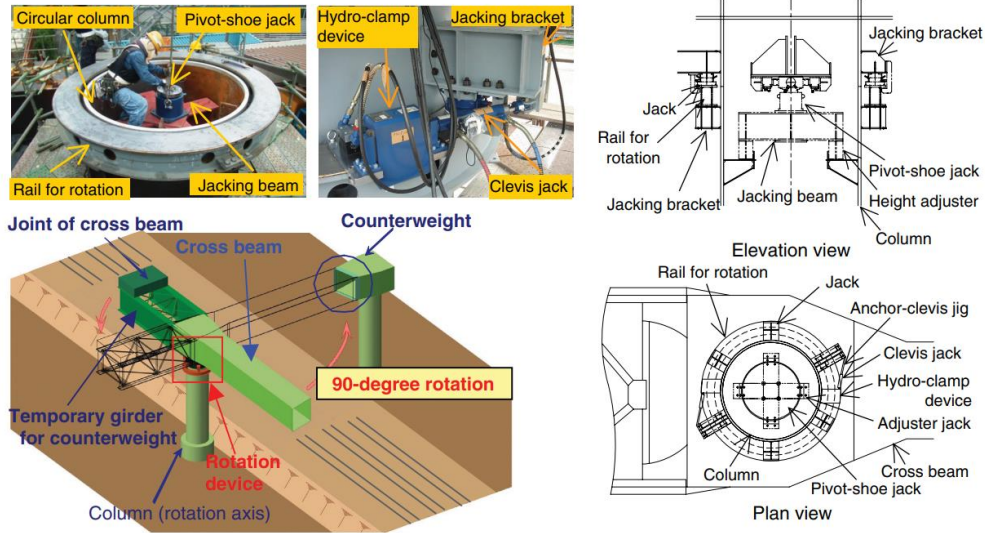
Figure 2.10. Balancing rotation method of cross beam end rotation device (Minami and Shimizu 2011)

2.2.3.3.2 LAUNCHING ERECTION METHOD OF SUPERSTRUCTURE

The launching devices used a crawler which enabled rapid launching and girders of varying lengths were temporarily connected to each other into two large blocks. Photographs of the installation work is shown in Figure 2.11.
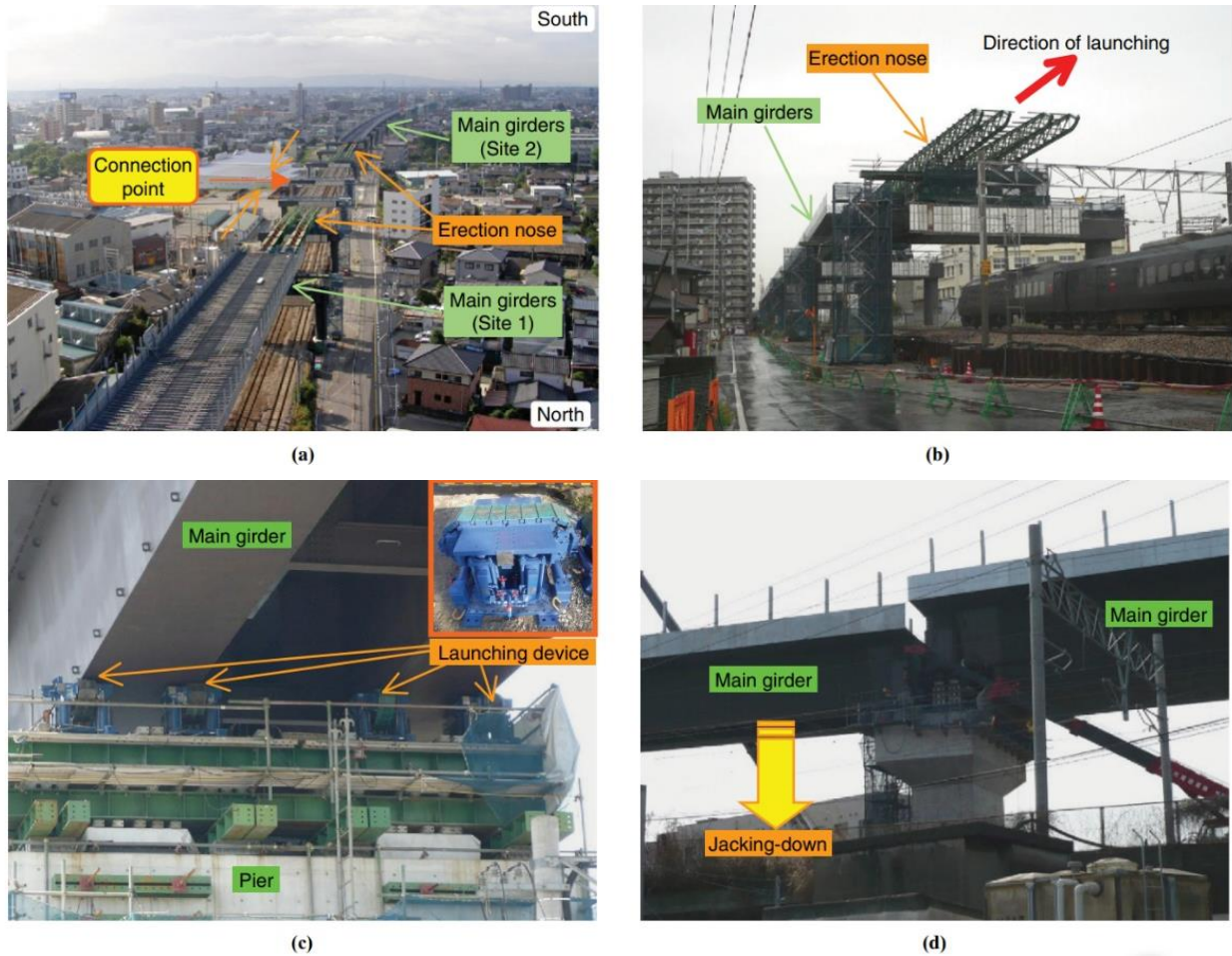
Figure 2.11. Launching erection of main girders of Matsubara Bridge: (a) launching of main girder (aerial); (b) launching of main girder (bottom angle); (c) launching device with a crawler, and (d) jacking down of main girder (Minami and Shimizu 2011)

2.3. CHINA

The HSR construction in China is relatively recent. However, China is currently leading the HSR construction with more than 50 percent of the global mileage overall (Figure 2.12), and the HSR network in China is still continuing the expansion (Yan et al. 2015). The China's HSR project was developed and approved with Medium- to Long-Term Railway Plan (MLTRP) in 2004 and implemented through the series of renewals of Five-Year Railway Planning Plans (FYP) at evey five-year which is currently under 2016–20 FYP. China initially considered a magnetic levitation (maglev) track system at the planning stage, but which turned out to be too expensive after a 30 km trial project. Then, the maglev plan was dropped and China decided to stay with the conventional track (Lawrence et al. 2019). Early version of China's HSR was developed based on Europian and Japanese HSR, but since then China has developed their own system and now working with the UIC to develop the international standards that are compliant with China's HSR.
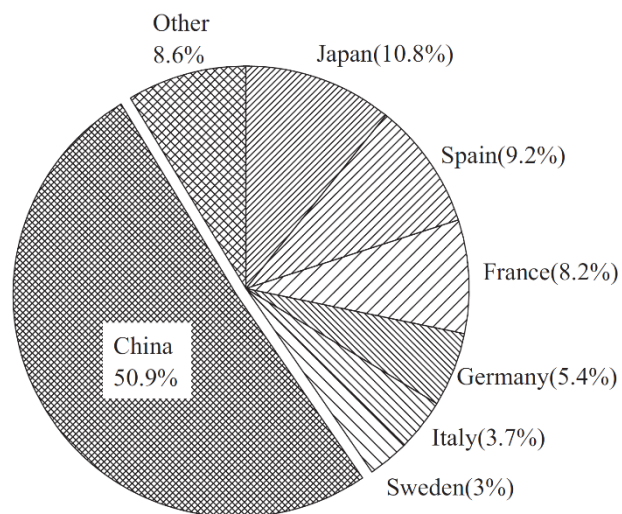
Figure 2.12. HSR mileage by countries (Yan et al. 2015)

Bridge is the key element of HSR infrastructure in China as it covers up to 70% of total mileage of HSR line (Figure 2.13). This high percentage is due to the decision not to interfere with the existing lines thus minimize the interreuption of HSR traffic (Yan et al. 2015). In China HSR, a short span is defined as a span length less than 30 m, while a span larger than 100 m is considered as a long span. The most typical China HSR bridges are simply supported bridges while continuous beam bridges are selectively adopted. For example, 90% of the bridges in the Beijing-Shanghai passenger dedicated line (PDL) are simply supported.

The following sections discuss the China HSR network in terms of the key issues considered in planning and construction of the HSR bridges. These issues include (i) design loads, (ii) requirements for structural deformations (including deflections and rotations) and induced vibrations, (iii) interactions of train-track-structure such as interactions of continuous welded rail (CWR)-structure and analytical aspects of HSR bridge statics/dynamics, and (iv) typical design and construction details to faciliate the faster construction to meet the aformentioned requirements.
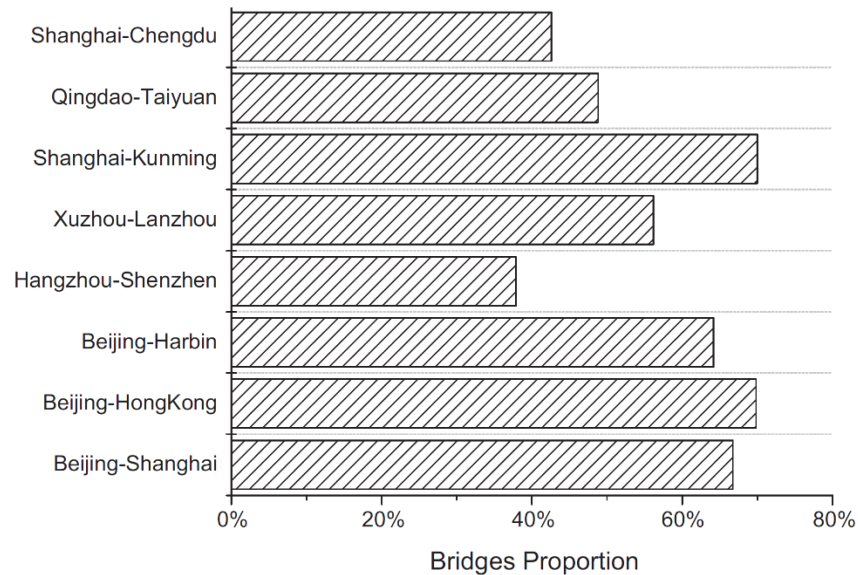
Figure 2.13. Percentage of bridge in the total mileage in major HSR lines of China (Yan et al. 2015)

2.3.1. HSR NETWORK

China has introduced the HSR work since 1990s and developed PDL designs / HSR code of prototype implementation and a set of standards and regulations, e.g., for 200–250 and 300–350 km/h (kph) speed HSRs. The first version of HSR network was planned with the MLTRP in 2004, whereby the high-speed passenger dedicated lines (PDLs) were proposed to connect the all major cities. The first version was with four horizontal and four vertical corridors but later expanded to eight horizontal and eight vertical corridors in the 2016 plan (Figure 2.14). The Beijing–Shanghai line (1,318 km) and the Beijing – Guangzhou line (2,105 km) had been completed by 2012 that connects China's three most dynamic economic clusters: (i) the Bohai Sea ring that connects Tianjin, Beijing and Hebei provinces, (ii) the Yangtze River Delta that connects cities in Jiangsu and Zhejiang provinces including Shanghai, and (iii) Pearl River Delta for Guangdong province including Guangzhou. A new generation of HSR lines introduced in 2008 had a maximum speed of 350 kph and was constructed between Beijing and Tianjin while a maximum speed of China HSR was about 250 kph before this new generation. Consequently, the current HSR lines have three types with different speeds: (i) PDLs at a maximum speed of 350 kph, (ii) secondary and reginoal lines with a maximum speed of 250 kph, and (iii) intercity lines with a maximum speed of 200 kph (Figure 2.15). China now plans to expand the network to 175,000 km lines including 38,000 kim of HSR lines to cover all major and mid-sized cities by 2025.

Figure 2.14. Planned high-speed rail corridors (Lawrence et al. 2019)

The average cost of a HSR double-track line (including signaling, electrification, and facilities) is around (i) Chinese¥ 139 million/km for a HSR line with 350 kph maximum speed, (ii) ¥ 114 million for a HSR line with 250 kph, or (iii) ¥ 104 million for a HSR line with 200 kph. Depending on engineering circumstances, project scope, and land acquisition and demolition costs, the project cost for the same target speed can vary by up to twice. However, these costs are overall at least 40 percent lower than in Europe's construction costs. Lowering the costs in the construction program was the major interest, and therefore, the China's HSR program encouraged to develop and utilize standardized designs and construction methods that can be re-used over multiple projects. The history of China's HSR planning and the current network is documented well in Lawrence et al. (Lawrence et al. 2019). Interested readers are referred for further details.

			350 kph	300 kph[a]	250 kph	200 kph
Alignment	Distance between centers of tracks of main line (m)		5.0	4.8	4.6	4.2
	Minimum horizontal radius (m)	Ballastless	Normal 7,000 Difficult 5,500	Normal 5,000 Difficult 4,000	Normal 3,200 Difficult 2,800	Normal 2,200 Difficult 2,000
		Ballasted	Normal 7,000 Difficult 6,000	Normal 5,000 Difficult 4,500	Normal 3,500 Difficult 3,000	
	Minimum vertical (m)		25,000	25,000	20,000	Normal 15,000 Difficult 10,000
Track	Type of track		Ballastless		Ballasted or ballastless	Mostly ballasted, sometimes ballastless
Subgrade	Subgrade width (m)	Ballastless	13.6	13.4	13.2	11.5 or 11.7 (without cable trough on the subgrade shoulder) 13 (with cable trough on the subgrade shoulder)
		Ballasted	n.a.		13.4	10.3 (without cable trough on the subgrade shoulder) 11.8 (with cable trough on the subgrade shoulder)
	Subgrade thickness (m)	Ballastless	2.7	2.7	2.7	2.7
		Ballasted	n.a.		3	3
	Postconstruction subgrade settlement (cm)	Ballastless	≤1.5	≤1.5	≤1.5	≤1.5
		Ballasted	n.a.		General sections ≤10. Transition sections at bridge abutments ≤5	General sections ≤15. Transition sections at bridge abutments ≤8
Bridge and culverts	Uniform settlement of abutment or pier (mm)	Ballastless	≤20	≤20	≤20	≤20
		Ballasted	n.a.		≤30	≤50
	Differential settlement of adjacent abutments and piers (mm)	Ballastless	≤5	≤5	≤5	≤10
		Ballasted	n.a.		≤15	≤20
Tunnel	Effective area (m²)		Double-track tunnels ≥100		Double-track tunnels ≥90	Double-track tunnels ≥72
			Single-track tunnels ≥70		Single-track tunnels ≥58	Single-track tunnels ≥35

Figure 2.15. HSR technical standards by maximum speed (Lawrence et al. 2019)

2.3.2. TRAIN LOAD MODEL

A set of transient loads is considered in the China HSR bridge design on top of the primary permanent loads such as bridge self-weight, which includes train dynamic load, interaction forces with CWR, lateral oscillation force, train induced earth pressure, etc. The train live load has two models (Figure 2.16): (i) ZK special live load that has been specifically developed for China's HSR bridges and (ii) ZK standard live load by a typical HSR train (Figure 2.17). The design live load for HSR bridges differs from country to country. For example, Europe usually uses UIC loads (2008), and the Shinkansen line in Japan uses so-called N and P loads (Institute of Railway Comprehensive Technology of Japan (IRCT-J) 2000). This standard live load for China HSR bridges is based on the UIC load model 71 with a factor of 0.8 (80%) except the intercity rail bridges with 0.6 of UIC load considered. The dynamic effects are conveniently considered by using a dynamic factor $(1 + \mu)$ multipled to the static load model. The factor μ is computed by $\mu = 1.44 / (L_\phi^{0.5} - 0.2) - 0.18$, where L_ϕ is the loading length in meters which is equal or larger than 3.61 m. L_ϕ may be considered as the span length for a simply supported span, and the average span length for continuous spans. For a HSR bridge more than five spans, a factor of 1.5 is multiplied to the span length to estimate L_ϕ (Zhou et al. 2012). However, it was also reported that the current ZK models appear to overestimate the design train loads (Yan et al. 2015).
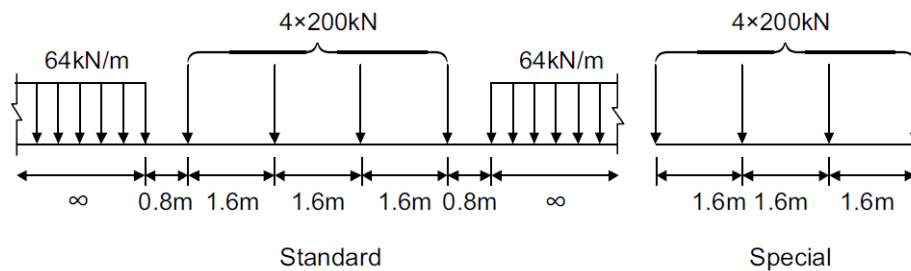
Figure 2.16. China's ZK live load models (Yan et al. 2015)

Figure 2.17. A typical high-speed train in China - CRH380b/bl train (Yan et al. 2015)

21

2.3.3. GENERAL DESIGN REQUIREMENTS

2.3.3.1. VIBRATION REQUIREMENTS

There are many factors influencing the dynamic interaction between the train and bridge including structural damping, size, speed and direction of train, track irregularities etc. UIC requires the lower and upper bounds per natural frequencies of the bridge with various span lengths: the lower bound is set to control any excessive vibration or resonance effects caused by the track-train interaction, while the upper bound is set the limit of dynamic responses caused by the track irregularities. Considering the vibration requirements by developed UIC was mostly targeted at HSRs with a speed up to 250 kph, China has developed a new set of requirements for the HSRs with a speed up to 350 kph. Table 2.5 is an exmple of the lower bounds which are higher than those specified by the UIC requirement. As discussed in Section 2.3.2, the dynamic effects are considered in the structural design by multiplying the dynamic load factor to the static load, although it was reported that some differences were observed between the field measurement and the computed dynamic effects using the dynamic factor (Zhou et al. 2012).

Table 2.5. Lower bounds of vertical natural frequency for double-track simple-span (Zhou et al. 2012)

Span Length m (ft)	Design Speed, km/h (mph)		
	250 (155)	300 (186)	350 (217)
12 (39)	100/L	100/L	120/L
16 (52)	100/L	100/L	120/L
20 (66)	100/L	100/L	120/L
24 (79)	100/L	120/L	140/L
32 (105)	120/L	130/L	150/L

2.3.3.2. STIFFNESS REQUIREMENTS

Requirements for girder stiffness are to ensure the stability of high-speed rail bridges as well as passenger comfort. To this end, the stiffness limit is defined by the girder deflection caused by live load in terms of the deflection to span ratio (∂/L). However, live loads used to estimate the overall girder deflection (∂) are different depending on the country (Zhou et al. 2012). Rotational stiffness is another important parameter in addition to the translational stiffnesses. For example, girder end rotation is limited, otherwise this rotation may result in pushdown and uplift force on both sides of girder ends which will in turn impact the ballast stability as well as the performance of rail-fastener-slab system in the bridge deck (Figure 2.18).
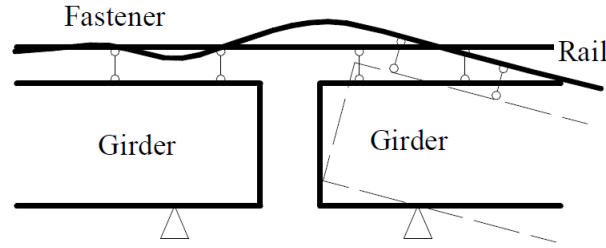
Figure 2.18. Impact of bridge girder end rotation on the rail-fastener-slab system (Zhou et al. 2012)

2.3.3.3. SERVICEABILITY REQUIREMENTS

The serviceability constrations of HSR bridge are defined with various considerations including (i) vertical deflection of the bridge girder to ensure the limited vibration, (ii) beam end rotation to ensure the track stability, (iii) time-dependent long-term deflections, (iv) deformation of substructure that threats the overall structural performance of HSR bridge, and others, which are summarized in Table 2.6. The requirements for a ballastless track bridge are typically more stringent and detailed than the one with ballast track bed.

Requirements of dynamic properties are summarized in Table 2.7 where the passenger comfort level on the HSR train is quantified in terms of Sperling's ride index. Other properties are required for the safety. These are the criteria provided as a guideline, which may require further analysis if one or some of there requirements are not met. For example, if the fundamental frquency of simple beam is lower than the minimum requirement, a more detailed analysis may need to be performed.

Table 2.6. Serviceability constrations for China HSR bridge (Yan et al. 2015)

Contents	Ballast track	Ballastless track
Design life	100 years	100 years
Live load	ZK (0.8 UIC)	ZK (0.8 UIC)
Vertical deflection of beam (mm)	$\leqslant 2.0$	$L/1400$ (250 km/h) $\sim L/1600$ (350 km/h), $L \leqslant 40$ m $L/1400$ (250 km/h) $\sim L/1900$ (350 km/h), 40 m $< L \leqslant 80$ m $L/1000$ (250 km/h) $\sim L/1500$ (350 km/h), $L > 80$ m
Relative beam end vertical rotation in neighboring beams (%)	$\leqslant 0.4$	$\leqslant 0.2$ (cantilever beyond support $\leqslant 0.55$ m) $\leqslant 0.3$ (0.55 m $<$ cantilever beyond support $\leqslant 0.75$ m)
Beam end horizontal rotation (%)	$\leqslant 0.1$	$\leqslant 0.1$
Lateral deflection of beam (mm)	$L/1400$ ($L \leqslant 80$ m) $L/1000$ ($L > 80$ m)	$L/1400$ ($L \leqslant 80$ m) $L/1000$ ($L > 80$ m)
Vertical deflection of track/3 m (mm)	1.5	1.5
Short-term substructure settlement (mm)	30	20
Uneven settlement between neighboring supports (mm)	15	5
Camber after laying track (mm)	20	10 ($L \leqslant 50$ m) Min. ($L/5000$, 20) ($L \leqslant 50$ m)

Table 2.7 Criteria for dynamic properties (Yan et al. 2015)

Contents	Criteria
Fundamental frequency of simple beam (Hz)	$>80/L_\varphi$ $(L_\varphi \leqslant 20$ m$)$ $>23.58L_\varphi^{-0.592}$ $(20$ m $\leqslant L_\varphi \leqslant 96$ m$)$
Derailment coefficient	$\leqslant 0.8$
Wheel loading reducing rate	$\leqslant 0.6$
Peak acceleration (g)	0.35 (Ballast track) 0.5 (Ballastless track)
Vehicle vertical acceleration (g)	$\leqslant 0.13$
Vehicle transverse acceleration (g)	$\leqslant 0.10$
Sperling's ride index	$\leqslant 2.5$ (very good) 2.5–2.75 (good) 2.75–3.0 (satisfactory)

2.3.3.4. OTHER ISSUES

High-speed train may cause aerodynamic impact to nearby infrastructure including buildings, overpasses, etc. However, recent studies showed that the impact can be ignored or at least insignificant if the clearance is over 7.25 m and the train speed is less than 500 kph.

The ballastless track is susceptible to the temperature effect (caused by direct sunlight, etc.) because the track is directly connected to the bridge deck. Therefore, uneven local deformation may occur depending on the temperature distribution. However, recent study (Gong-lian et al. 2013) showed that maximum daily temperature below 35°C may not cause significant impact the structural performance.

Figure 2.19. Beijing-Tianjin HSR bridge (Sweet 2014)

The span of HSR bridge span is mostly standardized to either 24 m or 32 m (Figure 2.19). The manufacturing was done at nearby facilities that is up to 8 km far from the construction site. An 18 axles transportation vehicle is used for the delivery of the casted bridge elements.

2.3.4. TYPICAL SUPER- AND SUBSTRUCTURES

Since 1990, China has looked into the most cost-effective bridge types including simply supported and continuous beams through extensive research programs. They identified the use of simply supported beam is the best option (Figure 2.20). Later, simply supported bridges with longer beams were explored, and 32m main span length is most frequently adopted to construct a HSR bridge in China due to the cost-effectiveness (Figure 2.21). Currently, the majority of HSR bridges in China are simply-supported prestressed concrete box girders with ballastless track (He et al. 2017; Yan et al. 2015) while the continuous beam is used for some short span existing lines.

Figure 2.20. Examples of simply-supported bridges in China (Su et al. 2019)

Figure 2.21. A 32m span simply supported bridge (Yan et al. 2015)

While simply supported bridge is the dominant type in China HSR, integral bridges are often used for cost-efficiency because it eliminates the issues related to maintenance and durability of expansion joints (Figure 2.22). This type of bridge can be further classified into fully integral or semi integral bridges. The superstructure of fully integral bridge is fully tied to the columns and abutments, while the superstructure of semi intergral bridge can move on the bearings.

Figure 2.22. Integral HSR bridges (Su et al. 2019)

2.3.4.1. SIMPLY-SUPPORTED BEAM

Bridge types with simply supported beams may be further categorized depending on the design train speed, track bed type, span length, etc (Figure 2.23). Two standard cross-section of simply supported beams are shown in Figure 2.24. These sections were determined to be the most cost-effective structural solution from experimental tests and numerical analyses. While the single cell box type is used for PDLs and freight-passenger joint lines, the double-cell type is typically used for the inter-city rail. The typical bearing layout for this type of simply supported beam is shown in Figure 2.25. The effectiveness of simply supported beams was proven with the structural performance data and economic evaluation. A typical precast concrete beam of 32m simply supported span with ballastless track bed showed 4.66 Hz natural frequency, 1/5147 of vertical deflection to span ratio (∂/L), and 0.075 % of beam end rotation. This performance could be obtained with a lower cost compared to other types.
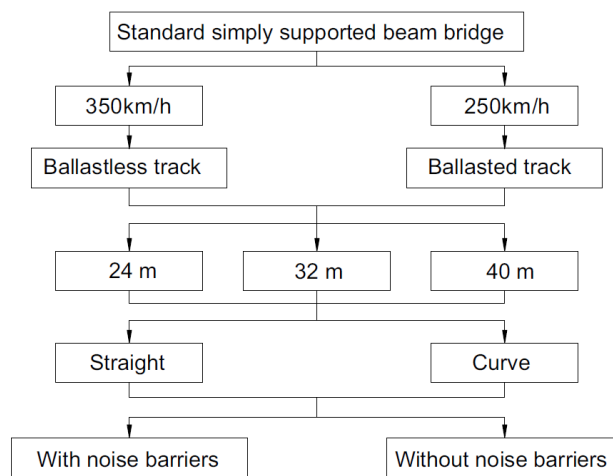
Figure 2.23. Simply supported HSR bridges with different design parameters (Yan et al. 2015)
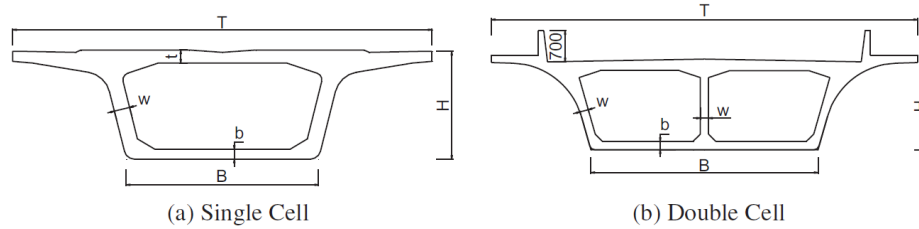
Section Type	Width (mm)	350 km/h		250 km/h	
		Ballast	Ballastless	Ballast	Ballastless
(a)	T	12600	12000	13000	11600
Single	B	5500	5500	5740	5300
Box	H	3072	3078	2700	2700
	t	384	300	340	285
	b	280	280	300	280
	w	450	450	475	450
(b)	Item	250 km/h			
Double	(mm)	Ballast		Ballastless	
Box	T	12200		11600	
	B	6500		6500	
	H	2700		2700	
	t	240		240	
	b	240		240	
	w	240		240	

Figure 2.24. Typical cross section of simply supported beam in HSR of China (Yan et al. 2015)
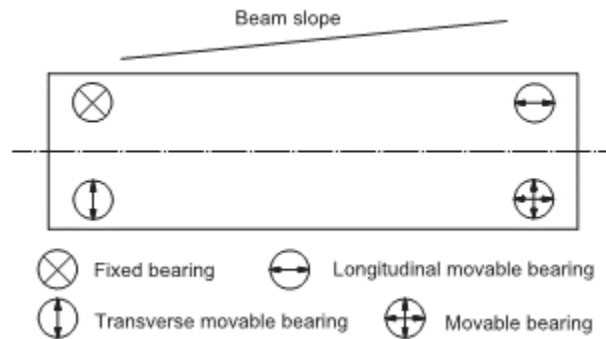
Figure 2.25. Bearing layout for simply-supported bridge (Yan et al. 2015)

2.3.4.2. CONTINUOUS BEAM

Bridge with continuous beams can be either with uniform depth or variable depth. The uniform-depth continuous beams typically consist of two to three spans. Span arrangement of 32 + 48 + 32 m is typically used for the continuous beam bridge, e.g., Beijing–Shanghai line. Figure 2.26 and Figure 2.27 show frequently used uniform and variable depth continuous beams in China HSR bridges. Greater section depths are typically adopted to limit short- and long-term deflections at the bridge surface level along with increased number of presstressed tendons. Therefore, continuous beam for HSR bridge commonly haa a thicker depth compared to that of conventional railway bridges.

Average speed (km/h)	Span (m)	Top width (m)	Bottom width (m)	Top flange (cm)		Bottom flange (cm)		Web (cm)	
				M	S	M	S	M	S
350	2 × 24	13.4	6.06	30	45	50	110	30	65
	3 × 24	13.4	6.06	30	45	50	110	30	65
	2 × 32	13.4	5.9	30	45	50	110	30	65
	3 × 32	13.4	5.9	30	45	50	110	30	65
	2 × 40	13.4	5.74	30	45	50	110	30	65
250	2 × 24	13.0	5.92	25	25	50	113	30	65
	3 × 24	13.0	5.92	25	25	50	113	30	65
	2 × 32	13.0	5.86	25	25	50	113	30	65
	3 × 32	13.0	5.86	25	25	50	113	30	65
	2 × 40	13.0	5.68	25	25	50	113	30	65

Note: M means the mid-span of the beam; S means the beam end of the side span.

Figure 2.26. Uniform depth continuous beam in China HSR (Yan et al. 2015)

Type	Span (m)	H (m)		B1 (m)	B2 (m)		D1 (cm)		D2 (cm)		W (cm)	
		Mid	Side		Mid	Side	Mid	Side	Mid	Side	Mid	Side
250 km/h ballast track bed	32 + 48 + 32	3.4	2.8	12.2	5.56	5.74	69	69	90	60	95	70
	40 + 56 + 40	4.4	2.8	12.2	6.35	5.74	69	59	100	60	110	70
	40 + 64 + 40	5.2	2.8	12.2	6.35	5.74	69	59	100	60	976	70
	48 + 80 + 48	6.4	3.8	12.2	6.4	6.4	78	78	100	75	100	75
	60 + 100 + 60	7.2	4.6	12.2	6.4	6.4	64	69	120	80	100	80
350 km/h ballastless track bed	40 + 56 + 40	4.35	3.05	12.0	7.7	6.7	40	65	80	60	80	60
	40 + 64 + 40	6.05	3.05	12.0	7.7	6.7	40	65	80	60	80	60
	48 + 80 + 48	6.65	3.85	12.0	7.7	6.7	40	65	100	80	90	60
	60 + 100 + 60	7.85	4.85	12.0	7.9	6.7	40	65	120	80	100	80

Note: Mid means the mid-span of the beam; Side means the end of the side span.

Figure 2.27. Variable depth continuous beam in China HSR (Yan et al. 2015)

2.3.4.3. DECK

Typical deck system was adopted for rapid HSR bridge construction in China with reserved spaces designed for auxillary equipment and facilities including cable conduits, noise barrier, etc. Ballastless track bed was primarily considered for PDL with a train speed higher than 300 kph and also for freight-passenger joint lines with 250 kph train speed in average. The drainage system slightly differs depending on the track bed type as shown in Figure 2.28.
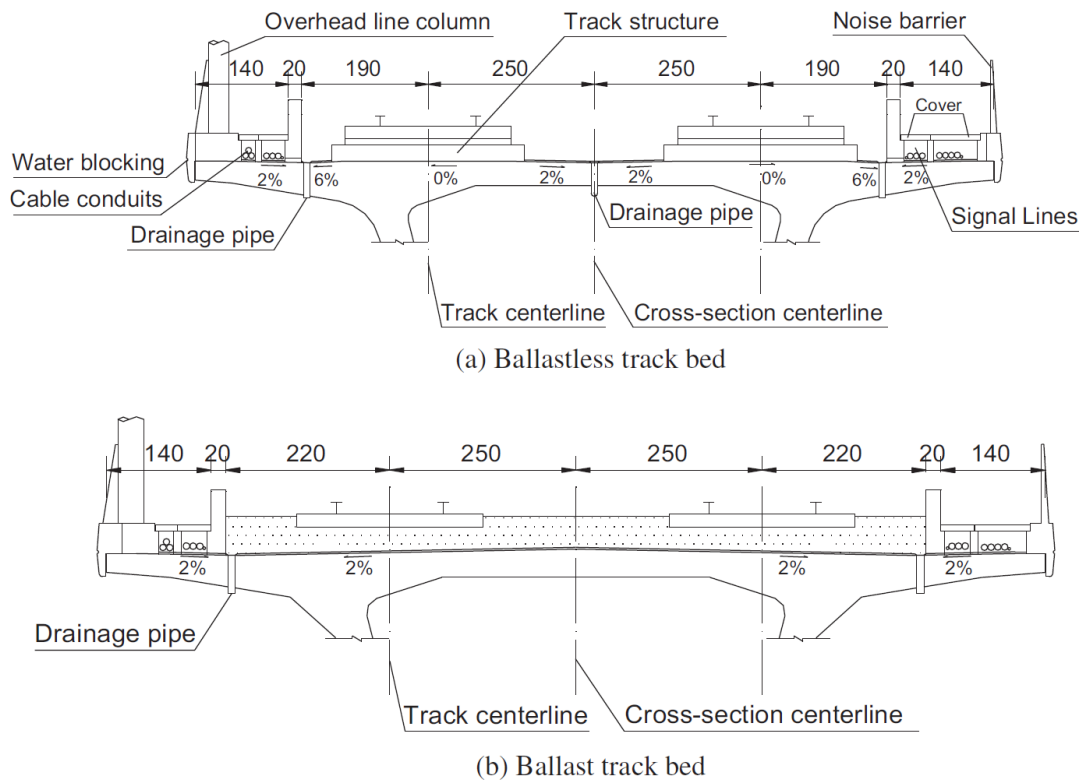
Figure 2.28. Bridge deck facilities in HSR of China (Yan et al. 2015)

2.3.4.4. PIERS

Two frequently used piers have the round ended and rectangular cross sections in China HSR bridges. On top of the criteria for soil strength and stability, particular consideration should be paid to differential settlement issue to determine the HSR bridge foundation. Four different diameters of 1.0, 1.25, 1.5, and 2.0 m were commonly considered driven pile groups. Pile spacing is usually twice the diameter of the pile (Yan et al. 2015).

2.3.5. TRACK SYSTEM

HSR system can be categorized into ballasted track and ballastless track system based on the track bed, and the ballastless track system can be further classified into discrete or continuous systems as shown in Figure 2.29. UIC specifies rail expansion devices (REDs) need to be used in the ballasted and discrete ballastless track systems to allow for the adjustment of rail length, and in return to alleviate additional stresses imposed on the rail caused by temperature issue, relative displacement between rail and deck, etc (Figure 2.30). However, REDs are not required for continuous ballastless track due to the sliding layer (Figure 2.29) that reduces the interaction between the track and bridge. Therefore, the continuous ballastless track is beneficial as it alleviates the issues related to track maintenance and service life.

Track type	Diagram
Ballasted	
Discrete ballastless	
Continuous ballastless	

Figure 2.29. Type of railway track (Su et al. 2019)

Figure 2.30. Rail expansion device (Connor 2019)

2.3.5.1. BALLASTLESS TRACK

The ballastless track has been extensively used for PDLs in China with many benefits including easy maintenance, lower weight, better control over the surface smoothness, etc. (He et al. 2017). The ballastless track systems were particularly preferred for the short to medium span HSR bridges. The construction cost of ballastless track is higher compared to that of ballasted track, but the maintenance cost is much lower in the long-term. China developed the HSR ballastless track technology based on Japanese and German standards, and the China Railway Track Network (CRTS) is constructed with four different types as shown in Figure 2.31: (i) Slab Type I based on Japanese Shinkansen track, (ii) Bi-Block Sleepers Type I based on German RHEDA 2000 track (iii) Slab Type II based on German Bögl track, and (iv) Slab Type III independently developed by China.

30

No.	Diagram	China
1		CRTS Slab Type I
2		CRTS Bi-Block Sleepers Type I
3		CRTS Slab Type II
4		CRTS Slab Type III

Figure 2.31. Slab track in China (Su et al. 2019)

2.3.5.2. CONTINUOUS-WELDED RAILS - STRUCTURE INTERACTIONS

Continuous-Welded Rails (CWR) is made of multiple rails that are joined by welding, thus a several miles long uninterrupted track can be formed. High speed rail often demands the use of CWR to facilitate passenger comfort for travel, for which a clear understanding of CWR-structure interactions is necessary including temperature effect on the track deformation, braking forces by train, etc. The longitudinal stiffness of substructure is an important parameter in designing the HSR with CWR, which is summarized in Table 2.8.

Table 2.8. Longitudinal stiffness limits for top of piers and abutments (Zhou et al. 2012)

Type	Span m (ft)	Min. Longitudinal Stiffness, kN/cm (kip/in)	
		Double-Track	Single-Track
Pier	≤ 12 (39)	100 (57)	60 (34)
	16 (52)	160 (91)	100 (57)
	20 (66)	190 (108)	120 (69)
	24 (79)	270 (154)	170 (97)
	32 (105)	350 (200)	220 (126)
	40 (131)	550 (314)	340 (194)
	48 (157)	720 (411)	450 (257)
Abutment		3,000 (1,713)	1,500 (857)

2.3.6. CONSTRUCTION

Multiple construcion methods have been adopted to erect bridge beams as shown in Figure 2.32. These methods include the conventional cast-in-place method (Figure 2.32a), cantilever method (Figure 2.32b), rotation method (Figure 2.32c), incremental launching method, etc. The cast-in-place method is suitable for low clearance bridge construction on a good soil condition. While the cast-in-place method is preferred for uniform depth beams, the cantilever method is frequently used for construction of variable depth beams. The rotation methods is preferred for bridge contruction over existing lines. The incremental launching method is often used with precast beams because it reduces the construction time by launching the beams in series. The beams were precasted in local factories that were contracted at every 30-40 km along the HSR line. Transported beams were located in place by erecting equipment (Figure 2.33). The bearings were placed before the installation of beams, and 2 mm of tolerance was allowed in the bearing height difference.

(a) Cast-in-place (b) Cantilever

(c) Rotation

Figure 2.32. Construction methods for HSR continuous beams (Yan et al. 2015)

Figure 2.33. Precast and erection (Yan et al. 2015)

2.3.7. CHALLENGES FOR RAILWAY BRIDGES

2.3.7.1. LONGER SPANS

Construction of longer span bridges are often required to cross a wide area, valleys, rivers, etc. For example, there are many big rivers in China that are in HSR lines such as Yangtze river. With the demands of longer span HSR bridges, the span length increases recently as shown in Figure 2.34. A variety of bridge types has been considered and will be constructed such as cable-stayed bridge and suspension bridge as shown in Figure 2.35. As of today, Tongling Yangtze River bridge on Hefei–Fuzhou HSR line has the longest main span length of 630 m (Qin and Gao 2017). However, longer span bridges are currently designed and/or constructed such as Wufengshan bridge and Hutong bridge on Yangtze River that has 1092m main span length (Figure 2.35). The design operation speed of these longest span bridges is 250 kph, but Jinan Yellow River Bridge with 168m main span length has the maximum design operation speed of 350 kph in China. Simply supported beams were typically considered for the non-main span for Wufengshan bridge. These HSR bridges are typically designed to support multi-modal transportation including highways, metro as well as HSR to save land use and construction cost. (Su et al. 2019)
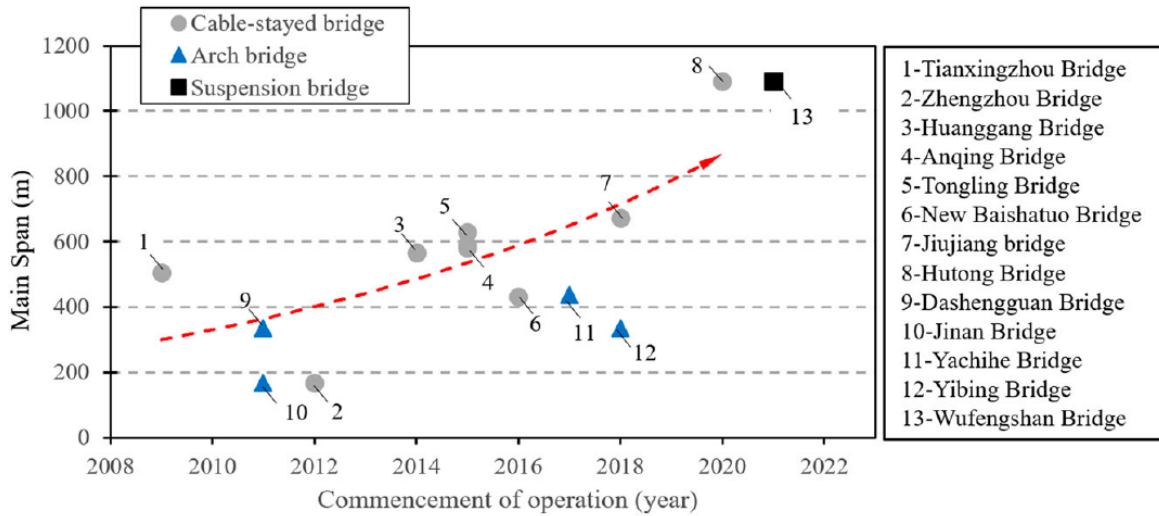
Figure 2.34. Long span HSR bridges construction in China (Su et al. 2019)
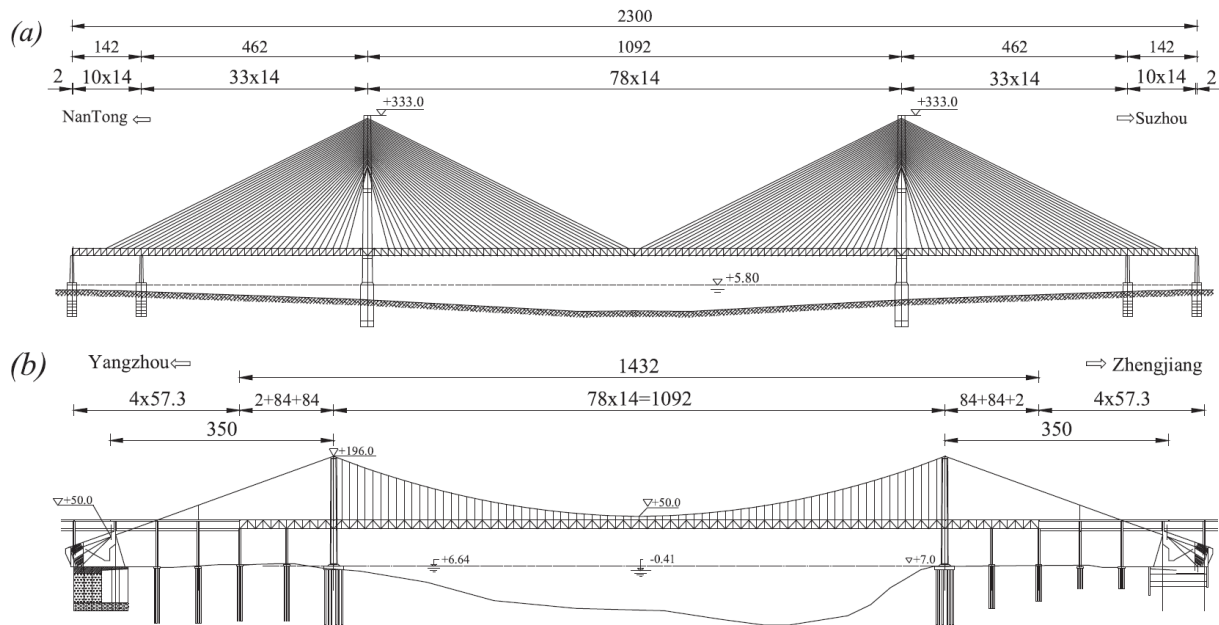
Figure 2.35. Examples of long span HSR bridges in China: (a) Hutong Yangtze River Bridge; (b) Wufengshan Yangtze River Bridge; Units are shown in meters (Su et al. 2019)

2.3.7.2. LIGHT STRUCTURES

The design of HSR bridges can be improved in terms of construction cost by using innovative technology optimizing material use, enhancing aesthestics while meeting the requirement of structural safety and serviceability. There is, however, a perspective that current China code may be too conservative. For example, Fanjiashan Bridge, a standard 32 m simple beam bridge based on the current code was tested with a CRH 380 high speed train (Figure 2.17). The mid-span

deflection was less than 0.5 mm when the train was unloaded (Figure 2.36) and about 1 mm when fully loaded, which is far less than the current limit of deflection-span ratio 1:1600 (Su et al. 2019).
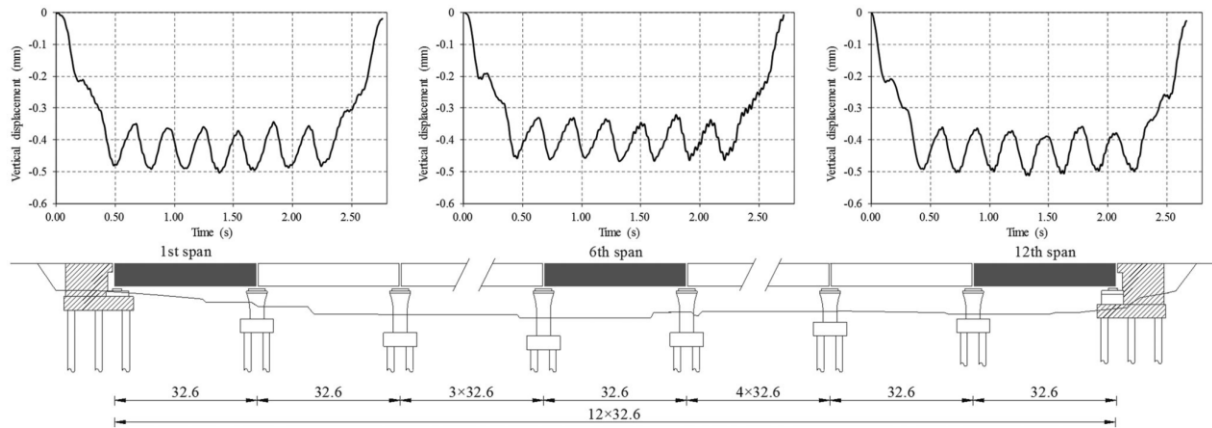
Figure 2.36. Mid-span deflection of Fanjiashan bridge; All units are meters (Su et al. 2019)

The wide use of simple beam concrete bridge in China HSR lines was mainly to faciliate the construction speed with a standardized material and structural type, but use of different materials and types may be able to manifest lighter structures. For example, Q420 and Q500 high performance steel with yield strengths of 420 and 500 MPa were used for Dashengguan Bridge and Hutong Bridge. Slim and yet robust load bearing system can be also realized with different types such as steel bridges, steel-concrete composite bridges.

2.3.7.3. DEFLECTION CONTROL

Robust deflection control is a challenging issue in designing HSR bridges considering the train speed is high as low as 250 kph. The requirement for ballastless track bridge is higher than the ballasted track bed. While the span lengths of recently constructed HSR bridges tend to be longer, no detailed guide has been given to the deflection limit. On the other hand, the deflection limits on the short span bridges are relatively clear which are defined in terms of four aspects: (i) vertical deflection should be less than 2 mm, (ii) the beam end rotation should be less than 0.4%, (iii) time dependent long-term deflection should be less than L/1000 where L is in m while the result should be interpreted in mm, and (iv) longitudinal deformation of substructure. China Ministry of Railways also defined a set of the deflection requirements on the continous short-length beams. For example, (i) the beam end rotation should be less than 0.2% for ballasted track bed and 0.1% for a ballastless bed and (ii) long-term vertical deflection should be less than 1.1 L/1000 where L is the main span, and the lateral deflection should be less than L/4000. However, these requirement were not set for other types of bridges, e.g., cable-stayed bridge. The dynamics of HSR bridges are important to understand to limit the deflection caused by dynamic responses. This may caused by seismic excitation, aerodynamic loading, thermal effect, etc. The dynamic responses of China HSR bridges were extensively studied (Hu et al. 2014).

2.3.7.4. CONCRETE SHRINKAGE AND CREEP

Concrete bridges are inevitably under the influence of shrinkage and creep effects that may impact the train performance and operation safety issue due to the shrinkage and creep induced

bridge structure deformation. Chen and Han (2018) studied the effects of shrinkage and creep on the dynamics of HSR bridge using a fully coupled train-track-bridge model (Figure 2.37). Their study considered a 32 m span simply supported box girder bridge because it is the most popular type of HSR bridge constructed in China. The train, track, and bridge models were developed and coupled for the interactions as shown in Figure 2.37. The cross-sections of beams considered in the analysis is shown in Figure 2.38. The JTG 2012 shrinkage and creep models defined in "Code for Design of Highway Reinforced Concrete and Prestressed Concrete Bridges and Culverts (JTG D62-2012)" (China Communication Press 2012) were considered for the analysis of the effects. Using the the shrinkage strain and the creep coefficient in the model, the time-dependent displacement at the mid-span of the bridge was estimated with the maximum deformation to be 6.85 mm as shown in Figure 2.39. Their study concluded that the shrinkage and creep have little impact on the structrure while it makes some distortion which results in tracks deformed. However, impact was shown to be more significant on the train's dynamic performance and passenger comforts.
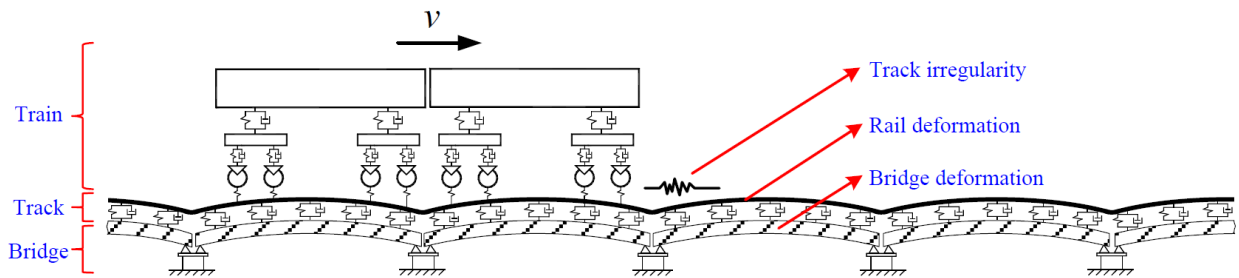
Figure 2.37. Coupled train-track-bridge model to study the effect of shrinkage and creep (Chen and Han 2018)
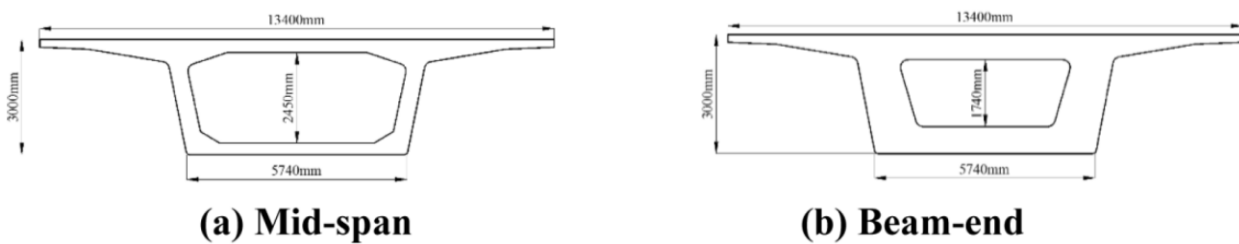
Figure 2.38. Cross-sections of the beams (Chen and Han 2018)
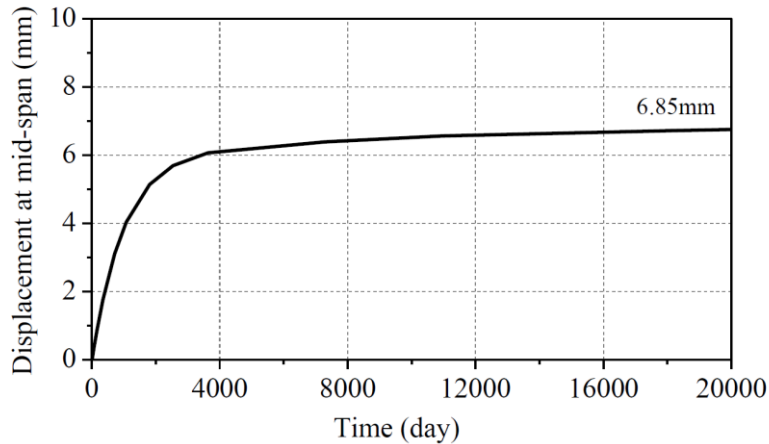
Figure 2.39. Displacement at the bridge mid-span (Chen and Han 2018)

2.3.8. MEDIUM SPAN (100–200 M)

Typical medium span bridges are considered to have a main span of about 100 m, which are often considered to cross existing lines of highways or railroads. While the prestressed concrete bridge is considered in many cases, other types such as tied steel arch or rigid frame were constructed recently as shown in Figure 2.40. A hybrid type integrating the steel arch and rigid frame has been also constructed as shown in the table (Hu et al. 2014). Sections below describe the three types of medium span bridges recently constructed.

Structural type	Bridge name	Main span (m)	HSR segment	Built
Tied steel arch	East Lake	112	Wuhan-Guangzhou	2008
	Hujiawan	112	Wuhan-Guangzhou	2008
	Liangjiawan	112	Wuhan-Guangzhou	2008
	Tingsihe	140	Wuhan-Guangzhou	2008
	Yandangshan	2 × 90	Ningbo-Wenzhou	2009
	Mulanxi	128	Fuzhou-Xiamen	2009
	Xinkaihe	138	Harbin-Dalian	2012
Rigid frame	Tianluo	160	Wenzhou-Fuzhou	2008
	Baimahe	3 × 145	Wenzhou-Fuzhou	2008
	Liuxihe	168	Wuhan-Guangzhou	2009
	Zinihe	2 × 168	Guangzhou-Shenzhen	2010
Hybrid steel arch with concrete girder	Kunyang	136	Wenzhou-Fuzhou	2007
	Yichang Yangzte	2 × 275	Yichang-Wanzhou	2008
	Shawan Channel	160	Guangzhou- Shenzhen	2009
	Liugangyong	160	Guangzhou- Hong Kong	2010
	Xiaolan Channel	220	Guangzhou-Zhuhai	2010
	Zhenjiang Channel	180	Beijing-Shanghai	2010
	Xianyang West	136	Xi'an-Baoji	2012
	Songhuajiang Channel	3 × 156.8	Harbin-Qiqihar	2013

Figure 2.40. Types of medium span HSR bridges in China (Hu et al. 2014)

2.3.8.1. TIED STEEL ARCH

Tied steel arch HSR bridges in China can be classified into (i) tubular arch and (ii) box arch types by the cross-section of the arch rib. The tubular arch type may be designed using concrete filled steel tubes (CFST). A 112 m long tubular arch type HSR bridge was standardized with inclined hangers that can be adopted to facilitate the bridge construction. Hujiawan bridge is an example of tubular arch type HSR bridge (Figure 2.41a). The standardized tubular arch type's rise to stretch

ratio is 1/5 with a 22.4 m height from the top to the deck level. Two identical circular tubes were used to form uniform-depth arch ribs which has 1.28 m diameter and 18 mm thickness. Two major arch ribs were designed to be inclined inward by approximately 9 degrees, which was proven to provide enhanced structural performance. The hangers are located 8 m apart. Pre-stressing tendons are part of the design in the main girder with 2.5 m depth and 17.8 m width. Tingsihe Bridge in Figure 2.41b is an example of box arch type that supports a double track HSR line. This bridge is 140 m long and the rise to stretch ratio is 1/5. The box arch with a rectangular cross section has a varying depth from 3 to 4.5 m while it is 2 m wide. Holes are placed in the hangers to improve the aerodynamic behavior. The cantilever construction method was used (Figure 2.32b) without using falsework.

Figure 2.41. Tied steel arch HSR bridges: (a) Hujiawan Bridge and (b) Tingsihe Bridge (Hu et al. 2014)

2.3.8.2. RIGID FRAME

Use of rigid frame between beam and column typically enables to have a larger span length bridge with a enhanced vertical stiffness. Despite of the advantage, rigid frame has been selectively used for good soil conditions in the construction site. Examples include Tianluo Bridge shown in Figure 2.42 which have similar configurations: Tianluo Bridge is composed of three spans of 88+160+88 m. Tianluo Bridge is constructed over a shallow strait and designed to resist wind speed of up to 56 m/s. As shown for Tianluo Bridge, a rigid frame bridge is often designed with two legs to enhance the overall stiffness of the bridge. A 8m spacing is used for the two legs in case of Tianluo Bridge, and the ratio of height to span length is 1/5. This ratio was considered to ensure a balanced stress distribution between the legs and the beam and improved longitudinal stiffness of the beam. The cross-sectional dimension of the leg is 10 m × 2.2 m each. C45 grade concrete was used for the legs and C30 grade concrete was used for the pile cap sitting on 12 drilled piles of 2.5 m diameter. The superstructure cross section of Tianluo bridge has a box shape with top and bottom widths of 13 m and 8.2 m, respectively. The pier dimension at the rigid connection has a box geometry with 9.8 m depth. Prestressing tendons are used in all three directions to make sure the the structure is under compressive stresses. The pulling stress in the presstressing jacks were in a range of 1230 to 1300 MPa. C60 Grade concrete was used because of high corrosion potential caused by the strait. Cantilever construction method was adopted for rigid frame construction.

Figure 2.42. Tianluo Bridge (Hu et al. 2014)

2.3.8.3. HYBRID STEEL ARCH FRAME

While steel arch and rigid frame systems have been adopted for mid-span bridge construction, hybrid type bridge that takes advantages of both systems was also considered as an alternative solution. Kunyang Bridge and Yichang Yangtze River Bridge shown in Figure 2.43 are the examples of the hybrid system. Kunyang Bridge has three spans of 64+136+64 m that supports a double-track joint passenger freight HSR line. The girder used in Kunyang Bridge is 11.5 m wide and has a double-box cross section that is 3.5 m deep at the mid-span and 7.0 m deep at the supports. The dimension is relatively smaller than that of the rigid frame bridges because the load is partially supported by the steel arch. The main arch's raise to stretch ratio is 1/5 and the roof tip is 27.2 m high. The arch ribs have uniform depth that is constructed with twin circular tubes of 2.8 m diameter. Nine lateral truss bracings are connected to the two arch ribs and 14 pairs of hangers were placed at 8 m spacing. The vertical deformation by dead load is 35 mm (Hu et al. 2014).

Figure 2.43. Kunyang Bridge (left) (Skyscraper City 2019) & Yichang Yangtze Bridge (right) (Ed Kay 2009)

2.3.9. LONG SPAN (200–500 M)

2.3.9.1. STEEL TRUSS ARCH

A economically viable steel truss arch would have a span of 300 m up to 400 m. Dongping Bridge (Figure 2.44a) is the first of this kind that was constructed in 2009 in the Wuhan-Guangzhou line. The bridge was built with high-performance steel that has a yield strength of 370 MPa to support four-track railway. The three spans are 99+242+99 m. Later in 2011, a longer span Dashengguan

Bridge (Figure 2.44b) was constructed with steel truss in the Beijing – Shanghai line. Dashengguan Bridge supports six track railway accommodating two HSR, two regular trains, and two subway trains and the steel truss bridge has 108+192+336+336+192+108 m spans. Similar to Dongping Bridge, the truss arch rib has a varied depth from 12 m at the top to 96 m at the deepest. This Dashengguan was built with steel that has even higher yield strength (420 MPa). The hybrid type of truss was used in the design of Minjiang Bridge (Figure 2.44c) with 99+198+99 m span (Hu et al. 2014).

(a) Dongping Bridge

(b) Dashengguan Bridge

(c) Minjiang Bridge

Figure 2.44. Long-span steel truss arch HSR bridges (Hu et al. 2014)

2.3.9.2. CABLE-STAYED BRIDGE WITH TRUSS GIRDER

In China, a cable-stayed system with truss girders has been a popular choice for long-span HSR bridges because it can accommodate different traffic modes at the same time. A good example is the Tianxingzhou Bridge (Figure 2.45a) with 98+196+504+196+98 m span (1092 m, in total). The bridge was designed to accommodate four-track lines on top of six-lane highways. The top level of truss system was used for highway traffic that is designed as a compsite system having 158 m long concrete plates from each ends and a 756 m long steel plate in the middle. The lower level is

for HSR lines for which ballast track bed was adopted. The reinforced concrete tower is 188.5 m high from the top of pile cap. Other cable-stayed bridges with truss girder include Yujiang Bridge (Figure 2.45b) with 36+96+228+96+36 m span and 105 m high concrete pylons constructed to serve the double HSR tracks with a design train speed of 300 km/h, and Zhengzhou Yellow River Bridge (Figure 2.45c), an eight-span (120+5x168+120 m) extra-dose bridge with six 37m high steel pylons (Hu et al. 2014).

(a) Tianxingzhou Bridge

(b) Yujiang Bridge

(c) Zhengzhou Bridge

Figure 2.45. Cable-stayed HSR bridges with truss girder (Hu et al. 2014)

2.3.9.3. SUSPENSION BRIDGES

The suspension bridge has not been a popular choice for railway because of the inherently large deformation. However, the recent advances in bridge construction has made possible the suspension technique as a good desgin option for a railway bridge. Examples include Jinshajian Bridge and Wufengshan Bridge shown in Figure 2.46. Jinshajian Bridge is to support the Lijiang-Shangri-la intercity railway and has span lengths with 98+660+98 m. Wufengshan Yangtze River Bridge is currently the longest suspension HSR bridge in the world with the spans with 84+84+1092+84+84 m (He et al. 2017).

(a) Jinshajiang suspension bridge   (b) Wufengshan bridge

Figure 2.46. Suspension HSR bridges in China (He et al. 2017)

2.3.10. PRECAST SEGMENTAL CONSTRUCTION

Precast segmental construction has been increasingly adopted in the bridge construction around the world because its many advantages including assured quality with the precast segments and faster construction as formwork is not needed. However, this construction method is relatively less popular in China because of the necessity of precise dimensional control of the precast elements. Furthermore, the structural design is affected by the construction method, e.g., the profiles of tendons are determined by how the construction is proceeded, which resulted in the late adoption of construction method. There are variations in the precast segmental construction methods including the precast segmental balanced cantilever construction (Section 2.3.10.1), precast segmenetal cable-stayed construction (Section 2.3.10.2), etc.

Liuhe bridge (Figure 2.47) is the first bridge constructed with the precast segmental method in China. Liuhe Bridge has three spans of 42 m lengths with a dual carriage ways. The precast segmental construction was adopted and the long line casting method was used to precate the bridge segments. A launching gantry was used to transport all segments into the place. The installed tendons in the bridge are shown in Figure 2.48.

Humin Elevated Viaduct is located in Shanghai and the construction was completed in 2003 (Figure 2.49). This Humin Elevated Viaduct is the second bridge constructed adopted the precast segmental construction method although only two sections (each composed of ten spans) were built with this method while the rest was constructed with the convenstional construction method sing the monolithic scaffolding. The length of viaduct is 5.56 km in length and the spans are in the range of 30 to 35 m, and each of which is composed of 11 to 13 segments. The segments are 2 m, 2.5 m, or 3 m in lengths and 2.1 m in height (Li et al. 2008).

Figure 2.47. Liuhe river bridge (Li et al. 2008)

Figure 2.48. Installed tendons in Liuhe river bridge (Li et al. 2008)

Figure 2.49. Humin Viaduct construction (Li et al. 2008)

Figure 2.50. Full span pre-casting (Rosignoli 2016)

China made significant investment on HSR bridges as China HSR lines are largely composed of bridges. For example, the 113 km Beijing-Tianjin route in China has 100 km of bridges (88%), and the 1318 km Beijing-Shanghai route has 1140 km of bridges (86%). Construction of HSR embankment is expensive with many requirements for safety and ride comfort. For example, the HSR embankments need costly transition wedges at the abutments. Long embankments may have many overpasses for better ground mobility. For these reasons, a shallow embankments were considered, but in case deep foundation option is cheaper, the prestressed concrete bridges were built as alternative to the embankment. Short prestressed concrete spans are often employed to better control the deformation and dynamic responses of the bridge structure. As a result, a large number of equal short spans were needed, for which precasting facilities and special transportation vehicles were developed.

2.3.10.1. PRECAST SEGMENTAL BALANCED CANTILEVER CONSTRUCTION

2.3.10.1.1 SECOND JIUJIANG BRIDGE

The Second Jiujiang Bridge constructed in 1996 is located in Guangdong Province and is the longest bridge in China among the bridges that adopted the precast segmental balanced cantilever construction. The longest cantilever length is 78.5 m and the 3m closure was finished with cast-in-place method. All the pre-stressing structure was internally placed.

Figure 2.51. Second Jiujiang Bridge (Li et al. 2008)

2.3.10.1.2 SUTONG CABLE-STAYED BRIDGE

The construction of Sutong Bridge was completed in 2007 with a total length of 8146 m in the deep water of Yangtze River (Figure 2.52). Launching gantry was used to transport the precast segments in place (Figure 2.53). Short-line match casting was used and the geometry errors were progressively corrected. Placement of unique segments were carefully planned such as the anchorage segments and deviator segments (Figure 2.54).

Figure 2.52. Sutong Bridge in deep water (Li et al. 2008)

Figure 2.53. Launching gantry adopted for construction (Li et al. 2008)

Figure 2.54. Deviator segments placement (Li et al. 2008)

2.3.10.2.   PRECAST SEGMENTAL CABLE-STAYED BRIDGE

2.3.10.2.1 YUNYANG BRIDGE OVER THE HANJIANG RIVER

Completed in 1993 and located in Hubei Province, Yunyang Bridge is a precast concrete bridge with cable-stayed double pylons that support 3 spans of 86 m + 414 m + 86 m (Figure 2.56). The concrete girder has a box-section with three cells. The segments have 3.7 m and 4.3 m in lengths and the weight of precast segments a weight up to 100 tons.

Figure 2.55. Yunyang Bridge under construction (Li et al. 2008)

2.3.10.2.2 *YILING BRIDGE OVER THE YANGTZE RIVER*

Located in in Yichang City in Sichuan Province, Yiling Bridge crossing Yangtze River is a 4-span cable bridge with a total length of 936 meters (composed of two 348 m main spans and 120 m side spans) as shown in Figure 2.56. The concrete girder has a box-girder of three cells with 23 m width that is composed of the precast segments has 3 m length. The two main spans (of 324 m) were built using the balanced cantilever system using the precast concrete girder.
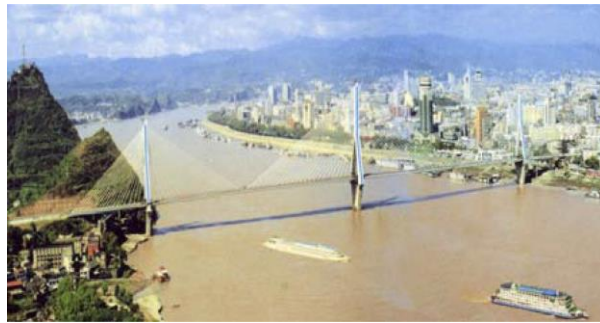
Figure 2.56. Yiling Bridge (Li et al. 2008)

2.3.11. HIGH PERFORMANCE SELF-COMPACTING CONCRETE

China has extensively used high performance self-compacting concrete (SCC) as a filling layer due to its great workability as well as to enhance the time dependent shrinkage and creep deformation of the HSR bridges. To this end, various efforts were made, e.g., the aggregate design was re-visited. Further, viscosity-enhancing compound was adopted to enhance the bonding in the prefabricated track slab. Calcium sulfoaluminate–based expansive agent was added to alleviate the shrinkage and creep deformation of SCC (Long et al. 2018).

2.4. EUROPE

Several European countries have implemented high-speed rail, with France, Italy, and Germany starting operations from 1981-1988. Spain, Belgium, the UK, Switzerland, and the Netherlands followed in the 1990s-2000s; Austria and Poland extended the reach of HSR in the 2010s. There are several more HSR lines under construction in other European countries (International Union of Railways 2015).

In Germany, simply supported post-tensioned concrete box girders are the most common HSR bridge type (Figure 2.57); however, other types have also been implemented in recent years. The history of German HSR can be divided into two eras corresponding with two bridge design guidelines: 1988-2006, and 2007-present (Kang et al. 2018).

In the initial years of German HSR development, simply supported spans were the most common and were usually 44 m. or 58 m. A standard cross-section of a simply supported 44 m. span is shown in Figure 2.57. This cross-section results in a span-depth ratio of 11:1, which is similar to those used in Chinese HSR bridges of similar spans (Yan et al. 2015). The distribution of HSR bridge types built in Germany from 1991-2006 is shown in Figure 2.58.
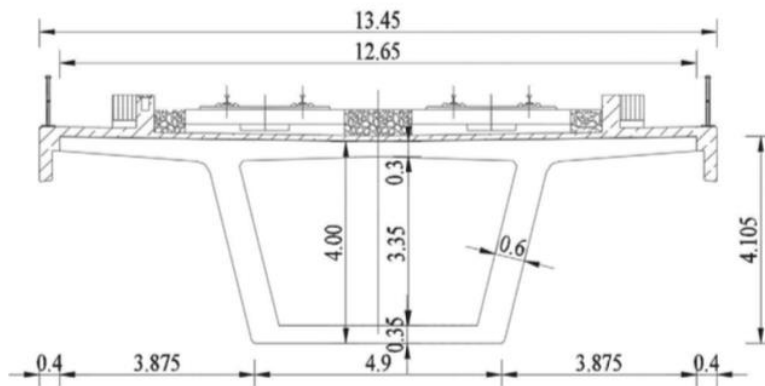
Figure 2.57. Cross-section of a 44 m. German simply-supported HSR bridge; Dimensions in m. (Kang et al. 2018)
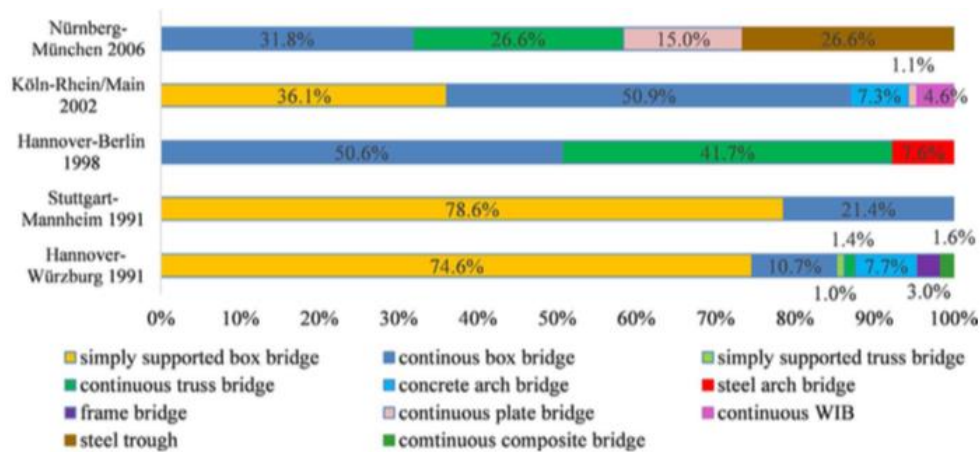
Figure 2.58. HSR bridges built in Germany from 1991-2006 (Kang et al. 2018)

In the mid-2000's, the German railway company Deutsche Bahn started encouraging innovative ideas that deviated from standard designs. The new guideline "Leitfaden Gestalten von Eisenbahnbrücken" (translated to "Design of Railway Bridges") was published in 2008. Rather than providing a set of standard designs, the guideline suggested design recommendations and provided examples of current innovations in railway bridge design but did not enforce them as a general rule. As a result, the variety of bridge types increased from 2007 onwards (Kang et al. 2018). The distribution of HSR bridges built in Germany from 2007-2017 is shown in Figure 2.59.
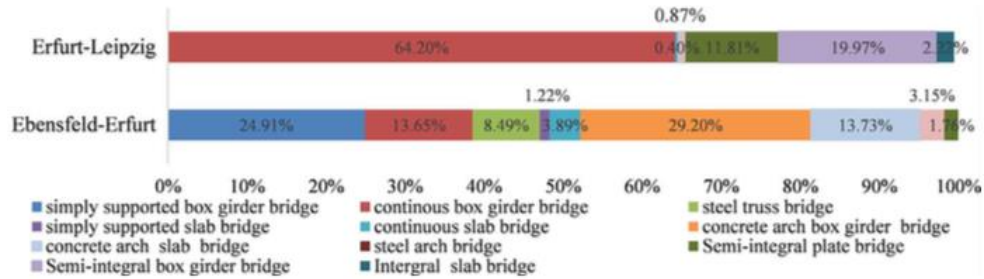
Figure 2.59. HSR bridges built in Germany from 2007-2017 (Kang et al. 2018)

Meanwhile, innovative HSR bridges are also being developed in Spain. A significant portion of Spanish HSR bridges exist in regions of moderate seismic hazard. One such bridge is the Archidona Viaduct in Southern Spain (Carlos and Miranda 2013).

The Archidona Viaduct is a composite steel-concrete viaduct in the Cordoba-Granada HSR line measuring 3150 m. (1.97 mi.) long. Its design constraints included the long length of the bridge; the desire to avoid track joints along the span; and the site, which had poor geotechnical soil properties and an expected peak ground acceleration of 0.14g for a 500-year return period.

To satisfy the previously outlined design constraints, the bridge was designed as a continuous beam with only two track expansion joints placed at the abutments. The viaduct consists of thirty typical 50 m. (164 ft.) spans, with a 35 m. (114 ft.) end span on either end of the bridge. These span lengths enabled the bridge to be constructed using cranes to erect prefabricated elements.

Due to the limited dilation length of the two expansion joints, longitudinal displacements needed to be kept at a minimum. A composite steel-concrete superstructure was selected in lieu of a typical prestressed concrete girder to minimize shrinkage and eliminate creep strains. The composite girder would also have less mass than an equivalent concrete girder, which helps reduce seismic forces on the bridge (Millanes et al. 2014). A typical cross-section is shown in Figure 2.60. The additional concrete on the bottom of the section helps with resisting negative bending moments and adds torsional stiffness (Manterola and Escamilla 2014).

Figure 2.60. Typical cross-section of Archidona Viaduct (Millanes et al. 2014)

To resist horizontal forces, the bridge has one fixed point in the middle of the total length. This central pier resisted all longitudinal forces (including braking and seismic actions) on the bridge. The other piers used spherical sliding bearings to allow longitudinal movement while resisting transverse displacement with a central shear key. A typical pier is shown in Figure 2.61.

Figure 2.61. Typical pier of Archidona Viaduct (Carlos and Miranda 2013)

2.5. *USA*

While the High-speed rail (HSR) efforts in the U.S. have been made as early as 1965, an operational HSR line is yet to be established. In 2008, the California HSR network was authorized by voters with Proposition 1A which would mark the largest project for American HSR, connecting the bay area to southern California. At the time of the proposal, the project was sold to voters with a projected cost of $33.6 billion; however, by 2018 the California High-Speed Rail Authority revised its estimate to $77.3 billion and up to $98.1 billion anticipating a 2033 completion year (California High-Speed Rail Authority 2018). The most construction progress has been made on HSR in California, which is expected to have an operating speed of 220 mph. HSR lines in a range of 90-125 mph is also planned in the Pacific Northwest, Midwest, and Texas (Federal Railroad Administration 2016). Unfortunately, the fluctuating project cost estimates and delays has led to cancelation of major federal grants which funded the project. Construction for the maiden California HSR infrastructure finally started in 2017 but in February 2019, it was announced that the construction of HSR lines in California would be postponed except the 119-mile segment in the Central Valley due to cost overruns and delays, and then it was confirmed by the Governor of California that the first service would be extended to the 171-mile stretch from Bakersfield to Merced (Figure 2.62). Other lower-speed train and bus services would be provided from both ends of this Bakersfield-Merced line to allow for pedestrian to travel to San Francisco and Los Angeles, which are planned to be planned to be offered in around 2026.

Figure 2.62. A construction site from Merced to Bakersfield route (ENR 2019)

On the contrary, an interstate project between California and Nevada and a project in Texas is progressing towards success as of 2020. XpressWest, a passenger rail project connecting Las Vegas and greater Los Angeles, has received the rights to build on the median of Interstate 15 which runs through Southern California and Intermountain West. This privately funded project was acquired by Florida-based passenger rail operator Virgin Trains USA and anticipates its first service

in 2023. An HSR line is also being proposed between Dallas and Houston by a private railroad company called Texas Central. Current plans include utilizing technology based on that of the Central Japan Railway Company with rolling stock based on an international version of the N700 Series Shinkansen.

Independent of the California HSR progress, privately funded HSR projects are bringing an upward trend to a successful implementation of monumental HSR in the United States. Thus, providing guidance on the modeling, analysis, and design of HSR infrastructure and structural systems could be greatly beneficial to inform future national and local HSR research and projects within the United States.

2.5.1. CALIFORNIA HIGH-SPEED RAIL

The first contract for California HSR was the Construction Package 1 (CP1) in August 2013. A 32-miles long construction was planned from Ave 19 in Madera County to south of American Avenue in Fresno County, which is about 32-miles long. This line includes 12 grade separations and five viaducts among which three of them are completed as of early 2021. The Fresno River Viaduct is the first structure built as a part of CA HSR in 2017 although the track and electrical work are still incomplete which will be done as the CA HSR line construction proceeds. The structure is 1600-feet long, 25 feet high, and runs over Fresno River in parallel with the BNSF railway bridge nearby. Tuolumne Street Bridge construction was also completed in 2017, which is designed high enough so that the high speed trains can pass through under the bridge.

The second contract was the Construction Package 2-3 (CP 2-3) in June 2015. A 60-miles long construction was planned as the extended line to CP1 starting from Fresno to one mile north of the Tulare-Kern county line. This HSR line is designed with 36 grade separations, five viaducts, under- and overpasses.

The third bundle for the High-Speed Rail construction is Construction Package 4 (CP4) that was awarded in February 2016. It has a 22-miles long HSR line that was planned to connect the end of CP2-3 lines with Poplar Avenue, north of the City of Shafter (Figure 2.63). A total of 12 structures are planned to be constructed or revamped in the CP4 line including five viaducts and relocation of a four-mile long Burlington Northern Santa Fe (BNSF) railway tracks. Some of the structures impact existing BNSF lines, e.g., State Route 46 (SR-46) underpass, Poso Avenue underpass, and Wasco viaduct (Marshall et al. 2019), and therefore were redesigned to accommodate the needs of HSR. For example, State Route 46 (SR-46) intersection is the underpass in which BNSF currently manage two tracks (Figure 2.64 and Figure 2.65). With construction of HSR, SR-46 underpass will be expanded to a structure that can accommodate four-tracks. The largest structure in CP4 is the Wasco Viaduct that intefere with the existing railway operated by BNSF. The Wasco Vidaduct is planned to be constructed as a 2400-foot long structure as shown in Figure 2.66 and Figure 2.67. The design-build construction packages of CP1, CP2-3 and CP4 are publicly available at the California HSR (California High Speed Rail Authority 2021).
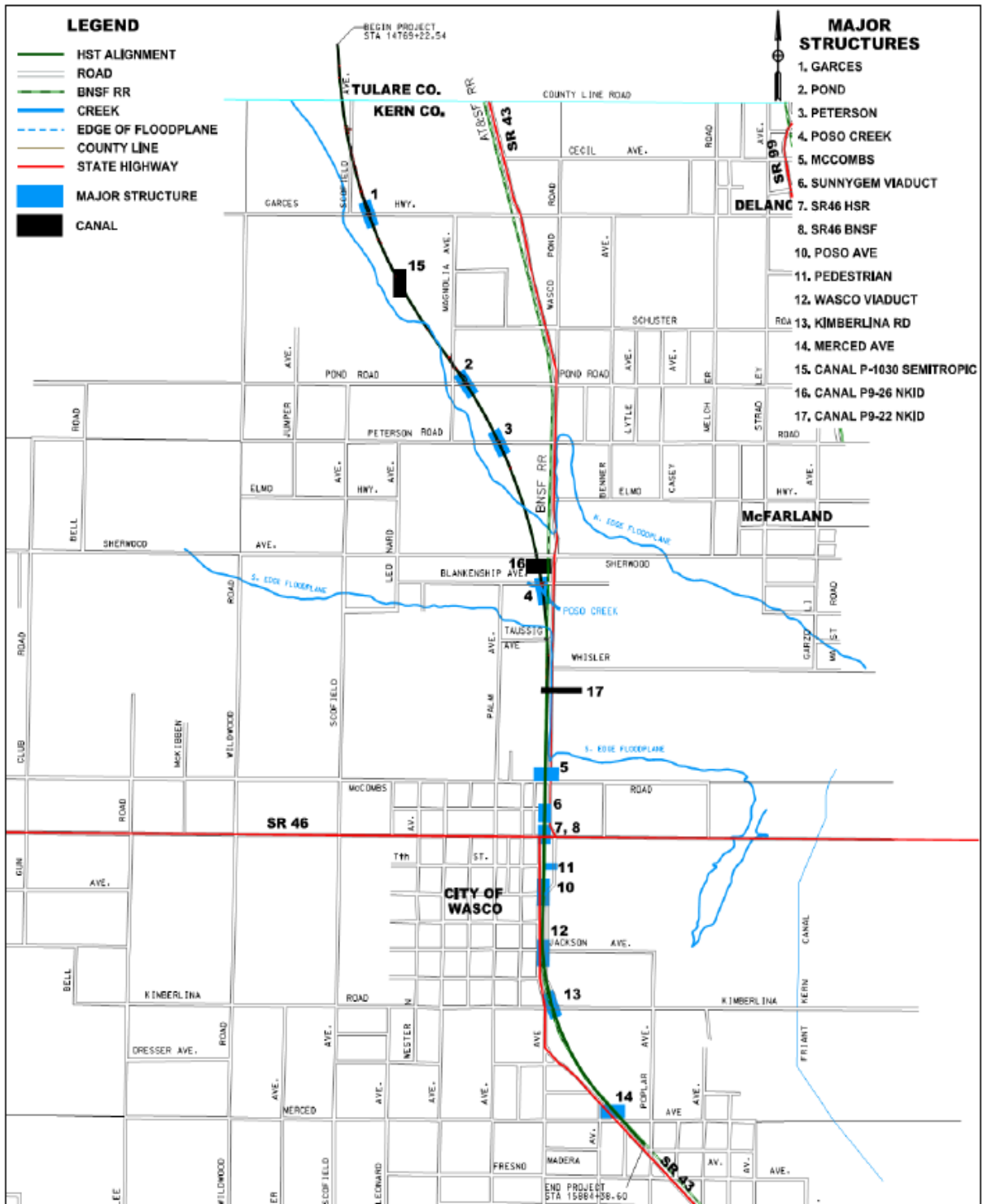
Figure 2.63. Map of Construction package 4 (Marshall et al. 2019)
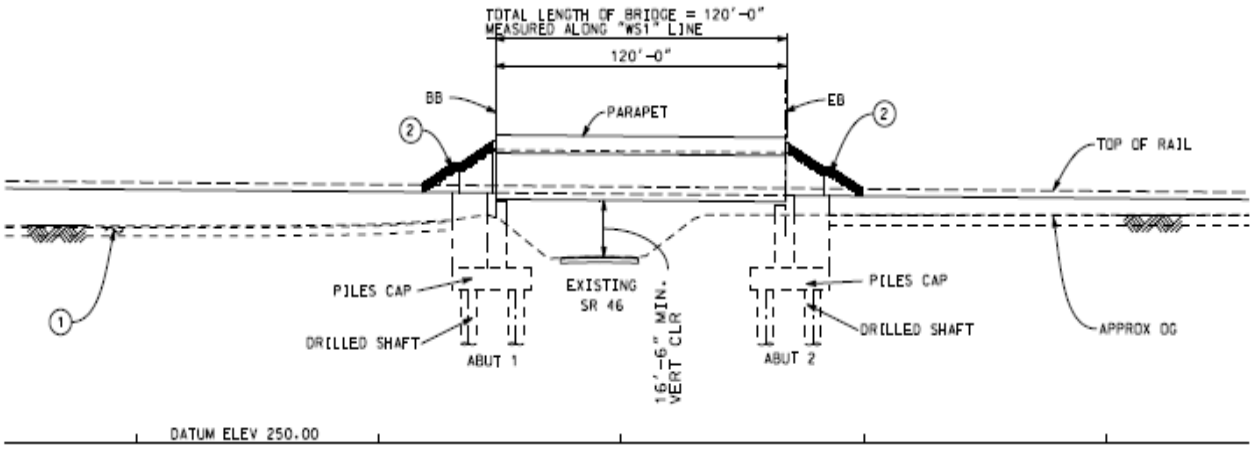
Figure 2.64. SR-46 elevation (California High-Speed Rail Project 2016)
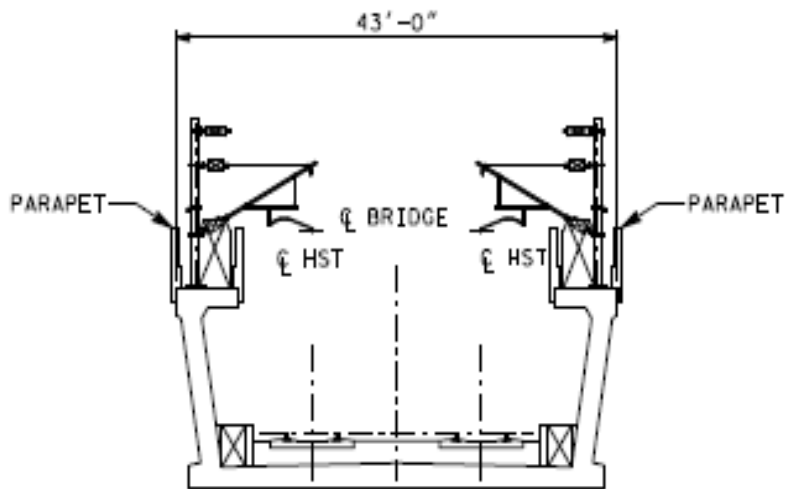
Figure 2.65. SR-46 section (California High-Speed Rail Project 2016)

Figure 2.66. Plan view of the Wasco Viaduct (Marshall and Keating 2016)
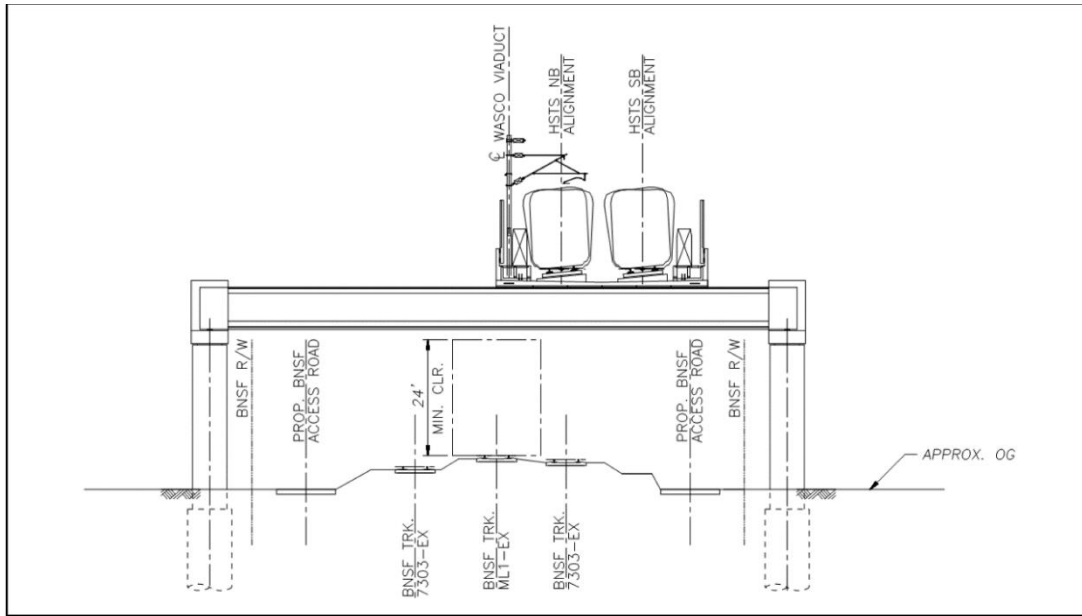
Figure 2.67. Wasco viaduct section (Marshall and Keating 2016)

A review of existing soil conditions along the planned HSR route from Madera to Shafter was studied using the preliminary geotechnical reports. The boring logs were cross referenced into a Google Earth data file facilitating easy access for future uses. Figure 2.68 shows a snip of the boring records implemented into Google Earth. Figure 2.69 through Figure 2.71 show various CPT and SPT records along the alignments. The soil conditions along the HSR route consisted primarily of sand with interbedded layers of clays, of which is typical in this geologic setting. Categories of soft to stiff soil conditions were interpreted from CPT data by using correlations to N60 values. Percentiles were used to quantify the variation and to then select worst case and best scenarios based upon provided data. Figure 2.72 and Figure 2.73 depicts the classifications from soft to stiff soil sites for construction packages 2 through 4. Preliminary estimation of drilled pier depths was estimated using available SPT data. The blow counts were used to estimate an effective friction angle and correlated to skin friction using methods described in the FHWA GEC 10. Approximate loading per column was taken at 1,000 kips. The approximate depth of the drilled pier was taken as 45 feet.

Figure 2.68. Google Earth Data File of Geotechnical Data
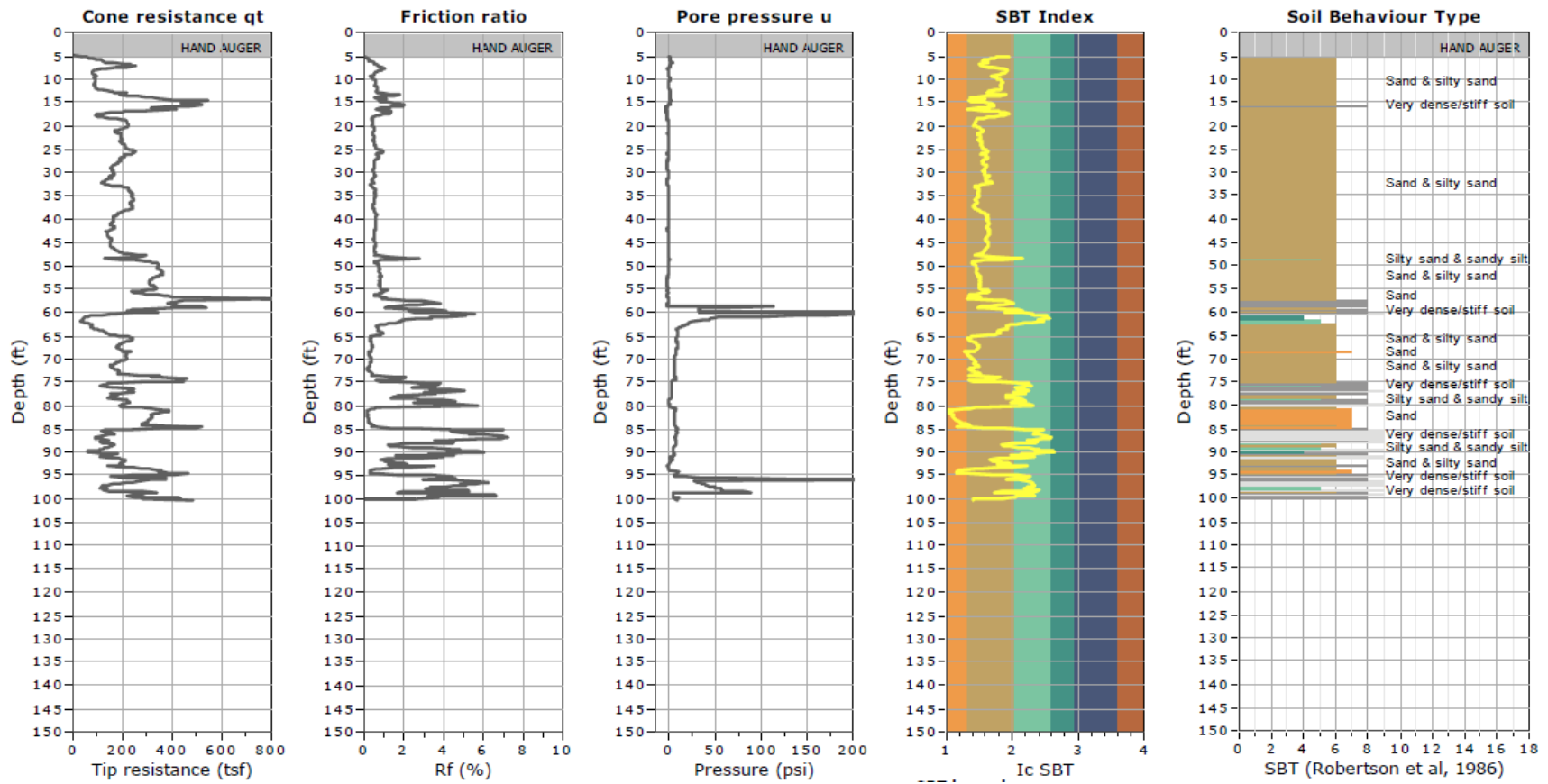
Figure 2.69. Example CPT Record for Construction Package 1
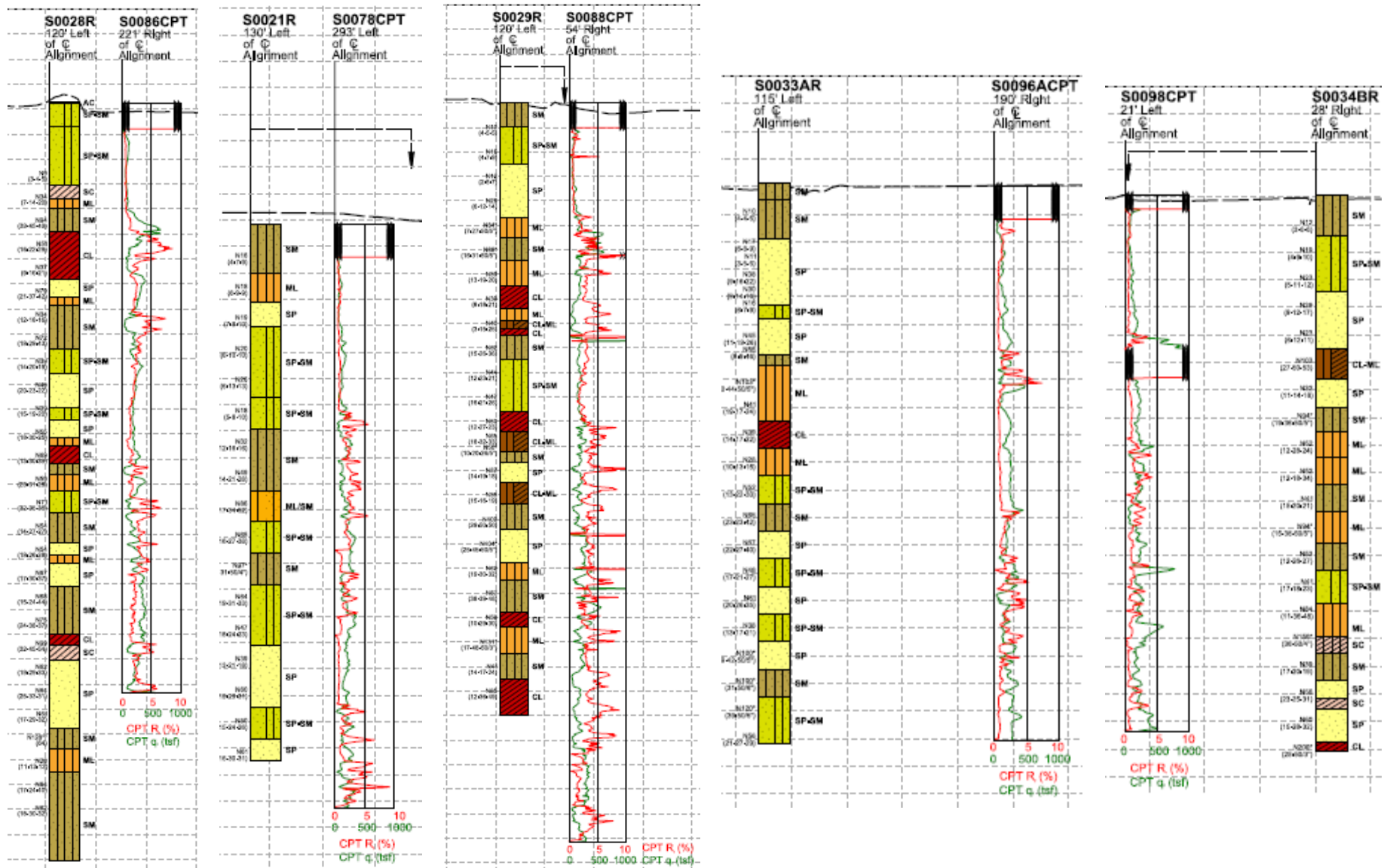
Figure 2.70. Example CPT and SPT Records for Construction Package 2-3
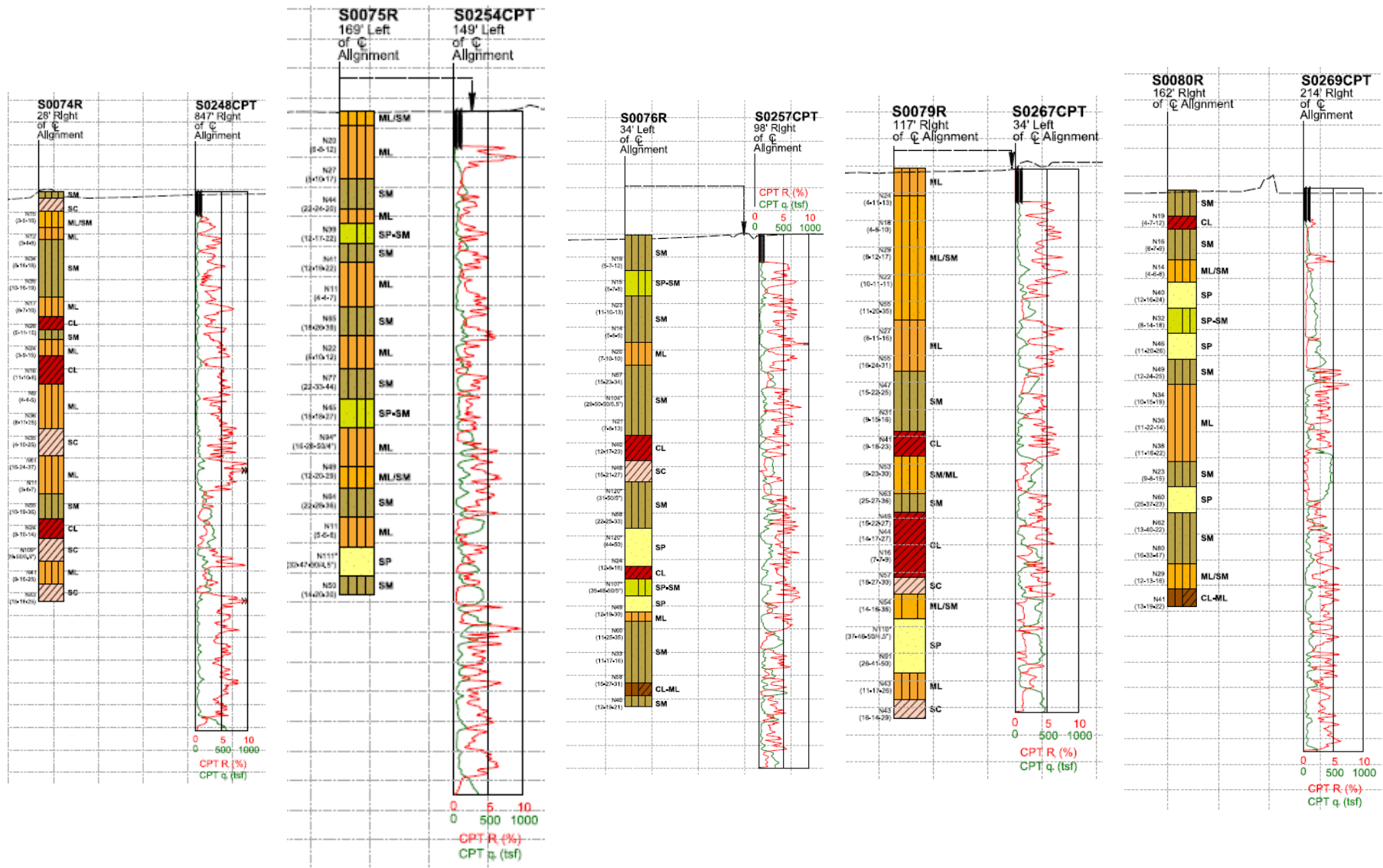
Figure 2.71. Example CPT and SPT Records for Construction Package 4
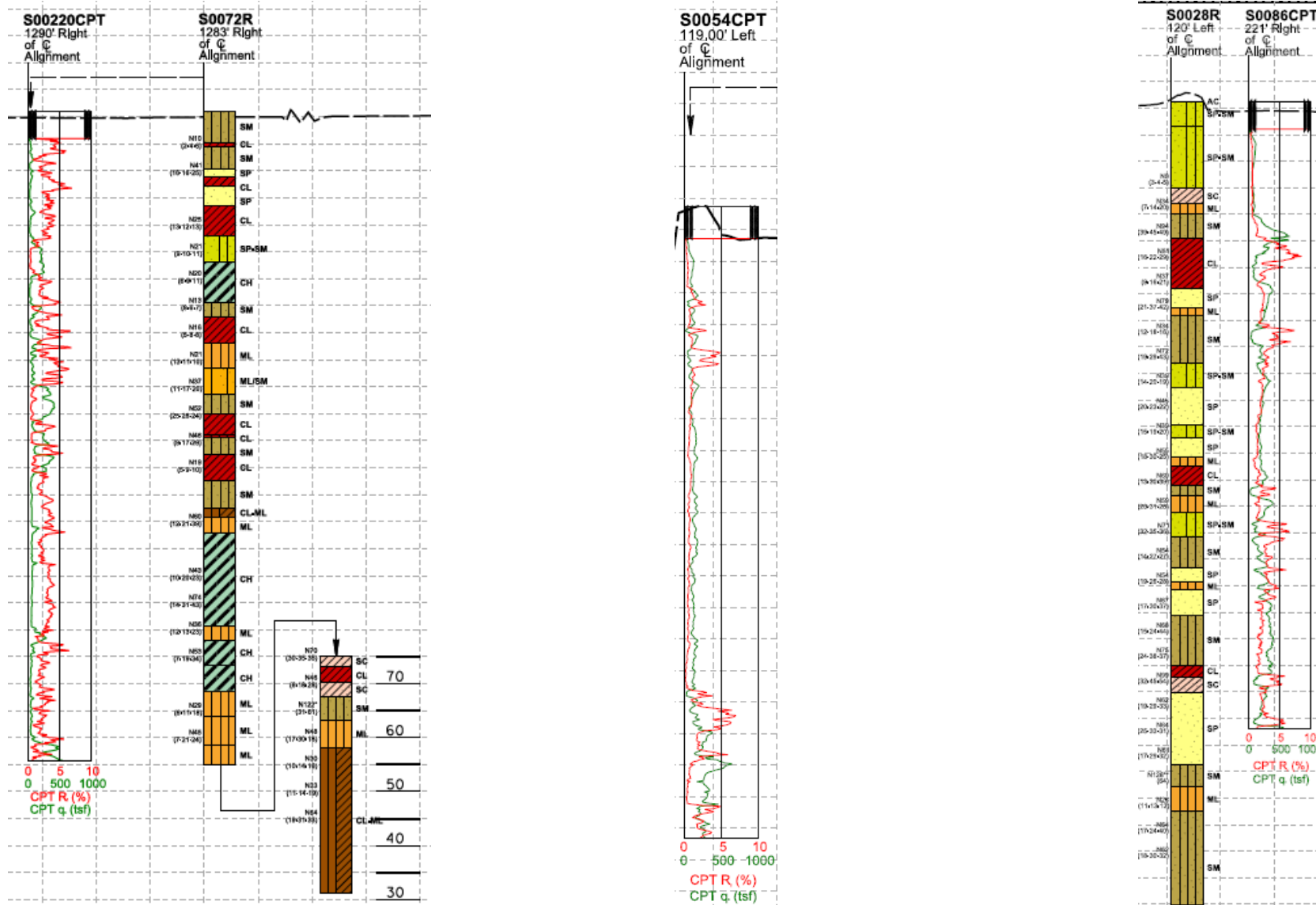
Figure 2.72. Soft to Stiff Soil Profiles for Construction Package 2-3

Figure 2.73. Soft to Stiff Soil Profiles for Construction Package 4

The cross-sections of HSR bridges along alignments in construction packages one through four are reviewed to identify the prototype CA HSR bridges for possible use in numerical modeling. First, the bridges are categorized into three groups of standard, complex, and non-standard structures of varying lengths: (i) Standard structures are those that are not complex structures and comply with the California High-Speed Train Project Guidelines for Standard Aerial Structures; (ii) Complex structures are those that have complex response during seismic events or one more of the following: irregular geometry, unusual framing, long spans, lightweight concrete, unusual geologic conditions, proximity to hazardous faults, and regions of severe ground motion; (iii) Non-standard structures are those that do not meet the requirements for either standard or complex structures. Grouping the bridges into different categories allows for selecting prototype bridges for analytical studies. The seven categories separating the bridge structures are standard viaducts, non-standard viaducts, underpasses, bridges, trench structure, box culverts, and retaining walls. In addition, standard viaducts consist of single-cell prestressed, precast concrete box girders with spans of 100 to 130 feet long. Non-standard viaducts consists of steel trusses, balanced cantilever structures, multi-cell cast-in-place (CIP) box girders used for wide station structures or maintenance tracks or elevated slab structures. Bridges include short structures such as the standard 120-foot PS/PC box girder spans carrying HSR over Tule River and Poso Creek. An example of the classifications is shown in Table 2.9. The most typical cross section is identified to the standard Caltrans single cell box girder shape depicted in Figure 2.74, and the cross section properties are shown in Figure 2.10. Other prominent structure types include multi-cell box girders, steel u girders, and truss structures.

Table 2.9. Classified CA HSR bridges

Bridge Type	Viaduct	Short Length
Standard Bridges	▪ *Fresno Viaduct (11155+36)* ▪ *Fresno Viaduct (11199+97)* ▪ *Viaduct Crossing E Conejo Avenue* ▪ *Viaduct Crossing S Peach Avenue* ▪ *Kings River Viaduct (1463+58)* ▪ *Kings River Viaduct (1466+97)* ▪ *Kings River Viaduct (1489+17)* ▪ *Kings River Viaduct (1525+33)* ▪ *Kings River Viaduct (1593+64)* ▪ *Hanford Viaduct (including Kings/Tulare Regional Station)* ▪ *Cross Creek Viaduct* ▪ *SR 43/BNSF Viaduct (2986+36)* ▪ *SR 43/BNSF Viaduct (3026+21)* ▪ *Wasco Viaduct* ▪ *Shafter Viaduct*	▪ *Poso Creek Viaduct* ▪ *State Route 46 Underpass*
Complex Bridges	▪ *Fresno Viaduct Golden State Boulevard* ▪ *Fresno Viaduct South Cedar Avenue* ▪ *Fresno Viaduct SR 99 Undercrossing*	

	▪ Kings River Viaduct (Steel Truss) ▪ Cole Slough Bridge ▪ Dutch John Cut ▪ Kings River Viaduct (Steel Truss) ▪ Kaweah SR Crossing ▪ Cross Creek Bridge (Steel Truss)	
Non-Standard Bridges	▪ Conejo Crossover Structure ▪ Hanford Viaduct (including Kings/Tulare Regional Station) ▪ Cross Creek Viaduct (Crossover Beam/Slab Structure) ▪ Cororan Crossover Structure (part of SR 43/BNSF Viaduct)	▪ Fresno Street Overpass ▪ Tulane St. HST Overpass ▪ Jensen Trench ▪ Whitney Ave/SR 137

Figure 2.74. Typical cross section of high-speed rail bridges in CP4

Table 2.10 Cross section properties

Area of Cross Section	*119.66 ft^2*
Moment of Inertia in x-axis (I_x)	*2260 ft^4*
Moment of Inertia in y-axis (I_y)	*11933 ft^4*
Torsional Constant	*4147 ft^4*
Weight per Unit Length	*17.95 kip/ft*

Figure 2.75. CA HSR Viaduct section (Parsons Brinckerhoff 2009)

The structure shown in Figure 2.75 is a composite structure of Caltrans highway.It includes a typical cast-in place construction which is using shoring and falsework for the time being. A single drilled concrete shaft braces a single circular column. That single circular column bolsters a multi-cellular box girder of concrete. Tracks are fixed. The poles which support the Overhead Contact System (OCS) are positioned away from of walkways.

2.5.2. TEXAS HIGH-SPEED RAIL

Texas is the the second largest state in the United States in terms of population, which has increased by almost 2 millions from 2010 to 2015 resulting in over 27 millions in 2015. The population in concentrated in 4 major cities: Dallas/Fort Worth, Houston, Austin, and San Antonio. In particular, the population increases in Dallas/Fort Worth and Houston areas are expected to be nearly doubled by 2040, a bullet train network was planned to accommodate the transportation demand. The Texas HSR is therefore planned as a 240-mile long HSR line to offer a total travel time less than 90 minutes between Dallas/Fort Worth and Houston areas (Figure 2.76) with 205 mph of the train operation speed. Considering the main purpose of the Texas HSR is to connect the two major cities, the station locations were only considered near the cities. In

case a utility corridor is included, an intermediate station would be established somewhere near Shiro, Bryan, and College Station area which has "significance as middle for advanced education and head bio-clinical and different administrations" (Hidema et al. 2017). HSR alignments are planned with the the existing transportation routes considered to minimize societal and environmental impacts. To this end, a broad variety of geostatic data was gathered and translated into usable information to determine, e.g., HSR facility locations, risk of natural hazards, etc. Optimal baseline alignments were identified after multiple iterations and analysis of alternatives. These baselines improve the general feasibility of the alignments as they are associated with environmental, operational, and urban constraints (Memon et al. 2014).

Figure 2.76. Proposed routes of the Texas HSR project (Hidema et al. 2017)

3. HSR BRIDGE DESIGN SPECIFICATIONS AND SELECTION METHODS

3.1. SUPERSTRUCTURE SYSTEMS

3.1.1. INTRODUCTION

High-speed railway bridges are subject to complex vehicle loading and stringent serviceability criteria, which lead to structural solutions different from those used for highway bridges or conventional railway bridges. Due to the high speed of the trains, track deformations – and thus, structural deformations – must be kept to a minimum to limit excess acceleration and ensure passenger comfort. Additionally, vibrations and resonance are of concern.

This section provides a review of selected HSR design criteria from California, China, and Europe. These include the California High Speed Rail (CAHSR) Design Criteria, the Chinese Code for Design of High-Speed Railway, and Eurocode EN 1990 and EN 1992. Eurocode directly adapts the loads and limits recommended in UIC Leaflets 776-1R and 776-2R, while the California and Chinese criteria reference the UIC Leaflets as a guide, but do not follow UIC in some cases (Muncke 2008). Because the static and dynamic service load cases tend to govern the superstructure selection, special emphasis will be placed on service limits and the corresponding loads. Load cases and serviceability limits – including vertical deflection, rotation, acceleration, and natural frequency bounds – are discussed.

3.1.2. LOADING

The superimposed dead load of railway bridges is significantly larger than that of highway bridges due to the track structures (ballast, rail and fasteners, cables, poles, and walls). The live loads are also greater since railway vehicles, particularly the locomotives, are much heavier than typical highway vehicles. Additionally, horizontal forces imposed by trains – including acceleration, braking and centrifugal forces – are much larger than those from roadway vehicles. For example, braking forces can be up to 14 times greater in railway bridges than in highway bridges (Marx and Schlaich 2009), and centrifugal loads from trains can be 3-15 times those induced by highway traffic (Sobrino 2008). Furthermore, "nosing" and "hunting" forces (lateral forces that arise from random imperfections in the rails and wheels) occur in rail bridges but not highway bridges.

Also of key concern are the seismic loads on bridges where applicable. The CAHSR Design Criteria specify two levels of design earthquakes: An Operating Basis Earthquake (OBE) with a return period of 50 years, and a Maximum Considered Earthquake (MCE) with a return period of 950 years. This roughly corresponds with the Level 1 and Level 3 ground motion levels for conventional railway bridges, as described in the AREMA Manual for Railway Engineering. For HSR bridges in China, the earthquake loading is the same as those for Chinese conventional railway bridges, as outlined in the Chinese Code for Seismic Design of Railway Engineering. There are three levels of earthquakes considered, with return periods of 50 years, 475 years, and 2475 years (labeled as the low, design, and high-level earthquakes, respectively).

While the aforementioned loads are to be considered in many analysis cases, the typical loads that control the superstructure type of HSR bridges tend to be the vertical live loads. In each country, there are several vertical live load patterns specified for HSR bridge design. These patterns

may include a service HSR train load, or a heavier maintenance train load, which are applied in different permutations (e.g., one train on the bridge, two trains, etc.) in several analyses (e.g., static and dynamic track serviceability analysis, rail-structure interaction analysis, etc.). Some examples of service and maintenance train loads will be outlined here.

3.1.2.1. HIGH-SPEED TRAINS

California has yet to select the specific trainset to be used on the CAHSR system. Therefore, the CAHSR design specifications outline five trainsets to represent possible service loads. One trainset is shown in Figure 3.1.
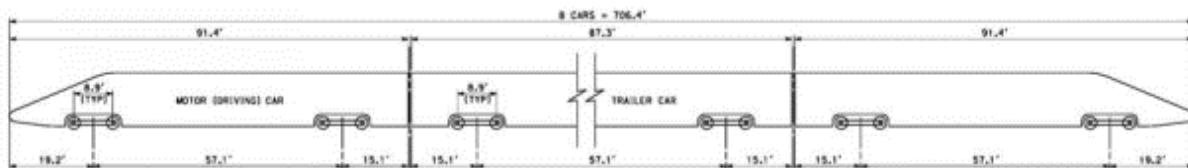
Maximum Axle Load = 18.7 tons   Train Weight (Empty) = 509 tons

Figure 3.1. California Type 1 trainset (California High-Speed Rail Authority 2019)

Eurocode design specifications require that either the actual trains or the UIC High Speed Load Model (HSLM) are used for dynamic analyses. Because the high-speed trainsets may differ between countries, only the HSLM is described here.

The UIC HSLM represents the loading from passenger trains exceeding 200 km/h. There are two models within the HSLM. Both models are a series of point loads, but they differ in magnitude and spacing:

- *HSLM-A consists of 10 trains. Analyses that require HSLM-A will indicate which of the 10 trains are to be used. The trains have varying numbers of train cars, axle spacing, and live load magnitude.*

- *HSLM-B is a series of equally spaced point loads, where the number of loads and their spacing is dependent on bridge span length.*

Depending on the bridge configuration, HSLM-A or HSLM-B will be specified. Usually, only one track is loaded with a single train per case. For more information, see UIC 776-2R Section A.4.1.

3.1.2.2. MAINTENANCE AND CONVENTIONAL TRAINS

While the high-speed trains are more representative of actual service loads, many of the static serviceability limits are based off of maintenance or conventional rail trains. A sampling of trains is outlined here.

The CAHSR Design Criteria frequently use the Modified Cooper E-50 load shown in Figure 3.2. This is representative of a maintenance train for high-speed rail lines.
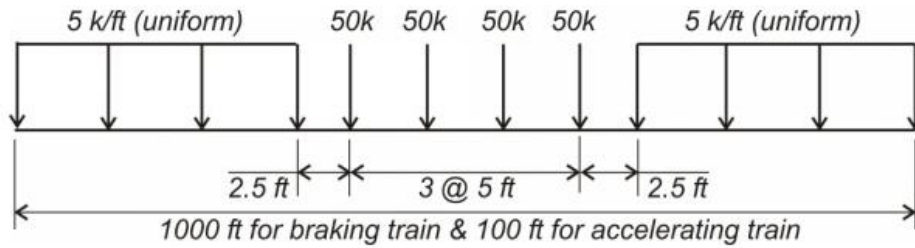
Figure 3.2. Modified Cooper E-50 load (California High-Speed Rail Authority 2019)

Eurocode references the UIC71 load shown in Figure 3.3. This load model is commonly used as a service train in conventional rail bridge design, but it is also used in high-speed rail design. It is similar in magnitude and distribution to the Modified Cooper E-50 loading.

(1) no limitation
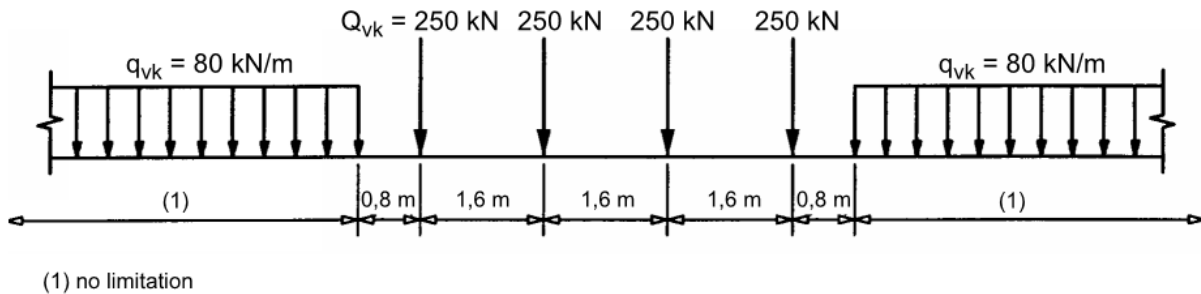
Figure 3.3. UIC Load Model 71 (UIC71) (International Union of Railways 2006)

The Chinese specification uses the Chinese ZK load (which is 80% of the UIC71 load) for typical high-speed rail bridges (Figure 3.4).
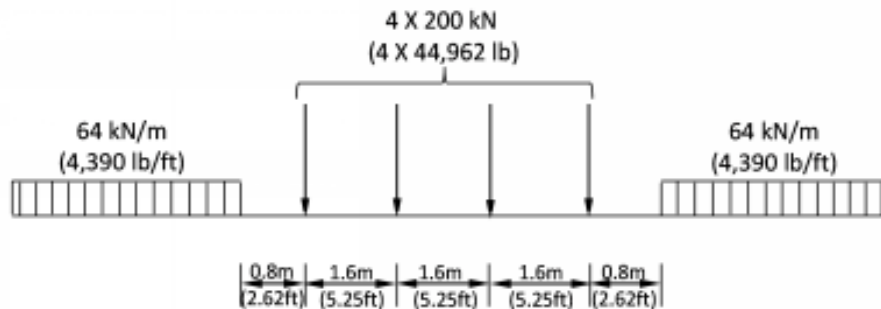
Figure 3.4. Chinese ZK load (Zhou et al. 2012)

3.1.3. SERVICEABILITY LIMITS

The serviceability limit states for high-speed rail address the same response quantities as do the limits specified in conventional rail codes, but the limiting values are more stringent due to the higher train speeds. Serviceability limits from the California, Chinese, and European design standards will be compared in this section.

3.1.3.1. VERTICAL DEFLECTION LIMITS

Many countries limit static vertical deflections of bridge decks as an indirect way to mitigate un-desired vehicle acceleration. The deflections are computed assuming static behavior in the inter-ests of simplicity, with an amplification factor to account approximately for the dynamic behavior. The vertical serviceability load cases and limits differ from country to country. For example, Euro-code suggests a limit based on a single loaded track considering a dynamic impact factor; mean-while, the Chinese code provides limits based on two tracks loaded but does not consider dynamic impact. In general, deflection limits are a function of train speed, span length, type of track (bal-lasted or ballastless), and span type (simply supported or continuous). A summary of require-ments from a few design standards is provided in Table 3.1. All limits reported in the table are for the highest design speeds designated.

Table 3.1. Load cases and limits for static vertical deflection

Design Standard	Load Case	Δ/L limit (ranges based on span)
Eurocode/UIC	Single track loaded UIC Load Model 71 with dynamic impact factor	1/2650-1/1500 (3+ simply sup-ported spans) For continuous beams, adjust the limit with factors
China	Two tracks loaded ZK design live load (80% of UIC71 load) on each track No dynamic impact considered	1/1600-1/1500 (3+ simply sup-ported spans) For continuous beams or single-track bridges, adjust the limit with factors
CAHSR	Check both 1 and 2 tracks loaded (2-track case usually controls) Modified Cooper E-50 maintenance train load with dynamic impact	Single track: 1/3500-1/2200 Double track: 1/2400-1/1100 (All types of spans)

A visual comparison of the different deflection limits vs. span length is shown in Figure 3.5. Note that here, they are expressed as span/deflection so that the linear features of the equations are apparent. The CAHSR deflection limit is stricter than the Eurocode/UIC limit for all span lengths. The CAHSR deflection limit is also stricter than the Chinese limit for spans under 200 ft, which are the most common span lengths used.
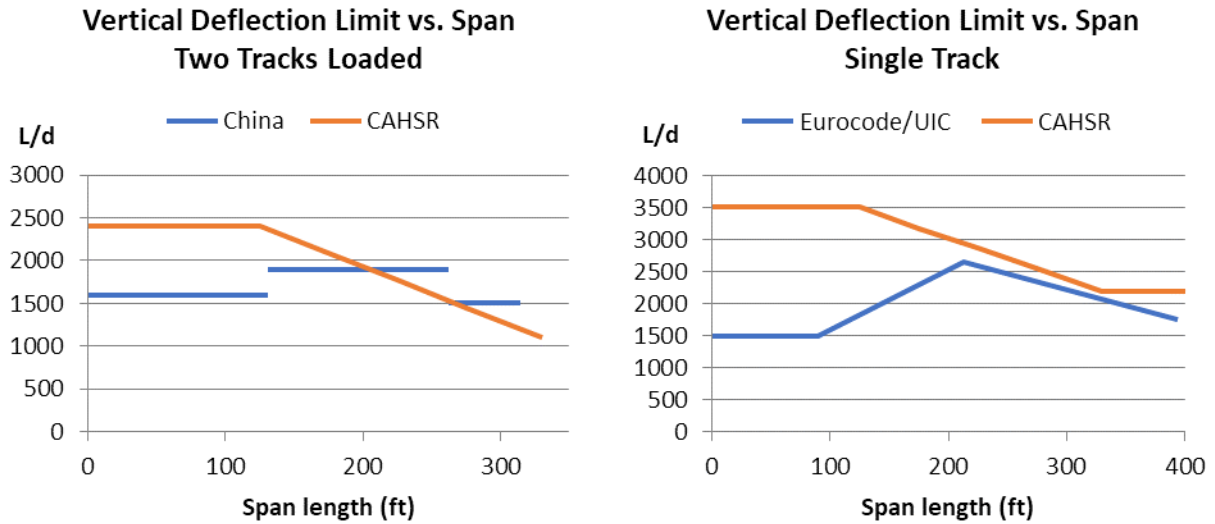
Figure 3.5. Comparison of vertical deflection limits vs. span length

3.1.3.2. ROTATION LIMITS

While the design standards limit vertical deflections to minimize passenger discomfort, they also specify rotation limits to keep the rail operational. End rotations impose additional axial and bending stresses on the rail, which can damage the rail fasteners. The rotations may also cause abrupt angular changes in track geometry, which leads to passenger discomfort (in mild scenarios) to train wheel unloading in more severe cases (California High-Speed Rail Authority 2019). These rotation limits are applied to the same load cases as the deflection limits.

The Chinese code limits rotation at the beam end depending on track type, location of beam end, and beam end overhang length (see Figure 3.6 and Table 3.2). The units are expressed in milliradians, and L_e is the beam end overhang length.
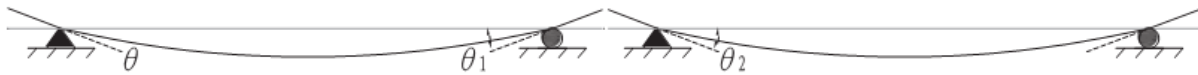
Figure 3.6. Sketch showing the rotation angle to be limited (He et al. 2017)

Table 3.2. Rotation limiting values for Chinese HSR bridges, where **Le** is the beam end overhang length.

Track type	Location	Limiting value (rad)
Ballasted	At abutment	$\theta \leq 2.0 \text{‰}$
	At pier	$\theta_1 + \theta_2 \leq 4.0 \text{‰}$
Ballastless	At abutment	$\begin{cases} \theta \leq 1.5 \text{‰}, & L_e \leq 0.55 \, m \\ \theta \leq 1.0 \text{‰}, & 0.55 \, m \leq L_e \leq 0.75 \, m \end{cases}$
	At pier	$\begin{cases} \theta \leq 1.5 \text{‰}, & L_e \leq 0.55 \, m \\ \theta \leq 1.0 \text{‰}, & 0.55 \, m \leq L_e \leq 0.75 \, m \end{cases}$

The CAHSR code has similar rotation limits, which are outlined in Table 3.3. There is no distinction between track type or location.

Table 3.3. Rotation limiting values from CAHSR Design Criteria

Load Case	θ (rad)
1 track loaded	1.2 ‰
2 tracks loaded	1.7 ‰

Typically, the rotation limits will only control superstructure selection for longer spans. Otherwise, vertical deflection and acceleration will likely control. Additional details on the controlling limits are provided in Section 3.1.4.4.

3.1.3.3. VERTICAL ACCELERATION LIMITS

The acceleration limit is one of the common criteria that controls bridge design. It exists to ensure track alignment, track stability, and passenger comfort (Andersson and Karoumi 2015). The modeling of the dynamic effects of the train, bridge, and possible ballast to analyze deck acceleration can be complex and varies depending on the design standard, and it will not be discussed here. Analysis results are then compared with the general acceleration limits summarized in Table 3.4.

Table 3.4. Load cases and limits for vertical acceleration

Design Standard	Load Case	Acceleration Limit
Eurocode/UIC	Single track loaded UIC High Speed Load Model (HSLM) or actual service train	Ballasted: 0.35 g Non-ballasted: 0.5 g
China	Single track loaded Actual service train	Ballasted: 0.35 g Non-ballasted: 0.5 g
CAHSR	Single track loaded Actual service train	0.5 g

3.1.3.4. VERTICAL NATURAL FREQUENCY BOUNDS

Natural frequency also needs to be limited to avoid resonance between the bridge and vehicle. UIC, China, and CAHSR all provide limits on the first natural frequency of vertical deflection. If girders do not satisfy the bounds, then additional train-structure dynamic analysis is required. The natural frequency limits for UIC and CAHSR are the same, which include an upper and lower bound. The lower limit is:

$$n_0 = \begin{cases} \dfrac{80}{L}, L \leq 20 \, m \\ 23.58L^{-0.592}, 20 < L \leq 96 \, m \end{cases}$$

And the upper limit is:

$$n_0 = 94.76L^{-0.748}$$

where the frequency, n_0, is in Hz and the span, L, is in meters.

These specifications were developed for UIC primarily for train speeds below 250 km/h (155 mph), but then applied to HSR as well (Zhou et al. 2012). Chinese engineers deemed the UIC lower bound not strict enough to prevent excessive vibration or resonance due to high-speed trains. Chinese studies also concluded that an upper limit is not necessary since tight construction tolerances would mitigate potential issues due to higher fundamental frequencies (Zhou et al. 2012). The Chinese lower frequency limits for common spans are listed in Table 3.5. As can be seen, higher vehicle speeds require more stringent frequency limits. Longer spans have inherently lower natural frequencies, and the lower frequency limits associated with them reflect this fact.

Table 3.5. Chinese lower bound frequency limits for common spans

Span Length, m (ft)	Design Speed, km/h (mph)		
	250 (155)	300 (186)	350 (217)
12 (39)	100/L	100/L	120/L
16 (52)	100/L	100/L	120/L
20 (66)	100/L	100/L	120/L
24 (79)	100/L	120/L	140/L
32 (105)	120/L	130/L	150/L

A graphical comparison of the UIC and Chinese natural frequency limits is shown in Figure 3.7. The actual natural frequency of an example simply supported prestressed concrete HSR bridge is plotted alongside these limits. This natural frequency was calculated using the following equation:

$$n_0 = \frac{\pi}{2L^2}\sqrt{\frac{Er^2}{\rho}}$$

Where:

n_0 = natural frequency

L = span

r = radius of gyration

E = modulus of elasticity

ρ = mass density

This can also be expressed as:

$$n_0 = \left(\frac{\pi}{2}\frac{r}{h}\sqrt{\frac{E}{\rho}}\right)\left(\frac{1}{L}\right)\left(\frac{h}{L}\right)$$

Where h = cross-section depth.

This arrangement of terms isolates key parameters into three groups. Assuming common material properties for a simply supported prestressed concrete HSR girder, the first group remains nearly

constant. If the natural frequency limits are limited to a multiple of $(1/L)$, as done in the Chinese code, then the second group is constant as well. Therefore, the maximum L/h ratio is fixed, and hence, the example bridge and China lower natural frequency limits follow the same curve in Figure 3.7.
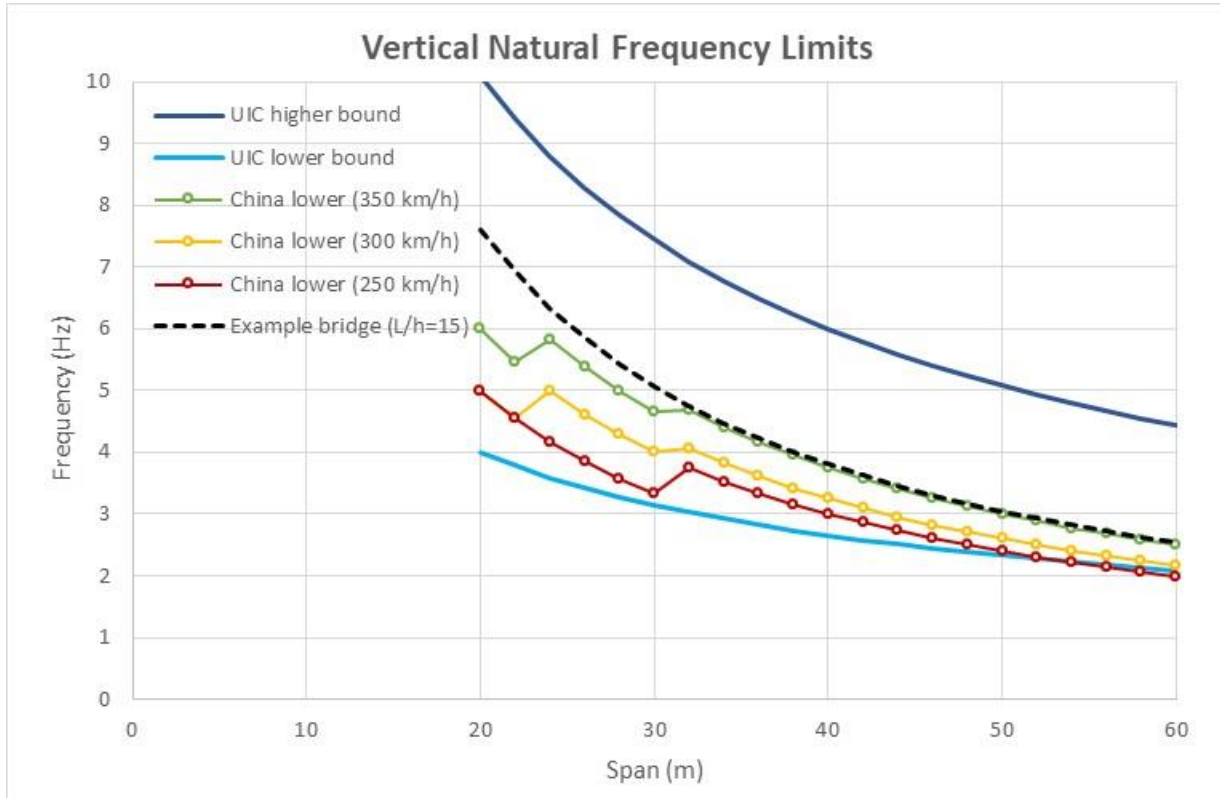
Figure 3.7. Comparison of vertical natural frequency limits from UIC and Chinese code. The "example bridge" curve shows the natural frequency of a simply supported HSR bridge with typical cross-section and material properties.

3.1.4. SUPERSTRUCTURE SELECTION

The strict serviceability criteria discussed in the previous sections imply the need for a stiff superstructure. Commonly, this need is addressed with a deep prestressed concrete box girder. While this cross-section helps satisfy serviceability criteria, it is much heavier than typical highway bridge sections and thus leads to issues with construction and seismic performance. The superstructure selection process to arrive at this typical prestressed concrete box girder as well as resolutions to construction and seismic issues, will be discussed in this section.

Lateral displacement and rotation limits also exist but are not discussed here. Among the serviceability limit states, the vertical deflection and acceleration limits most commonly control superstructure selection for short- to mid-length bridges. The influence of these limits on preliminary design are will be discussed.

3.1.4.1. MATERIALS

Concrete is much more common than steel for all HSR bridges around the world. Concrete HSR bridges are generally cheaper and require less frequent maintenance than steel bridges. Construction procedures for concrete HSR bridges are well-known, and engineering knowledge has been thoroughly developed (Manterola and Escamilla 2014).

On the other hand, steel can be preferable for long spans or where low girder height and light structural weight are needed. Steel may also be beneficial on sites with tough terrain for construction purposes, where prefabrication of members eliminates the need for formwork or shoring (Minami and Shimizu 2011). However, the lighter weight of steel structures leads to higher levels of vibration, which can cause fatigue damage.

Composite steel and concrete superstructures are also possible and can provide the necessary stiffness while reducing structural mass. They are used in areas with poor soil quality and in seismic areas. Existing composite HSR superstructures include steel box girders with a concrete deck (Zhou et al. 2012), composite trough made of steel webs and a concrete lower chord (Kang et al. 2018) as shown in Figure 3.8, or steel box girders with concrete on both the top and bottom flanges as shown in Section 0 with the Archidona Viaduct.

Figure 3.8. The Ingolstadt Rail Bridge, which is a composite trough bridge (Image credit: Janberg (Janberg 2020))

3.1.4.2. SPAN ARTICULATION

The most common type of HSR superstructure is a simply supported beam. However, continuous beams have also become increasingly used in recent years. Continuous spans are stiffer than simply-supported spans of equal proportions, meeting both static and dynamic criteria more efficiently (Kang et al. 2018). At the same time, they are more complicated for developing post-tensioning between spans and for analyzing secondary moment effects. Longer spans also require rail expansion devices, which impact rider comfort and require additional maintenance. For these reasons, some countries prefer shorter simply-supported spans as opposed to longer and fewer continuous spans (Combault 2013). Meanwhile, Germany is shifting away from simply-supported bridges and towards continuous beams (Kang et al. 2018).

Continuity can also be provided between the spans and the columns. This results in a moment connection at the span-column joints, taking advantage of frame action and thus reducing demands on the foundations. Since the superstructure and columns are monolithic, there are no

74

bearings, eliminating the risk of unseated spans during seismic events and the need for bearing maintenance. On the other hand, this fixity introduces moments caused by creep, shrinkage, and thermal effects. The construction of the superstructure-column joints is also more complicated with a fixed connection. This type of continuity has been used on some bridges in the Taiwan High Speed Rail system (Parsons Brinckerhoff 2009).

3.1.4.3. Cross-Sectional Shape

The most common cross-sectional shape for HSR bridges is a box girder, which efficiently provides the bending and torsional stiffness required to satisfy serviceability criteria. Both single- and double-cell box girders have been used, with the single-cell facilitating maintenance inspection more easily. Other common cross-sectional shapes and their benefits and drawbacks are outlined in Table 3.6. As an alternative to existing HSR superstructure configurations, a series of I-girders with a small top flange and large bottom flange may also be considered (Figure 3.9). This is similar to the I-girder in Table 3.6, but has optimized the relative flange sizes for flexural stiffness. By doing so, a smaller section can be used to provide the same stiffness as a larger typical I-girder. As a result, the girders can be precast in a plant and transported to site without special accommodations. This section shape would need to be further refined before it is implemented but is a promising option for accelerated bridge construction of HSR structures.
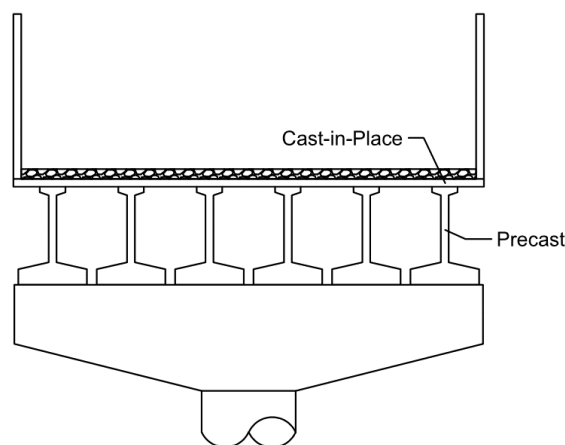
Figure 3.9. Alternative HSR cross-section

Table 3.6. Comparison of girder shapes (Evangelista and Vedova 2009)

Shape	Drawing	Pros	Cons
Box girder	W = 13.60 m Lmax = 43.20 m max 4.68 m	-High flexural and torsional efficiency -Often less pre-stressing costs	-May be visually un-appealing
U-girder or tub girder	W = 18.40 m Lmax = 31.50 m 3.50 m	-Built-in noise re-duction and train containment -Track level is at a lower elevation, meaning that em-bankments can be smaller -Lower track profile also shortens the moment arm for horizontal loads, re-sulting in smaller moments in the sub-structure	-May require more concrete (and thus self-weight) than the box girder since it is less efficient
I-gird-ers	W = 13.60 m Lmax = 46.17 m max 4.45 m	-Feasible to precast girders off-site -Precasting may al-low for faster pro-duction -Lighter loads for setting girders (may be beneficial where crane access is lim-ited)	-Need separate deck placement and con-nection after girders are set

3.1.4.4. SPAN-DEPTH RATIO

A study was performed to examine the typical span-depth ratio required in order to satisfy the CAHSR static serviceability criteria. A typical HSR prestressed concrete box girder section was as-sumed as a starting point. Then, the web height of the section was increased until static deflection and rotation criteria were satisfied for a given span. Natural frequency limits are also checked. This simple procedure was repeated for multiple span lengths and for simply supported, fixed-fixed, and 3+ continuous spans. The CAHSR criteria do not distinguish between support conditions, so the criteria remained the same across the different boundary cases. The results of the study are summarized in Figure 3.10, which shows the results derived from static deflection and rotation criteria.
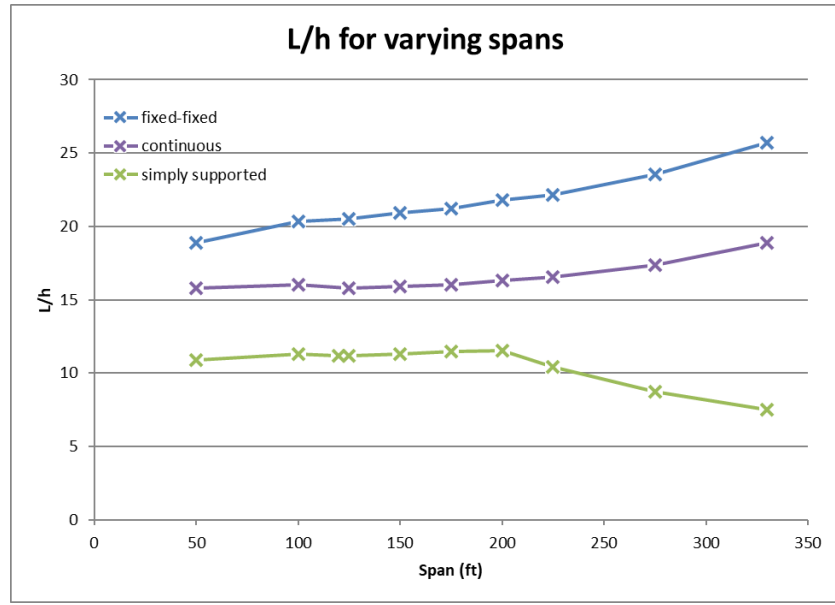
Figure 3.10. Required span-depth ratios based on CAHSR Design Criteria

The CAHSR limits lead to girders with a low span-depth ratio relative to that of highway bridges (e.g., $L/h \approx 10$ for short simply supported spans). For spans under 200 ft., the deflection limit was the controlling criterion; for spans greater than 200 ft., end rotation controlled. Natural frequency limits did not control for any simply supported spans, although they led to L/h ratios that were quite close to those dependent on deflection. For the fixed-fixed and continuous spans, all configurations had fundamental frequencies that exceeded the upper limit; this indicates that further analysis is needed to determine whether the fundamental frequency is acceptable or not. The precise reason for the upper limit is also unclear. The only explanation found was "the upper bound is to limit train-track dynamic responses due to track irregularities" (Zhou et al. 2012).

While this study was performed using a generic box girder section and CAHSR limits, most existing HSR concrete girder bridges have span-depth ratios similar to those in Figure 3.10. This demonstrates that the stringent track serviceability criteria are a significant driver for the cross-sectional depth of HSR bridges.

3.1.4.5. CONSTRUCTION METHODS

Construction methods can also influence the superstructure selection process, and vice versa. Many HSR bridges are cast-in-place (CIP), though segmental precasting and full-span precasting have been implemented as well. Existing HSR bridge construction methods are similar to highway bridge construction methods but occur on a larger scale. They include full staging with falsework, using a movable scaffolding system (MSS), cantilever construction, incremental launching, and rotation construction (Dong Kang and Suh 2003; Sobrino 2008; Yan et al. 2015)

77

Precasting of HSR bridges can lead to significant time savings, better quality control, and possible cost savings depending on the scope of work. In spite of the bulky superstructures, full span precasting of HSR bridges has been utilized in Italy, Taiwan, and Korea. Most commonly, precast facilities are located near the bridge site(s) and are specifically designated for HSR bridge construction. The spans are handled using custom equipment. For example, portal cranes are used to move the spans around the precast facility; special tire trolleys then transport the spans to site; and finally, a self-launching gantry positions and erects the span (Rosignoli 2016; Tai et al. 2010). In Taiwan, spans can also be transported from the storage yard to site either directly with portal cranes (bypassing the need for a transport trolley), or with a transportation trolley that has built-in hoisting equipment (so no portal crane is required). An example of a transportation trolley with lifting capability is shown in Figure 3.11.

Figure 3.11. Transporter with hoisting equipment used in Taiwan (Tai et al. 2010)

Due to the specialized equipment and potential need for new casting facilities, the up-front costs for precast are generally higher than for CIP structures. However, the time and material savings (due to less material wastage and tighter quality control) are significant and can offset the initial costs for larger scopes of work. In Korea, contractors estimate that on a bridge over 3 km (1.96 mi) long, cost savings of 20-30% can be achieved (Dong Kang and Suh 2003). Therefore, precasting should be considered for longer HSR bridges or where an expedited schedule is necessary.

3.1.4.6. CONCLUDING REMARKS

The superstructure selection process was outlined in this section. Material selection, span articulation, cross-sectional shape including span-depth ratio, and construction methods were discussed. Existing bridges demonstrate that a wide variety of superstructure types and construction methods can be used for HSR bridges; however, the most commonly used superstructure and construction method is a simply supported, CIP, post-tensioned concrete box girder.

3.2. SUBSTRUCTURE SYSTEMS

The substructure systems including piles, shafts, columns and column tops, pile tops are often built using Cast-In-Place concrete methods. The foundations that support the bridge colums can be classified into shallow and deep foundations. Considering a range of soil and rock properties can be encountered along the HSR lines to be constructed, different foundation types need to be considered to meet the strength/stability requirements and the cost effectiveness. In case the in-situ soil and rock conditions are competent, shallow foundations such as spread footings or mat foundations can be adopted, otherwise deep foundations such as drilled shafts and driven piles need to be considered. In areas of increasingly minimal soils, either Cast-In Drilled-Hole (CIDH) or Cast-In-Steel-Shell (CISS) piles can be used stretching down into capable material. The under reamed columns with various cross sections may be created using, e.g., belling tool with retractable wings.

The foundation design should meet all necessary performance requirements as defined in AASHTO LRFD Bridge Design Specifications such as lateral earth pressure, excessive deformation, stability issue, uplift pressure for all limit states given the field condition. The scour potential also need to be considered wherever applicable, e.g., near the water crossings. The type of foundation and the impact of foundation installation on existing facilities and neighboring foundations also needs to be taken into account (Gingery et al. 2011). The load and resistance factor design (LRFD) based on the probability of failure or reliability is currently adopted in the California HSR construction project. In LRFD, the likelihood of a load exceeding the capacity of the foundation is considered during the entire life span, and the method considers the following three limit states for foundation design:

- *Serviceability Limit State – Evaluation of performance that adversely affect the stability and displacement of the structure under normal service loads.*
- *Strength Limit State – Evaluation of limit states associated with the strength under various loading conditions.*
- *Extreme Event Limit State – Evaluation of strength and stability under extreme loading conditions caused by extreme events such as earthquakes.*

3.2.1. FOUNDATIONS

3.2.1.1. SHALLOW FOUNDATION

While the shallow foundation such as spread footings or mat foundation may not be the primary choice for the bridge foundation, it can be adopted in case in-situ soil or rock properties are competent at a shallow depth or those competent properties can be obtained at a shallow depth after ground improvement. However, shallow foundations are not ideal for soils that are potentially unstable, e.g., expansive, liquefiable, etc. The Federal Highway Administration (FHWA) developed a Geotechnical Engineering Circulars (GEC) for analysis and design procedures for highway bridges supported on the shallow foundation (Kimmerling 2002). ASHTO LRFD Bridge Design Specifications (BDS) can be also referenced as the guidance with regional amendments based on the geotechnical properties obtained with field investigations.

Driven piles and drilled shafts are the two most widely used deep foundation types. California High-Speed Rail Authority Construction Packages discuss the requirements for some deep foundation types including micropiles as well as drilled shaft and driven pile. (See Book III, Part A. 1 - Design Criteria Manual by California High-speed Rail Authority (2015)). The design of deep foundations should be based on the project-specific data in the geotechnical reports obtained with the field investigations, and no presumptive values shouldn't be used such as International building code (IBC) presumptive allowable bearing pressures that defines the allowable bearing stresses depending on soil/rock classification (International Code Council 2015). The decision of deep foundation can be made per many factors. For example, if there are existing obstacles to perform pile driving, e.g., thick boulder layer, low headroom due to existing bridges and facilities, noise/vibration sensitive environment, drilled shafts may be more feasible. Also, if a single shaft can be used per column (e.g., Figure 2.75), it can be more economical than using a pile group with a pile cap. On the other hand, pile driving can be cost effective if some number of drilled shafts need to be installed per column. For example, in Taiwan, drilled shafts, also called as bored piles in the country, have been preferred to driven piles due to concern of vibration and noise to nearby buildings and facilities, considering Taiwan is one of the most densely populated country. With the reverse circulation method introduced in 1960s, the drilled shaft construction became a popular deep foundation. The reverse circulation drilling uses a dual wall drill where the inner tube is used to continuously discharge the drilled cuttings into the external collector system, and therefore provides a high penetration rate. With the full-length casing method introduced in 1990s in Taiwan, the drilled shaft installation became more efficient in case gravelly soil and bed layers exist, and therefore, around 30,000 piles were installed along the 345 km of Taiwan High Speed Rail (THSR) lines (Chin and Chen 2007). Table 3.7 shows the factor of safety adopted in the THSR foundation design. A large span bridge imposes a higher load on each column and in turn the foundation, for which a higher capacity deep foundation may need to be considered, e.g., barrette, caisson, etc. The barrette foundation is different in the sense that a diaphragm wall machine is used for installation and various cross sections can be constructed, e.g., rectangle, cruciform, H-shape, etc.

Table 3.7. Factor of safety used in the THSR foundation design (Chin and Chen 2007)

	Safety Factor		
	Normal Load	Exceptional Load	Ultimate Load
End Bearing Capacity	3.0	2.0	1.25
Skin Friction	2.0	1.5	1.25
Pullout Resistance	No tension forces are permitted on piles.	2.5	1.5

General rules for the construction shall be adhered to to achieve the high quality of the constructed foundations. For example, the bottom cleanliness of drilled shaft should be checked such that a minimum of 50% of the botoom of the shaft should have less than 0.5" of sediment at the

time of concrete placement, and a maximum depth of sediments at any place of the bottom should not exceed 1.5". The thickness of steel casing should have at least ¾" in case permanent steel casing method is used for the drilled shaft construction. In with the geotechnical report, the groundwater properties should be included so that corrosion susceptiblity can be determined ahead. If the shafts are to be placed in an aggressively corrosive environments, support from the steel casing should not be expected in a long-term. At least 6" offset should be considered at the top of the shaft if the drilled shaft has a diameter larger than 5'. Further details can be found in Standard Specification on Drilled Concrete Piers and Shafts. The micropiles can be designed per AASHTO LRFD BDS with California Amendments, Article 10.9: Micropiles and FHWA-SA-97-070 (Tom Armour et al. 2000).

3.2.1.3. MICROPILE FOUNDATION

Micropile has been used for foundation retrofit. A literature shows on a micropile-based foundation seismic retrofit of the Boeing field control tower in Seattle, Washington (Parmantier et al. 2004). The original construction built in the 1960s was founded on timber piles of unknown length and soil borings performed indicated liquefiable soils in the depths of approximately 35 feet. The foundation retrofit included the use of drilled shafts adjacent to the tower, which was tied to new structural steel bracing which was added to increase the tower to overturning during design earthquake loading. The drilled shafts were placed outside the existing pile cap and consisted of dimensions 4 in diameter and 45 ft in depth. The pile configuration involved placing groups of four drilled shafts on the east and west side of the foundation.

Another case study demonstrated the use of micropile-based foundation groups in San Francisco bay area (Momenzadeh et al. 2013). The foundation retrofit consisted of the use Type "D" micropile groups through an existing foundation pile cap at 5 existing bents. The micropiles were one foot in diameter and consisted of high yield 2.25" treated steel rod extending over the entire length of the pile and a 9 5/8" diameter high yield N80 steel casing extending down to approximately the top of the bonded length of the pile. The micropiles were then subsequently load tested to confirm design assumptions. The piles performed well and reached close to the design limit of 0.5 inch in compression. Load testing also confirmed that under cyclic loading, the displacement shall not exceed the tension dead load, or the risk of pile failure is imminent.

There are two different design mechanisms contributed by micropiles when used as foundation supporting elements, which are (a) Direct structural support (Case 1 micropiles) and (b) Soil reinforcement (Case 2 micropiles). Case 1 micropiles are commonly referred to the case where vertically installed micropiles are directly supporting the foundation load. On the other hand, Case 2 micropiles are typically a network of reticulated elements working as a composite pile-soil foundation by encompassing and reinforcing the internal soil (Shu and Muhunthan 2010). On the other hand, (c) a third type of mechanism (hereafter, referred as Case 3) may be developed to 'significantly' enhance overall seismic performance of bridge in high seismic areas: The mechanism is realized by utilizing the dampers installed between the existing foundation and neighboring 'micropile islands'. This design was inspired by the micropile foundations with prefabricated caps used for transmission towers against high winds (American Galvanizers Association 2012). As the prefabricated cap is used along with the rapid micropile installation, the construction is fast. Furthermore, the seismic retrofit can be easier for the bridge foundations in locations with limited

access. Use of micropiles in seismic areas has many advantages as the system provides great ductility and flexibility. Case 3 mechanism may be combined with the other types of design mechanism (i.e., Case 1 or 2) to increase the resistance against the increased load due to HSR. Researchers have reported that use of micropiles have many benefits for bridge constructions (Herbst 1994; Mason 1993; Pearlman et al. 1993). Figure 3.12 shows an example of using mircopiles to enhance the performance of bridge foundation, in which a group of 4 micropiles with a diameter of 0.25 meters was used to enahnce the foundation of 6 piles. Alfach (Alfach 2019) showed the overall improved foundation performance with the battered pile fixed to the cap.
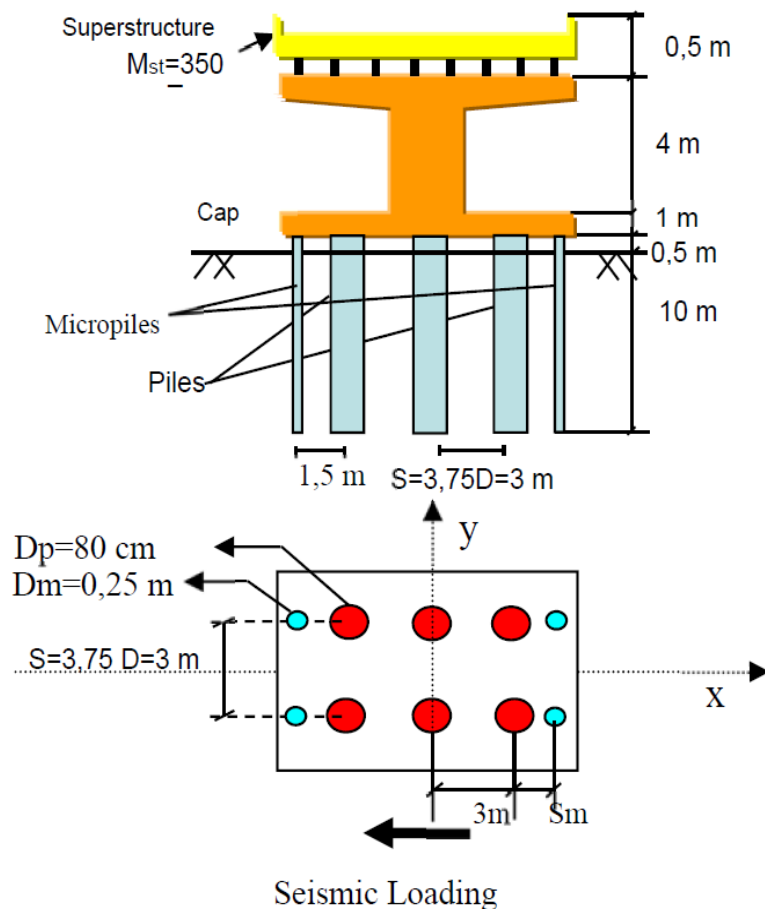
Figure 3.12. Bridge foundation reinforcement using micropiles (Alfach 2019)

3.2.2. DRAINAGE

Bridge drainage path can be designed by sloping the deck and the girders in the superstructure, from which the water is gathered and passed on to a funnel cast into the concrete substructure, and then pier columns and abutment walls to the foundations. However, it is important that the drain pipes do not go through the potential platic hinge areas. Further details can be found in the Drainage chapter in California High-Speed Rail Authority Construction Package 4 (California High-speed Rail Authority 2015).

3.2.3. GEOTECHNICAL DEMAND

3.2.3.1. UPLIFT AND DOWNDRAG FORCES

No net uplift force shall be acceptable for shallow foundations under any load combinations. On the other hand, no net uplift force is expected for deep foundation piles and multi-column bents under service load combinations, while the net uplift is allowable for ultimate limit states and extreme load conditions. In case the Maximum Considered Earthquake (MCE) counteracts 50% of the dead load action, hold-down gadgets should be implemented to lower it to less than 10%, where the the dead load refers to the dead load of structural and non-structural components as well as the permanent attachements. Potential downdrag on the deep foundations also should be taken into account. The CA HSR authority requires to document the required negative skin friction in the geotechnical report. Further details can be found in the Geotechnical chapter in California High-Speed Rail Authority Construction Package 4 (California High-speed Rail Authority 2015) or AASHTO LRFD BDS with California Amendments Article 3.11.8.

3.2.3.2. GROUND MOTIONS

Both Maximum Considered Earthquake (MCE) and Operating Basis Earthquake (OBE) should be considered in the design against seismic excitations. Per CA HSR Construction Package 4, MCE is defined as "ground motions corresponding to greater of (1) a probabilistic spectrum based upon a 10% probability of exceedance in 100 years (i.e., a return period of 950 years); and (2) a deterministic spectrum based upon the largest median response resulting from the maximum rupture (corresponding to Mmax) of any fault in the vicinity of the structure" and OBE is defined as "Ground motions corresponding to a probabilistic spectrum based upon an 86% probability of exceedance in 100 years (i.e., a return period of 50 years)." Figure 3.13 shows a design spectra for elevated structures adotped in CP4.
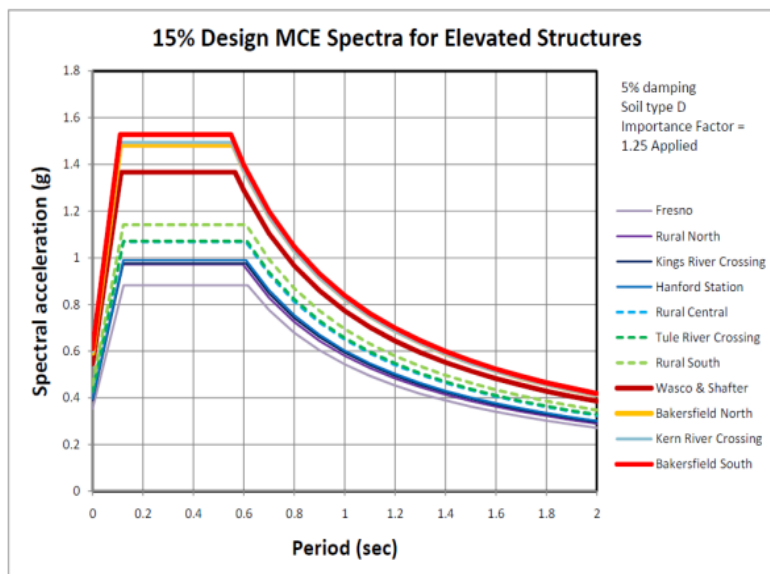
Figure 3.13. Design Spectrum of CP4 (California High-speed Rail Authority 2015)

3.2.3.3. EARTH PRESSURES

Vertical and lateral earth pressures along with other soil parameters should be determined to design the substructure elements. Loading from neighboring buildings or facilities shall be also considered for the estimation.

3.2.3.3.1 VERTICAL EARTH PRESSURE

The maximum depth should be considered to estimate the vertical earth pressure including ground surface, roadway crown, etc. To be on the conservative side, 100% of saturation ratio should be considered when estimating the soil unit weight.

3.2.3.3.2 LATERAL EARTH PRESSURE

The lateral static earth pressure shall be typically calculated for cantilever retaining walls which have the base and a free end that is not restrained against any lateral pressure. This deformation of the free end should not exceed 0.004H where the height 'H' is defined as the wall height from the base to the top. The limit states need to be computed based on the active and passive failures. While the aforementioned type of retaining wall is called as a yielding wall, the rigid wall is a type restricted at the top to control the deflection associated with the active pressure failure. The permanent lateral earth pressure for the walls can be estimated assuming equal fluid pressures at-rest and the Mohr-Coulomb yield criterion.

3.2.3.4. GROUND SETTLEMENT

Ground settlement includes elastic and plastic settlement including soil consolidation is caused by sustained loading and/or the temporal train-track interactions. The settlement is measured from the top of foundation, and the tolerable settlements need to meet the requirements in accordance with AASHTO LRFD Bridge Design Specifications. While there is no specific settlement requirement for MCE events, settlement limits under OBE loads are specified as shown in Table 3.8 where the allowable settlement for foundations is limited such that it should not exceed the sum of estimated settlements under the service 1 and OBE loads which includes post-liquefaction down drag, etc. The maximum horizontal drift between the top and bottom of a deep foundation is typically limited to less than 1.75" under OBE loading (Gingery et al. 2011). Further discussions on the settlement requirement may be found Section 12.8.6.18 in the Geotechnical chapter in CA HSR Authority Construction Package 4 (California High-speed Rail Authority 2015).

Table 3.8. Settlement limits for the combined service 1 and OBE loads (Gingery et al. 2011)

Settlement Criteria	Non-Ballasted Track	Ballasted Track
Differential settlement between adjacent supports [1]	<= L/1500 and 3/4", where L = smaller span	N/A [3]
Differential settlement between the abutment and approach embankment [2]	<= 3/8" over 62 feet	<= 3/4" over 62 feet
Differential settlement between the abutment and tunnel portal	<= 3/8" over 62 feet	N/A [3]
Uniform settlement at piers and abutments	<= 3/4"	N/A [3]

Notes:
1. The additional forces imposed on the structural system by differential settlements shall be calculated and considered as part of dead load in the design.
2. Prior to placement of tracks, the approach embankment shall be instrumented and monitored for a period of at least 6 to 12 months to ensure the embankment is in compliance with the settlement requirements set forth in the table above.
3. Not applicable based on the assumption that ballasted track will not be used for bridges, aerial structures or tunnels.
4. The settlements are calculated from the Service 1 load combination plus any settlements resulting from the OBE load combination (such as those resulting from post-liquefaction downdrag, seismic compaction, etc.).

3.2.3.5. HYDRAULIC PRESSURE

The impact of groundwater pore pressure caused by various hydrostatic and dynamic effects including buoyancy, wave loading and others should be considered in accordance with the requirements specified in Section 3.7 of the CBDS (Caltrans Bridge Design Specifications). To construct underground systems and the substructure of aerial systems and dwellings, including foundations and piling,The uplift pressure caused by the groundwater flow shall be considered with the highest water table location for conservative potential energy estimation or the extreme flooding condition described in the hydrologist report. The capacity of the structures against the uplift pressure can include the weight of constructed structures and other permanent dead loads. The possibility of design scour should be consulted with hydrology engineers and needs to be investigated in accordance with AASHTO LRFD BDS with California Amendments Article 3.7.5 (California High-speed Rail Authority 2015).

4. NUMERICAL MODELING STRATEGIES

4.1. SYNTHESIS OF NUMERICAL MODELING STUDIES ON THE TOPIC OF OF HSR SYSTEMS

Following the rapid growth of high-speed railway transportation and the advancement of railway technology driven by an increasing demand for more efficient, cost-effective, and safer railway transportation, precise analysis of dynamic interaction for vehicles and bridges has become an issue of great significance. To encourage comprehensive understanding of proper idealization of such systems, modeling techniques for train, track, and bridge systems from national and international studies, and available design guidelines have been studied and synthesized in their respective sections. The scope of the literature search conducted herein focuses mainly on the modeling of superstructure components, and only briefly touches upon the modeling methods of substructure components.

4.1.1. MODELING OF TRAIN SYSTEMS

High-speed train systems are mainly constituted by two vehicle systems: traditional vehicle systems and articulated vehicle systems. A traditional vehicle system is characterized by two bogies or trucks in the fore and rear parts of the car-body, and each passenger car behaves independently (Figure 4.1). Each vehicle has one car-body, two bogies, and four wheelsets. On the contrary, an articulated vehicle system as shown in Figure 4.2 connects successive passenger cars by a single bogie frame (Figure 4.2b), but the power car and motorized car at each end of the high-speed train are still supported by their own bogies like a traditional vehicle system (Figure 4.2d). The articulated vehicle system restrains the composition of the train but is proven to effectively improve the riding conditions compared to traditional vehicle systems by reducing the vibration generated in each car body (Song et al. 2003).
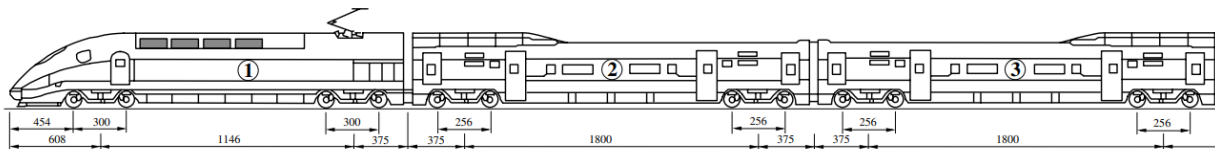
Figure 4.1. China-star high-speed train (Xia and Zhang 2005).
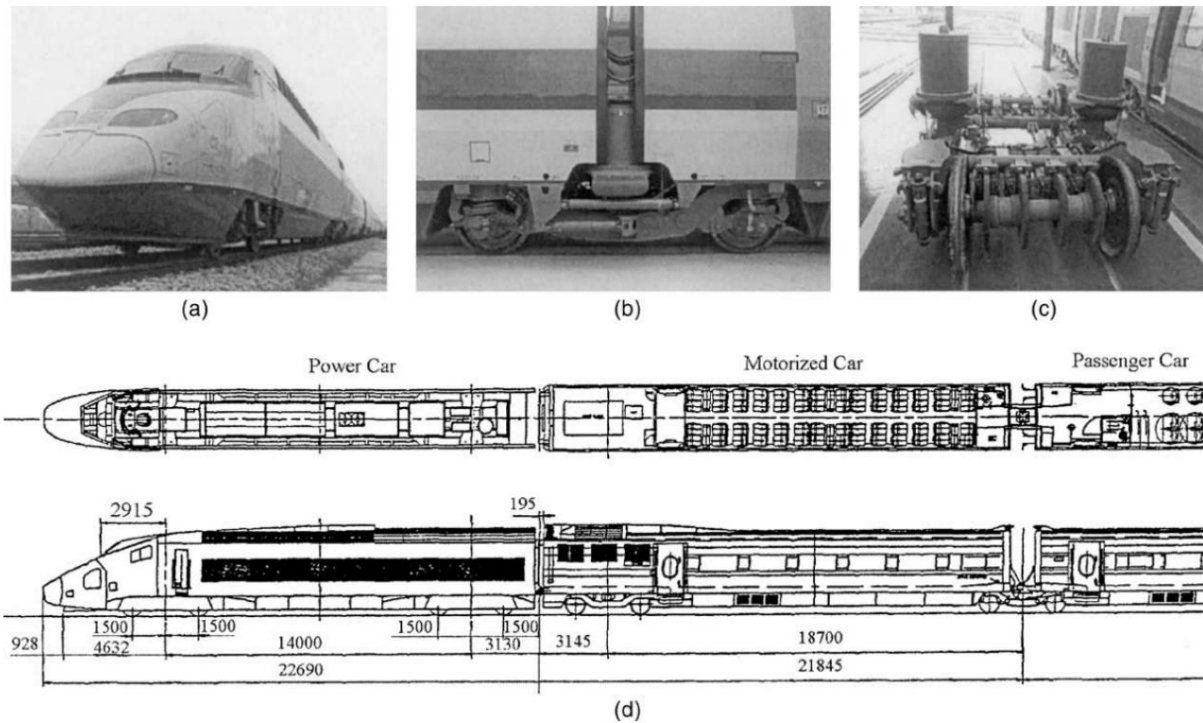
Figure 4.2. Views of the KHST (a) panoramic view, (b) articulated bogie located between the car bodies, (c) articulated bogie and (d) composition of the train (front power car) (Kwark et al. 2004).

4.1.1.1. TRADITIONAL VEHICLE SYSTEM

In early studies, vehicles were often approximated as a moving mass model to consider the inertial effects of moving vehicles and to allow the problem to be solved analytically. However, the effect of the suspension system must be considered for accurate vehicle response. The simplest model in this regard is a lumped mass supported by a spring-dashpot unit, often referred to as the sprung-mass model (Du et al. 2012; Hurty and Rubinstein 1964; Hutton and Cheung 1979; Mao et al. 2016; Matsuura 1976; Tanabe et al. 1987; Vijay K. Garg and Dukkipati 1984; Wu and Yang 2003; Xia and Zhang 2005; Yang and Lin 1995; Yang and Yau 1997; Zeng et al. 2015). The sprung-mass dynamic system can reflect the motions of the vehicle in both the vertical and horizontal directions. The car-body, bogies and wheelsets in each vehicle are assumed as rigid bodies, neglecting elastic deformation, and are connected to each other three-dimensionally by linear springs and dampers. The primary and secondary suspension systems of the bogies are simplified as an elastic system with linear springs and viscous dampers. Placement of the spring-dashpot units within each suspension system differ slightly among studies depending on the type of HSR train system and the specific bogie design, as can be seen by comparing the various train model schematics in Figure 4.3 through Figure 4.7.

Another method is to model the car-bodies, bogies, and wheelsets as beam finite elements and the suspension system as a variation of bilinear and multilinear springs in the three directions. Montenegro et al. (2016) have modeled all springs characterized by a bilinear behavior, except the one used to model the secondary transversal suspension which follows a multilinear law to

simulate the presence of rubber stoppers whose stiffness increases gradually (Figure 4.5). Nonlinear springs can be used to model the suspension system, but most of the studies have simplified the analysis by assuming a linear behavior.

The car-bodies and bogies are typically assumed to move along a well-maintained straight track at a constant speed, and the wheels and the track to always keep in contact, neglecting sliding, climbing or derailment phenomena (He et al. 2011; Liu et al. 2009; Mao et al. 2016; Song et al. 2003; Yu et al. 2016; Zeng et al. 2015). The assumption of perfect contact between wheel and track is commonly represented as the vehicle-track interaction by coupling the displacement degree-of-freedom (DOF) relationships between the rail and wheel-set subsystems. A Hertzian contact spring can be placed in-between each wheel and rail to accurately model the wheel-rail contact stiffness by consider the changing contact area caused by the indentation of the rail due to the geometry of the wheel (Connolly et al. 2013; Nguyen et al. 2009; Rocha et al. 2014)

The main difference of vehicle modeling among studies is the selection of the DOFs to be concerned in the car-body, bogies, and wheelsets. Each node has a maximum of six DOFs in finite element modeling but not every DOF is taken into consideration depending on the study. Typically, each car-body and each bogie have five DOFs in consideration: lateral displacement, roll displacement, yaw displacement, vertical displacement, and pitch displacement. The sliding displacement is often omitted because the high-speed train is assumed to be in motion and not stationary (Du et al. 2012; Liu et al. 2009; Tanabe et al. 1987; Xia et al. 2003) Although rolling and sliding motions would be excited due to torsional vibrations and track irregularities, these motions are commonly constrained for efficiency of formulation (Song et al. 2003). On the contrary, Xia and Zhang (Xia and Zhang 2005) and Liu et al. (Liu et al. 2009) have included the rolling motion in the concerned DOFs. If the train system is being modeled in a scenario where seismic loading is present, the rolling motion should be accounted for because the seismic loading would heavily excite the rolling motion in the car-bodies and bogies, as the wheelsets are assumed to stay in direct contact with the rails. The concerned DOFs for the wheelsets can be limited to the lateral displacement, vertical displacement, and the roll displacement (Liu et al. 2009; Mao et al. 2016). The other DOFs can be neglected because the wheelset is constantly in rotation and the wheels always stay in contact with the track system. Various schematics of traditional vehicle systems are shown in Figure 4.3, Figure 4.4, and Figure 4.5 as previously mentioned.
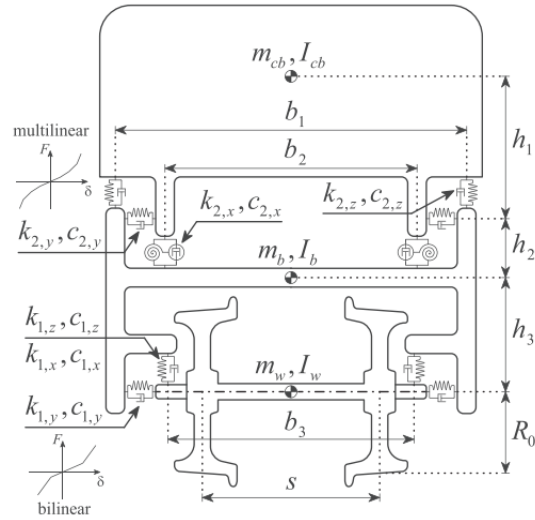
Figure 4.3. Front view of the sprung-mass dynamic car model (Montenegro et al. 2016).
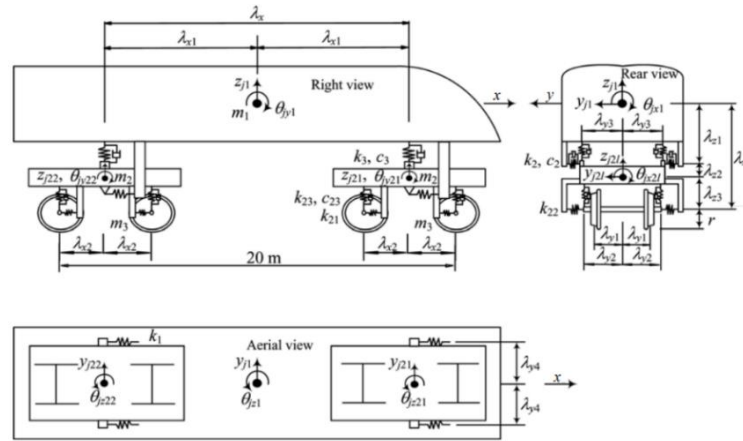
Figure 4.4. Tradition train system modeled (He et al. 2011).
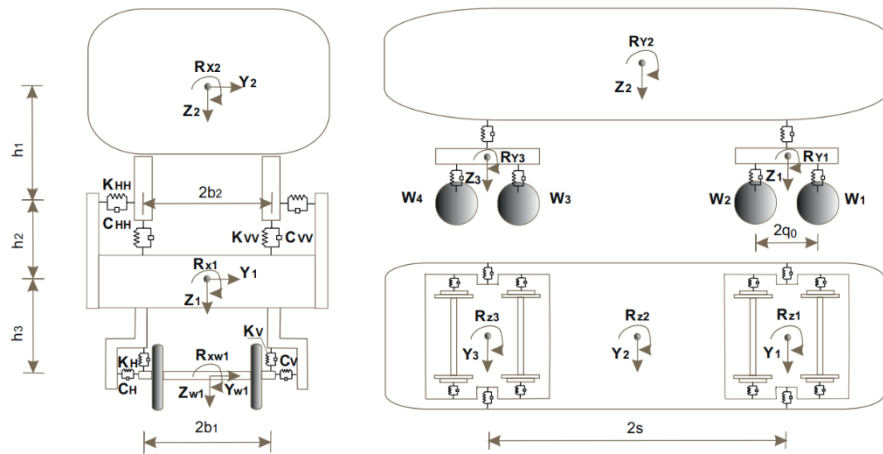
Figure 4.5. Traditional train system modeled (Liu et al. 2009).

For articulated vehicle systems, each passenger car no longer behaves independently, and the behavior of each bogie will be affected by the dynamic behavior of the fore and rear car-bodies. Aside from the coupling of intermediate passenger cars, the modeling procedure of articulated vehicle systems are similar to the traditional vehicle system. The model by Kwark et al. (Kwark et al. 2004) individually modeled the car-bodies, the bogie in between, and the wheels with DOFs as shown in Figure 4.6. Additional damping due to a central elastic hinge in-between adjacent car-bodies was modeled by transverse springs and dampers, also seen in the model by Xia et al. (Xia et al. 2003). Another method is to model the fore and rear car-body behavior as a single joint directly above the articulated bogie. In Song et al., (Song et al. 2003) study, the bouncing, sway-ing, pitching and yawing motions are considered for the non-articulated power cars and these motions were condensed into two DOFs by the bouncing motion and swaying motion at the joint for the articulated vehicles, as shown in Figure 4.7. The bogie considered the bouncing, sliding, swaying, pitching, rolling, and yawing motion, so each car had a total of 16 DOFs. The car-body masses are lumped at the joints and the bogies are connected through rigid bodies with masses. This method was also followed by Rocha et al. (Rocha et al. 2014).
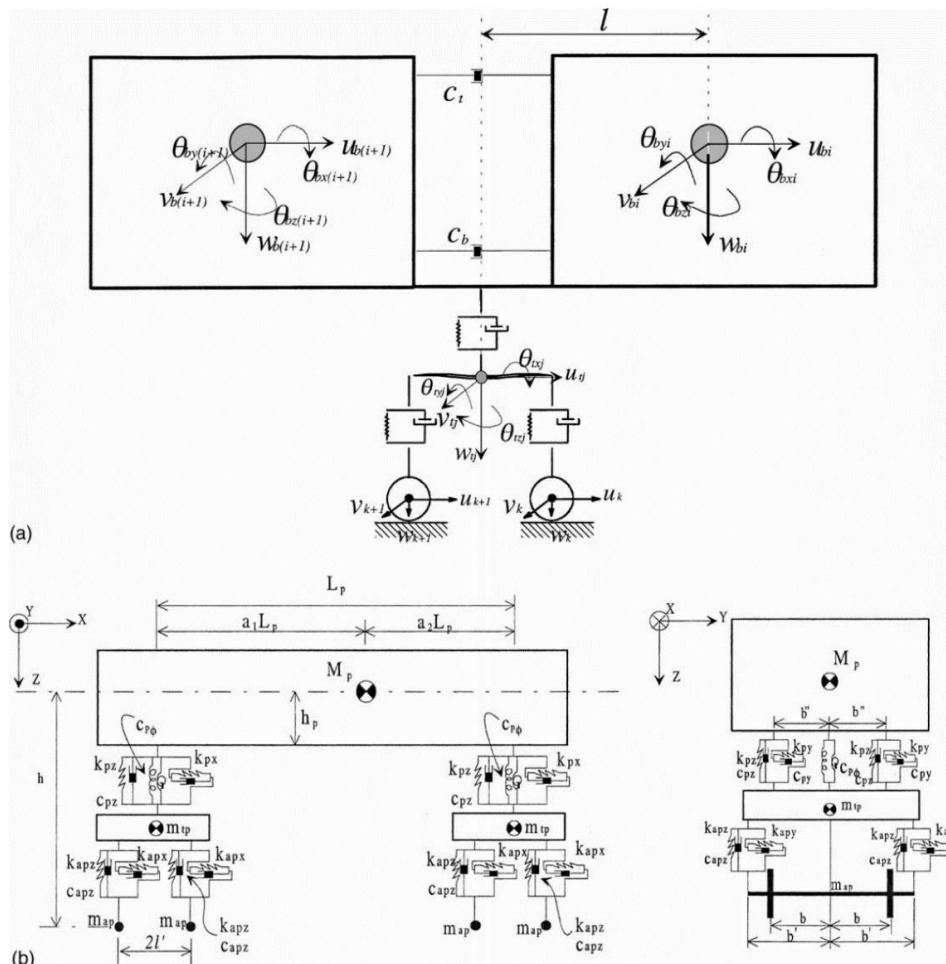
Figure 4.6. Articulated train system modeled by Kwark et al. (Kwark et al. 2004)
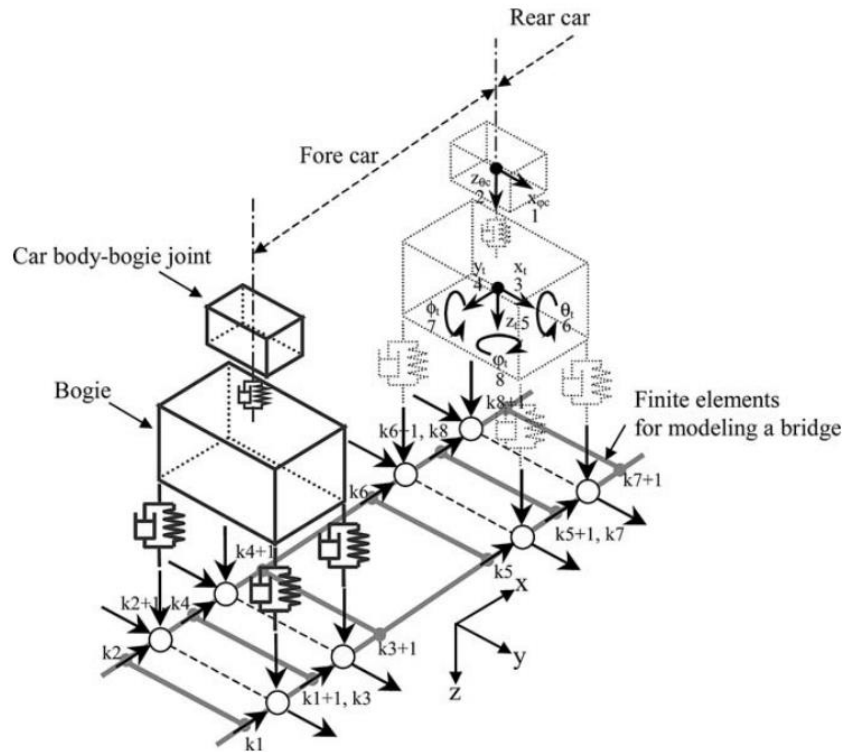
Figure 4.7. Bogie–bridge interaction system in an articulated train system modeled by Song et al. (Song et al. 2003).

4.1.2. MODELING OF RAILWAY TRACK SYSTEMS

4.1.2.1. RAIL

Rails in HSR systems mainly rest on two types of foundations: ballasted foundations and ballast-less foundations. For both systems, a single track consists of two rails that are designed to behave elastically as a capacity protected element. Therefore, they are modeled as a series of linear elastic beam-column elements, and this method is consistent throughout numerous research studies investigated for this report (Li et al. 2020; Li and Conte 2016; Liu et al. 2009; Zeng et al. 2015) If bridge abutments are being modeled, the rail elements should be extended past the abutments to the embankments to correctly represent the transition zone (Li and Conte 2016; Montenegro et al. 2016).

When the train system is being modeled as a moving load, rail irregularity is commonly considered to simulate the complex time-varying random dynamic behavior that occurs when a high-speed train crosses over a bridge. Safety, stability, comfort, service-life of train and track components, as well as the environmental noise of the train is influenced by irregularity in the rails (Lu et al. 2015). Vertical irregularity considers roughness of the rail surface, elastic deformation, inelastic deformation, inconsistency of gap components, and uneven subsidence of track foundations. Rail irregularities are approximately represented as stationary and ergodic processes in space due to its random nature and is most frequently characterized by power spectral density (PSD) functions (Nguyen et al. 2009; Rocha et al. 2014; Song et al. 2003; Yu and Mao 2018). The PSD functions are adjusted based on the characteristics of the rails used in each country.

91

4.1.2.2. BALLASTED TRACK SYSTEM

For ballasted track systems, rails rest on an elastic foundation composed of track ballast and railroad ties (Figure 4.8). Ballast is the crushed material placed on the top layer of a bridge superstructure to allow the embedment and support of railroad ties, also known as sleepers. The ballast is traditionally made of interlocking sharp-edged hard stone to stabilize the track system. Rails are fixed to railroad sleepers by fasteners. Rail pads are placed between the rail and tie to act as a damper that reduces fatigue cracking of fasteners due to impact. Rail ties are rectangular wood or reinforced concrete supports placed transverse to the rail and maintains correct gauge spacing between the rails.

A ballasted track system modeled by Song et al. (Song et al. 2003) is shown in Figure 4.9. The figure demonstrates a simple model with rails and sleepers as beam elements and ballast as Winkler springs to idealize a two-parameter elastic foundation that models the interaction between the track and the bridge deck. Ties were modeled as beam elements and lay on the ballast, modeled similar to the Winkler foundation consisting of infinite closely spaced linear springs. It is noted that the traditional Winkler foundation, based on the Winkler hypothesis, does not consider interaction of springs. On the contrary, the additional second parameter suggested by Zhaohua and Cook (1983) considers the effects of the interaction between the linear spring-dampers which accurately represents characteristics of practical foundations.

The ballasted track system modeled by Montenegro et al. (Montenegro et al. 2016) similarly modeled rails and sleepers as beam elements (Figure 2.2). The stiffness and damping of the rail pads/fasteners are combined and modeled as linear spring-dampers to simulate the dynamic behavior of this layer. The ballast and non-structural elements such as safeguard and edge beams of the deck were modeled as point mass elements. Spring-dampers are also used to idealize the stiffness and damping of the ballast layer in the longitudinal, transversal, and vertical directions.

Guo et al. (2012) modeled both the sleepers and ballast as point mass elements at an interval. The sleepers were connected to the rail through distributed spring-dampers simulating the dynamic behavior of rail pads. The vertical and horizontal stiffness and damping of the ballast were idealized with spring-dampers which also connect the ballast layer to the sleepers. Shear stiffness of the ballast layer was also explicitly modeled as spring-dampers, and rigid arms connected the ballast to the bridge deck (Figure 4.11).
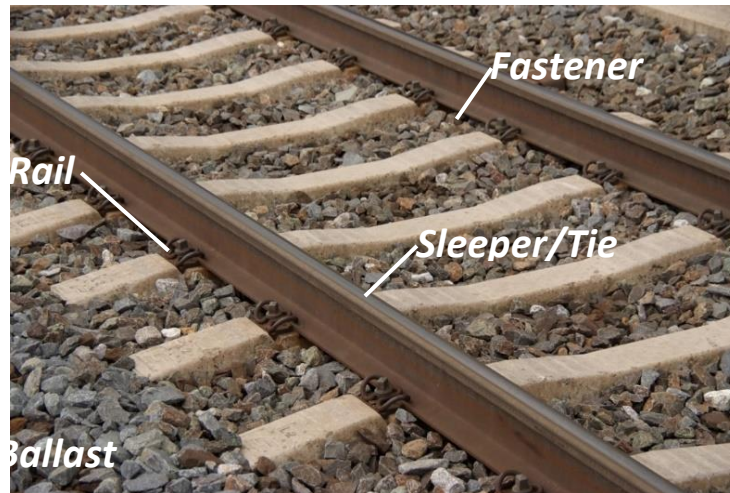
Figure 4.8. Photo of ballasted track system (Plasser American 2020).
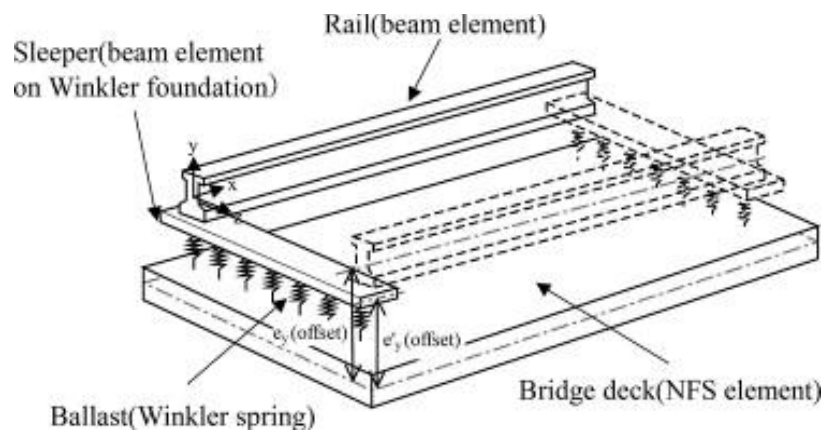
Figure 4.9. Ballasted track system modeled by Song et al. (Song et al. 2003).
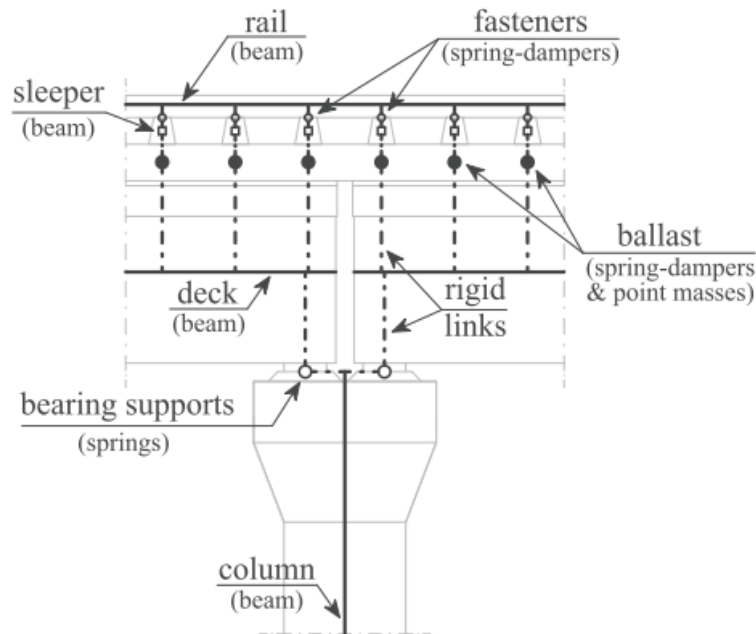
Figure 4.10. Ballasted track system modeled by Montenegro et al. (Montenegro et al. 2016).
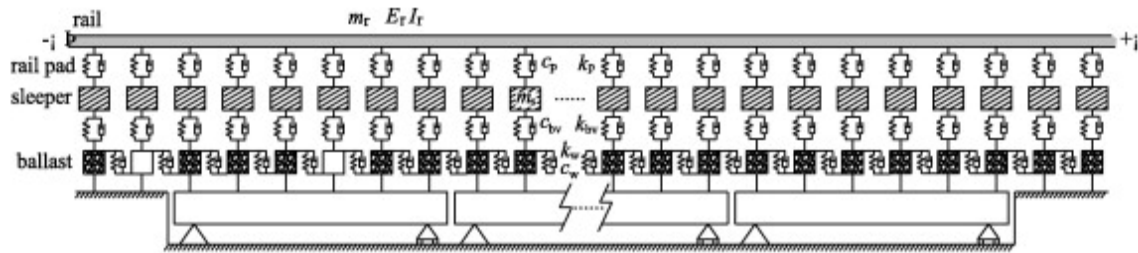
Figure 4.11. Ballasted track system modeled by Guo et al. (Guo et al. 2012).

4.1.2.3. BALLASTLESS TRACK SYSTEM

As the name suggests, ballastless track systems utilize slabs instead of ballast (Figure 4.12). The typical design includes continuous welded rails, track plates, base plates, and connecting members (Li et al. 2020; Li and Conte 2016) Connecting members can vary depending on regional design standards. In the study by Li et al. (Li et al. 2020), the China Railway Track System (CRTS) II ballastless track was adopted and includes sliding layers, shear cogging, concrete asphalt (CA) mortar layers, shear reinforcement, fasteners, and lateral blocks as connection members. Similarly, the Japanese reinforced concrete roadbed system (RCRS) slab track utilizes fasteners, track slabs and CA mortar (Figure 4.13). The study by Li and Conte (Li and Conte 2016) for the California High Speed Rail (CHSR) Authority adopted connecting members of direct fixation fasteners for rail-track slab attachment and cylinder bollards as shear reinforcement to anchor the track slab to the concrete base plate. Figure 4.14(a) demonstrates the modeling schematic of a CHSR ballastless track system Li and Conte (Li and Conte 2016). The rails were connected to the rigid deck

through direct fixation fasteners modeled as a series of three elastic and inelastic springs to rep-resent the behavior between the rails and track base.

To represent the rail-structure interaction, linear springs were used to model the vertical and transverse stiffness, and an elastic–perfectly–plastic (EPP) spring was used to model the re-sistance of the track base against the relative longitudinal displacement of the rail track. Addi-tionally, longitudinal boundary springs were modeled at each rail end because of the finite length modeling of the rail extensions to accurately capture seismic response performance. A nonlinear spring model, defined as a single element, denoted as series-parallel (S-P) spring model, was de-veloped to represent the longitudinal boundary spring. A mechanical model was developed to calibrate and validate the rail boundary spring model, and the cyclic hysteresis behavior of the mechanical and S-P model is shown in Figure 4.14(b). The closeness of the behavior validates the S-P model.

In the China Railway Track System (CRTS) study by Li et al. (Li et al. 2020), the track plate and base plate were modeled using linear elastic beam-column elements with their respective cross-section parameters because they are designed to behave elastically as capacity protected elements (Fig-ure 4.15). The connection components consisting of the sliding layer, CA mortar layer, fastener, shear reinforcement, and lateral block are simulated using nonlinear zero-length elements.
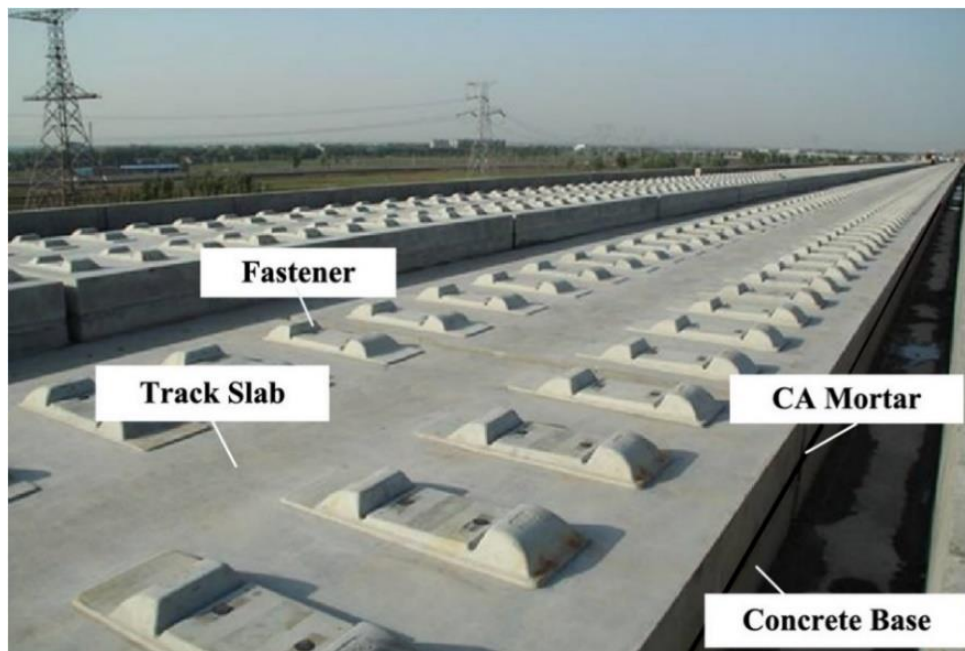
Figure 4.12. Photo of ballastless track system (Wang et al. 2019).
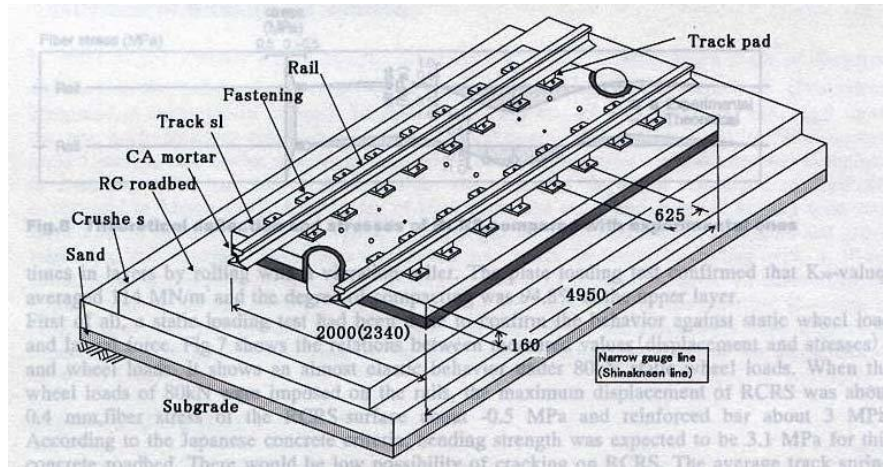
Figure 4.13. Japanese type RCRS slab track on grade (Tayabji and Bilow 2001).
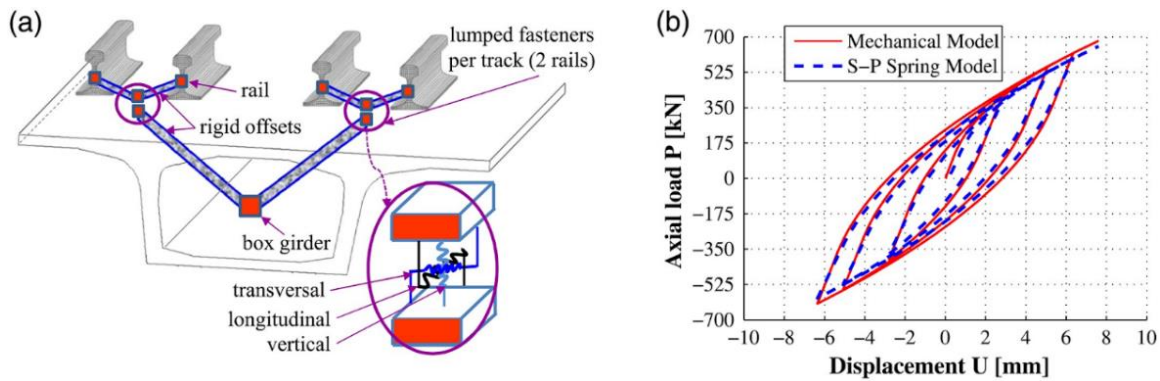
Figure 4.14. Track system scheme with fasteners (a) and longitudinal boundary spring hysteresis loop (b) by Li and Conte (Li and Conte 2016).
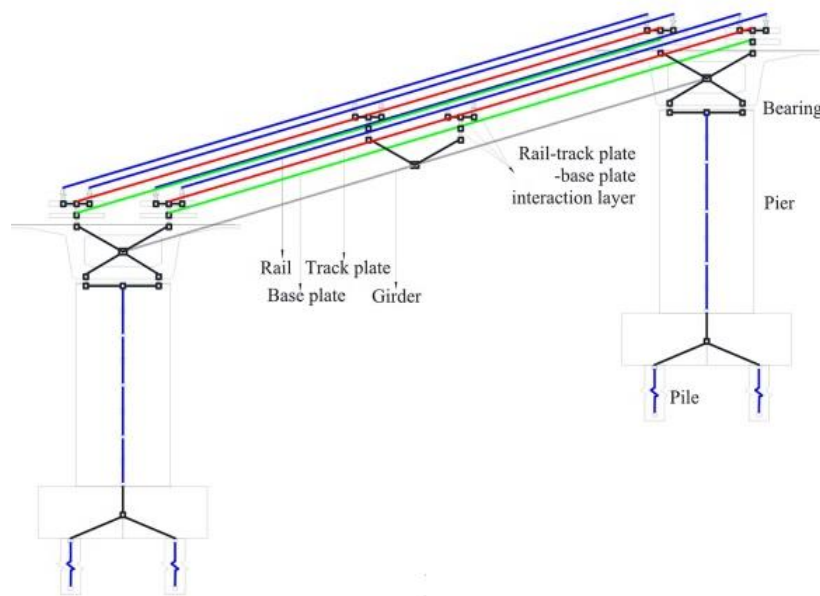
Figure 4.15. Modeling schematic of ballastless track system modeled by Li et al. (Li et al. 2020).

Concrete box girder bridges were found to be the common bridge type used in HSR systems. Such type is commonly modeled using three-dimensional linear elastic beam-column elements, even when representing bridges in highly seismic areas, since they are structurally designed to be capacity protected elements that need to remain essentially elastic (Kwark et al. 2004; Li et al. 2020; Li and Conte 2016; Montenegro et al. 2016) Figure 4.16 and Figure 4.17 schematically show example box-girder bridge idealization and modeling as relates to the track modeling for HSR systems from two previous studies. As shown in the figures, bridge spans are discretized into several nodal increments to allow for the representation of different section properties at the ends of each spans and to accommodate the rail track-to-deck connections and deck-to-bearing connections. Each increment was connected using linear elastic beam-column elements defined by the cross-sectional characteristics of the actual bridge being modeled, and rigid arms were used to connect the bridge girder to the rail and bearing systems. The increment lengths should be adjusted relative to the actual bridge span dimensions and based on the desired accuracy of bridge response values. Bridges have also been modelled as an assemblage of three-dimensional beam elements in the elastic domain with six DOFs at each node as illustrated in Figure 4.18 and Figure 4.19 (He et al. 2011; Li et al. 2020).

Three-dimensional shell elements have also been used to idealize bridges. Song et al. (Song et al. 2003) utilized nonconforming flat shell elements (NFS-series) formulated by a linear combination of the nonconforming membrane element with drilling DOF (NMD-series) and the nonconforming plate bending element (NPB-series). NFS elements with six DOFs per node are used to model the box-girder structure as shown in Figure 4.20. In-plane and out of-plane deformations are coupled and the consistent mass matrix of the NFS element is lumped at the element joints using the HRZ lumping scheme (Song et al. 2003). When the superstructure and track system are modeled using NFS elements, consisting of four nodes with six DOFs per node, it is common engineering practice to use a relatively fine finite element grid in areas of high stress gradients due to abrupt geometrical changes or concentrated loading and a course finite element grid in areas of uniform stress gradients. Transition zones between the fine and coarse grids are modeled using variable-node NFS elements (Song et al. 2003).

In another study, a combination of flat plate elements and beam elements were used to model a steel plate girder bridge. In Kim et al. (2005) study, a steel girder bridge was idealized by modeling the concrete decks as flat plate elements with four nodes and the steel girders, cross beams, and guard rails of the bridge as linear elastic beam elements with six DOF nodes. As a similar steel bridge, a steel box girder bridge has been idealized by modeling the concrete deck as a solid element and the steel box as shell elements (Liu et al. 2009). Headed shear studs that connect the concrete deck to the steel boxes are modeled as linear spring elements in the longitudinal direction and coupled in other directions (Queiroz et al. 2007).
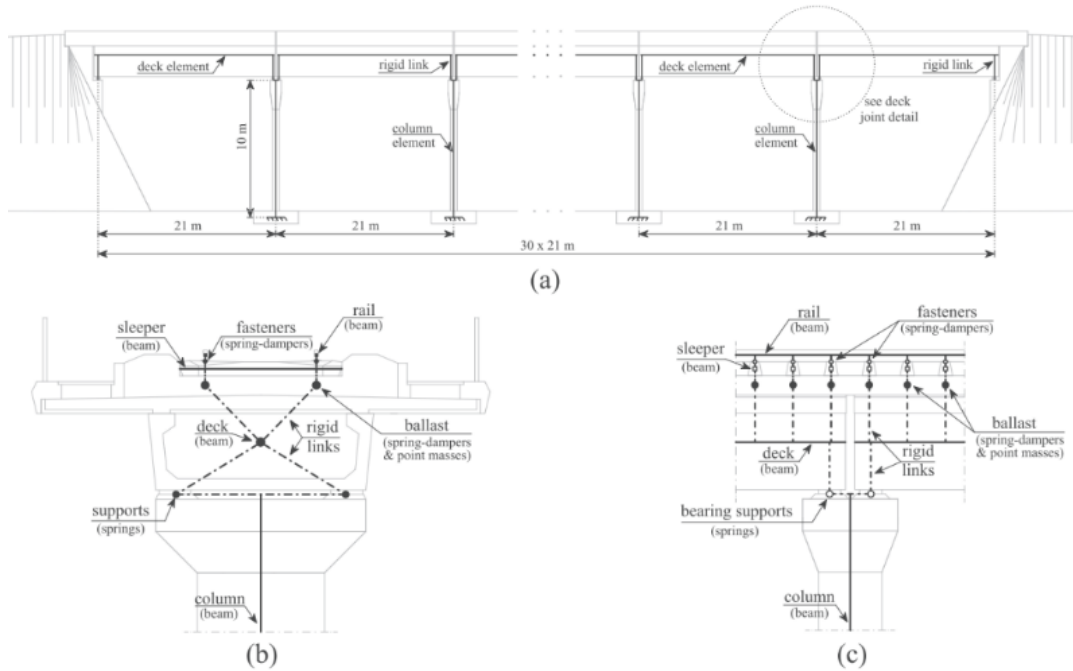
Figure 4.16. Modeling schematic of track-bridge system by Montenegro et al. (Montenegro et al. 2016)
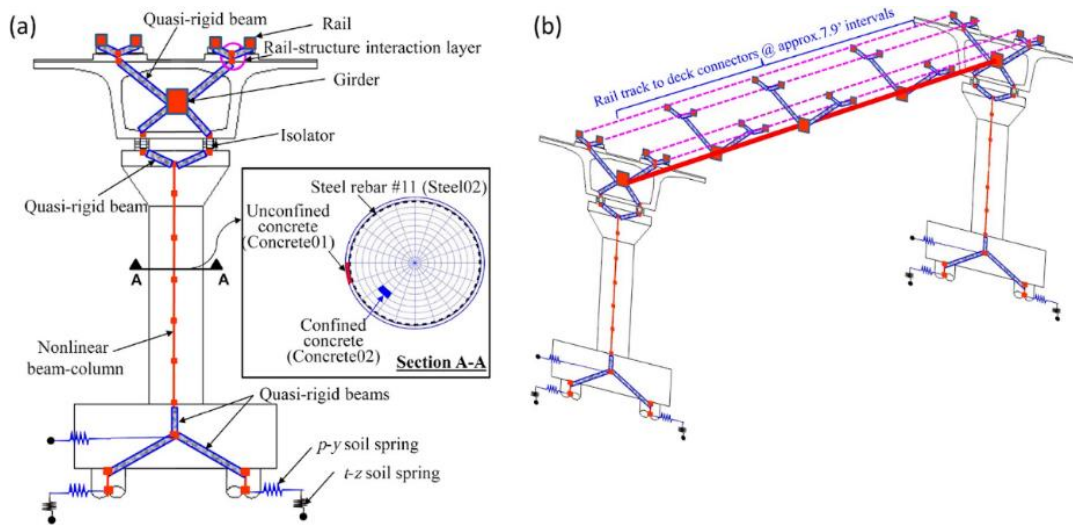
Figure 4.17. Modeling schematic of track-bridge system by Li and Conte (Li and Conte 2016).
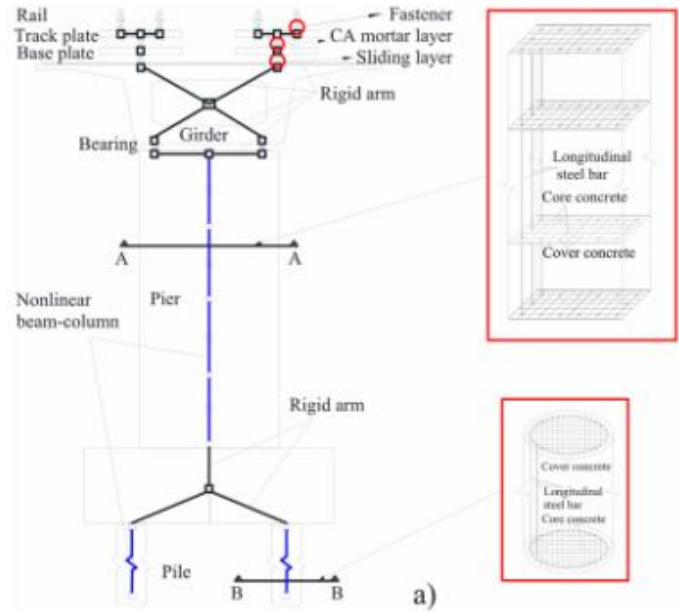
Figure 4.18. Modeling schematic of bridge system by Li et al. (Li et al. 2020).
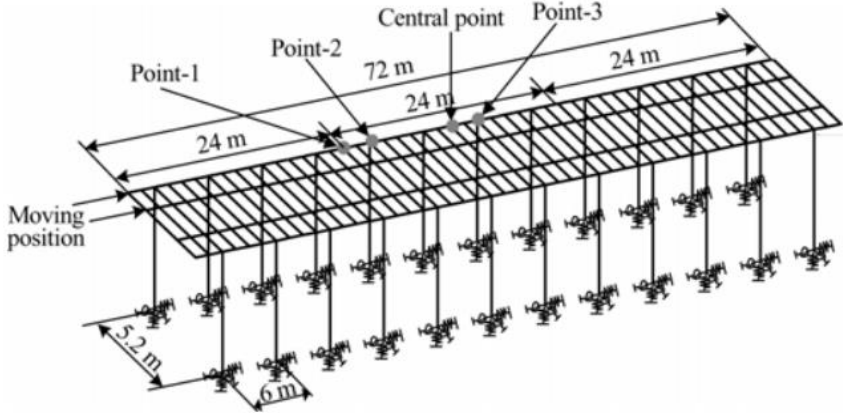
Figure 4.19. Modeling schematic of bridge system (He et al. 2011).
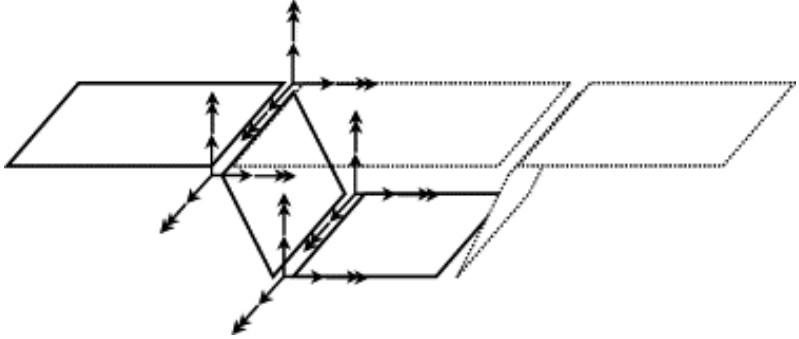
Figure 4.20. Concrete box girder modeled using shell elements by Song et al. (Song et al. 2003).

Pier columns can be modeled using a number of fiber-based elements such as displacement-based fiber-section beam-column elements (Li and Conte 2016), fiber-based force-based beam finite elements (Kaviani et al. 2012), and three-dimensional elastoplastic fiber elements (Li et al. 2020). Fiber based elements account for material nonlinearity, geometric nonlinearity, and bond slip effect of anchoring steel in joints, making it an accurate plastic hinge representation. Integration points are placed along the length of the element in each column to allow for inelastic behavior at every point. Column cross sections are discretized into fibers in polar coordinates as shown in the Section A-A examples in Figures 2-17, 2-18, and 2-21, with a specific nonlinear uniaxial material model assigned to each fiber, i.e. unconfined concrete, confined concrete, and steel rebar (Kaviani et al. 2012; Li et al. 2020; Li and Conte 2016). To obtain the behavior of the nonlinear column section, the fiber behavior over the column cross-section is integrated. Potential plastic hinge regions (bottom of column for seismically isolated bridges, and both top and bottom of column for non-isolated bridges) are modeled using a single element with length equal to the plastic hinge length, approximated as half the column diameter, to ensure mesh objectivity of the finite element response prediction. The portion of the column-bent embedded in the superstructure was modeled as a rigid element attached to the top of the nonlinear beam-column element, and the length of this rigid element is set equal to the distance between the top of the column and the centroid of the soffit-flange of the box-girder.

If a bridge is being modeled to observe the response under moderate earthquakes, the columns may be modeled with a linear elastic behavior, because unlike highway bridges, the HSR bridge columns generally do not experience significant damage in this case. An alternate methodology by Montenegro et al. (Montenegro et al. 2016) estimated the effective stiffness of the columns performed in the elastic domain, considering reduction in stiffness due to cracking. The material behavior of the columns should be decided based on the magnitude of the excitation applied to the structural model and the overall purpose of the model. A number of studies have completely omitted the modeling of bridge piers and limited their model to the train, track, and deck/girder system (Guo et al. 2012).
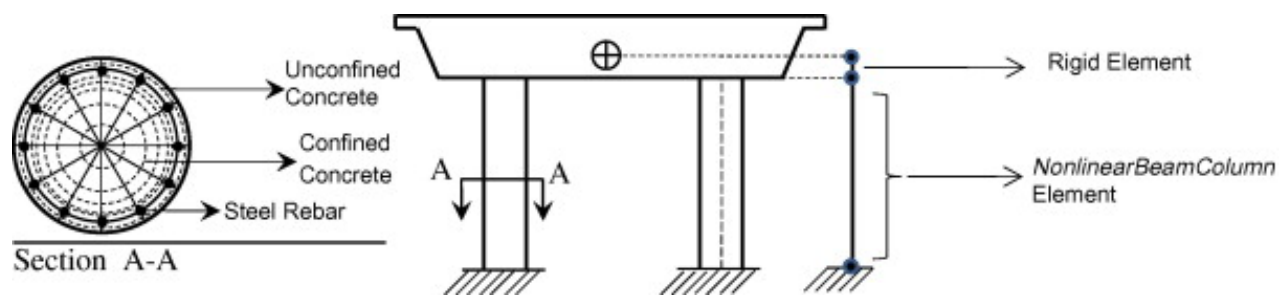
Figure 4.21. Modeling schematic of bridge pier columns using fiber-based elements (Kaviani et al. 2012)

Column supports can be modeled with a variety of complexities depending on the intended study or analysis emphasis on soil-structure interaction. If the focus of the model is to analyze the train-track-structure interactions, the soil-structure interaction can be simplified to a few springs modeled between the fixed base and the bottom of the column footing elements. He et al. (He et al. 2011) modeled the elastic effects of column footings, pile structures and the surrounding soil by placing longitudinal and transversal ground springs at the bottom of each column.

Li and Conte (Li and Conte 2016) have extensively modeled HSR bridge deep pile foundations using a variety of elements. The schematic from their study is shown in Figure 4.22, along with the geometric and material properties that represent the bridge site considered in their study. The well-established p-y approach was used in modeling the pile foundations and each pile was modeled through displacement-based nonlinear fiber-section beam-column elements. These piles were supported by a series of springs distributed along the length of the pile representing the resistance of the surrounding soil, p-y springs for horizontal resistance and t-z springs for vertical resistance. These springs represented the horizontal and vertical resistance of the surrounding soil, and Q-z springs were placed at the pile tips to represent the vertical soil end-bearing. Pile caps were considered essentially rigid and rigidly connected to the top of each pile, thus modeled as quasi-rigid beam elements to capture the various geometric offsets. Hyperbolic p-y springs were attached to the pile caps to represent the lateral soil resistance. Similarly, Li et al. (Li et al. 2020) have modeled pile foundations as three-dimensional elastoplastic fiber elements. The fiber elements were divided into 1 m intervals and connected to the soil through three translational and three rotational springs with constant spring values to simulate the pile-soil interaction (Figure 4.18).
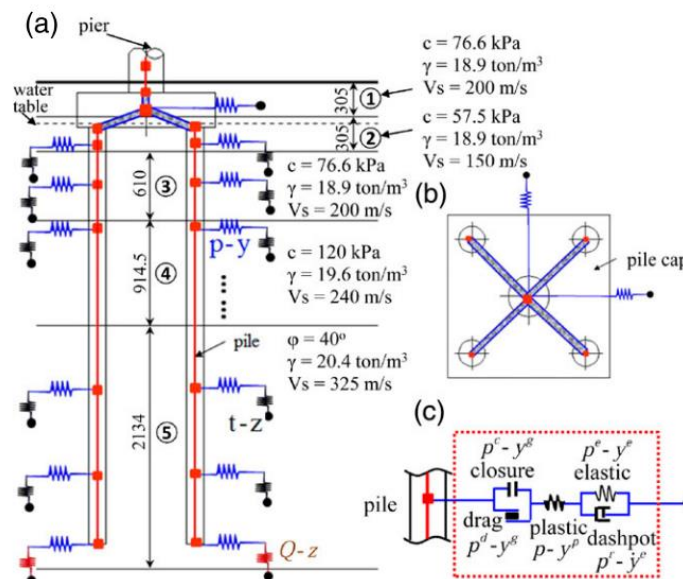
Figure 4.22. Pile foundation model using dynamic p-y approach: (a) schematic view of the FE model, (b) pile cap mode (Li and Conte 2016).

4.1.3.4. ISOLATION BEARING

A bridge bearing is a component of the bridge placed between the bridge superstructure girders and substructure pier/bent. Bearings transfer deck loads to piers or bents and allow specific movements and rotations of the superstructure. Studies that include bearings are limited but explicitly modeling bearings allows the user to capture the interaction between bridge decks and columns. Li and Conte (Li and Conte 2016) idealized a generic seismic isolation device with a material of bilinear inelastic force-deformation behavior. Each bearing is modeled as a zero-length element combined with two uncoupled bilinear inelastic materials for the horizontal behavior: one in the longitudinal direction and the other in the transverse direction of the bridge. Li et al. (Li et al. 2020) similarly idealized bearings as zero-length nonlinear connection elements. Each girder span was supported by four steel bearings, with alternation between fixed and spherical bearings to minimize torsional effects. An elastic-perfectly-plastic force-deformation material behavior was used to model the nonlinear characteristics of the bearings. Linear spring-dampers were used to idealize bearing supports in a study by Montenegro et al. (Montenegro et al. 2016) for moderate earthquakes.

4.1.4. GENERAL MODELING PROCEDURES

4.1.4.1. RIGID CONNECTION ARM

Connections between bridge and track elements are commonly modeled using a type of rigid arm or element. The use of rigid arms allows the user to simplify structural components connecting these elements to each other and allow load transfer throughout the structure. For this study, rigid arms are used to connect the centroid of bridge girders to the track system and bridge girder supports in a similar way to what have been adopted in previous studies and illustrated in Figure 4.16, Figure 4.17, Figure 4.18, Figure 4.22, and Figure 4.23.
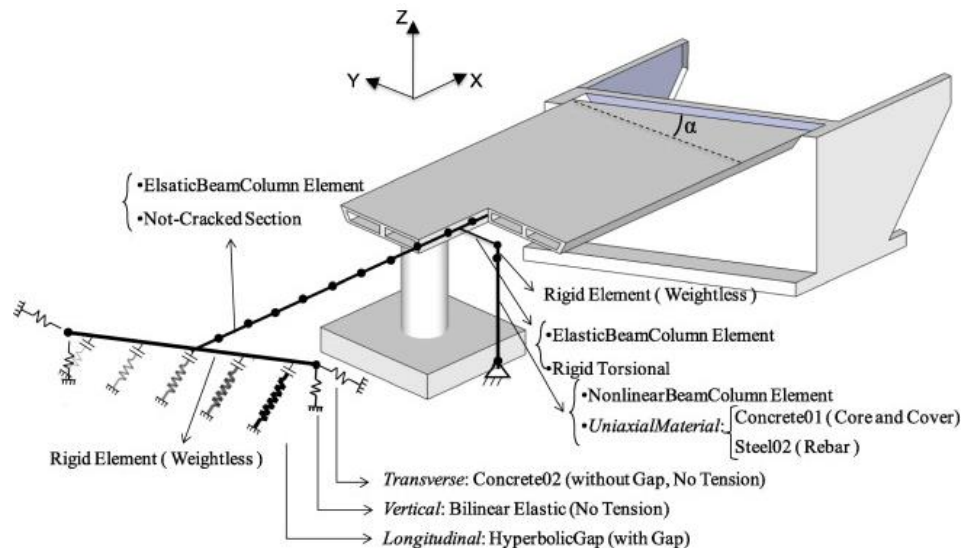
Figure 4.23. Modeling schematic of rigid connections (Kaviani et al. 2012).

Linear elastic beam-column elements assigned with exceedingly stiff properties, referred to as quasi-rigid objects, can be used to represent the rigid offset between respective element nodes such as the rail and deck. Quasi-rigid objects allow the user to extract the internal forces between

the two nodes in connection. The finite element model scheme utilizing quasi-rigid beam elements by Li and Conte (Li and Conte 2016) is displayed in Figure 4.17. The figure illustrates the use of quasi-rigid beam elements to connect the centroidal axis of the box girder deck to the track system along a single span. The rigid element also connects the isolation system to the column substructure and box girder deck at the ends of each bridge span.

Another method for modeling rigid arms is to use rigid links. A rigid link is an explicit command in different analysis platforms such as OpenSees that allows the user to constrain DOFs between a master node and slave node. The command offers two types: bar/rod and beam. The bar/rod type rigid link constrains only the translational DOFs of the slave node to be the exactly the same as those at the master node. The beam type rigid link constrains both the translational and rotational DOFs of the slave node to the master node. The advantage of using rigid links is the simplification of the element stiffness matrix. Rigid links reduce computational effort but does not allow the user to extract the internal forces between the two nodes connected by the rigid link. A modeling schematic by Montenegro et al. (Montenegro et al. 2016) utilizing rigid links, is shown in Figure 4.16. The placement and use of rigid links are almost identical to quasi-rigid objects discussed previously.

4.1.4.2. VISCOUS DAMPING

Energy dissipation can be idealized in finite element models through inelastic materials applied to elements, as mentioned in previous sections, and a method of viscous damping. Although the hysteretic damping included within the elements with nonlinear behavior can dissipate the majority of energy introduced by a seismic load, energy dissipation due to inherent non-hysteretic damping must be accounted for through the application of viscous damping to obtain a realistic result. A Rayleigh damping scheme with a specified damping ratio at two selected modes is commonly used to idealize such damping due to vibration and applies to all structural components of the bridge model that are not highly nonlinear elements (González et al. 2012; Lee et al. 2005, 2006; Wu and Yang 2003; Zeng et al. 2015) The Rayleigh damping scheme forms the damping matrix through a linear combination of the stiffness and mass matrices of the numerical model, and a damping ratio of 2% has been commonly used for HSR bridges (Li and Conte 2016; Montenegro et al. 2016; Song et al. 2003). Higher values of 3% and 5% have also been reported and used in other studies (He et al. 2011; Yu and Mao 2017). The damping coefficients are usually estimated based on the dominant transverse and longitudinal vibration modes, which are estimated from an eigenvalue analysis that uses the tangent stiffness matrix of the bridge system after application of the gravity loads through static analysis.

4.2. HSR BRIDGE NUMERICAL MODEL: SELECTION OF PROTOTYPE SYSTEM AND MODELING PROCEDURE

This section presents the process of formulating a sophisticated train-track-structure interaction model of a prototype HSR system. A prototype bridge, track, and train system were selected from the studies researched in the literature search. The prototype track-bridge system was selected based on the completeness of the design guideline provided in the reference study, such as bridge

dimensions and cross-sectional properties. Assumptions were made where information was omitted in the reference study. This was not a major issue because the purpose of this study was to demonstrate how to model an HSR system as opposed to discuss or assessing the viability of a certain design. Similarly, the prototype train system was selected from a reference study that explicitly stated the masses of the various train components, as well as the stiffness and damping properties of the primary and secondary suspension systems, which are critical to accurately simulating the dynamic behavior of an HSR system.

4.2.1. SELECTION OF PROTOTYPE HSR SYSTEM

4.2.1.1. TRAIN SYSTEM PROTOTYPE

The prototype train system selected for this study is the KTX-Sancheon high-speed train which is shown in Figure 4.24. Formerly known as the KTX-II, the KTX-Sancheon is the second commercial high-speed train operated in South Korea as part of the Korea Train eXpress (KTX), making its debut in 2010. The KTX-Sancheon consists of two power cars at both ends and an articulated set of eight intermediate passenger cars in-between. As mentioned previously, an articulated bogie system couples a passenger car with the fore and rear passenger car, improving riding conditions of the train. As can be seen in Figure 4.24, the power cars have two standard bogies, and the extreme intermediate passenger cars have a standard bogie and an articulated bogie coupling them with the intermediate passenger cars.

Figure 4.24. Photo of KTX-Sancheon (Kim 2014).

4.2.1.2. TRACK AND BRIDGE SYSTEM PROTOTYPE

The prototype track-bridge system selected for this study is a ballastless track prestressed concrete double-track simply supported girder bridge used in a publication by Li et al. (Li et al. 2020). The track-bridge system is from the Beijing to Xuzhou section of the Beijing-Shanghai high-speed railway. The bridge has 10 equal spans of 31.95 m with a total length of 319.5 m. The bridge superstructure is made of C50 concrete and is 13.40 m wide at the top, 5.74 m wide at the bottom, and 3.09 m deep from the top to bottom surface. Each girder end is supported by two spherical

steel bearings that rest on the 11 single column bents of 13.5 m height, made of C50 concrete and HRB335 steel bars. The bridge properties and overview as obtained from the reference study is shown in Figure 4.25.

The CRTS II slab ballastless track was adopted for the track system and comprises of base plates, track plates, rails and connecting members. The connecting members include sliding layers, shear cogging, CA layers, shear reinforcement, fasteners, and lateral blocks. The CHN60 rails are fixed to the base plate through WJ-8C fasteners. The track plate is made of C55 concrete and has a width and thickness of 2.55 m and 0.20 m, respectively. The track plate is connected to the C30 concrete base plate of 2.95 m width and 0.19 m thickness through the CA layer. Shear reinforcement bars are placed at the girder ends in the CA layer to withstand the deformation caused by rotation, and the sliding layer is arranged between the bridge deck and the base plate. The sliding layer, CA layer and fasteners allow for longitudinal slippage relative to the bridge and the lateral blocking provides support in the transverse direction relative to the bridge. The layout of the connection layers is shown in Figure 4.25(b) and Figure 4.26.

a) Elevation layout of high-speed railway bridge /cm

b) Schematic sketch of track and girder structure
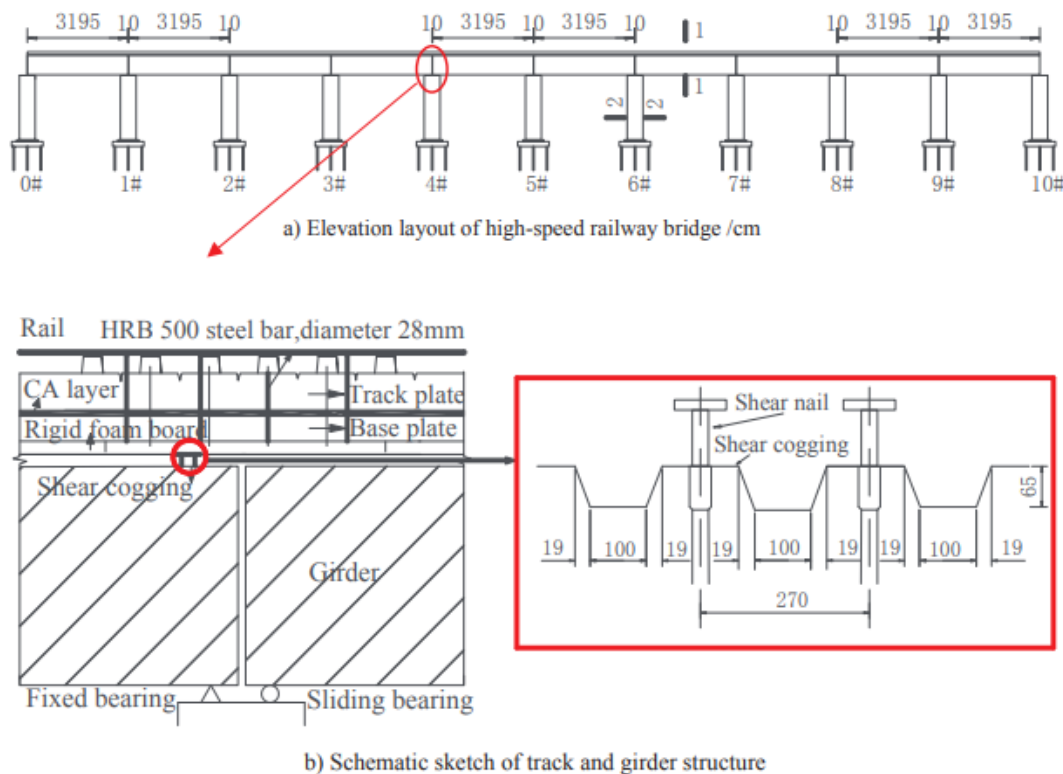
Figure 4.25. Schematic of the prototype bridge: a) Elevation layout of high-speed railway bridge/cm, b) Schematic sketch of track and girder structure (Li et al. 2020).
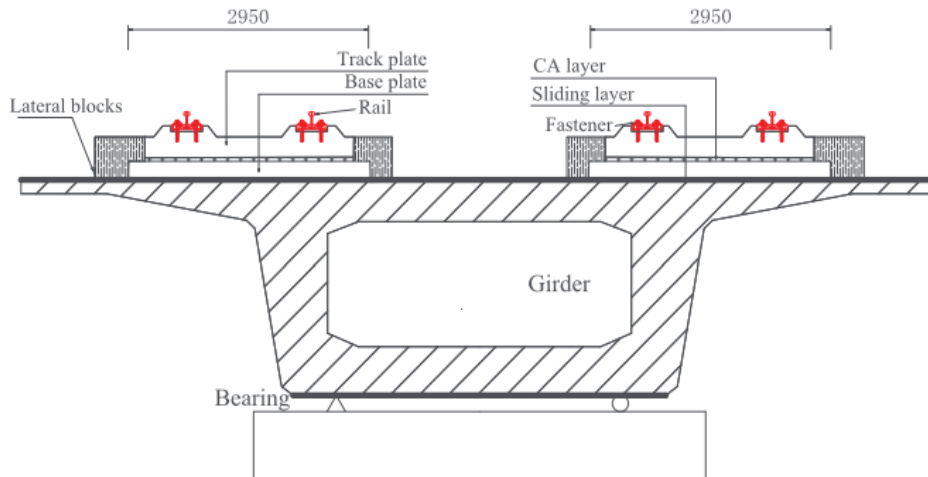
Figure 4.26. Schematic of typical bridge cross-section of track and girder structure (Li et al. 2020).

OpenSees is an object-oriented, open-source software framework that allows users to create both serial and parallel finite element computer applications for simulating the response of structural and geotechnical systems subjected to earthquakes and other hazards (Gregory L. Fenves et al. 2020a). OpenSees allows the user to build a structural model by using the numerous commands available in the program. The commands used in the model for this study are discussed in this section. For the convenience of the reader, the syntax and input parameter of the key OpenSees commands or functions used throughout this study are presented via series of screenshots provided in Appendix A. Moreover, sample scripts that represent or form the main sections of a typical HSR bridge model in OpenSees are provided in Appendix B. In the discussion presented in this section as well as the next section, specific figures from both Appendix A and Appendix B are explicitly referenced in the text for completeness and convenience. Figures from Appendix A and Appendix B use a numbering sequence that starts with A or B, respectively, such as Figure A-5 or Figure B-11 for instance.

To start a model, the user must define the spatial dimensions (1, 2, or 3) and the number of DOFs (1, 3, or 6) at each node, using the model command shown in Figure A-1. Since a three-dimensional model was created for this study, the spatial dimension was specified as 3 and the DOF at each node was specified as 6 to account for all translational and rotational movement. The user can then construct numerous nodes which will be used to construct the framework of the structure. The node command requires a unique tag number and the x, y, and z-coordinates to define the location (Figure A-2). OpenSees uses the numbers 1, 2, 3, 4, 5, and 6 to define the three translational and three rotational DOFs, respectively. For this specific model, the x-coordinates were modeled in direction 1, the y-coordinates in direction 2, and the z-coordinates in direction 3.

Single-point (SP) homogeneous boundary constraints can be implemented using the fix command, and multi-point (MP) constraint between nodes can be defined using the equalDOF command

(Figure A-3 and Figure A-4). The fix command is typically used at the base of the structure and was used at the foundation in this model. The equalDOF command was used to maintain structural stability between zero-length elements where stiffness was not defined for every DOF. The way in which the local coordinates of the elements correlate to the global coordinates of the model is defined using the geomTransf command (Figure A-5). This command defines how Open-Sees transforms the stiffness and resisting forces of the beam element from the local system to the global-coordinate system. Specifically, the basic linear geometric transformation method was selected for this study. Careful attention should be given towards assigning the vector orientations for elements since this could result in element cross-section properties such as inertia in the local y and z axis to be flipped if defined incorrectly. A very helpful visual demonstration is provided in the OpenSeesWiki (Gregory L. Fenves et al. 2020a) which should be referenced.

The next step is to define material properties used in the model. OpenSees has a wide variety of uniaxial materials, including steel and concrete materials. The uniaxialMaterial command is used to construct a material object which represents uniaxial stress-strain relationships (Gregory L. Fenves et al. 2020a). Steel01, Steel02, Concrete02, ViscousDamper and Elastic material commands were used in this study to model the nonlinear behavior of the train, track, and bridge system components (Figure A-6 through Figure A-10). The Steel01 material was used to simulate the behavior of bearings and the connection layers in the track system. Steel02, Concrete02 and Elastic materials were used to simulate the pier columns, and ViscousDamper materials were used to model the train suspension system. These materials were then specified as a parameter for the construction of elements.

Three types of elements were used in the model: elastic beam-column elements, displacement-based beam-column elements, zero-length elements, and two-node links (Figure A-11 through Figure A-14). The elastic beam-column elements were used to model the elastic capacity protected elements like the bridge girder. This element command requires the section properties and not the material behavior because they remain elastic. Displacement-based beam-column elements were used to model the pier column. To accurately model the behavior of the columns, the cross-section must be modeled using the section fiber command (Figure A-15). The patch and layer commands allow the construction of several fibers within a predefined cross-section to model the behavior of cover concrete, core concrete, and steel reinforcement with the material properties that were defined (Figure A-16 and Figure A-17). The specific details will be explained later in Section 3.3.4.3. The fiber section can then be aggregated into an existing elastic material using the section aggregator command (Figure A-18). The new aggregated material can then be used as the material parameter for the displacement-based beam-column elements. zeroLength element were used together with the Steel01 material to simulate the bridge bearings and track connection layers. twoNodeLink elements were used together with the ViscousDamper material to simulate the damping in the train suspension system, and the stiffness in the train suspension system was simulated using an elastic material. A complete list of elements and materials used in the prototype model is presented in Table 4.1.

The mass of each component in the model can be defined using the mass command in OpenSees (Figure A-19). The mass command allows the user to set the nodal mass values corresponding to each DOF. Defining masses allows the user to perform modal and dynamic analyses but is not required for static analysis. For this study, analysis of the modal and dynamic behavior of the

structure was of interest, so the mass command was used to set translational and rotational mass values at every appropriate node. Mass values were applied at the nodes representing the centroid of the train system components and bridge footings, and the masses of the rest of the track-bridge system components were distributed at every node along the entire length of the rails, track and base plates, bridge girder, and pier columns.

Table 4.1. Prototype HSR Model Element and Material.

Components	Material	Element
Bridge		
Main Girder	Elastic	elasticBeamColumn
Footing	Rigid	elasticBeamColumn
Column-fiber Section	Concrete02	dispBeamColumn
	Steel02	
Foundation Springs	Elastic	zeroLength
Fixed Bearing	Steel 01	zeroLength
Sliding Bearing	Steel 01	zeroLength
Track		
Base Plate	Elastic	elasticBeamColumn
Track Plate	Elastic	elasticBeamColumn
Rail	Elastic	elasticBeamColumn
Sliding Layer	Steel 01	zeroLength
CA Mortar Layer	Steel 01	zeroLength
Fasteners	Steel 01	zeroLength
Shear Reinforcement	Steel 01	zeroLength
Lateral Blocking	Steel 01	zeroLength
Train		
Car Body	Rigid	elasticBeamColumn
Bogie	Rigid	elasticBeamColumn
Axle	Rigid	elasticBeamColumn
Axle Box Suspension	ViscousDamper	twoNodeLink
Secondary Suspension	ViscousDamper	twoNodeLink

4.2.2.2. TRAIN SYSTEM MODEL

To model the KTX-Sancheon, a study by Kwark et al. (Kwark et al. 2004) was used as a reference due to the similarity of the train prototype selected. The train selected by Kwark et al. (Kwark et al. 2004) is a Korean High-Speed Train (KHST) with an articulated bogie system. Based on the train configuration described in the study and the year the paper was published, the prototype train system selected by Kwark et al. (Kwark et al. 2004) was assumed to be the KTX-I, which is the first set of trains used by the Korea Train eXpress (KTX). The 20-car formation (380.15 m long) of the

high-speed train entered service in 2004 and is optimized for high capacity. In comparison, the KTX-Sancheon is the second commercial high-speed train operated in South Korea and was created as a shorter companion to the KTX-I. Initially, the same train prototype was considered for this study; however, the train was exceptionally long (20 cars with a total length of 380.15 m) and was conceived as unfit for the prototype bridge selected. The transition was made to the KTX-Sancheon which has similar car-body and bogie systems with roughly half the total length (193.15 m). The configuration and numerical model discretization of the prototype train model used in this study is shown in Figure 4.27.
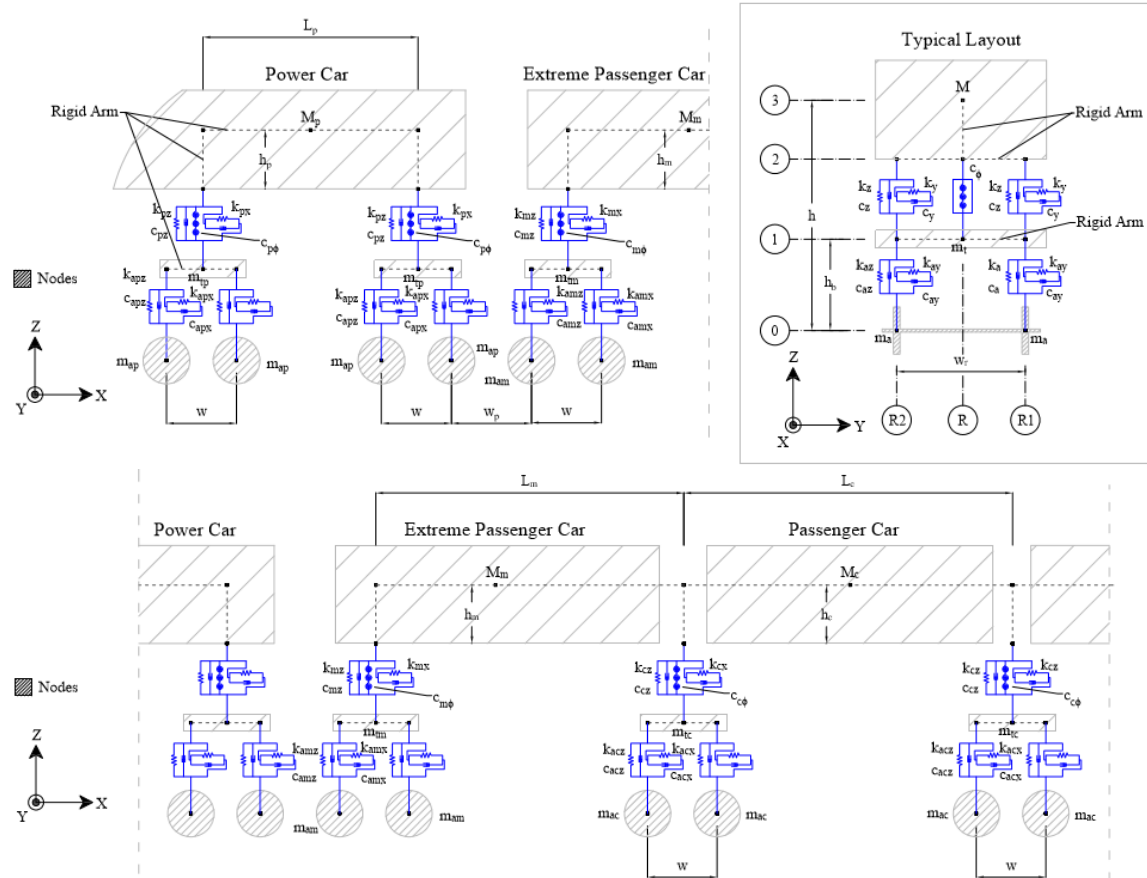
Figure 4.27. Schematic drawing for the numerical modeling of train system (Top: Cross-section, Bot: Elevation).

4.2.2.2.1 TRAIN SYSTEM MODEL GEOMETRY

Before defining the train nodes, lateral and vertical distances for the general location and geometric design of the train system were predefined to simplify the modeling process and allow for easy modification when necessary. As mentioned before, the track system of the prototype HSR bridge selected is a double track, which means there is a right (R) and left (L) track relative to the center of the bridge. From here onwards the right and left tracks will be referred to as track 1 and 2, respectively. Train dimensions retrieved from the reference study by Kwark et al. (Kwark et al. 2004) were used to define the train nodes. The train axle wheels are 3 m apart in the x-direction (w) and 2 m apart in the y-direction (w$_r$), so the rails for track system 1 were defined as R1 and R2

and are 1 m to the right and left of the track center line, respectively. Similarly, the rails for track system 2 were defined as R3 and R4. As previously mentioned, Appendix B provides scripts from the developed OpenSees model input file for completeness and step-by-step guidance. Figure B-1 in Appendix B is the first screenshot in the series of model definiton figures which shows the predefined gemoetric locations for train nodes. The lateral lengths of the power car (L_p), extreme passenger car (L_m), and intermediate passenger car (L_c) were defined respectively as 14.0 m, 18.7 m, 18.7 m, as well as the total length of the bridge system (L_T) as 193.15 m. The distance between the axle wheels of the power car and extreme passenger car is 3.275 m (w_p) (Kwark et al. 2004).

Various height parameters for the train system were also predefined. The rail height (h_r) was defined as 16.59 m, which is the sum of the column height (13.5 m) and girder depth (3.09 m). The height of centroid for the bogies (h_b) were defined as 0.56 m and the height of centroid for the power and passenger car-bodies (h) were defined as 1.72 m and 1.627 m, respectively. These values were retrieved from a study by Song et al. (Song et al. 2003) who similarly modeled a Korean high-speed train assumed to be the KTX-I based on the dynamic properties of the mass constituent elements. The vertical distance between the bottom of the car-body and center-of-mass of the power car (h_p), extreme passenger car (hm), and intermediate passenger car (h_c) were defined respectively as 0.605 m, 0.420 m, and 0.508 m. These values were taken from the reference study by Kwark et al. (Kwark et al. 2004). To expedite the process of shifting the train system along the length of the bridge, all train nodes were defined with an initial variable (x), which is the x-coordinate of the last wheel assuming the train is moving in the positive x-direction. This practice was beneficial to analyze various train load cases as part of the seismic analysis conducted in Section 4.4 and is recommended for future studies. The value (x) is adjusted depending on the load case being analyzed. Figure B-1 shows how the aforementioned parameters were defined and the "x" value shown in the snippet is for the load case where the train is loading the second to seventh spans of the bridge. A summary of all the parameters used for the train system is shown in Table 4.2.

Table 4.2. Dynamic Characteristics of Train Model.

Property	Power Car	Extreme Passenger Car	Intermediate Passenger Car
Mass of car-body (kg) [M]	54960	26000	26000
Primary sprung mass per bogie (kg) [m_t]	2420	2514	3050
Unsprung mass per axle (kg) [m_a]	2050	2050	2000
Primary stiffness per axle box (kN/m) [k_x, k_y, k_z]	40000, 9000, 1250	40000, 9000, 1250	55000, 11000, 800
Secondary stiffness per bogie side (kN/m) [k_{ax}, k_{ay}, k_{az}]	303, 303, 1270	100, 150, 370	100, 170, 303
Primary damper per axle box (kN-s/m) [c_x, c_y, c_z, c_ϕ]	0, 0, 10, 4230	0, 0, 10, 4230	0, 0, 6, 240
Secondary damper per bogie side (kN/m) [c_{ax}, c_{ay}, c_{az}]	0, 100, 20	0, 30, 20	0, 0, 0
Moment of inertia of car-body (Mg-m^2) [I_x, I_y, I_z]	59.4, 1132.8, 1112.9	33.94, 971.81, 971.81	33.94, 971.81, 971.81
Moment of inertia of bogie (Mg-m^2) [I_{tx}, I_{ty}, I_{tz}]	1.645, 2.593, 3.068	2.07, 3.26, 3.86	2.03, 3.20, 3.79
Moment of inertia of wheel (Mg-m^2) [I_{ax}, I_{ay}, I_{az}]	1.03, 0.0008, 1.03	1.03, 0.0008, 1.03	1.03, 0.0008, 1.03
Length of car-body (m) [L_p, L_m, L_c]	14.0	18.7	18.7
Height of centroid (m) [h, h_b]	1.72, 0.56	1.627, 0.56	1.627, 0.56
Height from secondary suspension arm to centroid (m) [h_p, h_m, h_c]	0.605	0.420	0.508

4.2.2.2.2 TRAIN SYSTEM NODES

Train nodes are created by defining the parameters specified for the node command (Figure A-2). For large scale structural models for an OpenSees model to be filled with thousands of nodes, which can be very confusing if the node tags (NodeTags) are not organized. Since this study is modeling the train system running on track 1, the train node tags were organized where any tag starting with a 7 specified an alignment on the right side of the train over R1 (rail 1), an 8 specified an alignment on the left side of the train over R2 (rail 2), and a 6 specified an alignment on the centerline of track 1 (R). This can be seen in the y-coordinate for the nodes defined in Figure B-2, Figure B-3, and Figure B-4. These figures in Appendix B are snippets of the rear power car, rear extreme passenger car, and first intermediate passenger car to demonstrate how they are defined in OpenSees. The second value of the node tag specifies the vertical grid of the train system as can be seen in the train model schematic (Figure 4.27). The value 0 is for the wheel nodes, 1 is for the bogie nodes, 2 is for the primary suspension nodes, and 3 is for the car-body nodes. The second to last number in the node tag specifies the bogie that the wheel, bogie, or suspension node is

associated with, and the last number further specifies the location of the node within axle (1 or 2), bogie (1 to 3), or suspension system (1 to 3). For example, NodeTag 70042 designates the node for wheel 2 on the right side of bogie 4, and NodeTag 71052 designates the node for bogie 5's center node. This trend is not followed for the car bodies. Instead, the last digit of the car-body node tags ranges from 1 to 23. Each car-body is constituted by three nodes and car-bodies for the articulated system share a node as can be seen in Figure 4.27.

All coordinates are defined using the predefined parameters as discussed in Section 3.2.2.1 above. This allows for simple adjustment of the train dimensions in the case of a parametric study or adjustment to a potential design. For the intermediate passenger cars, a value "n" was set to represent the respective number of the 6 intermediate passenger cars. A value of 1 was set for the first intermediate passenger car which was used to define the x-coordinates of the nodes, and each successive intermediate passenger car nodes were defined by increasing the n value by 1. The variable "x" previously defined and shown in Figure B-1 is included in the x-coordinates of every train node to shift the location of the entire train system along the length of the bridge. The z-coordinates were defined with the predefined train system heights as shown in Figure 4.27. Wheel nodes were modeled at the same height as rail nodes under the assumption of perfect contact and the height of the bogie nodes were modeled as the sum of the rail height and bogie height relative to the rail. The z-coordinate of car-bodies were defined as the sum of the height of their center-of-mass (h) assumed in Section 3.3.2.1 and the height of the rail (hr). and the top node of the secondary suspension system as the sum of car-body height (h) and the height of the rail (h_r), minus the respective cars vertical distance between the car-body center of mass to the bottom of the car-body. The node set up for the rear power car, rear intermediate passenger car, and first intermediate passenger car are illustrated in Appendix B in Figure B-2, Figure B-3, and Figure B-4.

4.2.2.2.3 TRAIN SYSTEM RIGID CONNECTIONS

The car-body and bogie are modeled as elastic beam-column elements with exceedingly stiff properties. The cross-sectional area, Young's modulus, shear modulus, torsional moment of inertia of the cross-section, and second moment of area about the local z and y-axis were assigned exceptionally large values to create a rigid element. Exceptionally stiff elements can potentially cause convergence issues depending on the type of convergence test type for analysis, so the values should be defined accordingly. The cross-section values used for this study as defined in Figure B-5, which were determined to provide appropriate stiffness relative to the rest of the elements in the model. Examples of the rigid elastic beam-column elements defined for the bogies are shown in Figure B-5 and Figure B-6. Similarly, Figure B-7 and Figure B-8 demonstrate the rigid elements for the primary suspension system. Since the KTX-Sancheon has an articulated bogie system, the passenger cars act as a coupled unit. The car-bodies for the extreme and intermediate passenger cars are modeled as rigid beam-column elements in series; however, the power cars are disconnected from the rest of the system. This is demonstrated in Figure B-9 where Node 63003 of the power car is not connected to Node 63004 of the extreme passenger car.

4.2.2.2.4 TRAIN SYSTEM SUSPENSIONS

Flexibility is provided in the train system through the primary suspensions system between the axles and bogies, and the secondary suspension system between the bogies and car-bodies. The

primary and secondary suspension system of the train were modeled using the twoNodeLink link element command in OpenSees. This command allows the user to construct a zero or non-zero length element defined by two nodes and apply material behavior to any transverse or rotational DOFs for a three-dimensional model. Uniaxial elastic materials were used to model the stiffness in the translational DOFs, and uniaxial viscous damper materials were used to model the vertical damping within the suspension system. Stiffness and damping coefficients for the suspension system of the power car, extreme passenger car, and intermediate passenger car were defined as given in the reference study (Kwark et al. 2004). The parallel material command was used to combine the stiffness and damping material in the z-direction to a single material. These materials were then used as the material parameters for the two-node link elements. The i-nodes shown are the bogie nodes and the j-nodes are the axle wheel nodes. The materials defined were applied in their respective directions and the orient command was used to manually instruct OpenSees of the element vector components. Since the primary suspension system only applies stiffness in the three translational DOFs, the equalDOF command was used to constrain the remaining DOFs between the bogie and axle nodes. Figure B-10 and Figure B-11 demonstrates how the primary suspension system of the power cars were modeled.

Similar process was performed for the secondary suspension systems; however, damping for the z-rotational DOF was also applied in addition to any translational damping (Figure B-12). As shown in the train model schematic in cross-section of the train model in Figure 4.27, the secondary suspension system has three layers: left, middle, and right. The left and right layers supply stiffness and damping in the translational DOFs and the middle layer supplies damping in the z-rotational DOF. Due to this DOF not having any stiffness, the DOF must be constrained for the stability of the model. However, if the displacement between the two-nodes constituting the middle layer of the secondary suspension system were constrained using the equalDOF command, the z-rotational damping would not activate due to the lack of displacement (x). Therefore, a relatively small stiffness value (1 kN/m) was applied in the z-rotational DOF to allow for the activation of the damping, and the rest of the DOFs were constrained using the equalDOF command (Figure B-13).

4.2.2.2.5 TRAIN SYSTEM MASSES

The train masses were modeled using the values given in the reference study (Kwark et al. 2004), included in Table 4.3. Since the extreme passenger car for the KTX-Sancheon is not motorized, unlike the KTX-I in the reference study, the translational mass and inertial mass values for the intermediate passenger car were used for the extreme passenger car as well. The masses were defined at the center-of-mass nodes for each car-body and bogie. The masses for the wheels are defined at every wheel node. Figure B-14 through Figure B-17 demonstrate how the car-body, bogie, and axle masses were defined in OpenSees. The inertial masses were used to define the rotational nodal masses.

Table 4.3. Masses for Track-Bridge System.

	Mass (Mg/node)	Moment of Inertia 1 (Mg-m²)	Moment of Inertia 2 (Mg-m²)	Moment of Inertia 3 (Mg-m²)
Girder	*63.7359*	*159.1817*	*61.1692*	*189.1868*
Column	*7.9940*	*27.2587*	*11.7515*	*23.8342*
Footing	*629.7408*	*7859.6900*	*7859.6900*	*14122.9870*
Rail	*0.1693*	*0.0025*	*0.1459*	*0.1446*
Track Plate	*3.5878*	*1.9561*	*3.0640*	*4.9961*
Base Plate	*3.9466*	*2.8739*	*3.3691*	*6.2193*

4.2.2.3. TRAIN SYSTEM MODEL

The track system comprises of rails, track plates, base plates, and the connection layers in between these components. The rails, track plates, and base plates were modeled as elasticBeamColumn elements and the connection layers were modeled as zeroLength elements. The rails, track plates, and base plates were discretized into equal intervals of 3.195 m and the connection layers were modeled at the end nodes of each interval. The train-track interaction was modeled by including and connecting the train wheel nodes as a member of the series of nodes creating the rail elements. This directly transfers the train loads to the track system, which then transfers the loads down to the bridge system through rigid arms connecting the track system to the bridge girder. The bridge girder was also discretized into equal increments of 3.195 m, which allowed for the track-bridge interaction to occur at an equal distribution along the entirety of the bridge length. A general schematic of the track system is shown in Figure 4.28 and Figure 4.29. The steps taken to model the track system nodes, elements, and masses are further discussed in detail in this section.
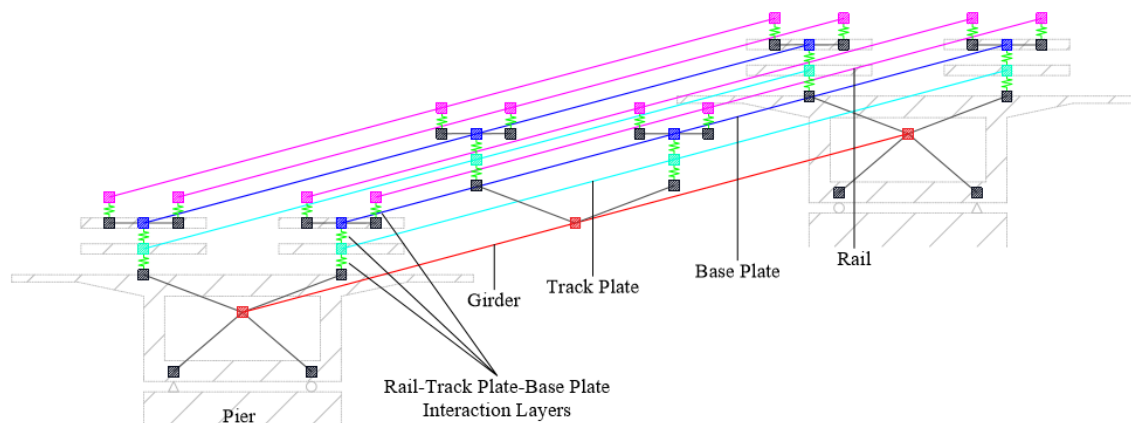
Figure 4.28. Schematic of track system.
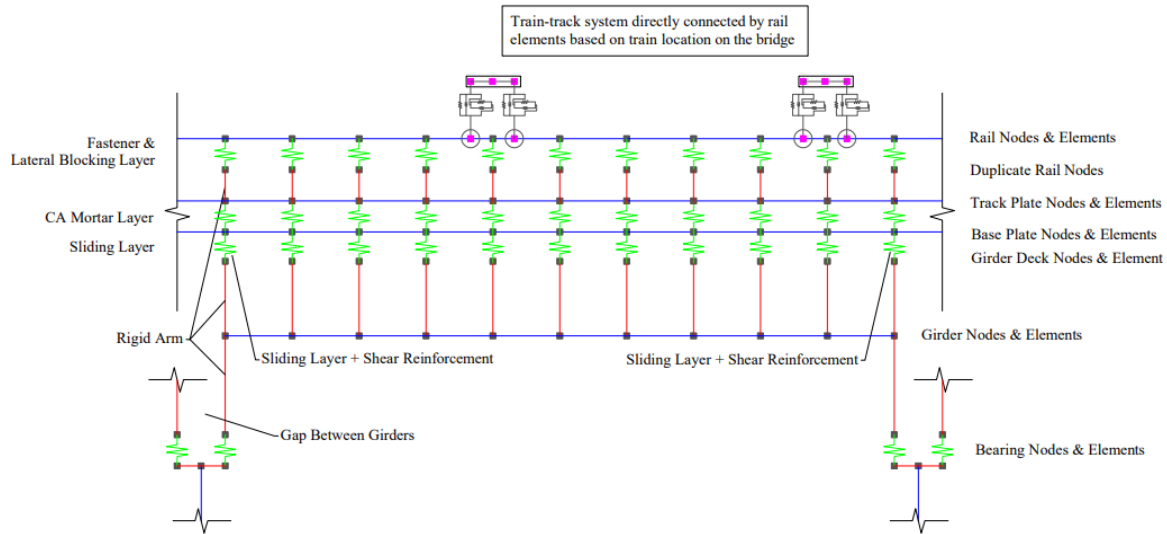
Figure 4.29. Schematic of track-bridge system.

4.2.2.3.1 TRACK SYSTEM ELASTIC ELEMENTS

The rails, track plate, and base plate were modeled as linear elastic beam-column elements because they are all designed to remain elastic as capacity protected elements. The location of the track plate and base plate nodes are the same, and rail nodes are located to the right and left of the track plate/base plate nodes by half the transverse train wheel spacing, defined earlier as R1 and R2 for track 1 and L1 and L2 for track 2, respectively. Figures B-18, B-19, and B-20 in Appendix B show sample node setup for rail, base plate, and track plate of one of the tracks, respectively. The elements were assigned cross section parameters as given in the study by Li et al. (Li et al. 2020). The rail, track plate, and base plate elements span the entirety of the bridge length. The process of modeling rail, track plate, and base plate elements are shown in Figure B-21, B-22, and Figure B-23, respectively.

To connect the train system to the track system, wheel nodes of the train were connected to neighboring rail nodes using the same linear elastic beam-column elements used for the rails. Since the train was placed on track 1 consisting of rails 1 and 2, the wheel nodes were modeled at the same y and z-coordinates as the rail nodes. The sequential order of the wheel nodes and rail nodes were organized offline and defined in OpenSees accordingly. This was done under the assumption that the train wheels are always in contact with the rails, which is a common assumption.

4.2.2.3.2 TRACK SYSTEM CONNECTION LAYERS

Zero-length elements were used to simulate the nonlinear behavior of the sliding layer, CA layer, shear reinforcement, lateral blocking, and fasteners. The nonlinear material behavior was assigned to the zero-length elements using the Steel01 material in OpenSees. The yield strengths were assigned as given by Li et al. (Li et al. 2020) and the initial elastic tangent was found by a quotient of the yield strength and relative displacement. The strain hardening ratio was assigned a value of zero to mirror the perfectly elastic-plastic behavioral graph from the reference study.

Figure 4.30 first shows the generalized elastic-plastic behavior along with the parameters of the different zero-length connection elements in the track-bridge system as adopted from Li et al. (Li et al. 2020). Next, dedicated plots were generated to demonstrate the behavior of five of those connection components in track systems and shown in Figure 4.31. Fasteners and lateral blocking were modeled between the duplicate rail nodes as demonstrated in Figure B-24 and Figure B-25 in Appendix B, respectively. The CA mortar layer was modeled between the track plate and base plate (Figure B-26), and the sliding layer was modeled between the base plate and rigid arm connecting the track system to the bridge girder (Figure B-27). Sample shear reinfrocement definition is also shown in Figure B-28. The fasteners, CA mortar layer, and sliding layer allow for longitudinal slippery relative to the bridge length. Multi-point constraints were used to constrain the remaining DOFs of the connection layer nodes that stiffness was not applied to through zero-length elements. For example, stiffness was applied in the longitudinal direction for the sliding layer to allow for movement based on the behavior of the material, so the equalDOF command was used to constrain the remaining 5 DOFs (Figure B-29).

Components	F_y/kN	d_y/mm
Sliding layer	6	0.5
CA layer	41.5	0.5
Fastener	15	2
Shear reinforcement	22.5	0.075
Lateral block	453	2
Fixed spherical steel bearing	5000	2
Sliding spherical steel bearing	470	2
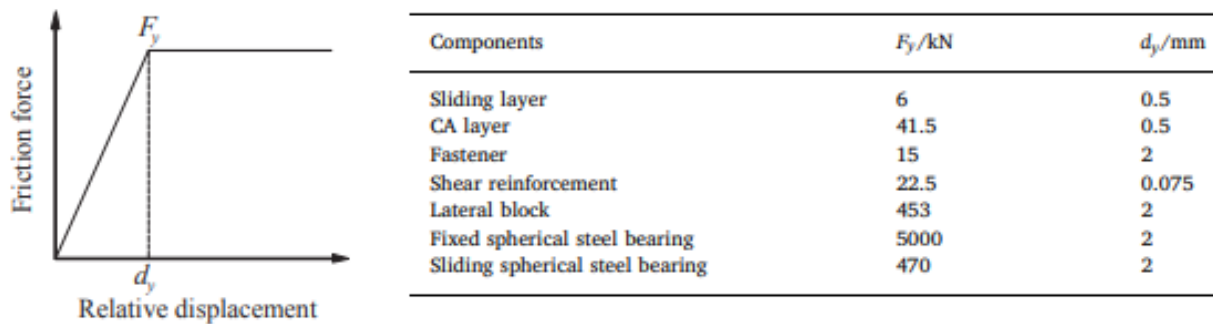
Figure 4.30. Parameters of zero-length connection elements in the track-bridge system as adopted from Li et al. (Li et al. 2020).
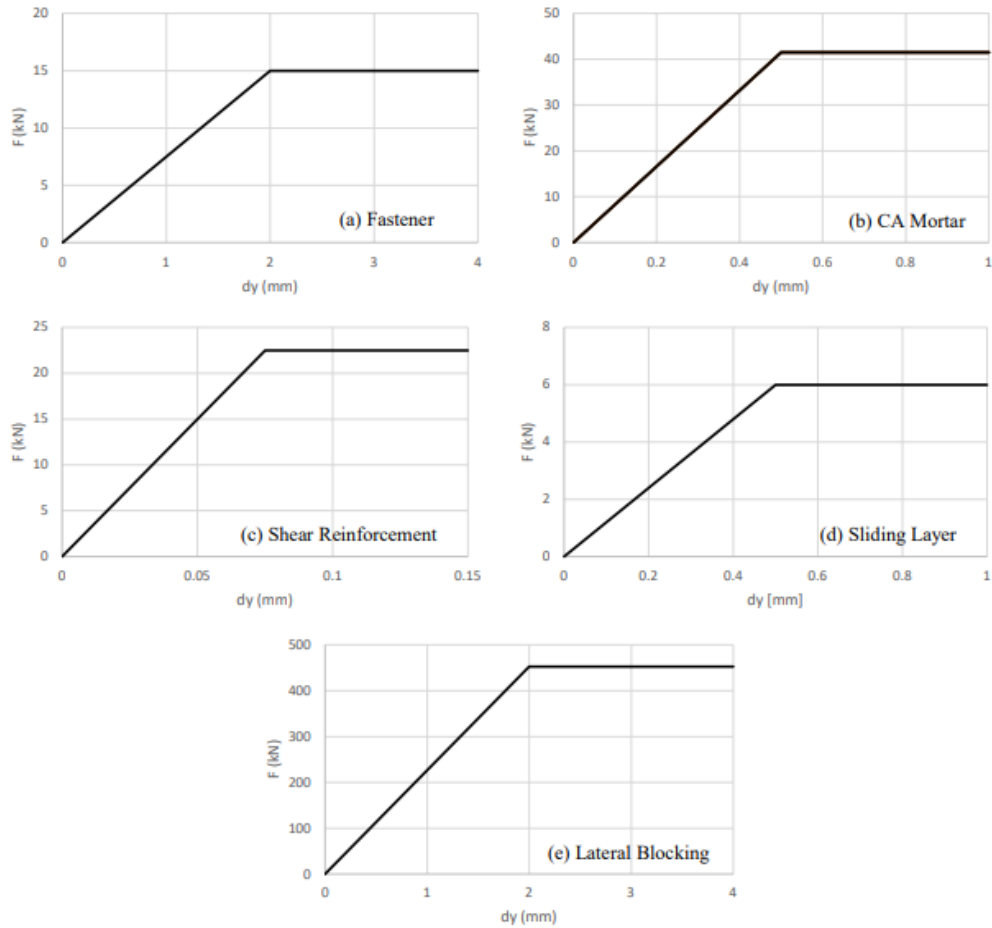
Figure 4.31. Force-deformation behavior of track system connection layers: (a) Fastener, (b) CA mortar, (c) Shear reinforcement, (d) Sliding layer, and (e) Lateral blocking

4.2.2.3.3 TRACK SYSTEM RIGID CONNECTIONS

Rigid elements were used in the track system to connect the track plate nodes to the rails. Specifically, the rigid arms branch out from each track plate node to duplicate rail nodes that were not used to model the rail elements. The rigid section properties to model rigid arms out of elastic beam-column elements were kept the same as what was used for the train system rigid bodies. Rigid arms were modeled at 3.195 m intervals for both tracks 1 and 2, which is the same intervals as the track system nodes. The location of the rigid arms can be seen in Figure 4.32.
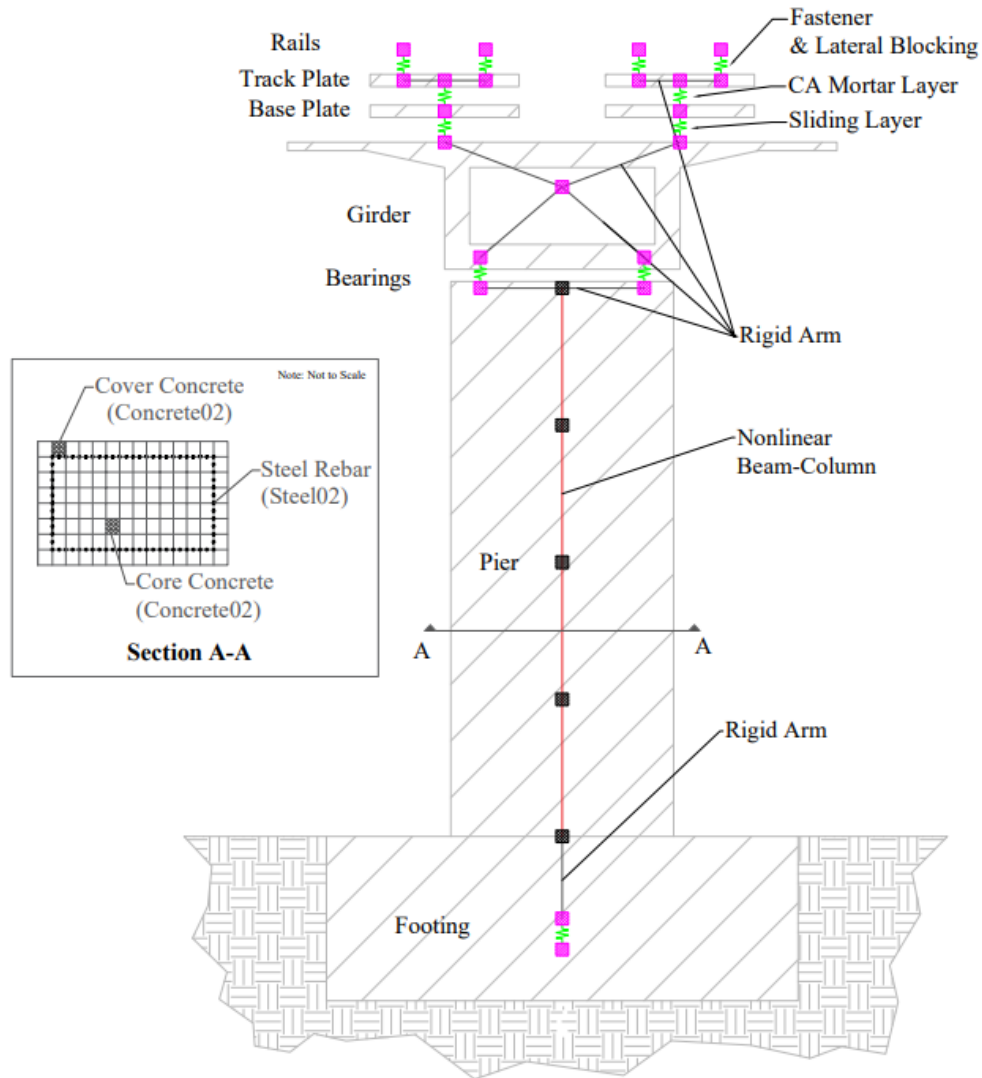
Figure 4.32. Schematic of track-bridge system.

4.2.2.3.4 TRACK SYSTEM RIGID MASSES

The masses for the rails, track plates, and base plates were assumed using approximate densities of steel and concrete. The steel rails were assumed to have a density of 7,700 kg/m³, and the concrete track plate and base plate were assumed to have a density of 2,400 kg/m³. These are very generic values and accurate densities should be utilized to accurately model the dynamic performance of HSR systems because the mass matrix is one of the key components of solving the equation-of-motion of the model. Mass per node was found by dividing the product of the given cross-sectional area and the length of the bridge by the number of nodes constituting the entire length (110 nodes). General mass moment of inertia equations for rectangular sections were used to solve for the moment of inertia in the three rotational DOFs. The masses used for the track system in this study is shown in Table 4.3. The mass per node was used for the nodal mass value in the translational DOFs and the inertial masses were used for the rotational DOFs (Figure B-30).

The bridge system comprises of girders, bearings, pier columns, and footings. Girders were modeled as elastic beam-column elements, and bearings were modeled as zero-length elements. Pier columns were modeled as displacement based elastoplastic fiber elements and columns footings were modeled as rigid elements. Rigid arms were used to connect each bridge component to one another as illustrated in the track-bridge system schematic shown in Figure 4.32.

4.2.2.4.1 TRAIN SYSTEM GIRDER

The prestressed concrete box-girder bridge is designed to be elastic, i.e., capacity protected component for seismic considerations, so linear elastic beam-column elements with equivalent section characteristics were used to model the superstructure. Each span was discretized into 10 equivalent lengths of 3.195 m by creating 11 nodes per girder span. Figure B-31 demonstrates how the nodes for the first two bride girder spans were defined. A 0.05 m gap was created between each bridge girder span to simulate the isolated movement allowed to each girder span by four steel bearings, two fixed and two sliding. The cross-sectional area, Young's modulus, shear modulus, torsional moment of inertia of the cross-section, and second moment of area about the local z and y-axis were assigned the values given by Li et al. (Li et al. 2020) and shown in Table 3-4. To simulate the process of bridge design, the Young's Modulus was decreased from $3.45e7$ kN/m^2 to $2.45e7$ kN/m^2 and the moment of inertia values were reduced by 30% to account for the reduction in concrete stiffness due to cracking. The process of modeling the first span of the bridge girder is shown in Figure B-32. For the first girder span, Node 90001 to Node 90011 were modeled in series with the elastic beam-column element, using predefined cross-sectional parameters. The distance between Node 90011 and Node 90012 demonstrates the gap between girders, so these nodes are not connected using the elastic element.

Table 4.4. Section parameters of elastic beam elements in track-bridge system as adopted from Li et al. (Li et al. 2020).

	Sectional area/m^2	Elastic modulus /kN/m^2	Shear modulus /kN/m^2	Torque /kN m	Inertia moment 1/m^4	Inertia moment 2 /m^4
Main girder	9.06	3.45×10^7	1.44×10^7	2.26×10^1	1.10×10^1	9.48×10^1
Base plate	5.61×10^{-1}	3.00×10^7	1.25×10^7	6.74×10^{-3}	1.69×10^{-3}	4.06×10^{-1}
Track plate	5.10×10^{-1}	3.55×10^7	1.48×10^7	6.80×10^{-3}	1.70×10^{-3}	2.76×10^{-1}
Rail	7.75×10^{-3}	2.06×10^8	8.05×10^6	2.00×10^{-6}	3.20×10^{-5}	5.00×10^{-6}

4.2.2.4.2 BRIDGE SYSTEM BEARINGS

The spherical steel bearings were modeled using zero-length elements. To use zero-length elements, the OpenSees user must create two nodes with the same coordinates, hence the zero-length. Since the bearings are located at the ends of each bridge span, two-sets of nodes were created accordingly. The fixed and sliding bearings were assumed to be 4 m apart, based on the box-girder dimensions, in the direction transverse to the bridge at the top of the 13.5 m tall pier columns. The nodes for the bearings supporting the first bridge span are shown in Figure B-33. One set of the bearing nodes were used to connect the bearing system to the bridge girder, and the other set of nodes were used to connect the bearings to the top of the pier columns, both through rigid arms.

The OpenSees material command Steel01 was used to define the bilinear behavior of the steel bearings within the zero-length elements. The required parameters for the zero-length elements for the steel bearings are shown in Figure 4.30. The yield strength was defined as given by the reference study in Figure 4.30 with a value of 5000 kN for the fixed bearing and 470 kN for the sliding bearing, and the elastic tangent or slope of the elastic region was found by a quotient of the yield strength and relative displacement also given in Figure 4.30. As previously mentioned, the strain-hardening ratio was set as 0 and the uniaxial material was applied into directions 1 and 2 to apply stiffness in the lateral translational DOFs. The behavior of the fixed and sliding bearing is shown in Figure 4.33. The fixed and sliding bearings were alternated as shown in Figure 4.34 to mirror the design of the actual bridge.

As previously mentioned, stiffness was only applied in the longitudinal and transverse DOFs, so the vertical DOF and the three rotational DOFs were constrained for structural stability. The high stiffness value for the fixed bearing idealizes the resistance it provides to constrain movement and the low value for the sliding bearing idealizes the slight resistance it provides despite allowing movement. The fixed and sliding bearings modeled to support the first span of the bridge are shown as examples in Appendix B in Figure B-34 and Figure B-35, respectively. For this study, the equalDOF command was used to constrain the rest of the DOFs and make sure duplicate bearing nodes will have the same movement (Figure B-36).
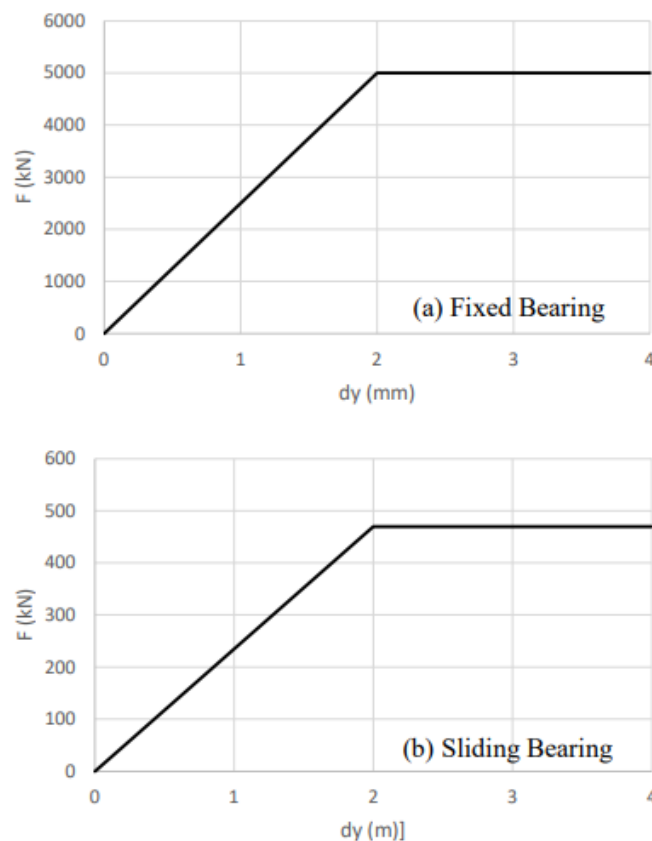
Figure 4.33. Force-deformation behavior of bridge bearings: (a) Fixed bearing, (b) Sliding bearing.
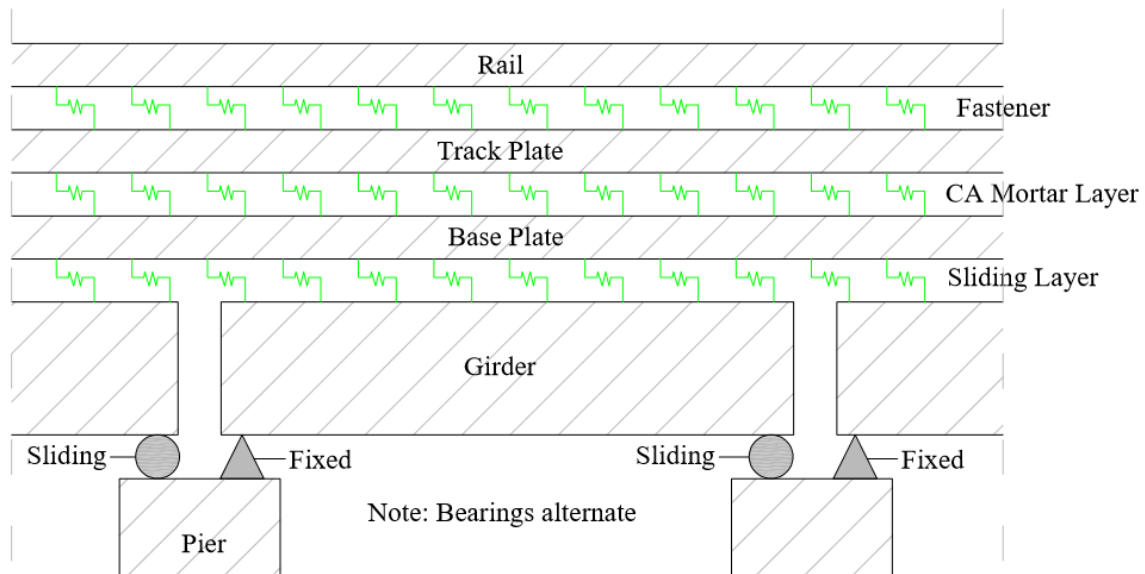
Figure 4.34. Finite element model of bridge.

4.2.2.4.3 BRIDGE SYSTEM PIER COLUMNS

Materials for the pier column cross-section were defined using uniaxial materials available within OpenSees and material strengths were input as parameters. The core concrete, cover concrete, and reinforcing steel strength assumptions were adopted from a sample code provided by the OpenSeesWiki (Gregory L. Fenves et al. 2020a) since the design guideline for the selected proto-type HSR bridge used herein did not provide sufficient information on specific material specifications for the bridge columns. The assumptions used for the concrete and reinforcing steel properties and input parameters are shown in Figure B-37. The cover and core concrete were modeled using the Concrete02 material and the longitudinal reinforcement was modeled using the Steel02 material in OpenSees; a typical modeling practice for bridge elements that has been adopted in many of the reviewed studies such as Li and Conte (Li and Conte 2016). For the Steel02 command, the R0, cR1, and cR2 parameters were defined as 15, 0.925, and 0.15, respectively, as recommended for general reinforcing bar by the OpenSeesWiki.

The pier cross-section was created using the fiber section command (Figure B-38). The cover and core concrete were defined within the section using the patch rect command to generate fibers over a rectangular cross-sectional area. The reinforcing steel was defined using layer straight commands to generate fibers along a straight line for the four sides of the rectangular cross-section. The material tag (matTag) for these commands reflects what was defined for the cover, core, and reinforcing steel materials.

The geometry of cross-section design, as well as the coordinates required in the command parameters to create the cross-section were predefined as shown in Figure B-39. A reinforcement ratio of 1.30% was assumed for the cross-section and this led to a preliminary design of 176- #11 bars, split into 60 bars on the long face and 28 bars on the short face of the cross-section. Transverse reinforcement was assumed as #4 bars and a clear cover of 0.04 m was also assumed. The design used for the cross-section does not reflect the actual design of the pier columns, but since the details are unknown, a general design was done based on engineering judgement. The design

specified in the section Fiber command was then aggregated into a uniaxial elastic material section using the section Aggregator command to create a single section force-deformation model. The torsion force-deformation (T) was selected as the force-deformation quantity parameter to be modeled by the section object.

The rectangular bridge pier columns were modeled as a series of four three-dimensional displacement based elastoplastic fiber elements using the dispBeamColumn command with the nonlinear fiber cross-section that was defined. Each pier was constituted by five nodes with equal 3.375 m intervals with five integration points each (Figure B-40). Integration of fiber characteristics over the pier cross-section allowed for the obtainment of nonlinear section characteristics. The process of modeling the first pier column is shown in Figure B-41.

4.2.2.4.4 Bridge System Column Footings and Soil

Column footing dimensions of the prototype bridge selected were not explicitly noted in the reference study, so generic dimensions of 4 m for the depth and 11 m for the width were assumed. The nodes were defined at -2 m to create nodes at the centroid of the footings. The column footings were modeled as rigid elements via the same method for all other rigid elements to connect the column base nodes to the footing nodes. Figure B-42 in Appendix B shows a sample for footing nodes and ground.

Due to the focus of the study being the dynamic interactions between the train-track-bridge systems, a simplistic method was used to model the interaction between the bridge and soil. Since California is projected to be the home of the largest HSR system in the United States, soil spring constants from a study by Abbasi (Abbasi 2018) were used to simulate the general soil properties of California. Since multi-column box-girder bridges in California typically have the pinned connection details in the foundation, there are no rotational stiffness defined at the column footings. Abbasi (Abbasi 2018) considered a wide range of soil profiles and foundation systems over the state of California and determined the stiffness of translational springs to be 115 MN/m. However, adjustments were made to accommodate the single column bent design of the bridge piers. Single column bents typically utilize fixed-base connections to provide stability to the cantilevered system. Accordingly, the footing nodes were fixed in the non-translational DOFs and the foundation nodes were fixed in all 6 DOFs to create a base for the entire model (Figure B-43).

The structure-soil interaction was simplified in-part due to the lack of information regarding the soil spring constants required to model the pile-soil interaction and the focus of the study being the train-track-structure interaction. If this information is available, a sophisticated soil-structure interaction model is recommended by explicitly modeling the piles as displacement based elastoplastic fiber elements, as done by Li et al. (Li et al. 2020) and Li and Conte (Li and Conte 2016). The process of modeling the column footings and the interaction with the soil for the model in place is shown in Figure B-43 and Figure B-44.

4.2.2.4.5 Bridge System Rigid Connections

Rigid elements are used in the bridge system to connect the bridge girder, bearing, pier column, and footing to one another. For the model in-place, the track system is connected to the bridge girder through two diagonal arms at an interval of 3.195 m, along the entire bridge length. Additionally, two diagonal rigid arms connected the bridge girder to the steel bearings isolating the

bridge girder from the pier columns, meaning the two nodes defining the ends of each bridge girder span had a total of four rigid arms. The bearings are connected to the pier columns through two horizontal arms in the y-direction at the top of the pier columns, and the column footings are idealized as a rigid arm. The location of rigid arms is shown in the track-bridge system schematic in Figure 4.32. The same rigid section properties were used as the rigid arms in the train and track system. Examples of all the rigid elastic beam-column elements used in the bridge system are shown in Figure B-45 through Figure B-48.

4.2.2.4.6 BRIDGE SYSTEM MASSES

For the dynamic equation of motion, masses for the concrete deck, pier column, and footing were assumed using a standard density of 2,400 kg/m^3. General mass moment of inertia equations for rectangular sections were used to solve for the very approximate mass moment of inertia in the three rotational DOFs. The masses of the bridge girder were distributed along the 10 spans, consisting of 11 nodes each. The masses of each pier column were distributed along the five nodes constituting the entire column. The masses were applied at the center-of-mass node for each footing. The masses for the bridge system in this study is shown in Table 4.3 as previously mentioned. Moroever, the process of applying the masses for sample different bridge components, i.e. box-girder, columns, and footings, are shown in Figure B-49, Figure B-50, and Figure B-51, respectively.

4.3. DEMONSTRATION OF GRAVITY, MODAL, & SEISMIC ANALYSIS OF HSR BRIDGE SYSTEM

In OpenSees, an analysis is performed through the aggregation of component objects. The component objects define the type of analysis that is performed on the model and consists of the following: constraints handler, DOF numberer, integrator, solution algorithm, system-of-equation constructor and solver, and convergence test. This section will discuss the component objects defined for the gravity load static analysis and the seismic load dynamic analysis, as well as how the modal analysis was performed. Static and dynamic analysis were performed for a load case without the train and an example load case with the train. The recorded data was analyzed to verify and observe the responses within the HSR bridge. This section serves to demonstrate the selection of analyses component objects for the prototype HSR model and present example studies that can be performed to understand the behavior of the model under various loading.

4.3.1. GRAVITY LOAD ANALYSIS

4.3.1.1. GRAVITY LOAD ANALYSIS SETUP

To perform a linear or nonlinear static gravity load analysis, loads must be applied to represent the self-weight of each structural component. Masses do not have to be defined for static analysis because inertial and damping effects are neglected. The masses defined in Section 3 were instead converted into forces (kN) and applied as vertical loads at the same nodes as the masses. This was done through the pattern plain command which allows the user to apply loads to specific nodes and elements. Train system car-body, bogie, and axle wheel and bridge foundation dead loads were applied at their center-of-mass nodes, and track-bridge system rail, track plate, base plate,

bridge girder, and pier column dead loads were distributed to each node formulating their respective elements. The train system, track system, and bridge system had a total weight of 3,989 kN, 16,992 kN, and 184,230 kN, respectively, with a total static weight of 205,211 kN. The static weights of the train-track-bridge system were used to verify the load transfer within the HSR model through comparison with column base reactions. As previously shown in Section 4.2, the step-by-step type of model and analysis definition demonstration is provided in Appendix B. As part of Appendix of B, Figure B-52 through Figure B-60 demonstrate the process of applying dead loads to each component of the HSR bridge system.

The constraints command handles how the constraint equations are enforced in the analysis. Constraint equations enforce a specified value for a DOF, or a relationship between DOFs (Gregory L. Fenves et al. 2020b). The type of constraint selected should depend on the type of constraints implemented in the user's model, homogeneous single-point constraints or non-homogenous single-point constraints. For this study, multi-point constraints were used (equalDOF), so the Transformation command was used to enforce the constraints using the transformation method.

The numberer command determines the mapping between equation numbers and DOF, and how DOF are numbered. The use of the plain numberer is recommended mostly for very small problems and for the sparse matrix solvers which provide their own numbering scheme. For this study, the RCM option was used for the numberer in the case of this large-scale system model. The RCM (Reverse Cuthill-McKee) algorithm optimizes node numbering to reduce bandwidth using a numbering graph, and outputs a warning when the structure is disconnected. The system command constructs the linear system-of-equations and solver objects to store and solve the linear system-of-equations (K.u = R), and each solver is tailored to a specific matrix topology. The UmfPack command was used to construct a large sparse system-of-equations object which will be factored and solved during the analysis using the UmfPack solver.

To perform nonlinear analysis, the user must define how OpenSees will deem whether the model has converged to the correct solution. The test command is used to select convergence test to determine if convergence has been achieved at the end of an iteration step. The command parameters allow the user to define the convergence tolerance, the maximum number of iterations that will be performed before OpenSees returns "failure to converge", and a flag to instruct OpenSees on how to print information on convergence. The NormDispIncr test type selected in this study uses the norm of the left-hand side solution vector of the matrix equation to determine if convergence has been reached. The test returns positive for convergence if the displacement increment in the linear system-of-equation is less than the specified tolerance. For this model, a tolerance of 1.0e-6 and a maximum number of iterations of 100 was deemed reasonable. A flag value of 1 was selected to instruct OpenSees to print convergence information on each step to monitor whether the model was operating correctly, but this does not affect the actual analysis.

The next step is to define a solution algorithm to instruct OpenSees on the sequence of steps to take to solve the nonlinear equation. The Newton command was used to solve the nonlinear residual equation using the Newton-Raphson algorithm, which is the most widely used robust method for solving nonlinear algebraic equations (Gregory L. Fenves et al. 2020b). The integrator command is used to determine the predictive time step for the analysis, specify the tangent matrix

and residual vector at any iteration, and determine the corrective time step based on the displacement increment. The LoadControl integrator type was selected and an initial load-increment factor (pseudo-time step) was defined as 0.1 to apply a tenth of the dead loads defined earlier at each step. The gravity load was applied through 10 loading steps to avoid convergence issues that might have happened if the large gravity loads is applied in one step.

Finally, the analysis command was used to specify a static analysis and the analyze command was used with the number of load steps parameter, to slowly apply the gravitational loads in 10 steps. The loadConst command was used to instruct OpenSees to maintain constant gravity loads and reset the time to zero before the transient analysis. This entire process of setting up the gravity analysis parameters then performing the analysis is demonstrated in Figure B-61 and Figure B-62, respectively.

4.3.1.2. GRAVITY LOAD ANALYSIS RESULTS

Sample studies were performed to demonstrate behavioral analysis that can be performed using the gravity analysis results obtained from the model. In high seismic areas, the main design considerations for HSR bridges are usually dictated by resonance and seismic forces. Nonetheless, the static analysis was performed as a precursor to the dynamic analysis and for verification of load transfer within the structure. Several loading scenarios could be considered for analyzing the HSR bridge system with respect to train position on the bridge as the train approaches and crosses the bridge. A list of 16 different scenarios that could be considered for the system in hand is provided in Table 4.5 as an example. Only few selected cases are included in this research, but the list is still provided to highlight and indicate how train position over the bridge can be represented. For gravity load analysis, two load cases from Table 4.5 were considered for the demonstration purposes as sample studies: (1) Load Case 1 where the train is not on the bridge, and Load Case 8 where the train is loading spans 2 through 7. The load cases are illustrated in Figure 4.35. For Load Case 1, the train model and train model gravity loads were completely omitted, leaving just the track and bridge model, along with their respective gravity loads. For Load Case 8, the very first train wheel was determined to be located 30.815 m along the bridge, the train system was connected to the track system accordingly.

The first exercise performed with the static analysis results was the verification of load transfer within the HSR system. Since loads were applied within the track and bridge subsystems, an error within either subsystem could cause the loads to incorrectly transfer through the structure. To perform this exercise, node recorders were used to extract the reactions at the column bases under Load Case 1 without the train and Load Case 8 with the train. The column base reactions in the vertical direction were tabulated in Table 4-2 for both load cases, and the distribution and sum of the reactions were observed to check for any red flags regarding the incorrect transfer loads. The sum of column base reactions in both load cases were found to be equal to the total loads applied for each load case, described in Section 4.2.1, which indicates all the loads were able to transfer to the column bases. The distribution of the interior column base reactions for Load Case 1, to the left and right of the center pier column #6, was symmetrical. The exterior columns had a difference of 33 kN which is not exceptionally large considering the scale of the reactions. For Load Case 8, an increase in the reactions for columns #2 through #8 were observed. This behavior verifies that the train loading over bridge girder spans #2 through #7 was properly

supported by the pier columns supporting those respective spans. The rest of the pier columns maintained the same reactions as Load Case 1 since they were not affected by the static loading of the train.

As a verification of static behavior of the model, vertical displacements of the bridge box-girder were analyzed for both load cases. Node recorders were used to output vertical nodal displacements along the entire bridge length. The recorded values were post-processed using Matlab to organize the data and plot a graph demonstrating the deformed shape of the bridge girder under gravity loads. An exaggerated view of the deflection in each bridge span under the loading scenarios of Load Case 1 and Load Case 8 is shown in Figure 4.36. The bridge span displacements were nearly identical among all the spans for Load Case 1. A maximum vertical displacement for the bridge was recorded at -0.408 mm at the center node of each span. For Load Case 8, an increase in vertical displacements for the spans loaded by the train was visibly apparent in the graph. Larger displacements were recorded at span 2 and span 7, which is due to these spans supporting the fore and rear power cars of the KTX-Sancheon model. The maximum vertical displacement for the bridge under Load Case 8 was recorded at -0.452 m at spans #2 and #7. As seen in Figure 4-2, the mass of the power cars is greater than two times that of the passenger cars, so the displacement trend observed from Load Case 8 were deemed reasonable.

Table 4.5. Example HSR bridge system load cases based on the train position above the bridge (the cases represent instances of the train crossing the bridge).

Case Number	Train Load Cases	x (m)
1	No train on bridge	NA
2	Train on entire bridge span 1	-161.155
3	Train on entire bridge spans 1-2	-129.16
4	Train on entire bridge spans 1-3	-97.165
5	Train on entire bridge spans 1-4	-65.17
6	Train on entire bridge spans 1-5	-33.175
7	Train on entire bridge spans 1-6	-1.18
8	Train on entire bridge spans 2-7	30.815
9	Train on entire bridge spans 3-8	62.81
10	Train on entire bridge spans 4-9	94.805
11	Train on entire bridge spans 5-10	126.8
12	Train on entire bridge spans 6-10	158.795
13	Train on entire bridge spans 7-10	190.79
14	Train on entire bridge spans 8-10	222.785
15	Train on entire bridge spans 9-10	254.78
16	Train on entire bridge span 10	286.775

* Train moving in the positive x direction

Table 4.6. Column Base Reactions (kN) in Direction 3 from Static Analysis.

Column	Column Base Reactions (kN)	
	Load Case 1	Load Case 8
1	14528.6	14520.8
2	19132.7	19790.2
3	19071.1	19758.7
4	19072.6	19506.9
5	19072.6	19530.6
6	19072.6	19534.3
7	19072.6	19766.4
8	19072.6	19681.1
9	19071.6	19066.3
10	19115.3	19115.4
11	14939.0	14939.1
Total	201221.3	205209.8
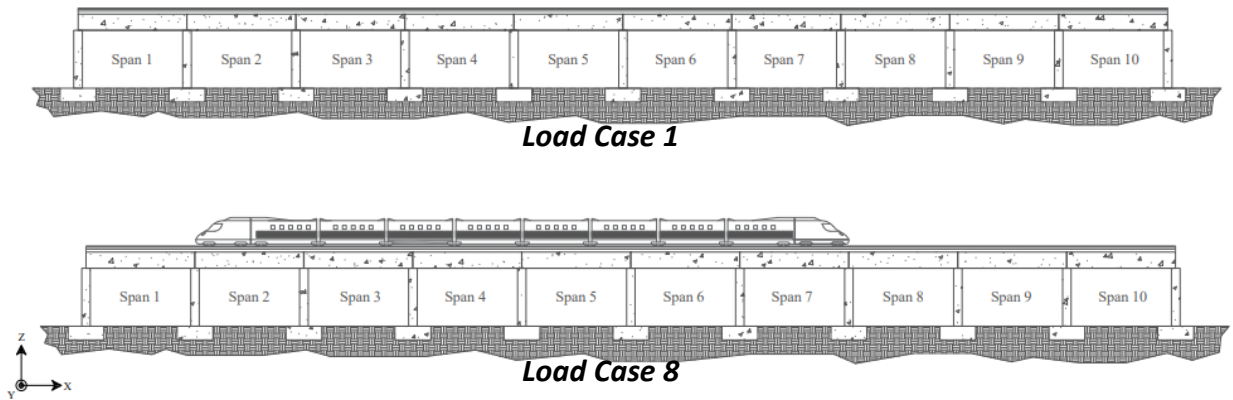
Figure 4.35. Train load cases used for Section 4.3.
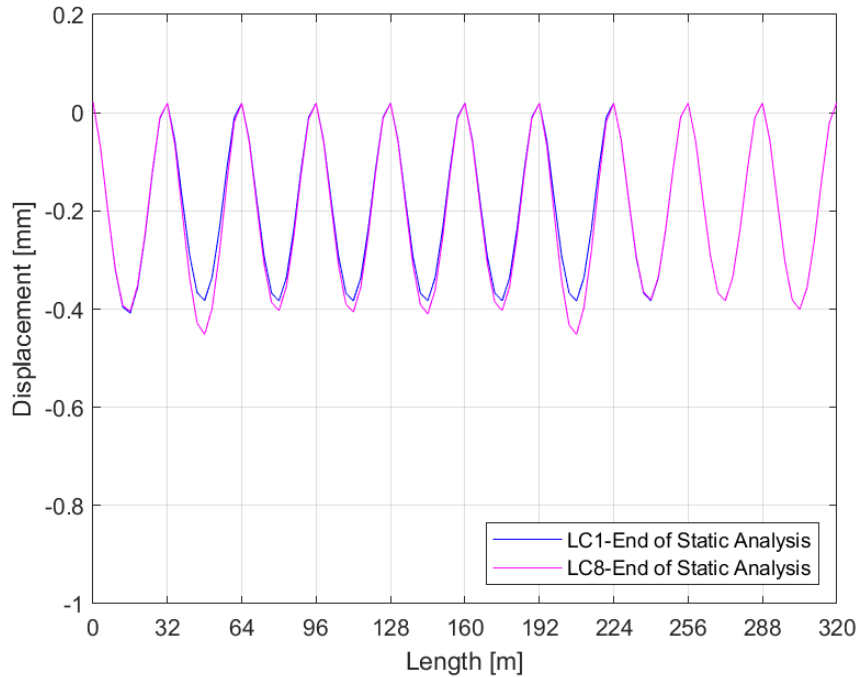
Figure 4.36. Vertical bridge girder displacements under static analysis for both load cases.

4.3.2. MODAL LOAD ANALYSIS

Analyzing modal characteristics is imperative to designing HSR bridges for seismic stability and riding comfort by minimizing resonance within the structure. Modal analysis of the bridge system was performed by using the eigen command which uses the overall mass and stiffness of the structure to determine the various vibration frequencies (or periods) along with mode shapes. The eigen command performs a generalized eigenvalue problem to determine a user specified number of eigenvalues and eigenvectors. For this study, the parameter for number of eigenvalues (λ) was defined as 10, for the first 10 modes which were then used to solve for the periods (T) of the structural model (Figure A-20). An open vector for the periods and the value for pi (π) were de-fined. The tcl commands `foreach` *and* `lappend` *were used to instruct OpenSees to take each eigenvalue from the lambda index and solve for periods using equations (1) and (2) below. An output file was then specified and a tcl command, open, was used to open the output file and the foreach and puts commands were used to record the periods that were solved. The output file was then closed using the tcl command, close, to allow OpenSees to continue with the rest of the analyses.*

$$\omega = \sqrt{\lambda} \qquad (1)$$

$$T = \frac{2\pi}{\omega} \qquad (2)$$

The modal analysis process covered in this section is demonstrated for a step-by-step procedure in Appendix B in Figure B-63. The first 10 periods obtained for the bridge system under the two sample load cases, i.e., without the train and with the train covering spans 2 through 7 of the

bridge, are tabulated in Table 4.7. The values shown in the table show that the first two modes are likely the dominant bridge modes in the transverse and longitudinal direction that are not sensitive to the train loading. Higher modes varied slightly which is attributed to the added train mass and specific train-track-bridge system vibration modes.

Table 4.7. Periods for first 10 modes.

| Mode | Period (seconds) | |
	Load Case 1	Load Case 8
1	0.691	0.704
2	0.691	0.699
3	0.560	0.662
4	0.407	0.594
5	0.349	0.561
6	0.264	0.546
7	0.209	0.537
8	0.204	0.513
9	0.170	0.504
10	0.147	0.463

4.3.3. SEISMIC LOAD ANALYSIS

4.3.3.1. SEISMIC LOAD ANALYSIS SETUP

To start off the set up for the seismic analysis, structural damping must be applied first to model the inherent damping and energy dissipation mechanisms within the structure. The Rayleigh command was used to apply classical Rayleigh damping, i.e., viscous damping proportional to a linear combination of mass and stiffness, to all previously defined elements and nodes in the structural model as demonstrated in Figure B-64. Due to the nature of the bridge system and model, the natural frequencies of the first and sixth modes were selected to solve the alpha and beta parameters for the Rayleigh command as defined from the OpenSees syntax shown in Appendix A in Figure A-21. A typical damping ratio of 2% was used for this study.

The set up for the seismic load analysis is overall similar to the gravity load analysis, with some differences to accommodate the transition from static analysis to transient analysis as depicted in Figure B-65. For the constraint handler, the transformation method was used again due to the use of multi-point constraints in the model. The RCM algorithm was also used as the DOF numberer to optimize node numbering and reduce bandwidth, and the Newton-Raphson method was used to advance the analysis to the next time step. The convergence test type was changed to the energy increment test which uses the dot product of the solution vector and norm of the right-hand side of the matrix equation to determine if convergence has been reached. The test returns positive for convergence if one half of the inner-product of the unbalanced load and displacement increments at the current iteration is less than the specified tolerance. The tolerance was decreased to 1.0e-8 to increase accuracy of the analysis and the maximum number of iterations was increased to 1000 to raise the chances of the model correctly converging. The OpenSees Manual

does not recommend a type of convergence test for static or dynamic analysis, but this is one area where informed user input is needed to properly obtain correct convergence. The same linear equation solver, UmfPack, was used to store and solve the system-of-equations in the analysis.

For the transient analysis, a numerical integrator is needed to solve the dynamic equation of motion that is needed to account for inertial and damping effects. For this study, the classical Newmark method was used to perform the numerical integration. The Newmark method is a two-parameter time-stepping method developed by Nathan M. Newmark. The gamma (g) and beta (b) parameter values depend on whether the average acceleration method or linear acceleration method is selected. For this study, the average acceleration method was selected because it is unconditionally stable, i.e., independent of the analysis time step, and the gamma = 0.5 and beta = 0.25 values were defined accordingly. Dynamic analyses could use any of several explicit or implicit integrator types as per the list provided in the OpenSeesWiki or OpenSees Manual, and users could select from the available methods based on the application or so. The analysis command was then used to instruct OpenSees to conduct a transient analysis with the parameters defined above.

Once the specifics of the transient analysis were defined, the ground motions to be used as the transient loads were defined. The ground motion selected for the sample transient analysis is from the 1994 Northridge earthquake recorded at the LA-Sepulveda VA Hospital. The acceleration time-history was retrieved from the Pacific Earthquake Engineering Research Center (PEER) ground motion database provided by the University of California, Berkeley. The downloaded acceleration time-history file was placed in the same OpenSees bin folder as the tcl file of the structural model to allow the code to call out the ground motion. The ReadSMDFile, available on the OpenSeesManual (Gregory L. Fenves et al. 2020b) and OpenSeesWiki online (Gregory L. Fenves et al. 2020a), was sourced to convert the PEER ground motion to a format readable by OpenSees. The sourced file removes the header text in the PEER ground motion file and converts the file extension from AT2 to g3. This process can be seen in Figure B-66. The analysis time-step (D_T) and total number of steps (N_{step}) were defined as 0.005 seconds and 9557, respectively, with maximum duration of the ground motion being 47.785 seconds.

Using the converted acceleration time-history file and the ground motion parameters defined, the timeSeries path command was used to define the time-series information for both ground motions (see Figure A-22 in Appendix A for OpenSees command details). A gravitational acceleration value of 9.81 m/s^2 was applied as the factor to retrieve the acceleration time-history values from the multiples of [g] format. The factor can be further increased if amplification of the ground motion is of interest. Unique load tags were created for each excitation, and the ground motions were then applied to the model using the UniformExcitation pattern command. The parameters required in the UniformExcitation pattern command are shown in Figure A-23. The respective unique pattern tag (patternTag), ground motion direction, and time-series information for each excitation defined earlier were used in the command. The process of applying the ground motion in both directions is shown in Figure B-67.

After completing the definition of dynamic analysis parameters and the transient loads, the analyze command was used to instruct OpenSees to perform the dynamic analysis with the time-stepping parameters previously defined for the ground motion. Figure B-68 demonstrates a loop

function created to run the dynamic analysis and engage additional algorithms and convergence test types if the initial dynamic analysis parameters are incapable of converging the model. The analyze command set to return "ok = 0" if the analysis at a time-step successfully converged to a solution. The loop command is set to start if "ok != 0", which means that the "ok" value is not 0. While the current time-step is less than the maximum duration of the ground motion, the loop attempts to converge the model using a norm displacement increment convergence test and the Newton-Raphson algorithm with initial stiffness iterations, the Broyden algorithm, and the Newton-Raphson algorithm with line search, in order.

4.3.3.2. SEISMIC LOAD ANALYSIS RESULTS

After the gravity load analysis was completed and damping was applied, dynamic analysis of the model was performed. The same two load cases were considered for the dynamic analysis: (1) Load Case 1 where the train is not on the bridge, and (2) Load Case 8 where the train is loading spans 2 through 7. Several sample exercises were conducted using the results from the two load cases to analyze the maximum forces and moments experienced by the prototype HSR bridge and observe the sensitivity of the results with and without train loading. This section aims to demonstrate the variety of studies that can be performed using the data output by OpenSees and the sample results presented shall not be taken as a reference for design.

As an extension to the exercise done for the static analysis, the vertical displacements of the bridge girders under seismic loading were plotted for both load cases. The maximum vertical displacement was recorded as -0.657 mm at girder spans #1 and #10 for Load Case 1. The bridge girder displacements at the end of the static analysis (start of dynamic analysis) and at a time-step of 4.185 seconds during the dynamic analysis, when the maximum displacement was recorded for Load Case 1, were plotted in Figure 4.37 as sample. For Load Case 8, the maximum vertical displacement of -0.636 mm was recorded at girder spans #2 and #7. The bridge girder displacements at the end of the static analysis and at a time-step of 3.915 seconds during the dynamic analysis, where the maximum displacement for Load Case 8 was observed, were also plotted as samples and shown in Figure 4.38. The vertical displacement trends for both load cases under seismic loading were found to be very similar to that of the static analysis. This behavior is understandable because only the two horizontal components of the ground motion were considered (which excites the lateral directions of the bridge) and the vertical excitation component was neglected. The box-girder is also designed to be a capacity protected element, meaning inelastic deformation is not expected to be caused by the ground motions. The minor increase in displacements is most likely caused by rotations at each girder-span end above the pier. It is noted that the box-girder is not continuously supported over the pier and the gap between each two successive girder spans allow for some minor rotation.

The second exercise conducted was the observation of transverse bridge displacement trends, which are crucial for seismic performance assessment. To observe the displacements experienced by the bridge during the ground motion, the transverse displacements were analyzed at the time-step at which the bridge experienced the largest transverse displacement between both load cases and the final time-step of the ground motion to see whether any residual displacements were observed. The maximum displacement during the ground motion between both load cases occurred at a time-step of 4.735 seconds for Load Case 1, with an absolute value of 291.7 mm.

The maximum transverse displacement recorded for Load Case 2 was 282.2 mm at a time-step of 4.750 seconds. The transverse displacements at the end of the ground motion were also analyzed to observe the residual displacements caused by the nonlinear effects of dynamic loading, and plastic damage, if any. The prototype HSR bridge under Load Case 1 had a residual displacement of 111.2 mm and Load Case 8 had a residual displacement of 116.6 mm. The displaced shapes of the bridge for the selected time steps mentioned above is shown in Figure 4.39 for Load Case 1 and Figure 4.40 for Load Case 8.

Similar to the previous displacement exercises, time-histories of pier column and girder end displacements were plotted to better understand the bridge behavior with and without train loading. The time-history graphs compare the relative drift between girder ends and the supporting columns and indicate whether residual displacements were observed due to nonlinear/plastic deformations induced by the cyclic loading of the ground motions. Four pier columns and their respective girder ends were considered in the shown sample time-history analysis: #2, #6, #8, and #11, to observe the magnitudes of drift along the bridge. Pier column displacements were recorded by outputting the transverse and longitudinal displacements of the top nodes and their histories were plotted through the total duration of the ground motion. Similarly, the translational displacements of the nodes defining the ends of each girder span were recorded and plotted. The displacement time-histories from the four piers are shown in Figure 4.41 through Figure 4.44 for Load Case 1 and Figure 4.45 through Figure 4.48 for Load Case 8. The figures include two subplots, which are designated as "a" and "b" to represent the displacement trends in the longitudinal and transverse direction, respectively. Based on the longitudinal displacement trends, the shapes are nearly identical between both load cases with Load Case 8 showing slightly larger drift between the column and girder for columns #6 and #8. From the displacement time-histories for the transverse direction shown in Figure 4.42(b), Figure 4.43(b), Figure 4.46(b), and Figure 4.47(b), all four columns showed similar trends within each load case. Comparing the displacement trend between the load cases, Load Case 1 had larger displacements in the 8 to 15 second range, and Load Case 8 had larger displacements in the 15 to 20 second range and showed larger oscillations throughout the rest of the ground motion which can be a result of additional mass due to train loading.

To further demonstrate other seismic performance metrics, hysteresis loops for the pier columns as obtained from force-displacement relationships were plotted. The same four columns (#2, #6, #8, and #11) were selected from the displacement time-history analysis and were analyzed under both load cases. Column forces were extracted from OpenSees by assigning element recorders with the force parameter for the fiber-based column element that was modeling the bottom of the pier columns. The shear force-displacement relationships from the two load cases were plotted in the two lateral directions 1 and 2, i.e., longitudinal and transverse directions, in Figure 4.49 and Figure 4.50, respectively. The main objective of graphing the force-displacement behavior of the pier columns was to identify extent of nonlinearity and damage in the columns. The nonlinearity is observed by observing whether the loading and unloading behavior follows a similar slope which signifies the column remains within the elastic region. From the hysteresis loops provided, the force-displacement behavior can be observed to be relatively linear for the four columns under both load cases with the transverse direction showing slight instances of nonlinearity. The residual

132

displacements previously shown are also indicators of nonlinear behavior. Given the observed residual displacements, this might be attributed to other components yielding or damage (e.g., bearings). However, it is beyond the scope of this study to interpret or assess the seismic behavior especially that no proper design was conducted for the bridge components and only demonstration is desired here.

As the last exercise in this part of the study, the internal forces and moments within the bridge girders were observed by plotting shear force and bending moment diagrams. Girder straining actions are usually more important for gravity load checks and design. However, for better demonstrations selected cases of girder straining actions are shown under the seismic loading as it accounts for gravity loads already in addition to any extra demands from the seismic loading. Forces in the bridge girder elements were recorded by assigning element recorders to all 100-elastic beam-column elements used to model the bridge with the force parameter. The recorders export the axial force, and shear forces and moments in the local y and z-axis of the element cross-section. The forces and moments were plotted along the length of the bridge for each load case at an arbitrary time-step of 4.600 seconds during the peak of the Northridge ground motion. The shear force diagrams and bending moment diagrams for Load Case 1 and Load Case 8 are shown in Figure 4.51 through Figure 4.56, and Figure 4.57 through Figure 4.62, respectively. Again, analyzing the obtained shear and bending moment values is not the goal here.
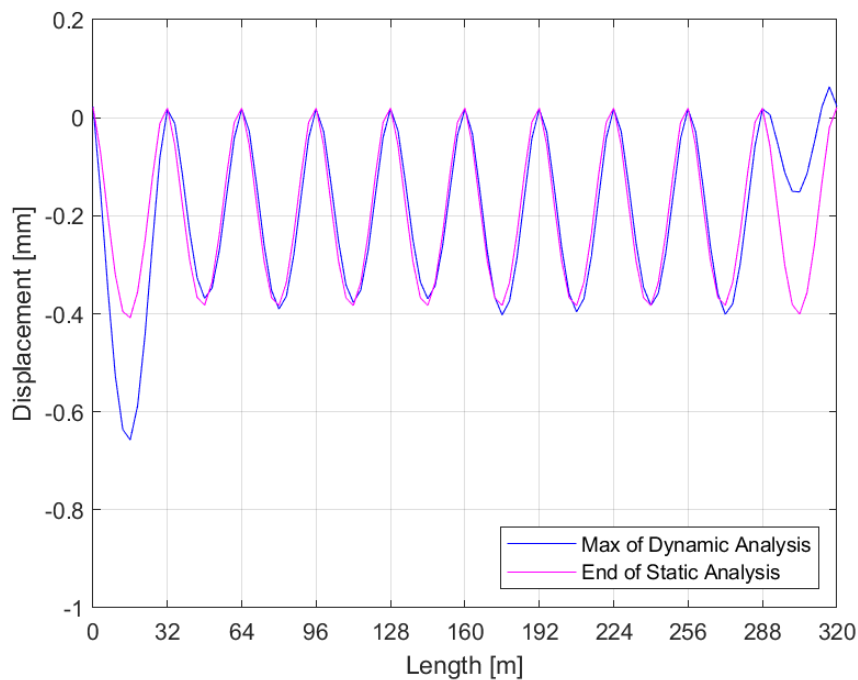
Figure 4.37. Vertical bridge girder displacements under Load Case 1.
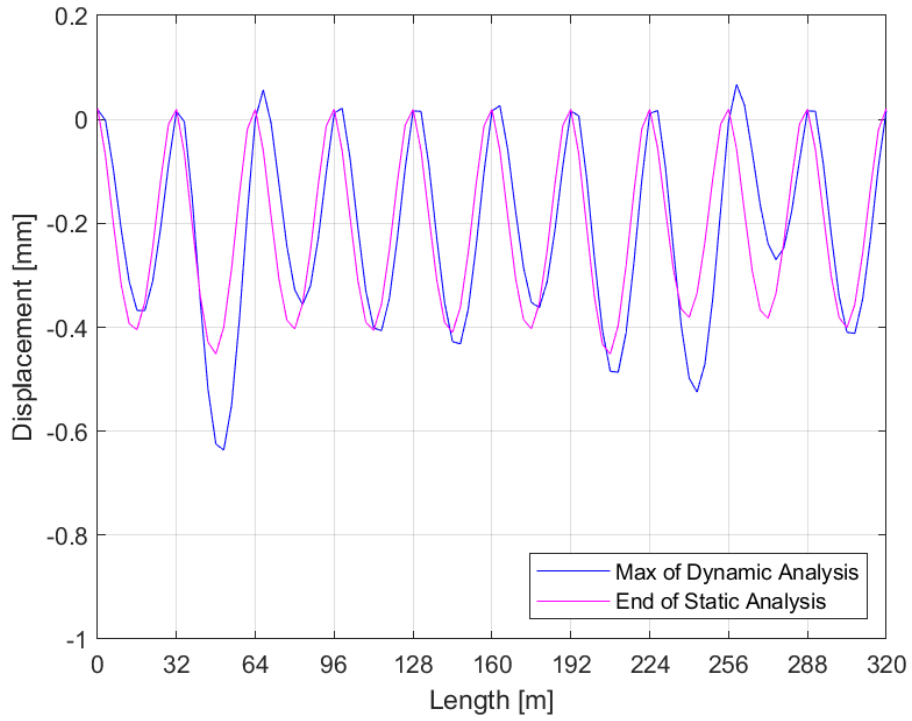
Figure 4.38. Vertical bridge girder displacements under for Load Case 8.
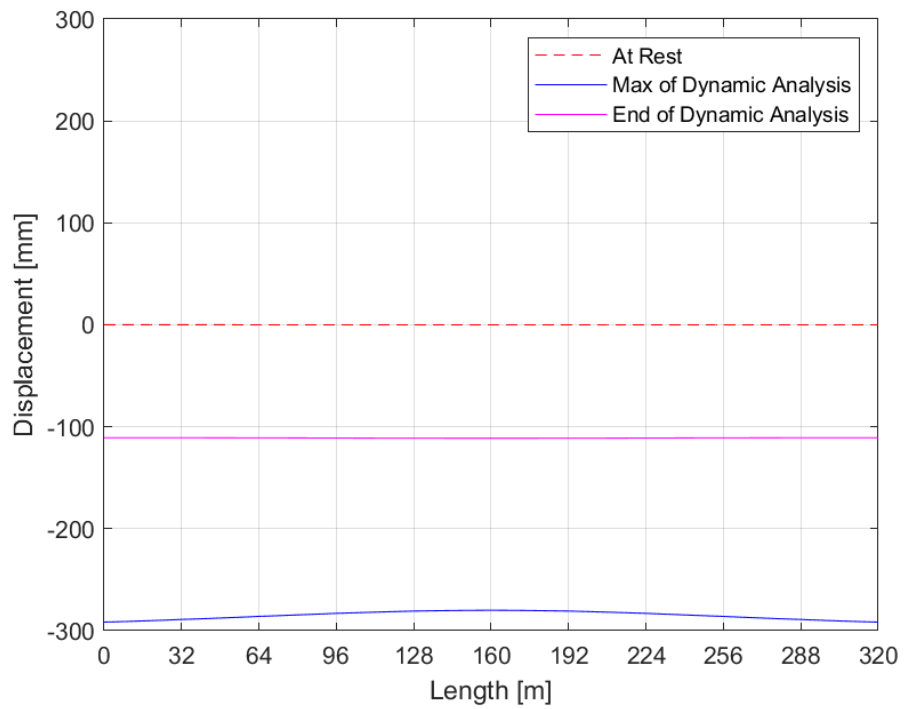
Figure 4.39. Transverse bridge girder displacements under Load Case 1.
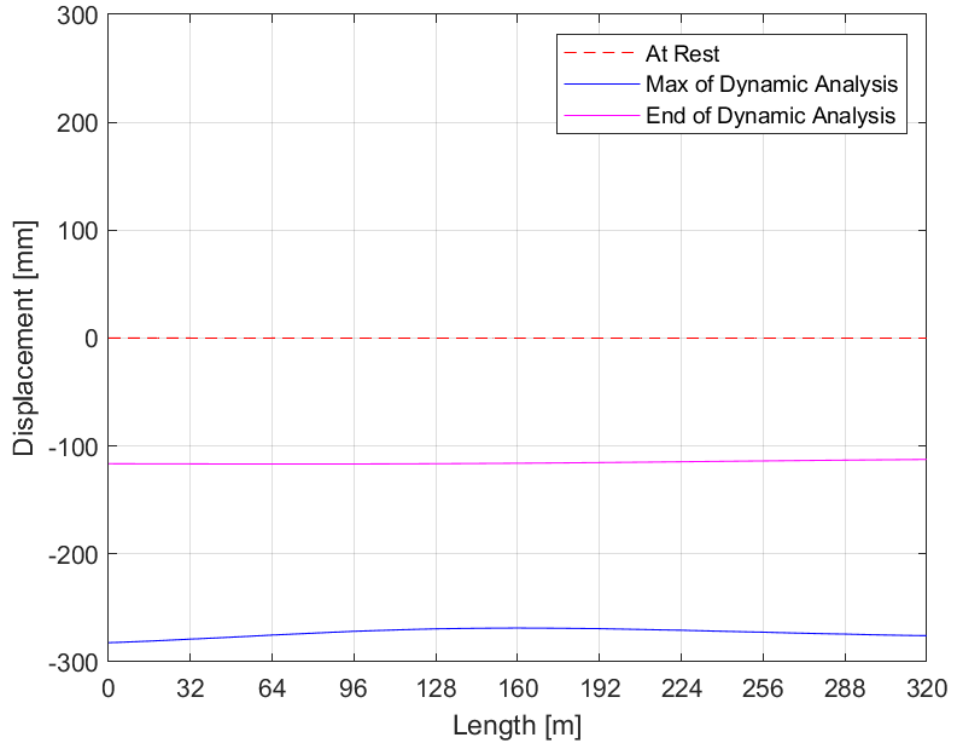
Figure 4.40. Transverse bridge girder displacements under Load Case 8.

(a)

135
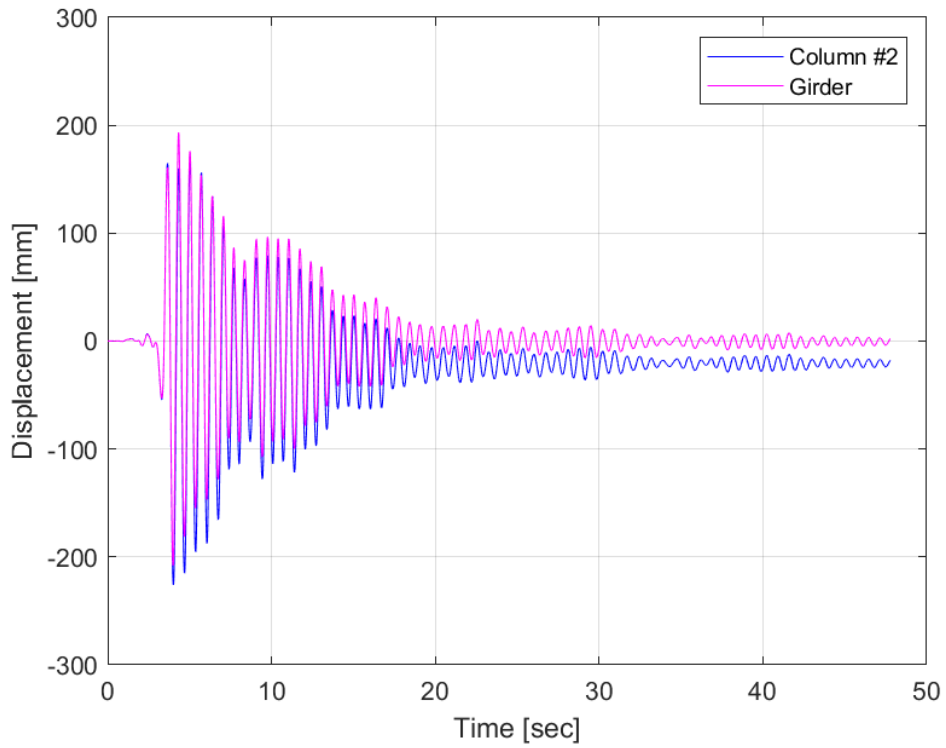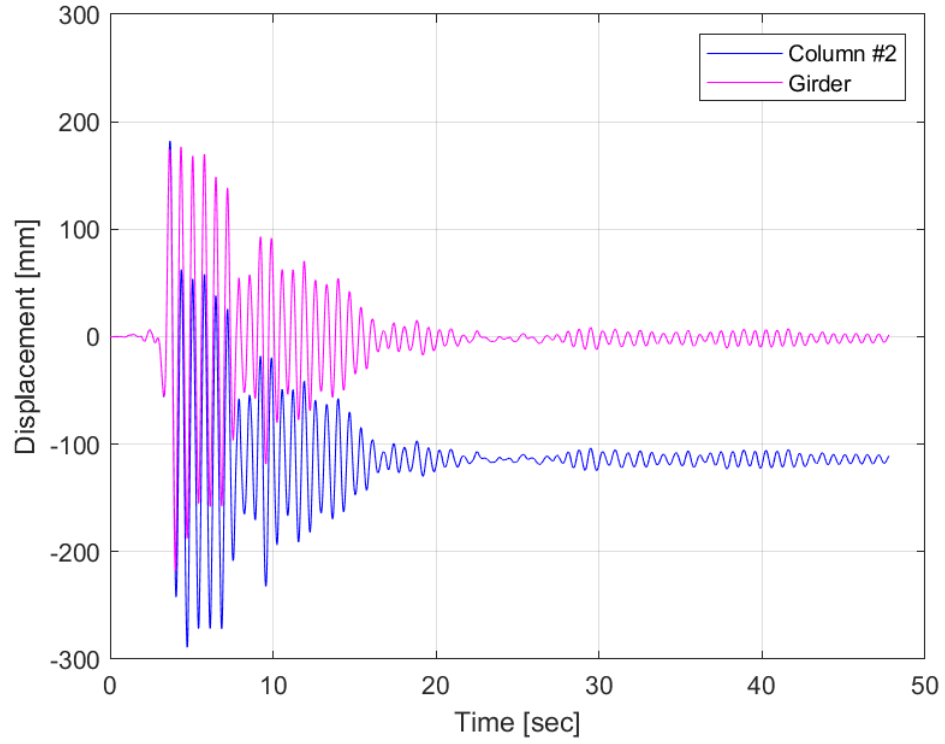
(b)

Figure 4.41. Displacement time-history of column #2 under Load Case 1 in:
(a) Longitudinal, (b) Transverse directions.

(a)
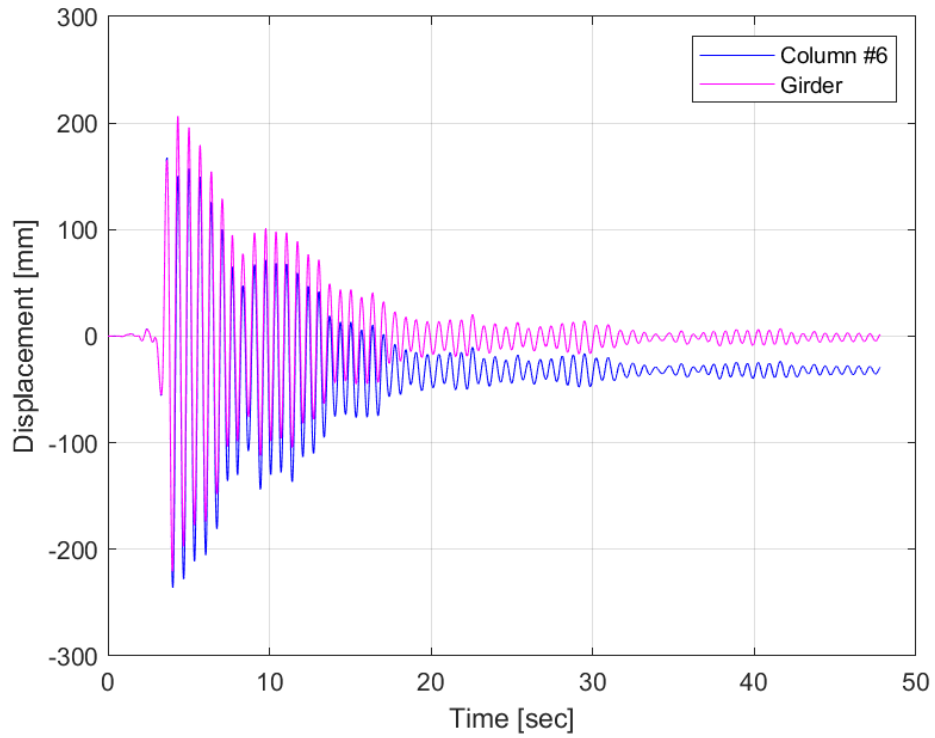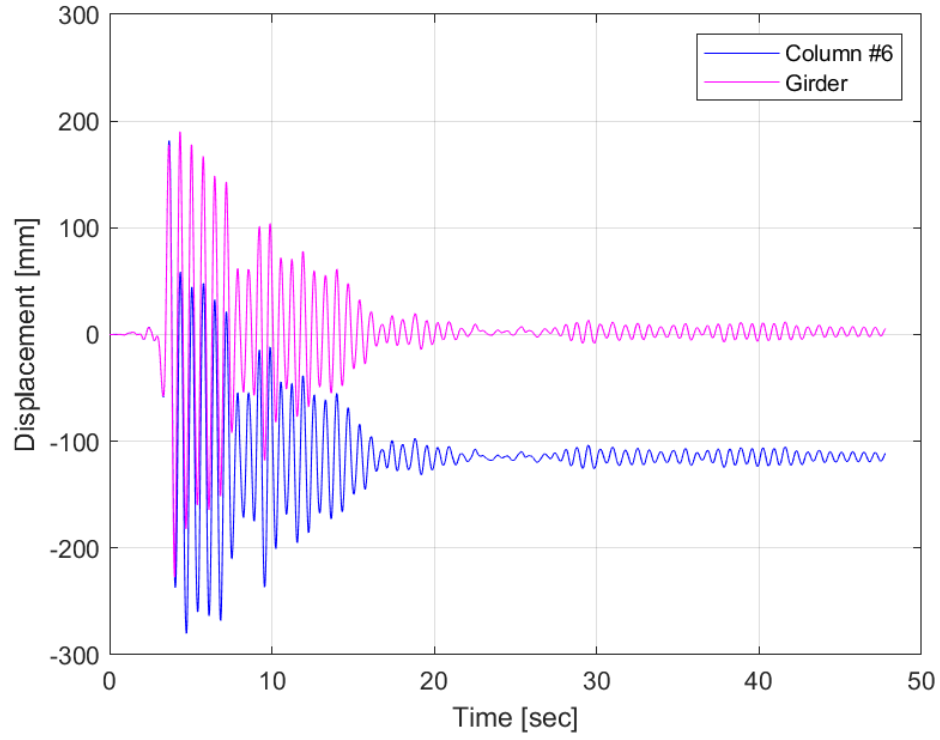
Figure 4.42. Displacement time-history of column #6 under Load Case 1 in:
(a) Longitudinal, (b) Transverse directions.

137

(b)
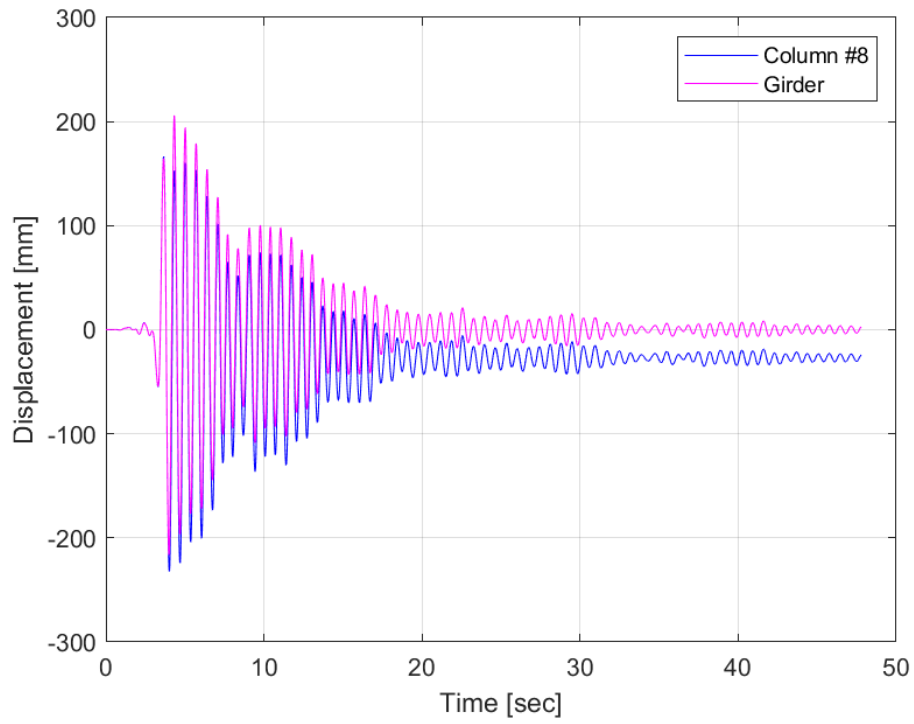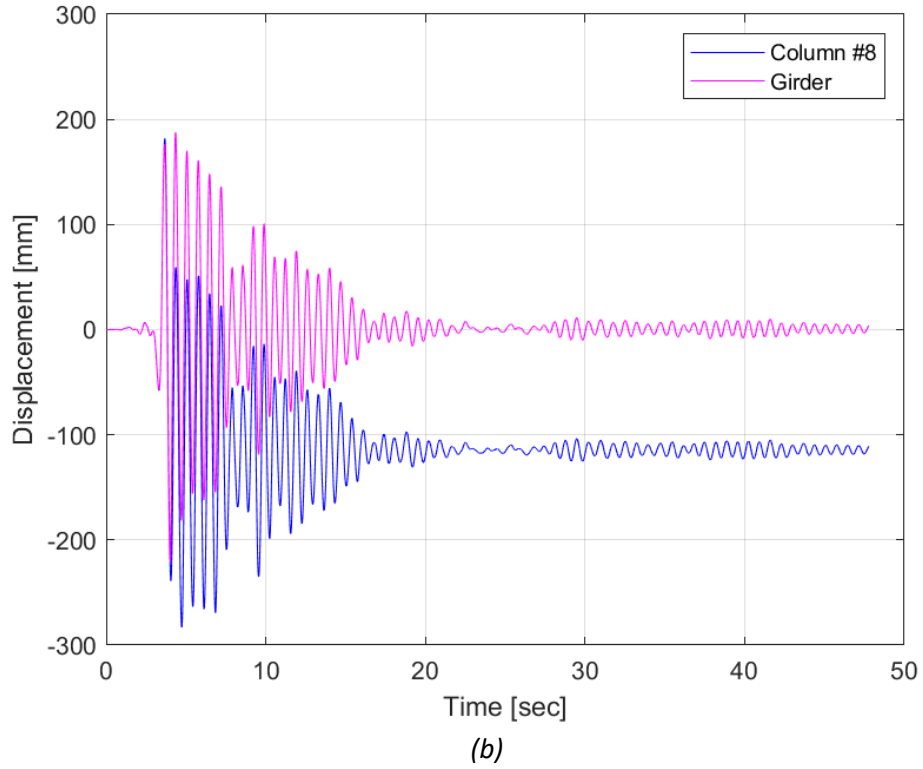
Figure 4.43. Displacement time-history of column #8 under Load Case 1 in:
(a) Longitudinal, (b) Transverse directions.

(a)

(b)
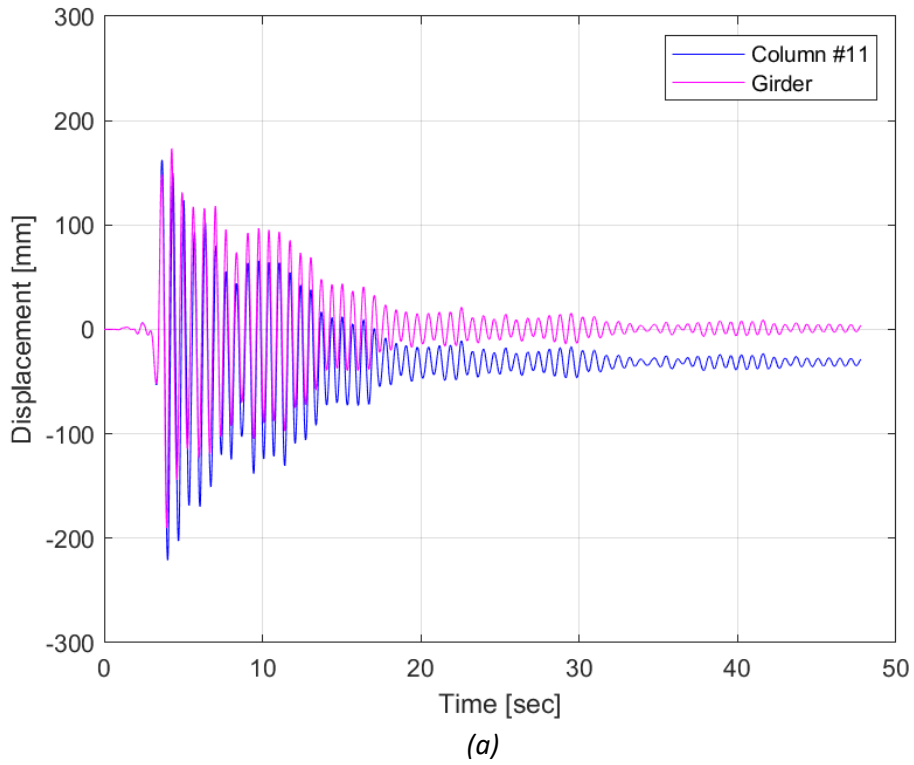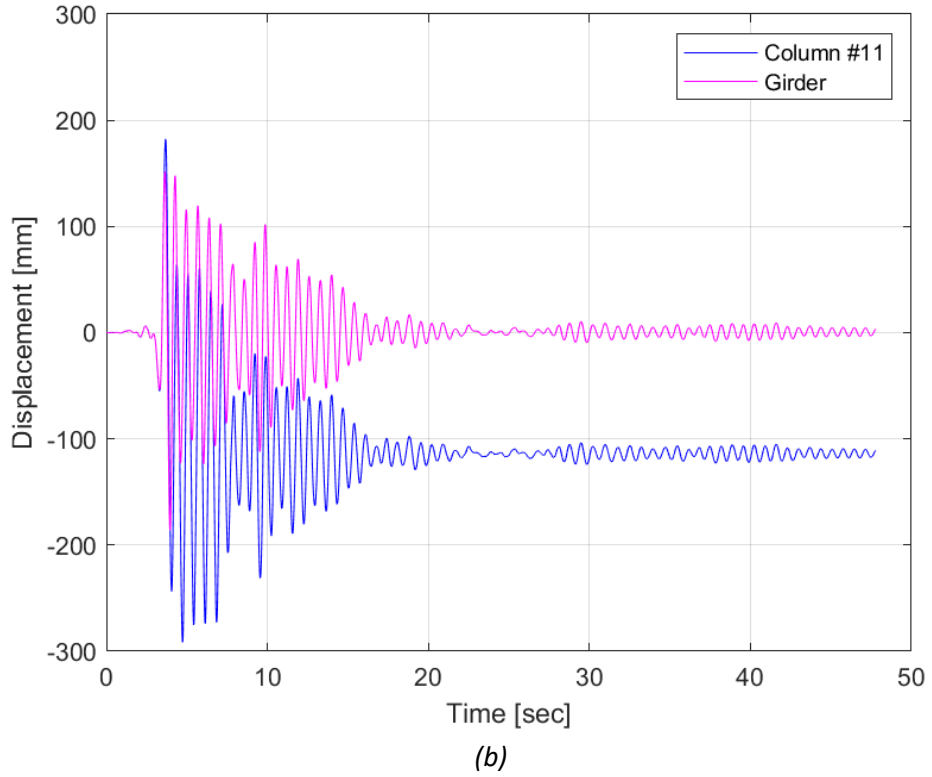
Figure 4.44. Displacement time-history of column #11 under Load Case 1 in:
(a) Longitudinal, (b) Transverse directions.

(a)

139

(b)
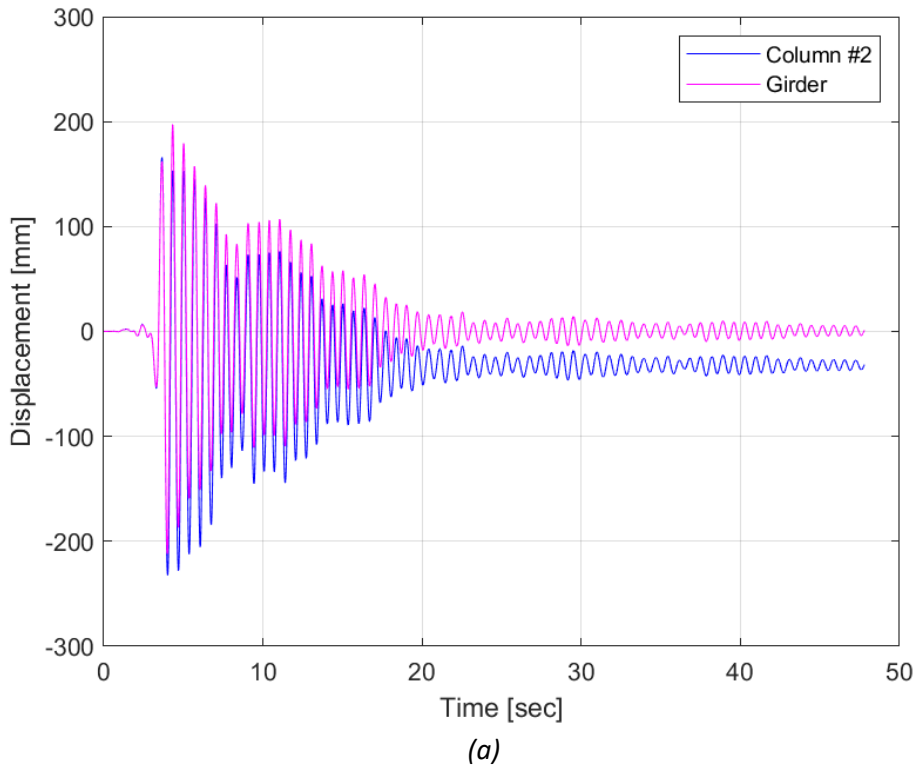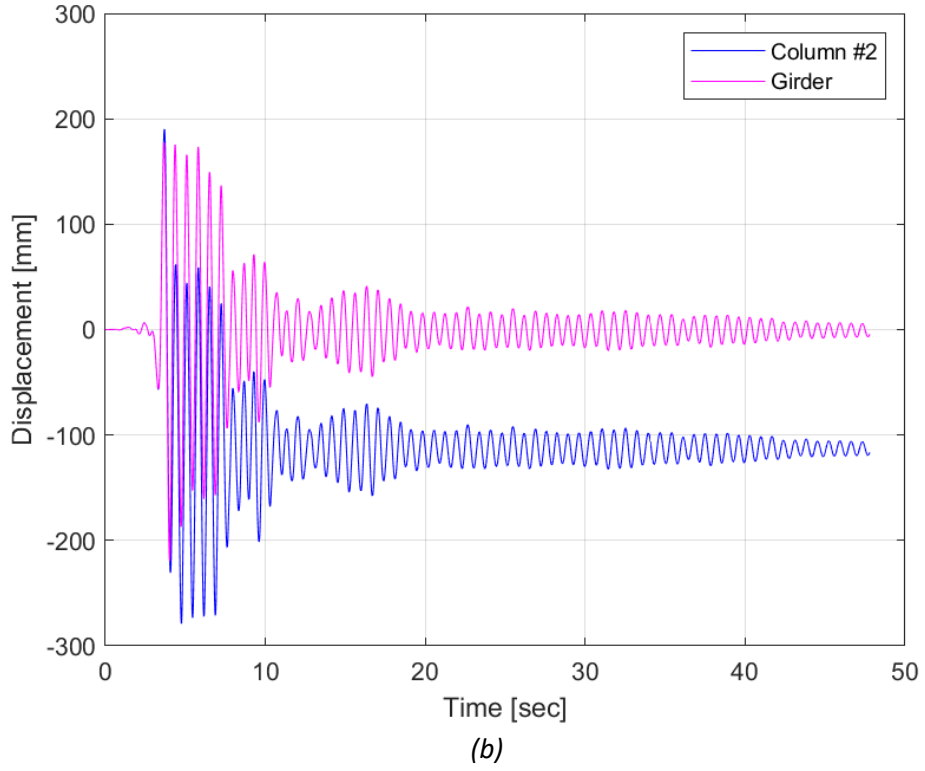
Figure 4.45. Displacement time-history of column #2 under Load Case 8 in:
(a) Longitudinal, (b) Transverse directions.

(a)
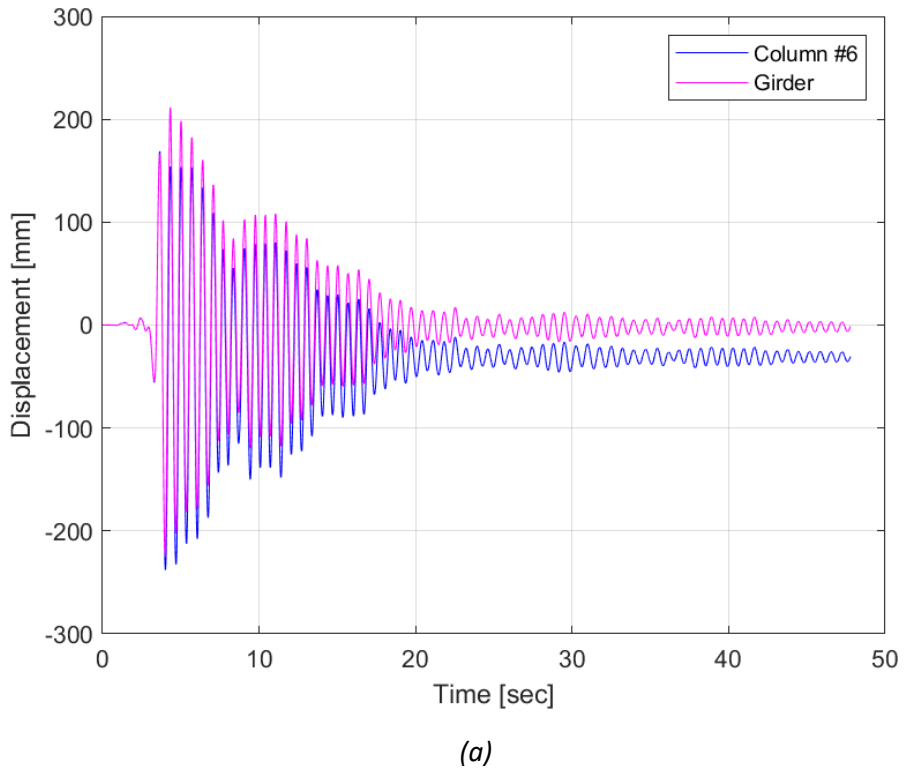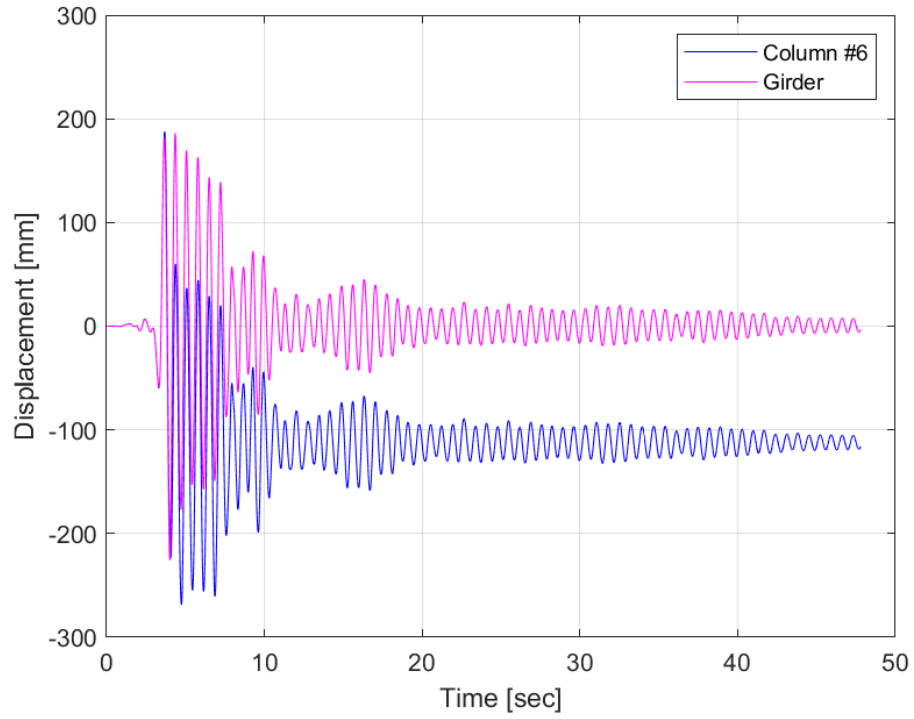
(b)

Figure 4.46. Displacement time-history of column #6 under Load Case 8 in:
(a) Longitudinal, (b) Transverse directions.

(a)

141
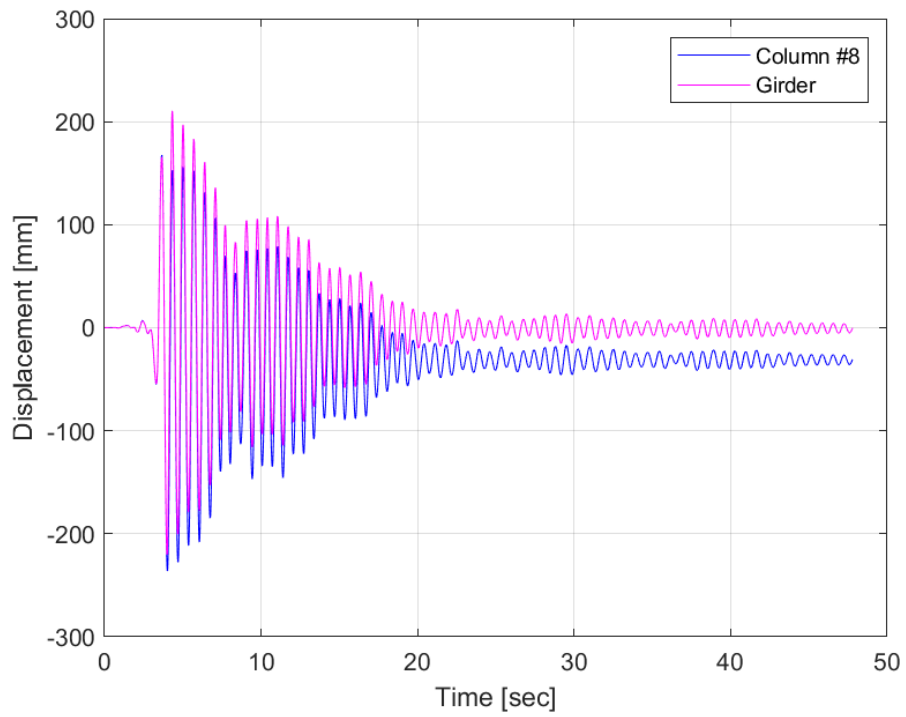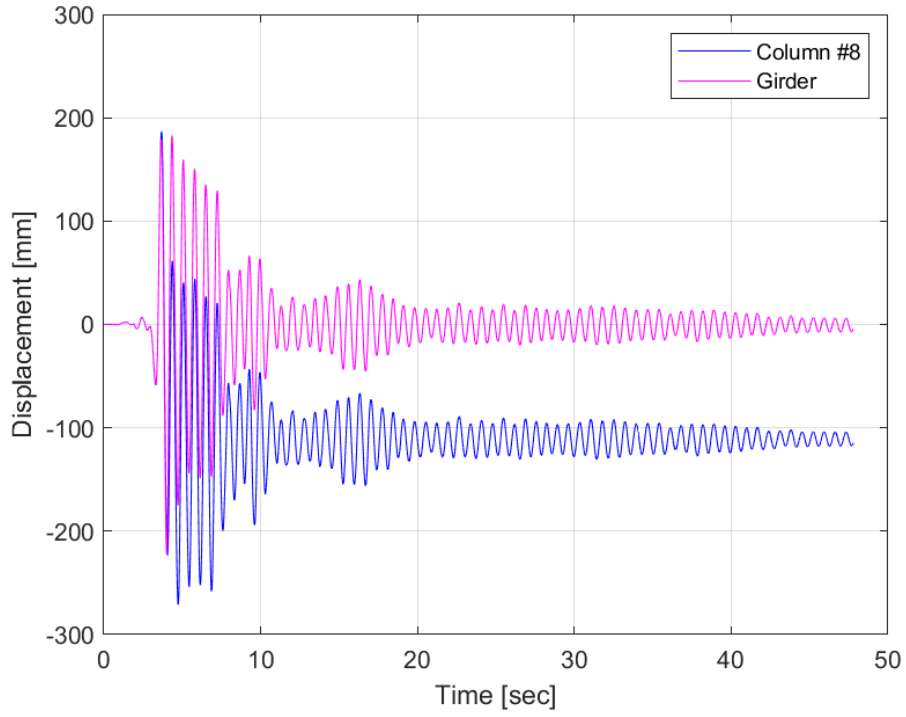
(b)

Figure 4.47. Displacement time-history of column #8 under Load Case 8 in:
(a) Longitudinal, (b) Transverse directions.
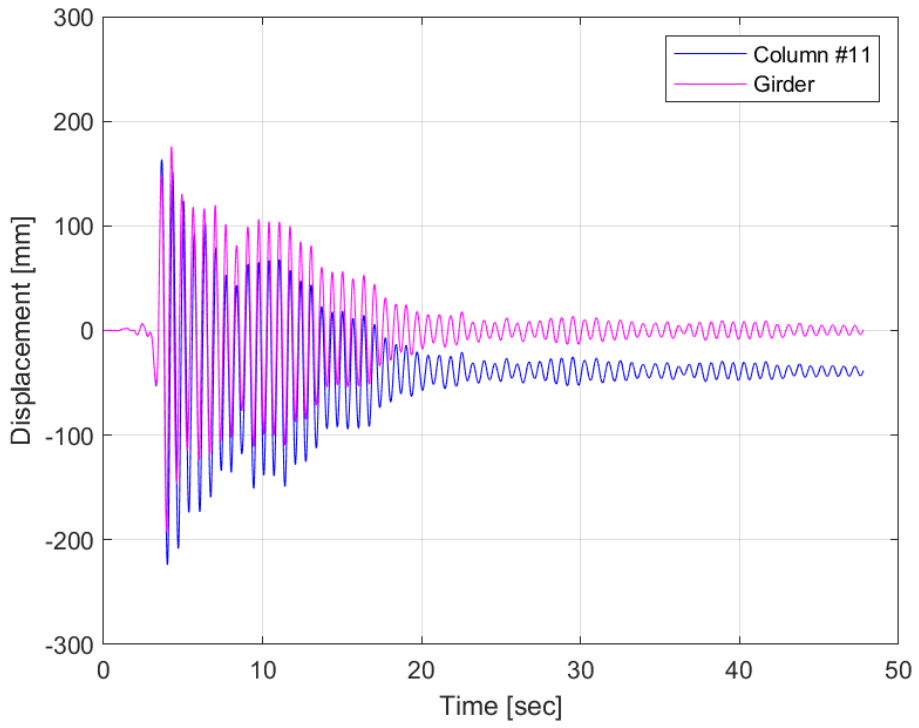
(a)
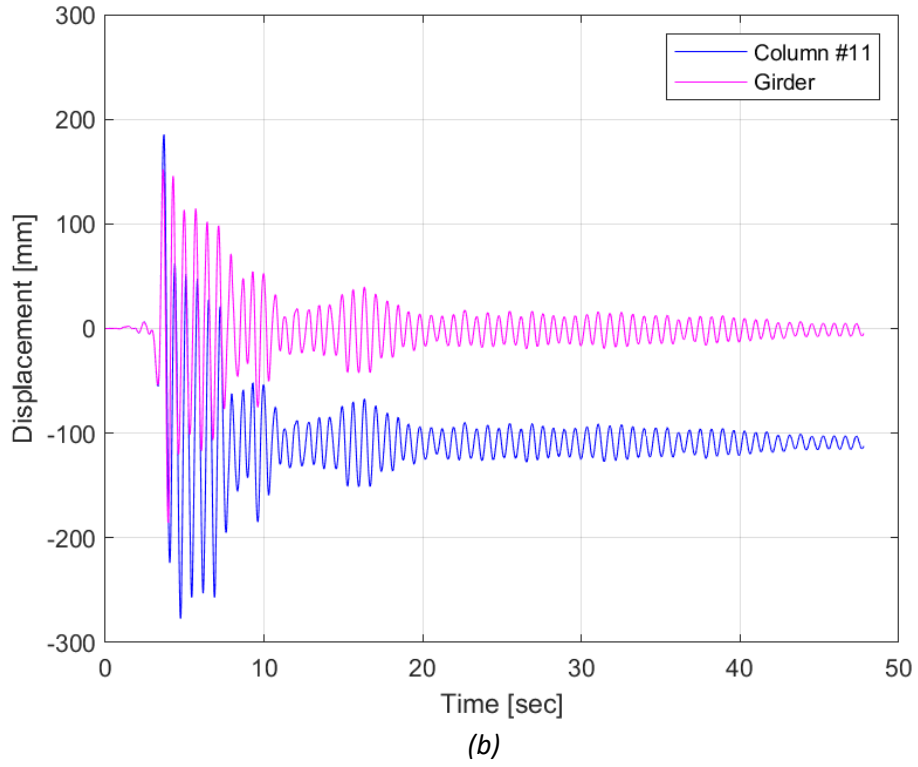
Figure 4.48. Displacement time-history of column #11 under Load Case 8 in:
(a) Longitudinal, (b) Transverse directions.

143

(b)
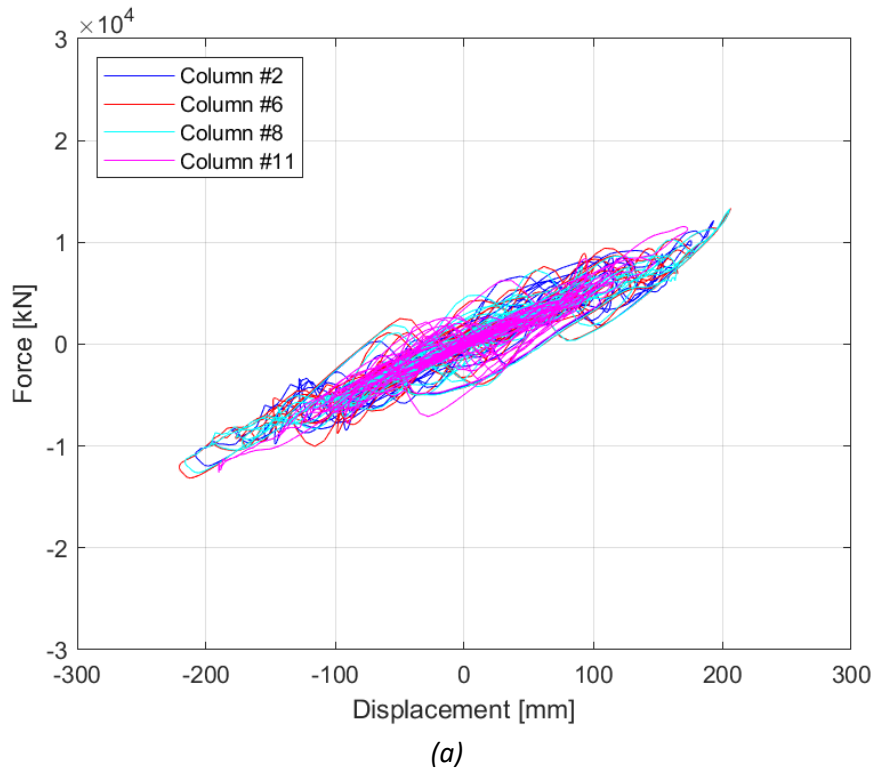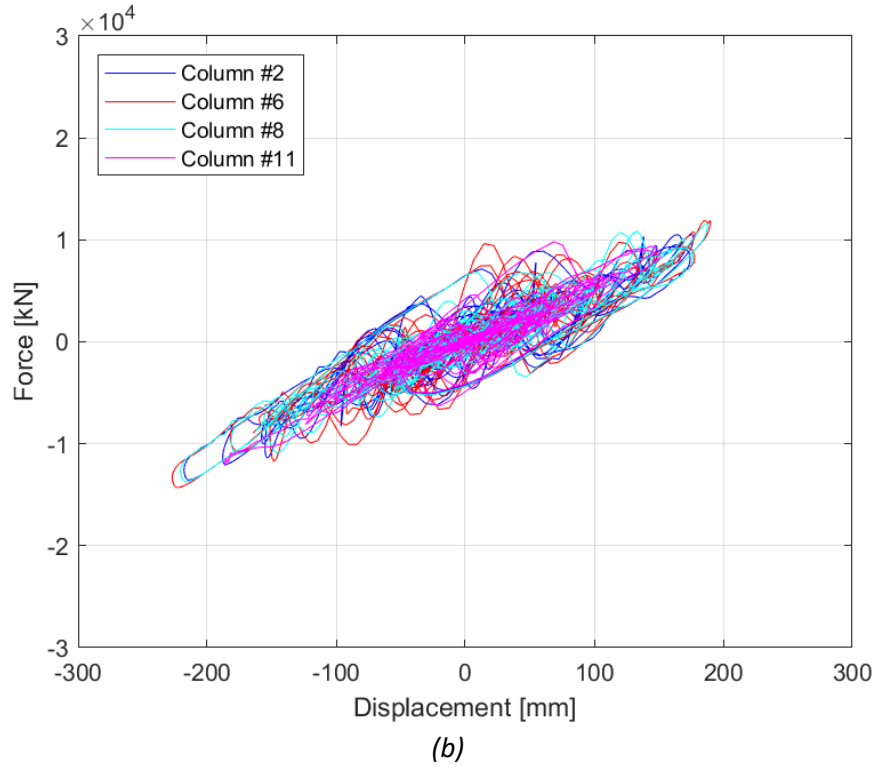
Figure 4.49. Force-displacement relationship of column #2, #6, #8, and #11 in the longitudinal direction for: (a) Load Case 1, (b) Load Case 8.

(a)

144
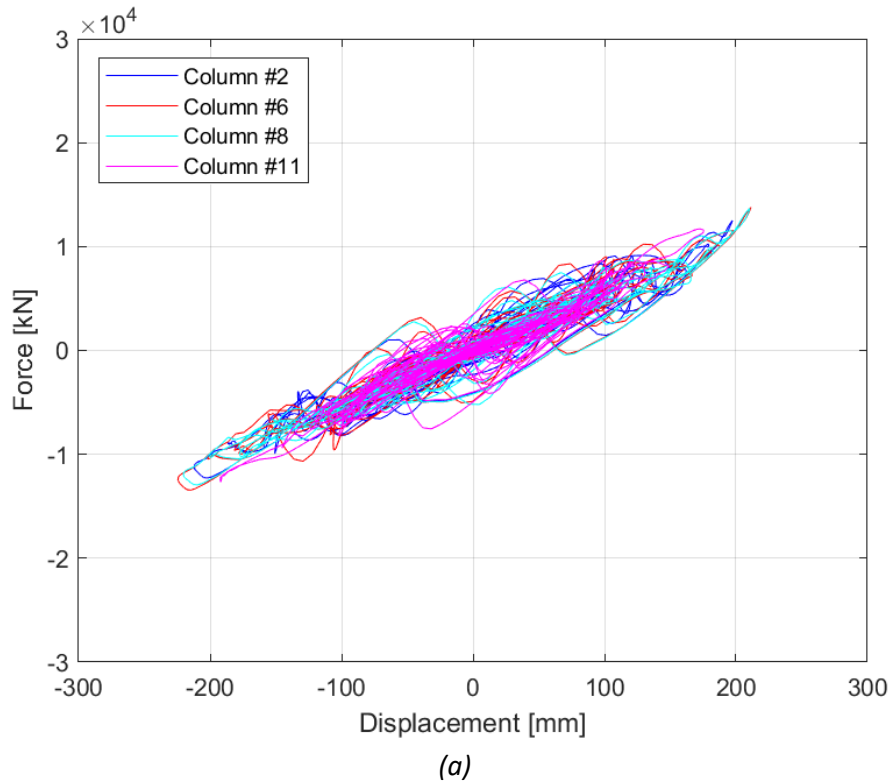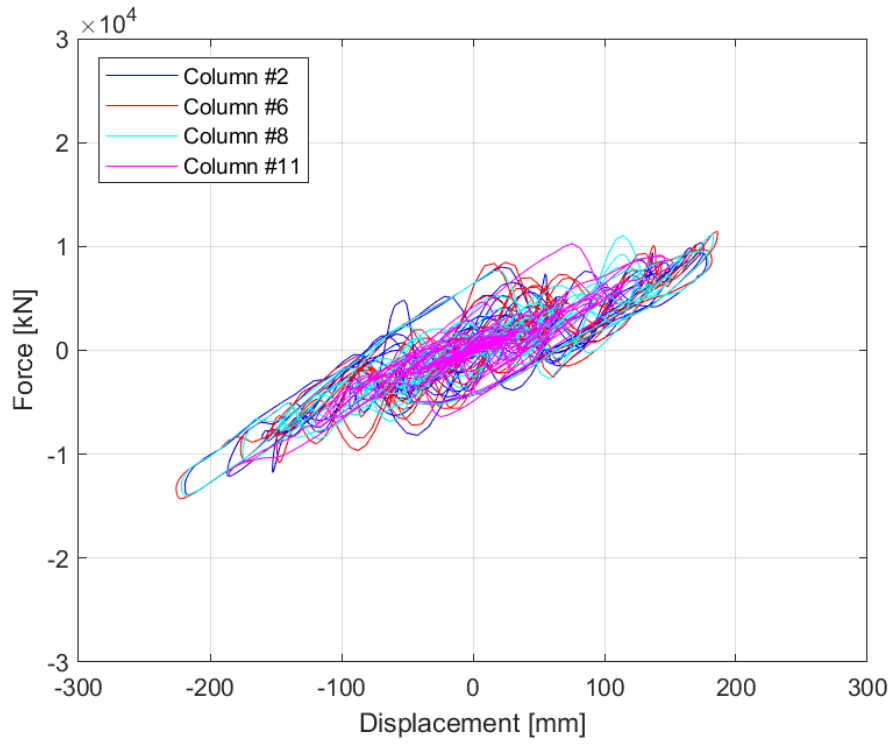
(b)

Figure 4.50. Force-displacement relationship of column #2, #6, #8, and #11 in the transverse direction for: (a) Load Case 1, (b) Load Case 8.
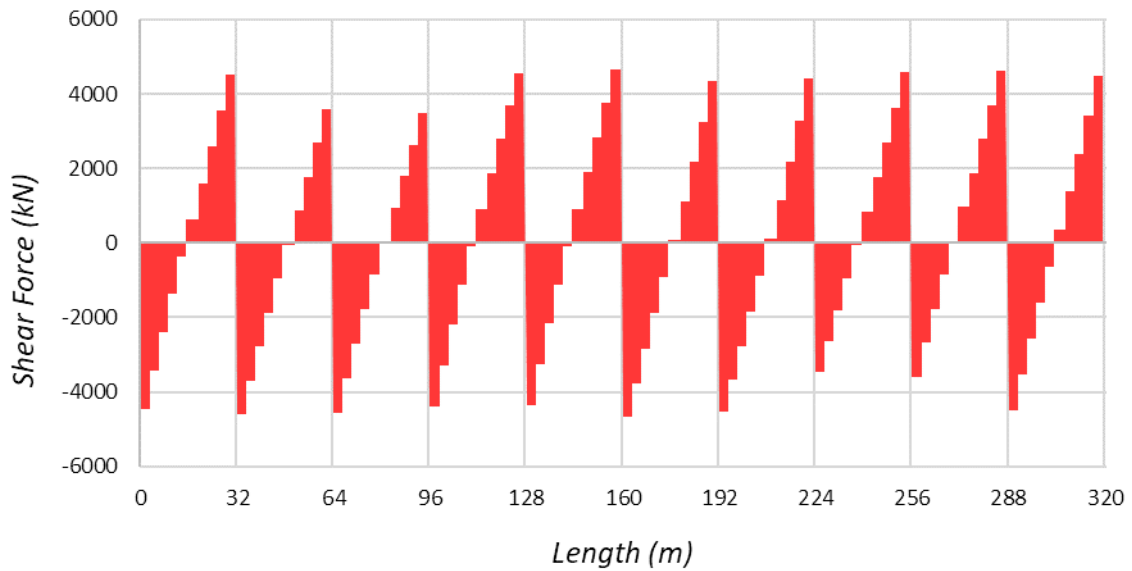
Figure 4.51. Bridge girder shear in the longitudinal direction (Vx) for Load Case 1.
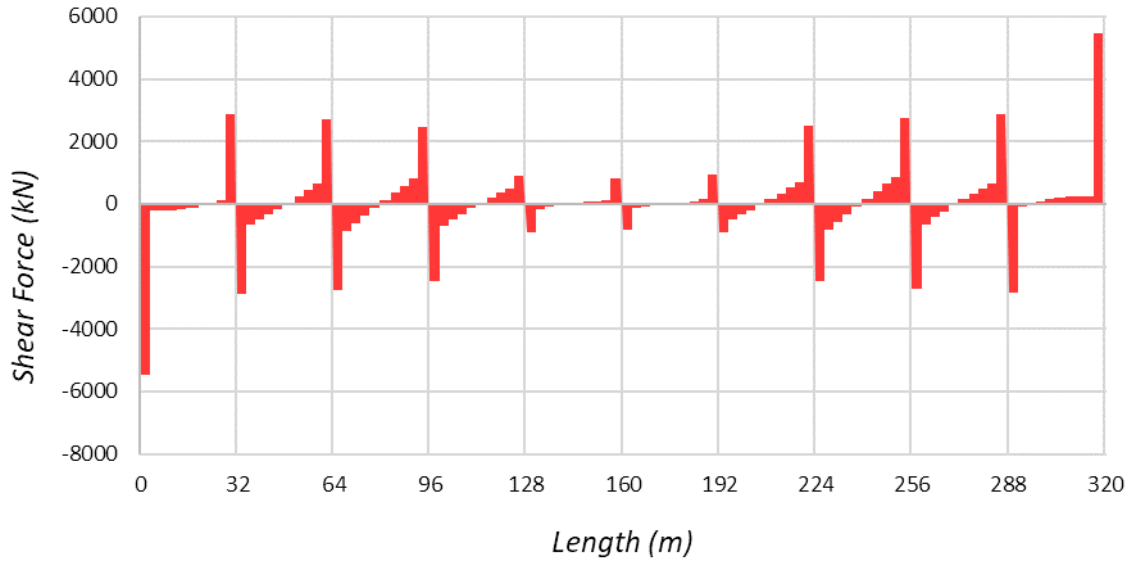
Figure 4.52. Bridge girder shear in the transverse direction (Vy) for Load Case 1.
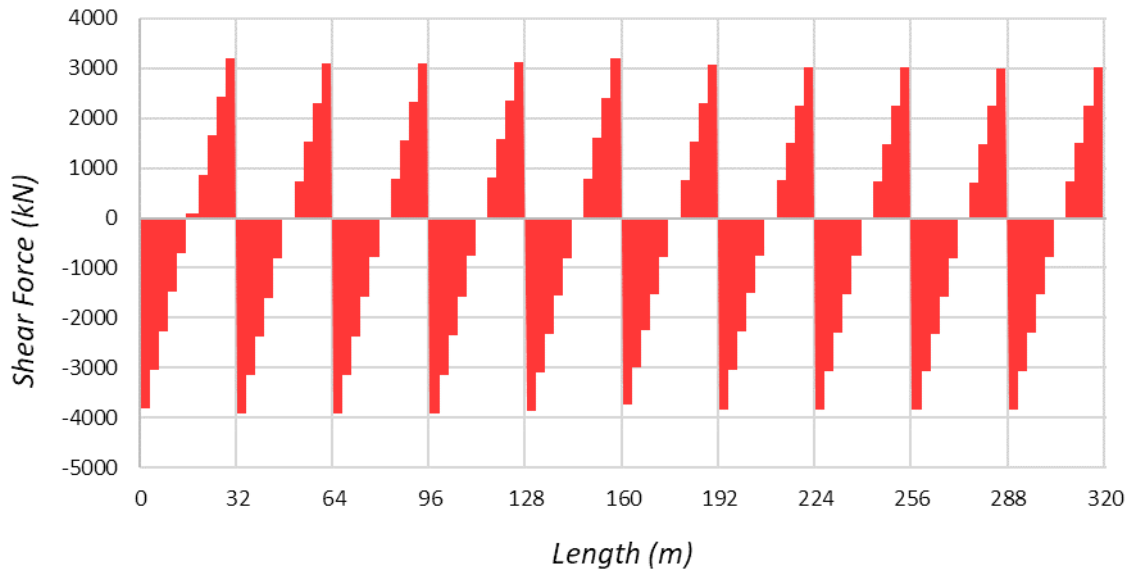
Figure 4.53. Bridge girder shear in the vertical direction (Vz) for Load Case 1.
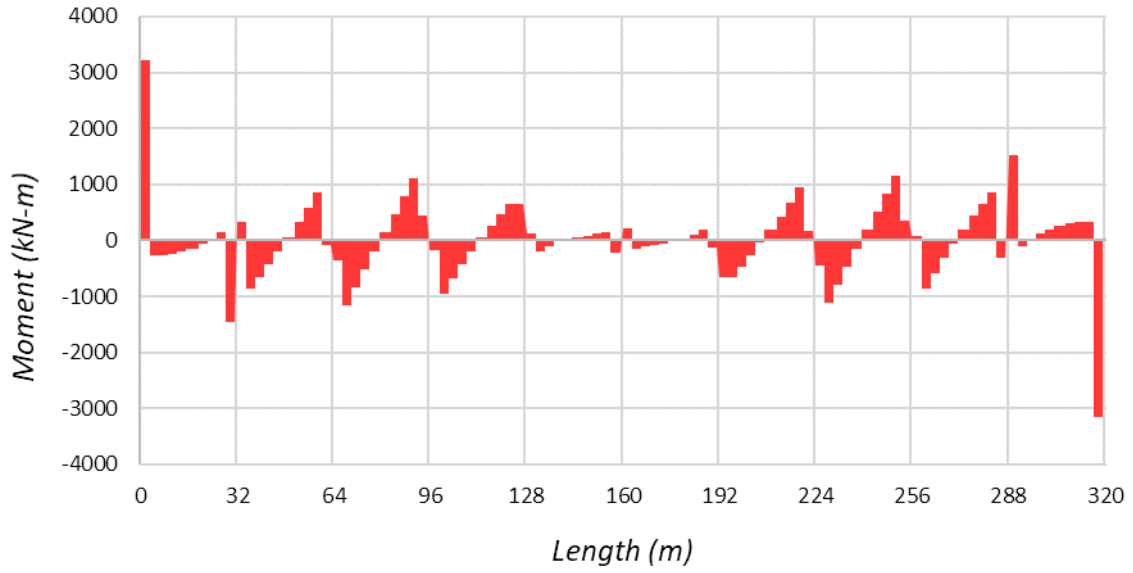
Figure 4.54. Bridge girder moment in the longitudinal direction (Mx) for Load Case 1.
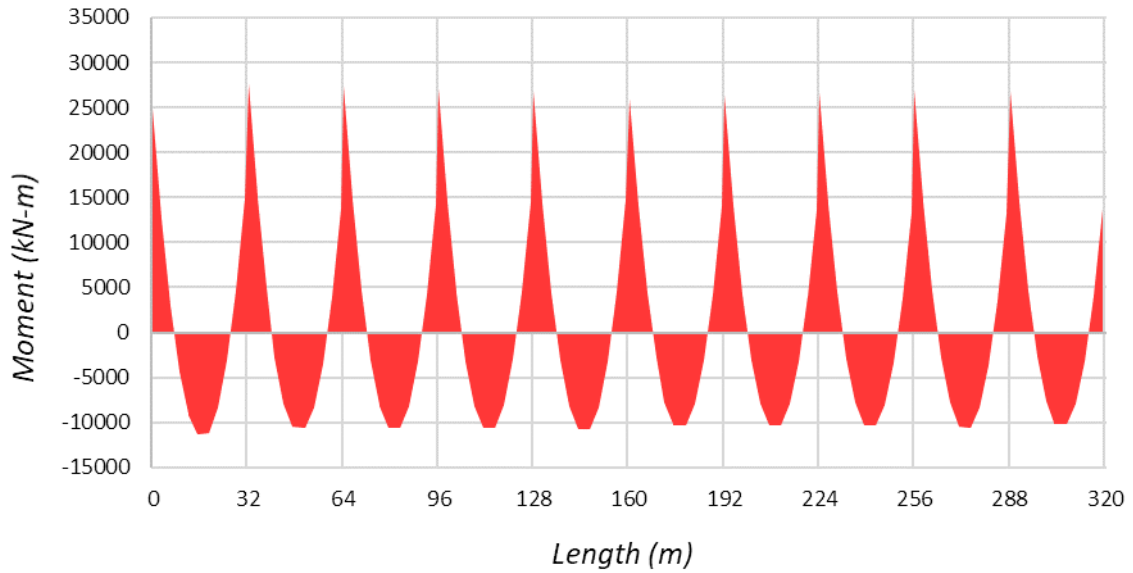
Figure 4.55. Bridge girder moment in the transverse direction (My) for Load Case 1.
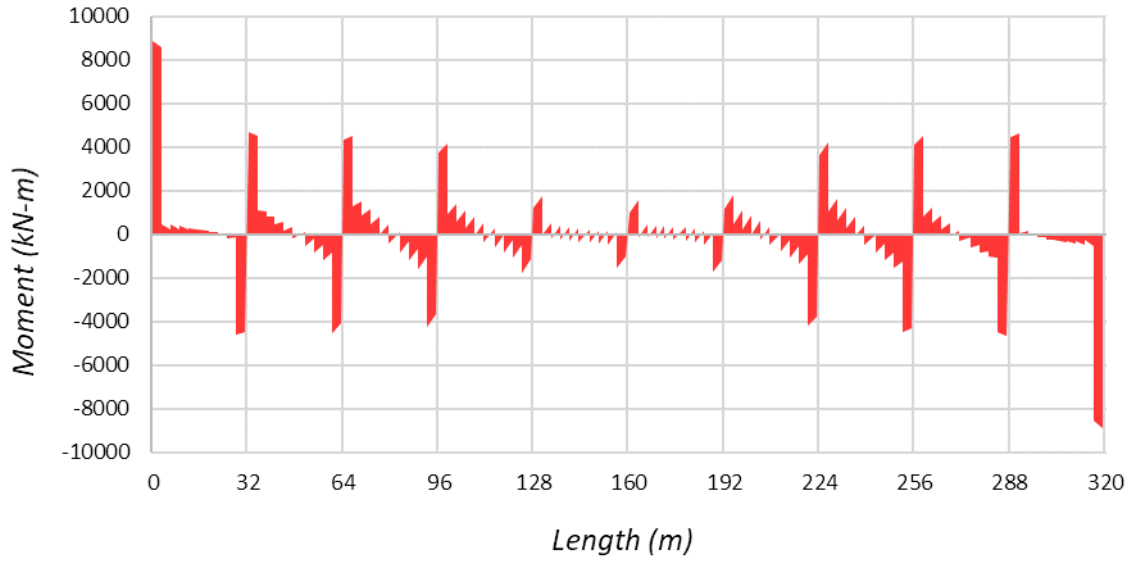
Figure 4.56. Bridge girder moment in the vertical direction (Mz) for Load Case 1.
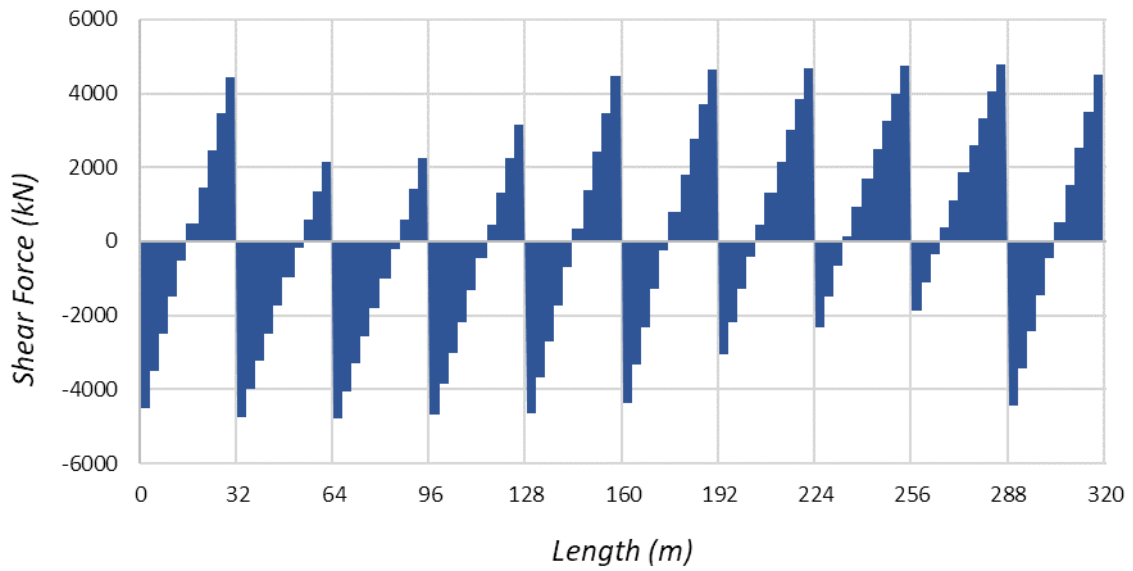
Figure 4.57. Bridge girder shear in the longitudinal direction (Vx) for Load Case 8.
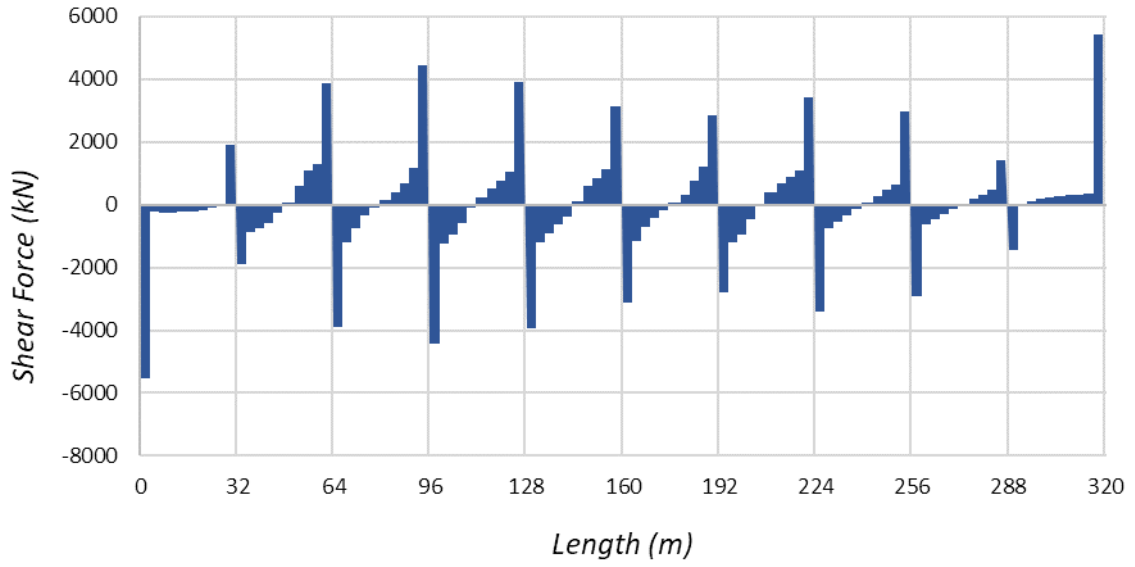
Figure 4.58. Bridge girder shear in the transverse direction (Vy) for Load Case 8.
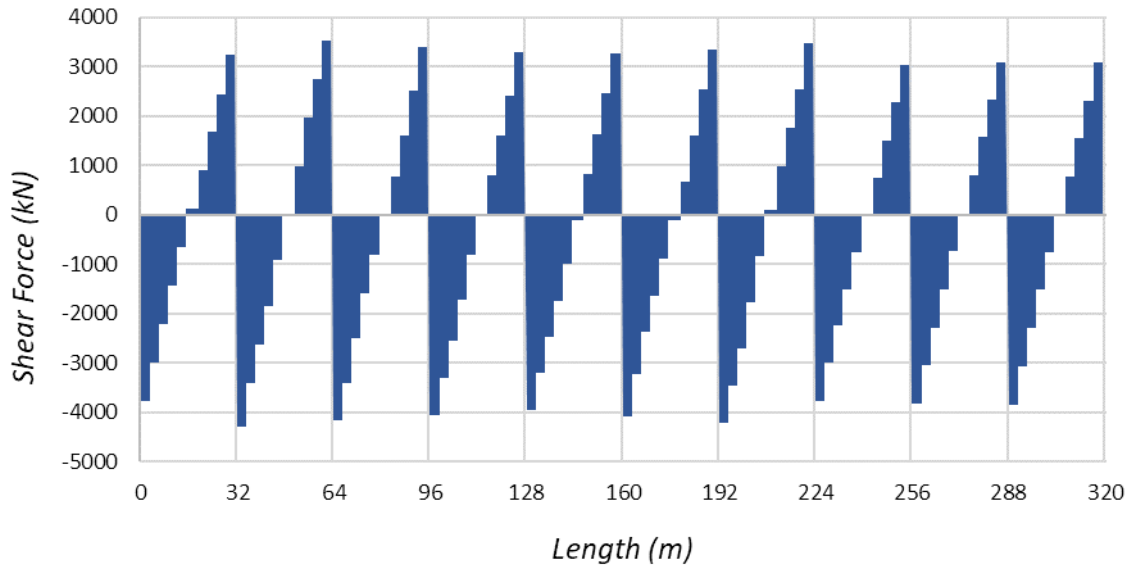
Figure 4.59. Bridge girder shear in the vertical direction (Vz) for Load Case 8.
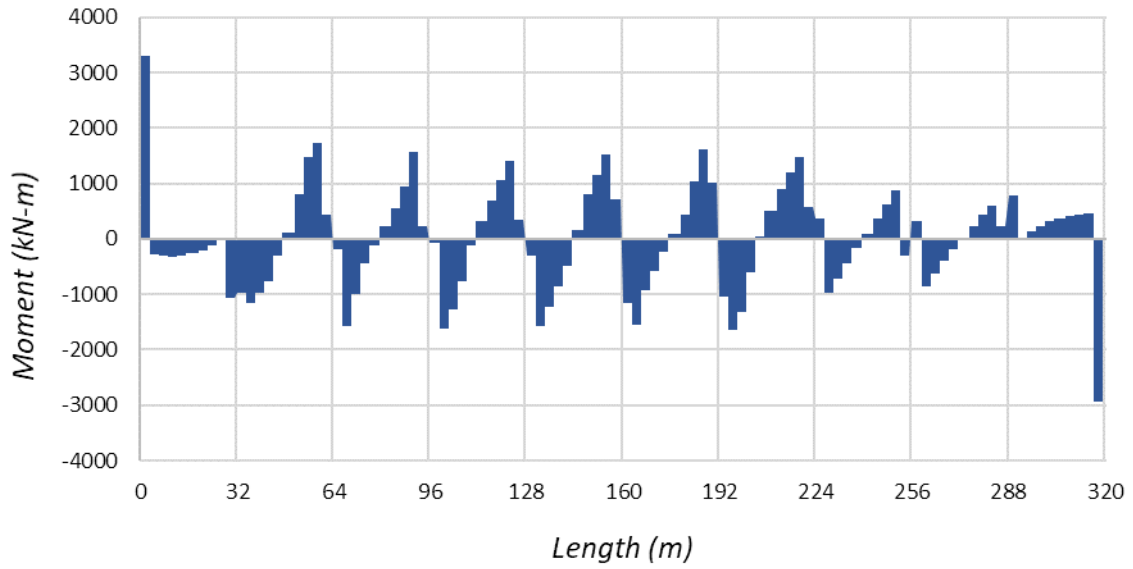
Figure 4.60. Bridge girder moment in the longitudinal direction (Mx) for Load Case 8.
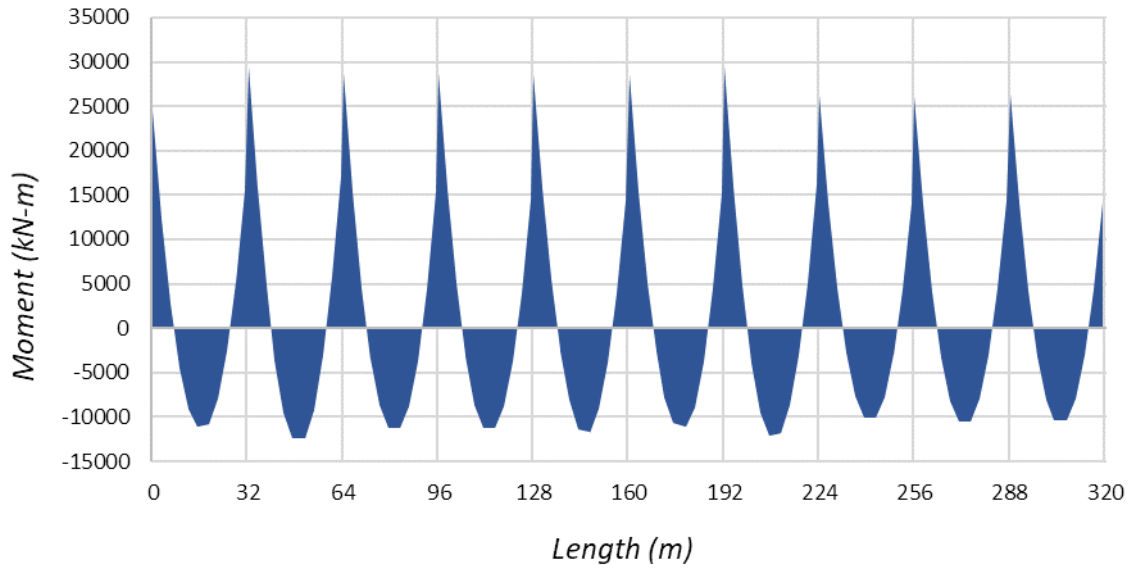
Figure 4.61. Bridge girder moment in the transverse direction (My) for Load Case 8.
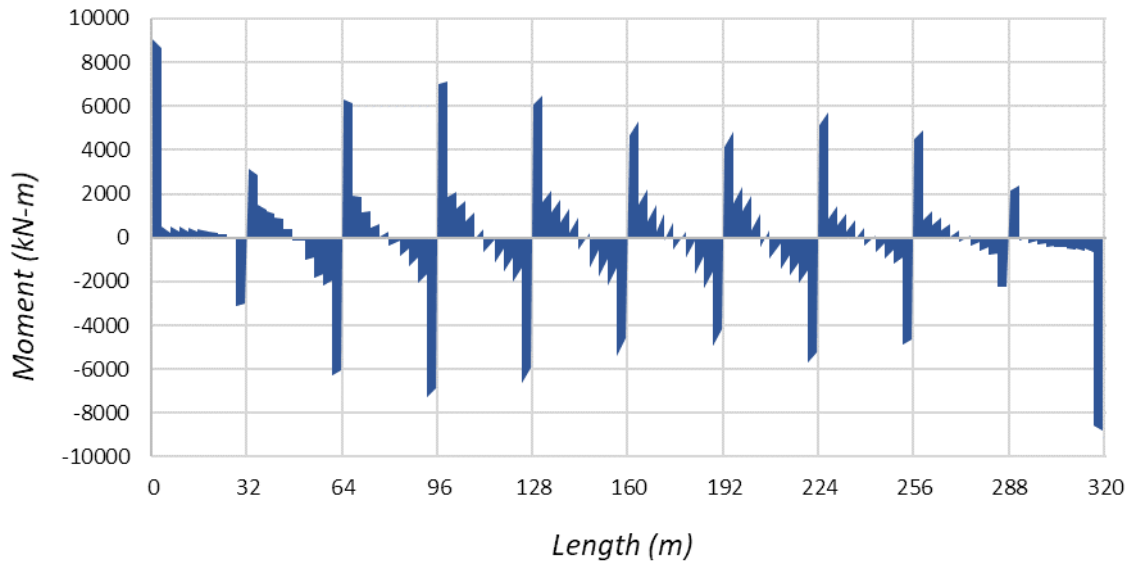
Figure 4.62. Bridge girder moment in the vertical direction (Mz) for Load Case 8.

4.4. *SEISMIC RESPONSE OF PROTOTYPE HSR BRIDGE SYSTEM: IN-DEPTH STUDY*

Seismic loads pose a great threat to the stability of HSR bridges that can be built in high seismic regions, such as California in the United States. A proper design guideline and code are required to assess the seismic performance of an HSR bridge, which is not fully mature and developed for the United States yet. Nonetheless, this section further extends the brief seismic analysis presented above by providing a more in-depth demonstration of the attributes of a comprehensive analysis of the structural behavior of HSR system with focus on bridge components. The more in-depth demonstration of nonlinear time history analysis of HSR bridge systems performed in this section considered three load cases and three ground motions applied with various intensities.

The three load cases were again selected from the 16 sample cases previously outlined in Table 4.5 for the selected train and bridge prototypes used in this study. These are Load Case 1, Load Case 6, and Load Case 9. Load Case 1 was selected similar to the sample analysis conducted in the previous section to demonstrate the HSR bridge response without any loading from the train. Load cases 6 and 9 were selected to demonstrate the prototype HSR bridge behavior under partial and full train loading. The load cases are illustrated in Table 4.8. The prototype HSR bridge model under each of these load cases was subjected to three ground motions sourced from the PEER Ground Motion Database by the University of California, Berkeley. The acceleration time histories of the three selected ground motions are shown in Table 4.9. The first record is the same 1994 Northridge earthquake record from the Sepulveda VA Hospital station as used before in the previous section. The two additional ground motions include one from the 1995 Kobe earthquake recorded at the Takatori station, and another one from the 1989 Loma Prieta earthquake recorded at the LGPC station. Each of the three ground motions were applied with two intensity levels at 100% and 200% scale of the original record. An additional analysis was performed for the Northridge record scaled at 300% to explore the seismic response of the HSR bridge at higher seismic demands.

151
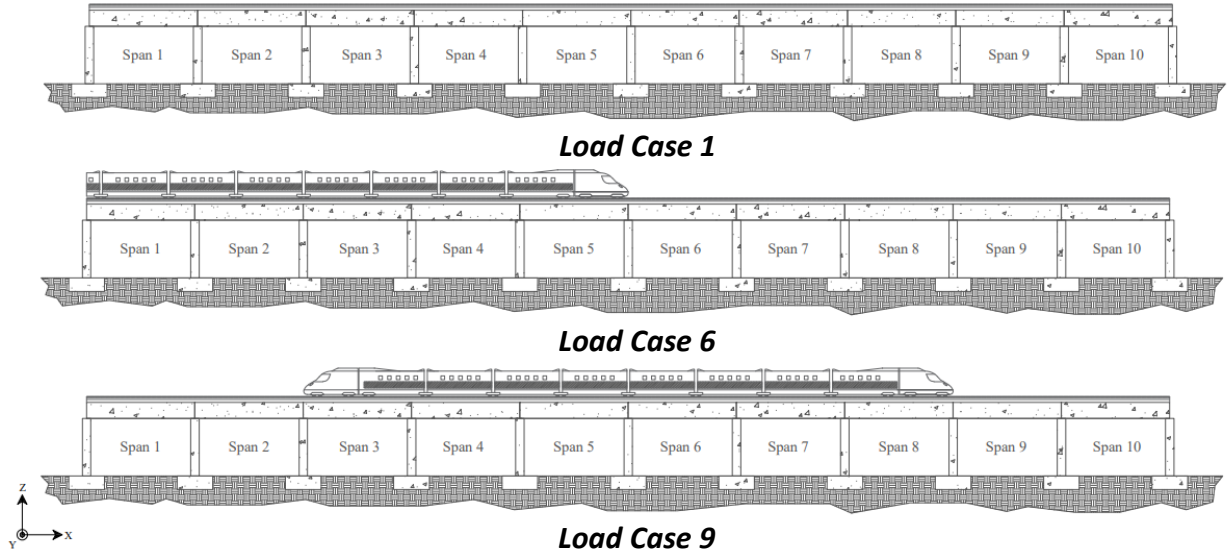
Figure 4.63. Train load cases used in the seismic analysis in this section.
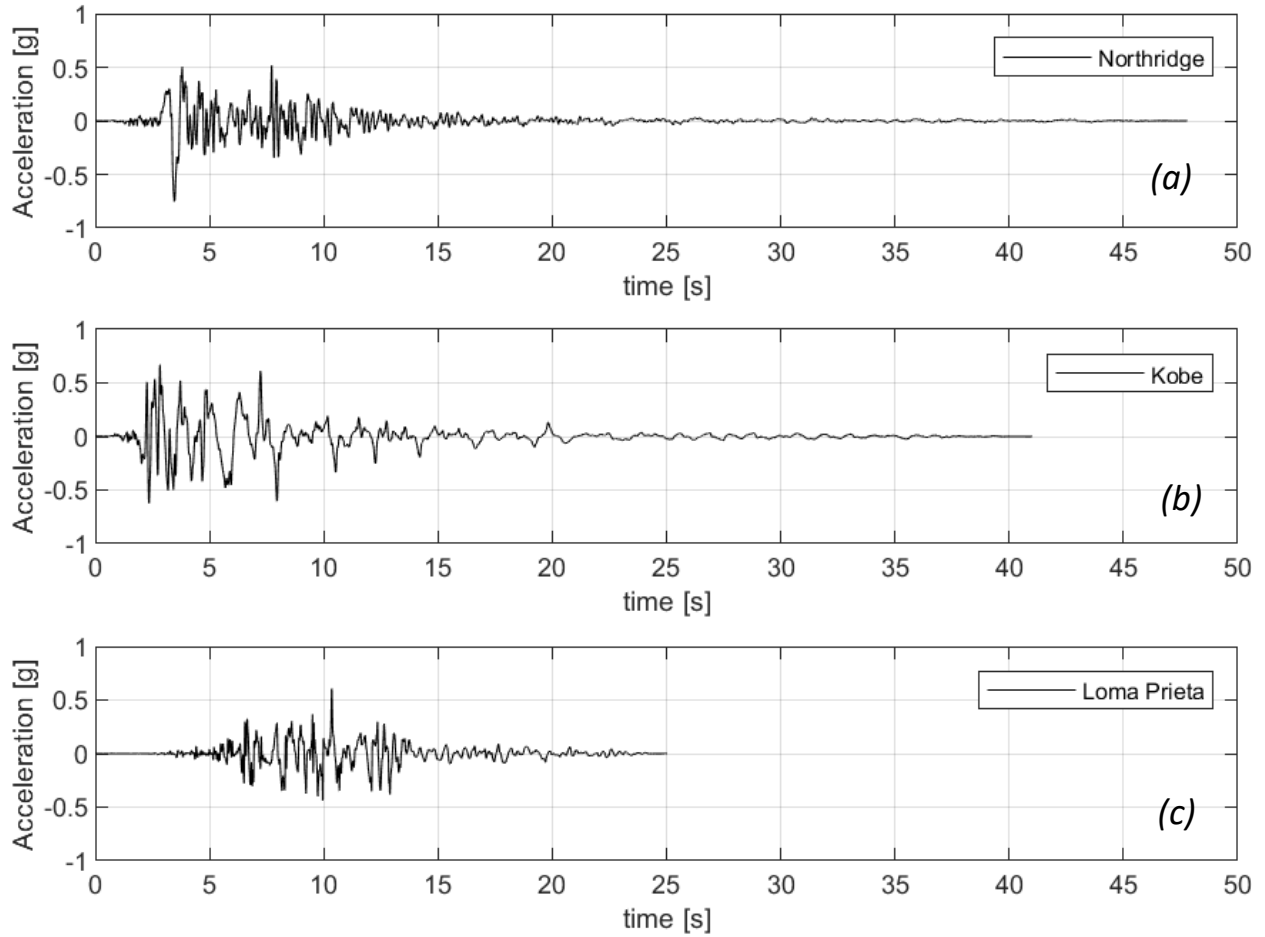
Figure 4.64. PEER database ground motions used for the seismic performance assessment:
(a) Northridge, (b) Kobe, and (c) Loma Prieta.

In addition to what was presented in Section 4.3 as sample seismic analysis, this section provides a deeper look at both global and local behavior of selected bridge components from the 100% and 200% scale ground motion runs. A comprehensive summary of the maximum selected local and global responses of the HSR bridge are tabulated and provided here. Additional displacement time-histories, force-displacement relationships, and moment-curvature relationships are plotted to compare the effect of ground motion intensity and train loading scenarios on the HSR bridge. Moreover, results from the 300% scale Northridge record to assess the extent of nonlinear and inelastic behavior of the HSR bridge columns as well as the force-deformation behavior of selected track-bridge interaction zero-length elements to observe the load transfer within the system during seismic events.

4.4.1. MAXIMUM RESPONSE TABLES

The behavior of the prototype HSR bridge was analyzed by tabulating the maximum responses under the various loading scenarios. A total of 12 tables were created to analyze the maximum responses of the prototype HSR bridge. The local maximum responses of the pier columns and bridge girder spans under each load case (1, 6, and 9) were tabulated for the three ground motions at an amplification of 100% and 200%, resulting in 6 tables. The shear, moment, and curvature in the transverse and the longitudinal directions were recorded for the pier columns. However, only the longitudinal shear and moment for the bridge box-girder spans were recorded at each end of the spans since the in-plane responses were not of interest. The other 6 tables demonstrate the global maximum displacement and acceleration of the bridge girder nodes directly above the pier columns for the same load variations. The values in the tables represent the absolute maximum responses (positive or negative) and the maximum response within each category was highlighted to help visualize the trends under each load case.

Observing the tabulated maximum local responses of the pier columns and girder spans presented in Table 4.8 through Table 4.13, there is an obvious increase in magnitude for all presented values when comparing the maximum response under the original 100% scaled ground motion to the 200% scaled ground motion. The columns experienced a significant increase due to the larger seismic forces applied at the base of the model connected to the column footings through translational springs. Column shear, moment, and curvature showed an average increase of 70%, 28%, and 32% about the longitudinal axis, and an average increase of 56%, 19%, and 30% about the transverse axis. The box-girder sections were assumed to be less affected by the earthquake intensity because they are capacity protected elements and should not see higher demands beyond what is dictated by the columns' capacity.

The magnitude of the maximum local responses for Load Case 1, 6, and 9 were compared among all of the considered loading scenarios to identify the impact of train loading. The Load Case 6 train loading is heavily shifted to one side of the bridge and imposes less total weight of the train on the bridge, relative to full train load in Load Case 9, due to a portion of the train not being on the bridge. Yet, the bridge seismic response due to both load cases with partial and full train load on top of the bridge were similar. Comparing the average responses between Load Case 1 with no train loading to Load Cases 6 and 9 with train loading, the most notable change was in the maximum longitudinal moment response where an average increase of 10% and 12% was observed for Load Case 6 and 9, respectively. The maximum column shear response showed small

153

increases of less than 2% and the maximum transverse column moment increased by 4% for both load cases. Load Case 9 showed 6% increase for the maximum column curvature in both directions and Load Case 6 increased by 4% for both directions. The in-plane girder shear and moment also increased by 5% for Load Case 6 and 6% for Load Case 9. When comparing the two load cases with train loading, Load Case 9 had slightly larger responses on average when compared against Load Case 6.

The maximum global response in terms of the displacement and acceleration measured at the girder nodes directly above the respective pier columns were obtained under the three different ground motions and are tabulated in Table 4.14 through Table 4.19. Each table compares results from the three selected load cases. Thus, the six tables represent the six ground motion scenarios: 3 different records × 2 different seismic intensities. On average, the higher intensity ground motions at 200% scale increased the longitudinal and transverse maximum global displacements by 111% and 87%, respectively, as well as the longitudinal and transverse maximum global accelerations by 54% and 55%, respectively. When comparing Load Case 1 to Load Case 6 and 9, the most notable change was increase in the average maximum longitudinal displacement by 4% for both load cases. The maximum transverse displacement increased by 3% for Load Case 6 but did not change for Load Case 9. The increase in maximum acceleration for either load case was insignificant with less than 1% increase and the transverse acceleration for Load Case 9 even decreased by 3%. The minimal increase in the longitudinal acceleration and decrease in the transverse acceleration for the load cases with train loading can be assumed to follow the fundamental concept of Newton's Second Law of Motion. The addition of train loading increases the mass and in-turn decreases the acceleration of the bridge to maintain force equilibrium; however, this is assuming a perfectly linear system which is not the case for this study since inelastic material behavior have been modeled. Seismic response of the prototype HSR bridge will vary as the stiffness of the structure changes throughout the cyclic loading of the seismic forces and the overall mass changes based on the load case. Ultimately, the lack of major change in local and global response due to additional train loading could be a result of the inherent conservative design nature of HSR bridges. Compared to similar highway bridges, HSR bridge columns are designed to be much stiffer to minimize lateral deformations to improve the train and track stability as well as the riding comfort of passengers. HSR bridges feature massive columns with larger force and moment capacities, relative to equivalent highway bridges, which indirectly result in HSR bridges withstanding larger earthquake forces before failure.

Table 4.8. Maximum Local Responses – Northridge 100% Scale.

Member ID	LC1						LC6						LC9					
	Shear Long (kN)	Shear Trans (kN)	Moment Long (kN-m)	Moment Trans (kN-m)	Curvature Long (1/m*10^-6)	Curvature Trans (1/m*10^-6)	Shear Long (kN)	Shear Trans (kN)	Moment Long (kN-m)	Moment Trans (kN-m)	Curvature Long (1/m*10^-6)	Curvature Trans (1/m*10^-6)	Shear Long (kN)	Shear Trans (kN)	Moment Long (kN-m)	Moment Trans (kN-m)	Curvature Long (1/m*10^-6)	Curvature Trans (1/m*10^-6)
Columns																		
1	12275	11907	151849	150935	5.41115	3.6981	12422.8	11944.4	153028	150033	5.41941	3.89747	12437.9	11843	152118	150278	5.40287	3.73938
2	12139.6	13550	209734	232044	7.36617	5.66054	12476.7	14063	210456	240450	7.01737	5.4112	12490.1	13728.8	215793	235574	7.50425	5.75906
3	12859.2	13708.3	210118	234453	7.02843	5.30174	13339.3	14352.7	232814	244012	7.84353	5.97026	13356.1	13954.6	234245	243050	7.94912	6.03848
4	13258.3	13721.5	210939	234834	7.0626	5.27189	13610.6	14203.3	210842	244499	7.11357	5.50165	13663.2	14021.5	213835	243314	7.08676	5.48557
5	13365.7	14047.6	210939	235179	7.1229	5.50255	13770.8	14229.3	212045	239368	7.16862	5.38151	13801.5	14184.5	212137	245451	7.13918	5.49617
6	13320.8	14309.5	211007	236872	7.15251	5.43494	13717	14242.9	214807	244416	7.1018	5.49007	13753.1	14291.9	212750	245455	7.1478	5.5029
7	13368.2	14046.1	211333	235138	7.12706	5.5076	13778.5	14021.2	212103	242456	7.13283	5.48129	13797.5	14184.6	212081	245393	7.1431	5.5019
8	13259.2	13725.8	211147	234877	7.06274	5.27728	13612.9	13716.5	213501	237046	7.06994	5.40843	13658.2	14037.6	211293	245531	7.14937	5.51575
9	12858.1	13707	210541	234440	7.02732	5.30118	13236.6	13547.9	238736	244999	7.7545	5.83619	13345.7	13981.1	238770	244187	8.08671	6.11182
10	12139.3	13550.6	208201	232096	7.34406	5.6722	12461.5	13285.8	208189	230721	6.96425	5.33878	12485.6	13766.2	209233	232733	6.98815	5.43353
11	12603.9	12169.3	169872	155746	5.48013	4.30796	12450.1	11857.8	167967	165218	5.57852	4.34042	12659.2	12042.6	168648	165987	5.5765	4.34327
Long. Girder																		
S1-L	4249.26	NR	28142.2	NR	NR	NR	4720	NR	30867	NR	NR	NR	4366.01	NR	29280.2	NR	NR	NR
S1-R	4523.86	NR	35581.7	NR	NR	NR	4777.25	NR	37026.6	NR	NR	NR	4414.67	NR	35350.4	NR	NR	NR
S2-L	4528.71	NR	31278.9	NR	NR	NR	4763.85	NR	34406.5	NR	NR	NR	4601.22	NR	33261.9	NR	NR	NR
S2-R	4607.31	NR	36807.2	NR	NR	NR	4810.39	NR	38131.5	NR	NR	NR	4615.77	NR	37201	NR	NR	NR
S3-L	4628.05	NR	33189.6	NR	NR	NR	4480.13	NR	32922	NR	NR	NR	4845.49	NR	35341.8	NR	NR	NR
S3-R	4559.36	NR	36821.6	NR	NR	NR	4708.54	NR	37941	NR	NR	NR	4960.25	NR	39749.2	NR	NR	NR
S4-L	4448.05	NR	31915.9	NR	NR	NR	4600.01	NR	32157.7	NR	NR	NR	4451.39	NR	32485.1	NR	NR	NR
S4-R	4624.44	NR	37117.6	NR	NR	NR	4749.83	NR	37766.3	NR	NR	NR	4810.66	NR	37964.9	NR	NR	NR
S5-L	4359.03	NR	30665.4	NR	NR	NR	4671.02	NR	34922.3	NR	NR	NR	4377.22	NR	31865.1	NR	NR	NR
S5-R	4559.82	NR	36634.2	NR	NR	NR	4962.56	NR	39008.5	NR	NR	NR	4721.4	NR	37513	NR	NR	NR
S6-L	4275.74	NR	30736.7	NR	NR	NR	4294.8	NR	31305.1	NR	NR	NR	4356.86	NR	32199.1	NR	NR	NR
S6-R	4580.36	NR	18128.6	NR	NR	NR	4352.85	NR	17954	NR	NR	NR	4503.42	NR	18078	NR	NR	NR
S7-L	3770.44	NR	18106.6	NR	NR	NR	3561.85	NR	17938.3	NR	NR	NR	3597.58	NR	18060.6	NR	NR	NR
S7-R	4611.25	NR	36843.4	NR	NR	NR	4560.33	NR	36621.6	NR	NR	NR	4792.65	NR	38123.6	NR	NR	NR
S8-L	4582.72	NR	32888.4	NR	NR	NR	4622.42	NR	34322.2	NR	NR	NR	4996.97	NR	36406.6	NR	NR	NR
S8-R	4565.15	NR	36635.2	NR	NR	NR	4498.31	NR	36489.8	NR	NR	NR	5001.73	NR	39461	NR	NR	NR
S9-L	4545	NR	31721.5	NR	NR	NR	4442.28	NR	31360.8	NR	NR	NR	4495.7	NR	32748.1	NR	NR	NR
S9-R	4682.04	NR	36740	NR	NR	NR	4515.52	NR	36560.9	NR	NR	NR	4596.1	NR	36596.3	NR	NR	NR
S10-L	4319.29	NR	30788.8	NR	NR	NR	4184.43	NR	29786.8	NR	NR	NR	4229.61	NR	30970.6	NR	NR	NR
S10-R	4463.03	NR	33056.3	NR	NR	NR	4329.4	NR	32397.5	NR	NR	NR	4387.44	NR	32682.7	NR	NR	NR

Table 4.9. Maximum Local Responses – Northridge 200% Scale.

Member ID	LC1						LC6						LC9					
	Shear Long (kN)	Shear Trans (kN)	Moment Long (kN-m)	Moment Trans (kN-m)	Curvature Long (1/m*10^-6)	Curvature Trans (1/m*10^-6)	Shear Long (kN)	Shear Trans (kN)	Moment Long (kN-m)	Moment Trans (kN-m)	Curvature Long (1/m*10^-6)	Curvature Trans (1/m*10^-6)	Shear Long (kN)	Shear Trans (kN)	Moment Long (kN-m)	Moment Trans (kN-m)	Curvature Long (1/m*10^-6)	Curvature Trans (1/m*10^-6)
Columns																		
1	20152.7	22146.5	190602	209865	7.00727	5.2734	20719.5	23078.4	194594	232675	7.33951	5.85553	20754.9	23545.4	204927	231068	7.25686	5.69594
2	17084.8	22655.5	243403	278781	9.62929	7.44995	17206.6	23525.9	266737	302135	9.13953	7.03529	17196.8	23922.4	274384	295901	9.35216	7.1118
3	17342	22319.8	241642	289519	9.46651	7.191	17469.2	23374.2	264985	299544	9.25183	7.10208	17492.6	23773	279593	303647	9.45321	7.25856
4	17572.4	22504.2	242350	292998	9.53332	7.27315	17763.4	23652.1	263819	304077	9.30209	7.16542	17752	24083.2	273577	305148	9.19906	7.10607
5	17750.7	22863	242633	295158	9.56806	7.30668	17966.1	24118.1	261716	306859	9.31858	7.20032	17988.5	24531.5	264792	306115	9.15409	6.97717
6	17758.1	22949.9	242890	289233	9.55678	7.29323	17957.7	24194	265034	306437	9.40173	7.24145	17969.9	24647.3	265440	305918	9.13021	6.99337
7	17753	22863.7	242731	295133	9.56814	7.30742	17970.8	24029.8	262488	303768	9.36128	7.23338	17961.5	24515.6	264656	306256	9.14575	7.01521
8	17569.4	22527	242354	293030	9.53566	7.27484	17731.6	23528.2	264075	299540	9.31224	7.17816	17744.8	24025.9	257955	303791	9.15903	7.0545
9	17335.8	22337.5	242211	289532	9.46736	7.1919	17478.5	23227.2	270904	299456	9.49071	7.32262	17473.3	23713.4	265271	300861	9.21683	7.04442
10	17115.9	22667.2	243626	279916	9.60255	7.44459	17214.1	23496.5	275967	292447	9.37865	7.14331	17196.7	23963.2	273211	290999	9.34182	7.11047
11	20151.2	22146.5	204065	198594	6.21755	4.81196	20731.2	23338.4	205219	207401	6.1281	4.74792	20753.6	23473.3	206101	211862	6.29587	4.86896
Long. Girder																		
S1-L	4755.73	NR	31968.1	NR	NR	NR	5105.45	NR	34369.3	NR	NR	NR	4732.45	NR	33582	NR	NR	NR
S1-R	4984.97	NR	39200.6	NR	NR	NR	5063.32	NR	39513.3	NR	NR	NR	4820.44	NR	38117.7	NR	NR	NR
S2-L	4707.7	NR	33866.7	NR	NR	NR	4639.89	NR	37186.1	NR	NR	NR	4718.67	NR	35394.5	NR	NR	NR
S2-R	5080.08	NR	39799.6	NR	NR	NR	5087.51	NR	40304.3	NR	NR	NR	4866.94	NR	39247.4	NR	NR	NR
S3-L	4721.37	NR	33973.9	NR	NR	NR	4588.66	NR	34632.5	NR	NR	NR	5007.36	NR	36144.7	NR	NR	NR
S3-R	4699.26	NR	39007.7	NR	NR	NR	4827.88	NR	40302.1	NR	NR	NR	5060.25	NR	41989.4	NR	NR	NR
S4-L	4661.32	NR	34143.5	NR	NR	NR	4796.73	NR	34920	NR	NR	NR	4985.45	NR	35965.6	NR	NR	NR
S4-R	4678.83	NR	39119.8	NR	NR	NR	4880.98	NR	40475.7	NR	NR	NR	4932.37	NR	40444	NR	NR	NR
S5-L	4709.23	NR	34120	NR	NR	NR	4953.79	NR	36820	NR	NR	NR	4577.62	NR	35729.8	NR	NR	NR
S5-R	4693.49	NR	38791	NR	NR	NR	5077.49	NR	41572.7	NR	NR	NR	4838.41	NR	39848	NR	NR	NR
S6-L	4746.34	NR	34234.2	NR	NR	NR	4559.8	NR	34167.5	NR	NR	NR	4524.27	NR	35732.3	NR	NR	NR
S6-R	4771.79	NR	21583.3	NR	NR	NR	4548.78	NR	21200.3	NR	NR	NR	4643.89	NR	21687.8	NR	NR	NR
S7-L	3878.25	NR	21613	NR	NR	NR	3710.37	NR	21220.2	NR	NR	NR	3746.69	NR	21690.8	NR	NR	NR
S7-R	4720.16	NR	38911.3	NR	NR	NR	4676.62	NR	38957.6	NR	NR	NR	4898.65	NR	40469.3	NR	NR	NR
S8-L	4696.16	NR	34334.8	NR	NR	NR	4428.73	NR	34009	NR	NR	NR	4900.96	NR	37247	NR	NR	NR
S8-R	4699.85	NR	38752.3	NR	NR	NR	4673.45	NR	39024.1	NR	NR	NR	5105.31	NR	41558.5	NR	NR	NR
S9-L	4535.27	NR	33654.1	NR	NR	NR	4595.69	NR	36013.1	NR	NR	NR	4710.92	NR	35935	NR	NR	NR
S9-R	4931.36	NR	39146.5	NR	NR	NR	4705.11	NR	39190.6	NR	NR	NR	4688.15	NR	39323.2	NR	NR	NR
S10-L	4777.57	NR	37057.4	NR	NR	NR	4706.12	NR	35888.4	NR	NR	NR	4705.99	NR	36483.7	NR	NR	NR
S10-R	5081.84	NR	37999.3	NR	NR	NR	5008.66	NR	37477.6	NR	NR	NR	4987.95	NR	37372.5	NR	NR	NR

Table 4.10. Maximum Local Responses – Kobe 100% Scale.

Member ID	LC1						LC6						LC9					
	Shear Long (kN)	Shear Trans (kN)	Moment Long (kN-m)	Moment Trans (kN-m)	Curvature Long (1/m*10^-6)	Curvature Trans (1/m*10^-6)	Shear Long (kN)	Shear Trans (kN)	Moment Long (kN-m)	Moment Trans (kN-m)	Curvature Long (1/m*10^-6)	Curvature Trans (1/m*10^-6)	Shear Long (kN)	Shear Trans (kN)	Moment Long (kN-m)	Moment Trans (kN-m)	Curvature Long (1/m*10^-6)	Curvature Trans (1/m*10^-6)
Columns																		
1	6842.45	8109.37	127960	133318	4.87947	3.4002	7285.29	7692.3	130692	132320	4.90077	3.41558	7330.79	7719.35	129415	132523	4.86118	3.39022
2	6481.78	9435.41	152482	206944	5.68237	4.54798	6689.65	9978.51	159062	212987	5.69277	4.6711	6531.22	9931.94	155022	207516	5.53066	4.48544
3	6583.86	7942.98	147228	206859	5.61823	4.28045	6678.79	8183.46	149464	211335	5.49168	4.30567	6764.32	8076.88	150264	211354	5.49097	4.27324
4	6553.46	7554.41	149248	207191	5.3409	4.43362	6781.09	7790.09	157674	211460	5.66492	4.42625	6841.63	7479.63	164509	211277	5.36275	4.23135
5	6734.85	7237.97	149619	214377	5.93882	4.88066	6927.39	7898.16	144733	213947	5.76678	4.43761	6980.66	7764.29	154784	211400	5.65427	4.39664
6	7354.78	8085.57	145059	209173	5.80052	4.50659	7239.29	8238.39	151609	213804	5.89383	4.42065	7335.8	8353.99	150737	213228	5.94126	4.42391
7	6710.87	7271.82	149848	208405	5.6074	4.48985	6925.32	7351.16	151601	208066	5.61963	4.27139	6934.52	7756.07	155475	211070	5.67654	4.40343
8	6546.59	7534.98	149336	207586	5.32395	4.41378	6808.99	7187.21	161465	206112	5.37757	4.32048	6784.16	7432.73	161450	211116	5.44874	4.23418
9	6626.4	7901.77	147301	207481	5.57534	4.26632	6730.05	7693.34	149645	204934	5.4075	4.28778	6794.6	8046.95	154950	210508	5.42327	4.21701
10	6503.19	9430.09	152067	200593	5.71556	4.56559	6634.11	9634.42	152469	196778	5.50469	4.35323	6534.2	9875.7	153508	196050	5.72868	4.67844
11	6839.1	8105.63	138042	133431	5.64877	4.48034	7289.2	7794.25	143808	141281	5.42658	4.34666	7337.27	7781.06	140961	140867	5.39112	4.32932
Long. Girder																		
S1-L	3975.21	NR	25144.1	NR	NR	NR	4255.66	NR	27520.9	NR	NR	NR	4073.83	NR	26104.7	NR	NR	NR
S1-R	4309	NR	33374.2	NR	NR	NR	4628.39	NR	35081.5	NR	NR	NR	4288.96	NR	33332.9	NR	NR	NR
S2-L	3971.04	NR	26913.8	NR	NR	NR	4239.29	NR	29739.1	NR	NR	NR	4018.86	NR	27379.5	NR	NR	NR
S2-R	4381.58	NR	33736.3	NR	NR	NR	4581.46	NR	34980.6	NR	NR	NR	4370.93	NR	33602.3	NR	NR	NR
S3-L	4071.31	NR	27761.1	NR	NR	NR	4068	NR	29053	NR	NR	NR	4386.35	NR	30572.5	NR	NR	NR
S3-R	4318.78	NR	33099.9	NR	NR	NR	4469.12	NR	34692.3	NR	NR	NR	4691.63	NR	36032.5	NR	NR	NR
S4-L	4061.79	NR	27603.8	NR	NR	NR	4233.91	NR	28521.1	NR	NR	NR	4191.64	NR	28645.4	NR	NR	NR
S4-R	4286.46	NR	33089.7	NR	NR	NR	4550.09	NR	35109.9	NR	NR	NR	4567.19	NR	34606.4	NR	NR	NR
S5-L	4099.45	NR	28170.5	NR	NR	NR	4438.85	NR	30919.7	NR	NR	NR	4154.84	NR	28790.2	NR	NR	NR
S5-R	4304.81	NR	33645.1	NR	NR	NR	4751.93	NR	36420.6	NR	NR	NR	4540.2	NR	34856.8	NR	NR	NR
S6-L	4130.95	NR	28267.3	NR	NR	NR	4009.89	NR	27632.1	NR	NR	NR	4078.52	NR	28269.2	NR	NR	NR
S6-R	4070.1	NR	14421	NR	NR	NR	3965.1	NR	14615.6	NR	NR	NR	4224.2	NR	14525.9	NR	NR	NR
S7-L	3273.88	NR	14433.8	NR	NR	NR	3184.54	NR	14623.3	NR	NR	NR	3319.56	NR	14534.6	NR	NR	NR
S7-R	4319.93	NR	33041.1	NR	NR	NR	4275.36	NR	33031.7	NR	NR	NR	4556.21	NR	34853.8	NR	NR	NR
S8-L	4048.41	NR	28091.1	NR	NR	NR	4035.02	NR	28624.8	NR	NR	NR	4489.57	NR	31457.9	NR	NR	NR
S8-R	4325.47	NR	33449.3	NR	NR	NR	4254.86	NR	32863.8	NR	NR	NR	4708.34	NR	35710.3	NR	NR	NR
S9-L	4097.17	NR	27315	NR	NR	NR	4054.86	NR	27225.2	NR	NR	NR	4031.02	NR	27390.9	NR	NR	NR
S9-R	4357.47	NR	33600.7	NR	NR	NR	4318.24	NR	33535.1	NR	NR	NR	4301.59	NR	33269.4	NR	NR	NR
S10-L	4215.23	NR	27443	NR	NR	NR	3954.54	NR	27187.8	NR	NR	NR	3952.54	NR	27243.4	NR	NR	NR
S10-R	4262.95	NR	31549.7	NR	NR	NR	4223.26	NR	31072.6	NR	NR	NR	4224.54	NR	31223.5	NR	NR	NR

Table 4.11. Maximum Local Responses – Kobe 200% Scale.

Member ID	LC1						LC6						LC9					
	Shear Long (kN)	Shear Trans (kN)	Moment Long (kN-m)	Moment Trans (kN-m)	Curvature Long (1/m*10^-6)	Curvature Trans (1/m*10^-6)	Shear Long (kN)	Shear Trans (kN)	Moment Long (kN-m)	Moment Trans (kN-m)	Curvature Long (1/m*10^-6)	Curvature Trans (1/m*10^-6)	Shear Long (kN)	Shear Trans (kN)	Moment Long (kN-m)	Moment Trans (kN-m)	Curvature Long (1/m*10^-6)	Curvature Trans (1/m*10^-6)
Columns																		
1	13716.3	12749	149482	144193	5.27707	3.58005	13921	14125.1	149748	144340	5.2799	3.57615	13943.6	13961.9	148665	143423	5.24562	3.55812
2	13422.4	14302.9	208222	233769	7.49649	5.69571	13403.4	14061	209223	238697	7.19138	5.34883	13474.3	13674.2	209502	234145	7.51944	5.7105
3	11992.3	12894.7	209583	233683	7.67266	5.83275	12069.2	13393.6	210916	237778	7.7646	5.90552	11954.3	13159.2	208154	237203	7.74261	5.84001
4	12291.3	12865.4	211518	234634	7.24206	5.56671	12112.1	12874.6	230850	249906	8.83907	6.84503	12497.4	13016.5	214639	239571	7.70273	5.88979
5	12986.2	12674.2	212410	234179	7.29024	5.6256	13417.1	12741.2	212563	236406	7.3021	5.63304	13503.9	12899.5	236359	248338	9.02336	6.92826
6	12152.8	12610.5	213599	233568	7.28118	5.61594	12801.9	12626.8	241418	251446	9.1849	7.03165	12319.6	13012.2	238505	248224	9.06442	6.94811
7	12992.4	12673.4	212404	234148	7.28743	5.61305	13491.3	12419.3	213743	233147	7.27847	5.61632	13572.5	12922.8	214488	236729	7.26236	5.60993
8	12268.3	12872.6	211513	234509	7.23472	5.58531	12535.4	12374.9	227362	246263	8.79005	6.79716	12550.3	13138.5	229051	247450	8.66734	6.71856
9	12002	12897.5	210450	233683	7.66997	5.85466	11968.5	13019.3	225467	250427	8.79389	6.82875	11980	13084.5	213370	245759	7.631	5.81854
10	13413.9	14306.3	208258	234168	8.17172	6.13608	13317.9	14082.4	225780	250207	8.7294	6.78618	13351	13497.5	208537	233973	7.61943	5.82539
11	13716.4	12743.6	160327	145102	5.59314	4.45932	13864	12841.2	161418	142795	5.36289	4.32393	13913.5	13825.1	161653	144242	5.38167	4.34128
Long. Girder																		
S1-L	4226.03	NR	27795.7	NR	NR	NR	4377.69	NR	28588.9	NR	NR	NR	4125.19	NR	27588.6	NR	NR	NR
S1-R	4478.98	NR	35831.9	NR	NR	NR	4775.86	NR	37249.1	NR	NR	NR	4451.8	NR	35752.1	NR	NR	NR
S2-L	4407.42	NR	31814.9	NR	NR	NR	4497.64	NR	32479.5	NR	NR	NR	4392.12	NR	32113.5	NR	NR	NR
S2-R	4632.74	NR	37258.8	NR	NR	NR	4766.05	NR	38054.7	NR	NR	NR	4601	NR	37111.5	NR	NR	NR
S3-L	4320.26	NR	31254.8	NR	NR	NR	4554.22	NR	33712	NR	NR	NR	4757.83	NR	34140.9	NR	NR	NR
S3-R	4562.08	NR	36603.5	NR	NR	NR	4694.15	NR	38092.9	NR	NR	NR	4986.02	NR	40205.3	NR	NR	NR
S4-L	4307.38	NR	31231.7	NR	NR	NR	4574.54	NR	33256.7	NR	NR	NR	4476.65	NR	32908.8	NR	NR	NR
S4-R	4611.87	NR	37127.6	NR	NR	NR	4757.13	NR	38166.7	NR	NR	NR	4825.82	NR	38211.5	NR	NR	NR
S5-L	4348.48	NR	31386.2	NR	NR	NR	4691.34	NR	34647.4	NR	NR	NR	4495.87	NR	34563.2	NR	NR	NR
S5-R	4672.97	NR	37416.7	NR	NR	NR	4989.26	NR	39650	NR	NR	NR	4772.22	NR	37986.8	NR	NR	NR
S6-L	4302.84	NR	31195.9	NR	NR	NR	4310.07	NR	32372.1	NR	NR	NR	4396.99	NR	33204.1	NR	NR	NR
S6-R	4339.42	NR	17537.2	NR	NR	NR	4293.02	NR	17962	NR	NR	NR	4553.17	NR	18332.2	NR	NR	NR
S7-L	3529.41	NR	17509.1	NR	NR	NR	3505.91	NR	17948.1	NR	NR	NR	3643.5	NR	18329	NR	NR	NR
S7-R	4583.08	NR	37017.3	NR	NR	NR	4566.1	NR	36805.4	NR	NR	NR	4794.28	NR	38181.5	NR	NR	NR
S8-L	4423.87	NR	31812.3	NR	NR	NR	4337.7	NR	32997.6	NR	NR	NR	4715.96	NR	35681.2	NR	NR	NR
S8-R	4527.46	NR	36818.9	NR	NR	NR	4500.57	NR	36546.3	NR	NR	NR	4943.07	NR	39369.2	NR	NR	NR
S9-L	4336.16	NR	31686.5	NR	NR	NR	4279.28	NR	33077.4	NR	NR	NR	4405.32	NR	32413.8	NR	NR	NR
S9-R	4626.66	NR	37728.1	NR	NR	NR	4520.3	NR	36870.5	NR	NR	NR	4553.61	NR	37056.6	NR	NR	NR
S10-L	4185.51	NR	30762.5	NR	NR	NR	4237.82	NR	32213.2	NR	NR	NR	4194.21	NR	30462.3	NR	NR	NR
S10-R	4372.06	NR	32576.7	NR	NR	NR	4328.48	NR	32365.3	NR	NR	NR	4340.75	NR	32532.5	NR	NR	NR

Table 4.12. Maximum Local Responses – Loma Prieta 100% Scale.

Member ID	LC1						LC6						LC9					
	Shear Long (kN)	Shear Trans (kN)	Moment Long (kN-m)	Moment Trans (kN-m)	Curvature Long (1/m*10^-6)	Curvature Trans (1/m*10^-6)	Shear Long (kN)	Shear Trans (kN)	Moment Long (kN-m)	Moment Trans (kN-m)	Curvature Long (1/m*10^-6)	Curvature Trans (1/m*10^-6)	Shear Long (kN)	Shear Trans (kN)	Moment Long (kN-m)	Moment Trans (kN-m)	Curvature Long (1/m*10^-6)	Curvature Trans (1/m*10^-6)
Columns																		
1	18090.3	17832.4	164586	169323	6.17969	4.56933	18371.3	17455.8	166636	178540	6.29184	4.66569	18377.1	17132.1	165050	176353	6.24588	4.61246
2	16081	16619.4	261783	265299	9.39466	7.21671	16266.1	17074.8	227660	260074	8.0638	6.25632	16267.6	16262.7	227321	244129	7.49701	5.74717
3	17865.4	16149.3	262337	273088	9.45647	7.29856	18006.7	16484.6	227950	268104	7.97688	6.12987	18001	15949.5	225390	268975	8.01144	6.1399
4	18190.1	16317.4	261967	271696	9.45463	7.30875	18585.7	16420.9	228535	241843	7.54876	5.71088	18612.1	15978.6	230277	241309	7.51171	5.69014
5	18816.4	16905.2	262771	264270	9.28755	7.15381	19247.4	17031.7	227535	268825	8.09598	6.19242	19264.5	16671.9	230478	242194	7.61735	5.7205
6	18737.3	17212.7	259179	260556	9.19193	7.06837	19191.5	17021.1	231792	252511	7.82044	6.02074	19203.1	16992.4	272540	276239	9.08128	6.90757
7	18816.5	16893.4	266148	269914	9.38724	7.17197	19251.3	16476.6	228634	245295	7.59148	5.68077	19264.1	16709.1	229791	242830	7.59818	5.72358
8	18190.1	16317.3	262716	281712	9.34399	7.31966	18599.7	15877.7	228366	243601	7.55562	5.71659	18611.6	16071.9	227104	240894	7.60195	5.7456
9	17865.4	16149.3	263859	275056	9.4392	7.28442	18004	15787.2	227543	242109	7.46174	5.71401	18012.3	15952.5	231866	258731	7.88486	6.02266
10	16009.3	16614.4	259004	263083	9.1868	7.09524	16232.4	16199.6	226313	243698	7.52181	5.77986	16254.9	16471.3	270091	279718	9.02614	6.81032
11	17982.1	17804.2	180699	161837	5.57519	4.31428	18246.3	17425.3	181121	164967	5.50602	4.269	18302.6	17404.2	181250	166101	5.45412	4.22745
Long. Girder																		
S1-L	4570.9	NR	30467.4	NR	NR	NR	4576.52	NR	30361.2	NR	NR	NR	4280.99	NR	28825.7	NR	NR	NR
S1-R	4587.57	NR	36808.4	NR	NR	NR	4820.43	NR	37936.3	NR	NR	NR	4492.72	NR	36370.3	NR	NR	NR
S2-L	4566.76	NR	33468.1	NR	NR	NR	4519.04	NR	34720.3	NR	NR	NR	4289.43	NR	33399.5	NR	NR	NR
S2-R	4764.7	NR	38077.3	NR	NR	NR	4868.81	NR	38914.4	NR	NR	NR	4643.47	NR	37883.7	NR	NR	NR
S3-L	4847.43	NR	34474	NR	NR	NR	4460.22	NR	34690.6	NR	NR	NR	4765.03	NR	36291.9	NR	NR	NR
S3-R	4634.89	NR	37473.2	NR	NR	NR	4737.63	NR	38558	NR	NR	NR	5024.07	NR	40431.5	NR	NR	NR
S4-L	4577.96	NR	33654.4	NR	NR	NR	4687.38	NR	33943.3	NR	NR	NR	4671.77	NR	33364.5	NR	NR	NR
S4-R	4652.22	NR	37243.8	NR	NR	NR	4802.48	NR	38741.8	NR	NR	NR	4864.24	NR	38454.5	NR	NR	NR
S5-L	4720.05	NR	35298.8	NR	NR	NR	4827.54	NR	34980.8	NR	NR	NR	4609.41	NR	34241.7	NR	NR	NR
S5-R	4758.32	NR	37840.4	NR	NR	NR	5000.92	NR	39668.2	NR	NR	NR	4805.48	NR	38383.4	NR	NR	NR
S6-L	4744.11	NR	34435.6	NR	NR	NR	4344.72	NR	32975.5	NR	NR	NR	4440.88	NR	33934.9	NR	NR	NR
S6-R	4678.54	NR	19763.4	NR	NR	NR	4348.49	NR	19178.4	NR	NR	NR	4602.33	NR	19737.6	NR	NR	NR
S7-L	3901.85	NR	19751.9	NR	NR	NR	3575.32	NR	19161.9	NR	NR	NR	3702.69	NR	19725.2	NR	NR	NR
S7-R	4606.92	NR	37075.9	NR	NR	NR	4575.35	NR	37009	NR	NR	NR	4782.66	NR	38419.5	NR	NR	NR
S8-L	4551.16	NR	33239.8	NR	NR	NR	4208.02	NR	32117.1	NR	NR	NR	4802.79	NR	36417.7	NR	NR	NR
S8-R	4749.99	NR	37743.9	NR	NR	NR	4648.75	NR	37235	NR	NR	NR	5099.81	NR	40443.3	NR	NR	NR
S9-L	4644.09	NR	34045.8	NR	NR	NR	4414.33	NR	31729.8	NR	NR	NR	4525.49	NR	34106.8	NR	NR	NR
S9-R	4784.92	NR	38203.2	NR	NR	NR	4637.13	NR	37391.4	NR	NR	NR	4614.36	NR	37525.6	NR	NR	NR
S10-L	4539.52	NR	33100.4	NR	NR	NR	4315.75	NR	31373.9	NR	NR	NR	4301.34	NR	31641.1	NR	NR	NR
S10-R	4585.58	NR	34549.2	NR	NR	NR	4424.55	NR	33518.6	NR	NR	NR	4384.02	NR	33416.5	NR	NR	NR

Table 4.13. Maximum Local Responses – Loma Prieta 200% Scale.

Member ID	LC1 Shear Long (kN)	LC1 Shear Trans (kN)	LC1 Moment Long (kN-m)	LC1 Moment Trans (kN-m)	LC1 Curvature Long (1/m*10^-6)	LC1 Curvature Trans (1/m*10^-6)	LC6 Shear Long (kN)	LC6 Shear Trans (kN)	LC6 Moment Long (kN-m)	LC6 Moment Trans (kN-m)	LC6 Curvature Long (1/m*10^-6)	LC6 Curvature Trans (1/m*10^-6)	LC9 Shear Long (kN)	LC9 Shear Trans (kN)	LC9 Moment Long (kN-m)	LC9 Moment Trans (kN-m)	LC9 Curvature Long (1/m*10^-6)	LC9 Curvature Trans (1/m*10^-6)
									Columns									
1	11039.9	10544.1	135087	140500	5.11384	3.81802	11305.2	11474.3	138647	146522	5.2021	3.88601	11336.9	11792.1	137200	146071	5.11743	3.81271
2	9217.77	9975.57	163239	207450	5.84277	4.33635	10080.1	10715.6	172205	207610	5.96079	4.46486	10003.5	9647.59	169645	207322	5.99219	4.38254
3	10197	8599.32	165228	210016	5.65301	4.33877	10649	9333.28	205387	236119	7.25016	5.62403	10741.7	9352.97	205407	234324	7.22202	5.6023
4	9636.05	9588.47	169382	210595	5.75228	4.39446	9661.1	9978.15	206843	239960	7.23388	5.64704	9709.17	10345.2	206611	235611	7.21229	5.58597
5	10438.3	9052.15	181871	209318	5.90334	4.3139	10676.4	9788.66	185150	210743	6.01122	4.44738	10709.6	9986.87	182819	210623	5.92948	4.36553
6	11409.9	10587.3	183095	218731	6.75596	5.2808	11052.3	10477.1	189745	211515	5.86136	4.39481	11015.7	10703.9	188377	210965	5.84681	4.46908
7	10444.9	9058.73	180419	209269	5.90949	4.31781	10633.9	9619.61	220075	234284	7.37663	5.64273	10673.5	9903.76	221710	244823	7.56149	5.80688
8	9634.6	9588.12	169381	210572	5.7305	4.40536	9720.39	9873.2	213394	240924	7.2062	5.62137	9724.77	9959.28	207770	236367	7.36674	5.72358
9	10195.4	8598.25	167180	209951	5.63985	4.33742	10633.8	9023.38	210641	238619	7.2221	5.61405	10720.3	9013.87	209664	234911	7.2859	5.62821
10	9187.01	9990.2	161952	207631	5.85199	4.34094	10071.4	9425.46	167786	206890	5.9542	4.36225	10006.6	9417.3	170362	207614	6.00885	4.38921
11	11039.7	10542.9	157986	148487	5.64344	4.37684	11319.1	11444.8	164824	157860	5.49628	4.27008	11343.3	11281.5	167561	159726	5.53455	4.28566
									Long. Girder									
S1-L	4250.15	NR	26733.9	NR	NR	NR	4350.67	NR	27643.7	NR	NR	NR	4020.73	NR	25793.5	NR	NR	NR
S1-R	4335.4	NR	33574	NR	NR	NR	4659.17	NR	35384.8	NR	NR	NR	4300.83	NR	33400.8	NR	NR	NR
S2-L	4304.55	NR	29791.6	NR	NR	NR	4432.43	NR	31755.6	NR	NR	NR	4238.88	NR	31061	NR	NR	NR
S2-R	4369.46	NR	33278.6	NR	NR	NR	4629.46	NR	34991.8	NR	NR	NR	4421.39	NR	33926.7	NR	NR	NR
S3-L	4414.68	NR	30501.2	NR	NR	NR	4499.63	NR	32464.9	NR	NR	NR	4570.18	NR	34532.5	NR	NR	NR
S3-R	4311.09	NR	33595.5	NR	NR	NR	4479.39	NR	35027.5	NR	NR	NR	4731.2	NR	36740.1	NR	NR	NR
S4-L	4178.14	NR	29519.5	NR	NR	NR	4628.78	NR	32375.1	NR	NR	NR	4537.59	NR	32164.8	NR	NR	NR
S4-R	4304.15	NR	33305.9	NR	NR	NR	4553.26	NR	35232.7	NR	NR	NR	4620.82	NR	35182.5	NR	NR	NR
S5-L	4488.74	NR	31948.3	NR	NR	NR	4767.62	NR	35595.6	NR	NR	NR	4536.66	NR	33955.1	NR	NR	NR
S5-R	4373.2	NR	35128	NR	NR	NR	4737.1	NR	36519	NR	NR	NR	4522.89	NR	34869.6	NR	NR	NR
S6-L	4428.07	NR	30998.6	NR	NR	NR	4339.99	NR	31534.5	NR	NR	NR	4469.16	NR	33180.4	NR	NR	NR
S6-R	4114.69	NR	16532	NR	NR	NR	4301.54	NR	19004.5	NR	NR	NR	4584.82	NR	18552.6	NR	NR	NR
S7-L	3402.83	NR	16541.3	NR	NR	NR	3527.87	NR	19001.7	NR	NR	NR	3663	NR	18561.4	NR	NR	NR
S7-R	4330.45	NR	33233.7	NR	NR	NR	4332.01	NR	33915.3	NR	NR	NR	4590.55	NR	35539.9	NR	NR	NR
S8-L	4309.83	NR	28752	NR	NR	NR	4353.25	NR	33146.4	NR	NR	NR	4753.57	NR	34902.7	NR	NR	NR
S8-R	4309.83	NR	33301.9	NR	NR	NR	4308.07	NR	33607.5	NR	NR	NR	4758.58	NR	36250.9	NR	NR	NR
S9-L	4318.04	NR	29812.7	NR	NR	NR	4294.22	NR	30476.6	NR	NR	NR	4332.22	NR	30671.5	NR	NR	NR
S9-R	4353.26	NR	33767.9	NR	NR	NR	4337.66	NR	33660.5	NR	NR	NR	4340.04	NR	33699.5	NR	NR	NR
S10-L	4207.2	NR	29001.9	NR	NR	NR	4137.79	NR	28556.2	NR	NR	NR	4144.47	NR	28549.6	NR	NR	NR
S10-R	4282.96	NR	31674.7	NR	NR	NR	4259.17	NR	31511	NR	NR	NR	4265.45	NR	31581.1	NR	NR	NR

Table 4.14. Maximum Global Responses – Northridge 100% Scale.

Node	LC1				LC6				LC9			
	Displacement (mm)		Acceleration (m/s2)		Displacement (mm)		Acceleration (m/s2)		Displacement (mm)		Acceleration (m/s2)	
	long.	trans.	long.	trans.	long.	trans.	long.	trans.	long.	trans.	long.	trans.
1	220.173	291.638	18.1297	20.7431	224.07	283.923	18.106	21.7147	224.291	274.967	18.1087	20.2731
2	226.489	289.063	17.9711	17.7602	230.575	281.393	18.1384	17.0194	230.771	272.699	18.1432	16.8891
3	230.808	286.113	18.0509	18.176	236.204	278.63	18.1385	16.3869	236.351	270.187	18.1435	16.0106
4	230.928	283.275	18.0482	17.5288	235.722	276.194	18.1384	16.9118	235.793	267.833	18.1434	16.1048
5	234.024	281.201	18.0472	17.9692	239.76	274.362	18.1353	19.5949	239.985	266.171	18.1398	16.684
6	234.013	280.436	18.0561	24.6424	239.69	273.54	18.1349	18.2082	240.004	265.658	18.1393	21.5007
7	230.932	281.198	18.0549	17.8171	235.485	273.957	18.1399	16.0272	235.808	266.396	18.1439	16.5026
8	230.816	283.277	18.0587	17.5404	235.87	275.447	18.1394	15.7514	236.362	268.144	18.1439	16.2389
9	226.518	286.131	17.9451	18.1577	231.274	277.687	18.1378	16.0623	230.801	270.513	18.1444	16.0502
10	220.184	289.104	18.0018	17.7816	224.196	279.945	18.1004	17.026	224.278	272.921	18.1095	16.868
11	220.18	291.704	18.1302	20.7981	224.195	282.021	18.1067	20.276	224.277	275.002	18.1083	20.3591

Table 4.15. Maximum Global Responses – Northridge 200% Scale.

Node	LC1				LC6				LC9			
	Displacement (mm)		Acceleration (m/s2)		Displacement (mm)		Acceleration (m/s2)		Displacement (mm)		Acceleration (m/s2)	
	long.	trans.	long.	trans.	long.	trans.	long.	trans.	long.	trans.	long.	trans.
1	422.714	517.01	24.7193	23.6438	427.985	551.491	24.8429	27.0323	427.782	543.11	24.8501	22.0936
2	426.462	517.437	24.7217	21.3772	431.459	550.132	24.8443	22.0753	431.767	543.835	24.8518	20.7823
3	429.899	517.826	24.7251	22.58	435.35	548.392	24.8469	22.4465	434.763	544.538	24.8537	21.6196
4	431.001	518.226	24.7259	22.9845	436.201	546.241	24.8473	22.4698	436.986	545.091	24.8553	22.1671
5	432.085	518.566	24.7284	22.7514	437.257	543.647	24.8488	24.1219	437.664	545.463	24.8563	22.2856
6	432.34	518.698	24.7279	26.4511	436.941	540.621	24.8485	22.0339	438.063	545.639	24.8567	24.5155
7	430.778	518.548	24.7258	22.7452	436.581	537.316	24.8478	21.9863	437.229	545.547	24.8556	22.2459
8	429.592	518.194	24.7248	22.9748	434.913	534.079	24.8467	21.9043	435.606	545.25	24.8546	22.1465
9	426.417	517.781	24.7227	22.5685	432.408	531.195	24.8454	21.4894	432.068	544.76	24.8522	21.7005
10	422.676	517.384	24.7209	21.3646	427.834	528.818	24.843	20.6958	428.194	544.113	24.8505	20.8681
11	422.675	516.948	24.7191	23.6489	427.834	526.734	24.843	21.9246	428.194	543.457	24.8505	23.3678

Table 4.16. Maximum Global Responses – Kobe 100% Scale.

Node	LC1 Displacement (mm)		LC1 Acceleration (m/s2)		LC6 Displacement (mm)		LC6 Acceleration (m/s2)		LC9 Displacement (mm)		LC9 Acceleration (m/s2)	
	long.	trans.	long.	trans.	long.	trans.	long.	trans.	long.	trans.	long.	trans.
1	220.77	336.095	20.5924	28.031	218.571	334.959	20.7562	26.1702	220.43	341.439	20.7711	26.0713
2	265.195	333.987	19.2497	21.8164	284.984	331.812	19.7819	21.6328	283.869	339.63	19.2868	23.3982
3	261.045	331.542	20.888	21.072	304.214	328.245	21.2213	20.5624	303.634	337.526	21.6827	20.069
4	266.3	329.193	19.7873	20.0552	305.785	324.813	20.5616	19.3183	301.246	335.384	20.0416	17.9761
5	284.246	327.52	21.0722	19.0784	317.917	322.511	21.543	19.5075	319.615	333.621	22.3597	17.1697
6	284.63	326.994	20.5083	20.0989	315.635	321.47	20.98	18.1445	320.202	332.723	22.0692	17.5461
7	266.145	327.522	19.8137	19.0643	304.331	321.284	21.2745	17.872	302.896	332.603	21.0173	18.1102
8	261.039	329.2	20.4293	20.0061	300.956	321.428	21.0604	18.3273	302.355	333.759	20.462	19.9144
9	264.922	331.55	19.6444	21.127	283.654	322.202	19.183	20.3455	283.181	335.751	19.3969	21.1202
10	221.159	333.997	22.4902	21.9048	219.418	323.187	21.4383	22.3114	220.248	338.034	21.1615	22.3699
11	220.861	336.09	20.5787	27.9978	219.414	324.035	20.6994	23.9808	220.248	340.086	20.5854	23.4458

Table 4.17. Maximum Global Responses – Kobe 200% Scale

Node	LC1 Displacement (mm)		LC1 Acceleration (m/s2)		LC6 Displacement (mm)		LC6 Acceleration (m/s2)		LC9 Displacement (mm)		LC9 Acceleration (m/s2)	
	long.	trans.	long.	trans.	long.	trans.	long.	trans.	long.	trans.	long.	trans.
1	122.818	158.586	10.9737	13.9866	127.837	170.99	11.5296	15.9968	128.317	160.334	11.1577	15.8894
2	125.143	158.688	10.4641	12.224	129.559	169.513	11.4144	12.5048	130.079	161.024	11.3599	12.9179
3	126.474	158.63	10.9184	12.1794	130.327	167.648	11.0288	12.6313	130.736	161.468	11.0676	12.5226
4	129.241	158.469	11.0576	11.6836	133.414	165.437	11.7255	12.3095	133.757	161.519	11.693	12.0023
5	129.764	158.666	10.7749	12.5503	134.135	162.715	10.8223	12.6439	134.403	161.526	10.7358	12.4405
6	129.83	158.814	10.767	12.9141	134.155	160.065	10.91	12.7983	134.438	161.537	10.9568	12.7415
7	129.376	158.677	11.0974	12.5843	133.636	157.312	11.2486	12.2959	133.834	161.63	11.1822	12.4268
8	126.642	158.498	10.8513	11.7487	130.469	154.814	11.0251	11.5919	130.803	161.665	11.0176	11.9377
9	125.33	158.652	10.4747	12.216	129.638	152.685	10.9823	11.8426	130.149	161.561	11.3729	12.4574
10	122.97	158.691	10.3778	12.2146	128.211	150.865	10.7215	12.7505	128.506	161.01	10.6466	12.897
11	122.723	158.567	10.9395	13.9902	128.095	149.171	11.1773	14.8811	128.386	160.245	11.0822	15.7895

Table 4.18. Maximum Global Responses – Loma Prieta 100% Scale.

Node	LC1				LC6				LC9			
	Displacement (mm)		Acceleration (m/s2)		Displacement (mm)		Acceleration (m/s2)		Displacement (mm)		Acceleration (m/s2)	
	long.	trans.	long.	trans.	long.	trans.	long.	trans.	long.	trans.	long.	trans.
1	145.243	165.033	15.4967	16.2067	147.999	171.773	16.5199	16.9416	148.238	164.692	16.2405	16.4247
2	147.687	164.9	16.8363	15.0463	150.913	170.721	17.8373	14.8667	151.083	164.78	17.6233	14.6924
3	149.406	165.036	18.0338	14.5144	152.698	169.797	17.7442	15.5009	152.79	165.145	17.8242	16.0599
4	152.098	165.553	16.0938	15.2267	155.435	169.131	16.4774	16.6474	155.655	165.751	16.4812	17.0599
5	153.403	166.022	17.6241	14.3871	156.941	168.396	17.6083	16.1842	157.053	166.228	17.3691	16.4378
6	153.426	166.201	17.3278	14.7155	156.952	167.286	17.4853	16.4443	157.073	166.462	17.6411	16.9073
7	152.098	166.019	16.1601	14.3982	155.448	165.776	15.9866	15.7566	155.662	166.333	16.023	16.1117
8	149.513	165.557	17.1067	15.3135	152.758	164.043	17.2487	16.4158	152.888	165.841	17.2617	16.5182
9	147.807	165.056	16.1149	14.571	151.021	162.236	16.6822	15.356	151.137	165.114	16.6537	15.3428
10	145.28	164.929	15.3265	15.0201	148.161	160.729	15.9113	14.3049	148.277	164.606	15.8868	14.6136
11	145.154	165.04	15.5009	16.2427	148.022	159.622	16.3261	15.6704	148.143	164.325	16.2378	16.204

Table 4.19. Maximum Global Responses – Loma Prieta 200% Scale.

Node	LC1				LC6				LC9			
	Displacement (mm)		Acceleration (m/s2)		Displacement (mm)		Acceleration (m/s2)		Displacement (mm)		Acceleration (m/s2)	
	long.	trans.	long.	trans.	long.	trans.	long.	trans.	long.	trans.	long.	trans.
1	264.389	272.622	23.4207	26.5507	276.593	280.476	23.8302	24.9355	275.791	268.434	23.8784	23.8155
2	315.641	273.261	23.7626	19.2035	325.263	279.987	22.3963	19.5038	323.419	269.462	22.4035	18.7076
3	330.49	273.86	23.0078	21.3331	332.701	279.209	22.4536	19.0579	329.384	270.481	22.4447	20.0264
4	321.998	274.318	22.4954	23.6247	330.335	278.018	22.4823	20.1828	327.975	271.388	22.4813	20.6076
5	332.32	274.529	22.5585	23.4402	340.503	276.263	22.4869	23.7959	338.808	271.916	22.4878	22.5551
6	332.264	274.591	22.4913	30.9524	340.029	274.003	22.5093	28.6083	338.049	272.225	22.5041	27.0224
7	321.941	274.556	22.6067	24.0565	328.535	271.505	22.5194	24.1969	328.366	272.349	22.5146	22.2059
8	330.567	274.363	23.0276	23.4175	333.045	268.845	22.5375	21.5324	331.101	272.164	22.552	21.9325
9	315.708	273.914	23.2407	21.3233	320.775	266.129	22.5934	20.1864	322.911	271.551	22.5981	20.4836
10	264.261	273.324	22.7976	19.2562	274.668	263.473	22.3295	20.4392	276.248	270.599	22.3201	18.9951
11	264.229	272.697	23.4237	26.5554	274.616	261.065	23.859	23.844	276.18	269.704	23.8413	23.4235

The behavioral graphs plotted for the additional seismic analysis conducted in this section include displacement time-histories, force-displacement relationships, and moment-curvature relation-ships of selected columns in the longitudinal and transverse directions. The displacement time-history graphs demonstrated the displacement amplitudes and trends along with residual dis-placements at the end of the ground motion duration. The force-displacement and moment-cur-vature relationships graphs serve to demonstrate the full range of response of the prototype HSR bridge system throughout the course of the ground motions whether it remains linear elastic or started getting nonlinear. The graphs were plotted for the data retrieved from the prototype HSR bridge response under the three earthquakes at 100% and 200% amplification.

Displacement time-histories for Load Cases 1, 6, and 9 under all three ground motions are shown in Figure 4.65 through Figure 4.68 for the transverse and longitudinal directions and at 100% and 200% seismic intensity. Each of the four figures provides nine subplots where each subplot com-pares the displacement at the girder end node above columns #3, #6, and #11 to visually assess the displacement trends of the interior and exterior columns. The nine subplots represent the three different ground motion records × the three train loading cases. Observing the figures for the 100% scale, the time-histories for the Kobe and Loma Prieta earthquakes oscillated about the 0 mm displacement mark for both directions, i.e., no residual displacements were observed to indicate the columns among other components stayed linear throughout the ground motion du-ration. The time-histories for the Northridge earthquake were shifted to oscillate about the 40 mm mark for the longitudinal direction and about the 110 mm mark for the transverse direction. These are residual displacements, i.e., plastic damage, which indicate that either the columns underwent nonlinear inelastic behavior or other components simulating the train-track-super-structure-substructure interaction might have yielded. However, given that the 200% run of the Northridge record rendered higher force demands in the columns, the columns were obviously well below their capacities as a result of the 100% run. Therefore, the residual displacements ob-served in the 100% or 200% Northridge earthquake cases are not likely associated with the col-umns, which motivated an additional analysis case at 300% as discussed later in this section. It is also noted from the Figure 4.64 through Figure 4.67 that the overall displacement trends for the three load cases were nearly identical between Load Case 1, 6, and 9 for each direction barring any apparent variations in the displacement amplitudes after the 8 second mark.

For the 200% scale, larger residual drift between the interior and exterior columns become appar-ent for all three ground motions in the longitudinal direction. The relative drift stayed similar be-tween the three load cases for the Northridge and Loma Prieta earthquakes, and showed a slight increase for the load cases with train loading for the Kobe earthquake. The transverse displace-ments heavily increased for the Northridge earthquake, oscillating about the 240 mm line for the load cases with train loading and the 140 mm line for the load case with no train loading. In comparison, the Kobe and Loma Prieta earthquakes had small residual transverse displacements which were nearly consistent among the load cases.

Based on the displacement time-history graphs for both scales, the addition of train loading had higher influence towards the displacement trends for ground motions scaled at 200%. The dis-placement trends under the Loma Prieta earthquake lacked any variation among the load cases

for either scale, but the Northridge and Kobe earthquakes showed definite signs of increased residual displacement for the load cases with train loading under the 200% earthquakes. Displacement time-histories for Load Case 6 and 9 also oscillate at a larger magnitude towards the middle to end of the ground motion for the transverse direction which proves the addition of train loading does increase the magnitude of bridge vibration despite the peak displacement values being relatively similar for all the load cases.

Similar to the displacement time-history graphs, the force-displacement and moment-curvature behavioral graphs were compiled in four figures, with each figure presenting a respective direction and ground motion scale. Observing the force-displacement relationships shown in Figure 4.69 and Figure 4.71 for columns #6, #8, and #11 and the moment-curvature relationships shown in Figure 4.73 and Figure 4.75 for columns #1, #6, and #10, the columns showed glimpses of inelastic response but stayed relatively linear elastic. However, the columns clearly demonstrate signs of nonlinearity under the 200% scale Northridge earthquake in the force-displacement graphs for both directions, shown in Figure 4.70 and Figure 4.72, where larger or fatter hysteresis loops were recorded. The moment-curvature graphs for the 200% scale ground motions presented in Figure 4.74 and Figure 4.76 also showed instances of large nonlinearity for all of the ground motions. In comparison to the transverse moment-curvature graphs, the longitudinal moment-curvature relationship behaved along a lower slope. This can be assumed to be a result of the geometric orientation of the rectangular pier columns providing higher resistance to rotation in the transverse direction compared to the longitudinal direction.

Although the force-displacement behaviors were similar among the three load cases, the moment-curvature behaviors showed that the columns experienced larger responses for Load Cases 6 and 9 for the ground motions scaled at 200%, which was an observation also seen in the displacement time-histories. In general, the influence of train loading becomes more apparent when the columns start to experience some nonlinearity due to large seismic loading. This can be tied to the inherent design of HSR bridges being very stiff and high capacity, which results in a bridge that can behave consistently regardless of various loading scenarios but only up to a certain seismic demand level. However, further research is necessary to fully validate this observation and tie it to proper seismic design and assessment framework.

Regardless of the onset of nonlinear column behavior shown under the 200% scale runs, it is not conclusive whether any of the columns reached its ultimate capacity already. Thus, it was of interest to pick the most damaging ground motion out of the three utilized ones, i.e., the Northridge record, and apply it at 300% scale. This mainly aimed at understanding whether the residual displacements observed at least at the 200% scale were related to the column's nonlinear behavior. It was also desired to confirm whether the column reached its capacity during the 200% run or still had more capacity that can be rendered at an even larger seismic intensity. The displacement time-history, force-displacement, and moment-curvature relationships are shown in both the transverse and longitudinal directions under the 300% Northridge record in Figure 4.77 through Figure 4.82. Observing the displacement time-histories, it can be confirmed that the columns approached their capacity and might have failed under excessive nonlinear demands that reached about 1400 mm as suggested by the residual displacement values that surpassed 500 mm for both directions. Unlike the response at 100% and 200% scales, no other bridge component is likely to lead to 500 mm residual displacements except the main lateral support system, i.e., columns.

The force-displacement and moment-curvature graphs for both directions confirm the large non-linear response and inelasticity within the columns as demonstrated through the large hysteresis loops that stray from the core elastic behavior. Analyzing the seismic performance of the prototype HSR bridge under the 300% scale further supports the perspective that a by-product of the HSR bridge column's large stiffness requirement is the large force and moment capacity that can help the columns remain almost linear elastic under moderate seismic intensities. In other words, the large column nonlinearities were not observed until the 300% intensity where the force and moment values suggest that these are at the capacity of the analyzed columns. A formal design guideline and code would be necessary in the near future to do a proper seismic assessment of HSR bridge behavior under simultaneous train and seismic loading, which is a future work that can stem from the research presented in this study.

Finally, the force-deformation behavior of selected track-bridge interaction elements for the prototype HSR bridge were obtained and plotted under the Northridge record scaled at 300% and under the same train loading cases. Force and deformation were output for the zero-length elements idealizing the fasteners, CA layers, and sliding layers at locations directly above columns #4 and #6, which were selected arbitrarily. The force-deformation behavior for fasteners supporting rail 1 and rail 2 of track 1 is shown in Figure 4.83 and Figure 4.84 respectively. Similarly, the force-deformation behavior for the CA layers supporting track 1, and the sliding layers supporting track 1 at the locations indicated above are plotted in Figure 4.85 and Figure 4.86, respectively. These graphs compare the demand and performance of the interaction elements under three levels of seismic intensity.

From this brief analysis, it is apparent that the fasteners and CA layers operate within its elastic capacities which were defined as part of the modeling of the material behaviors (see Figure 4.30 and Figure 4.31. Contrarily, the sliding layer has clearly exceeded its yield capacity and is deforming heavily due to the lack of capacity. The sliding layer in a ballastless track system connects the track system to the bridge deck and is prone to be firstly damaged under earthquakes. The sliding layer is also implemented in ballastless track systems to effectively dissipate seismic energy through the damage of the layer (Guo et al. 2020). However, the damage observed in the sliding layer for this study is excessive and does raise some concern. An obvious issue could be the lack of resistance provided in the interaction layers of the track system due to the large sub-spans or intervals used to model elements and springs along the length of the bridge. The reference study that the prototype track-bridge system was based off modeled each girder span as 50 elements of identical lengths opposed to the 10 elements used for this study, which was a limitation to expedite the modeling process given the overall goal that the model in-place is for demonstration purposes. This modeling limitation significantly decreased the number of springs modeled per interaction layer because the springs were modeled at intervals five times larger than that of the reference study for instance. Nonetheless, it is again noted that the provided analysis in this section or previous ones were intended to only demonstrate the capabilities associated with the developed HSR bridge system model, and touch on the potential response metrics that could be assessed against a formal future design framework.
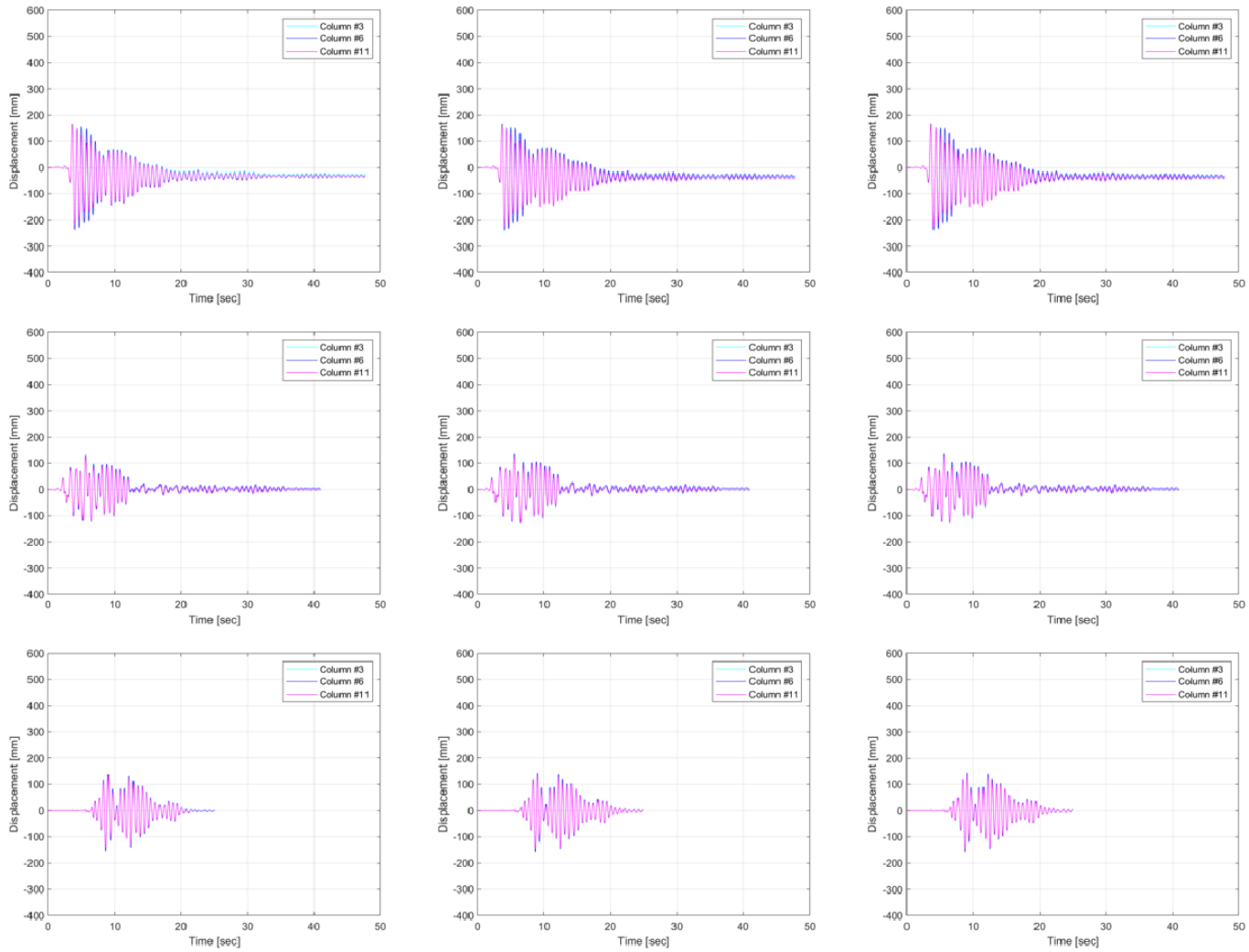
Figure 4.65. Longitudinal displacement time-history for columns #3, #6, and #11 at 100% – (Row: (1) Northridge, (2) Kobe, and (3) Loma Prieta, Column: (1) Load Case 1, (2) Load Case 6, and (3) Load Case 9).
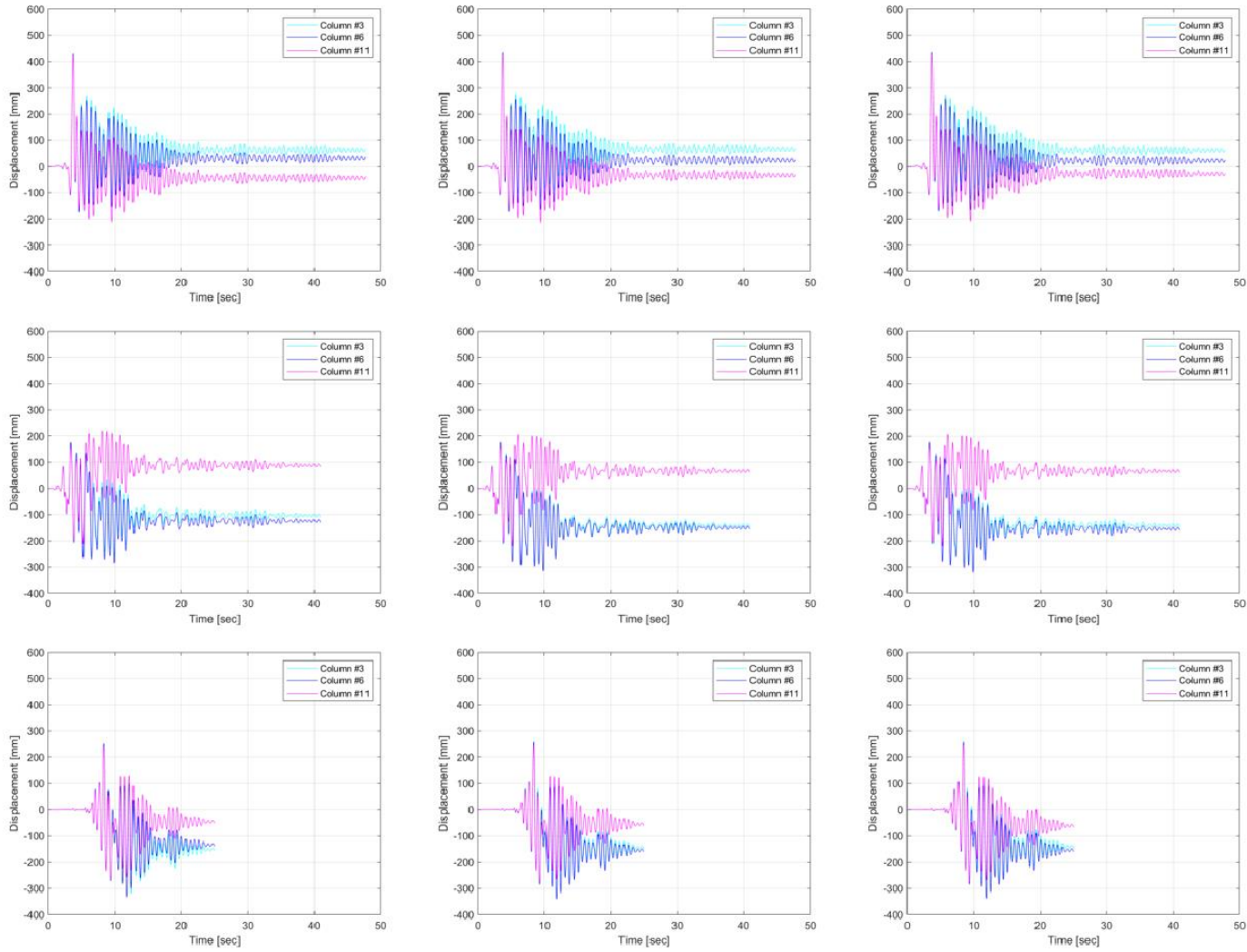
Figure 4.66. Longitudinal displacement time-history for columns #3, #6, and #11 at 200% – (Row: (1) Northridge, (2) Kobe, and (3) Loma Prieta, Column: (1) Load Case 1, (2) Load Case 6, and (3) Load Case 9).

171
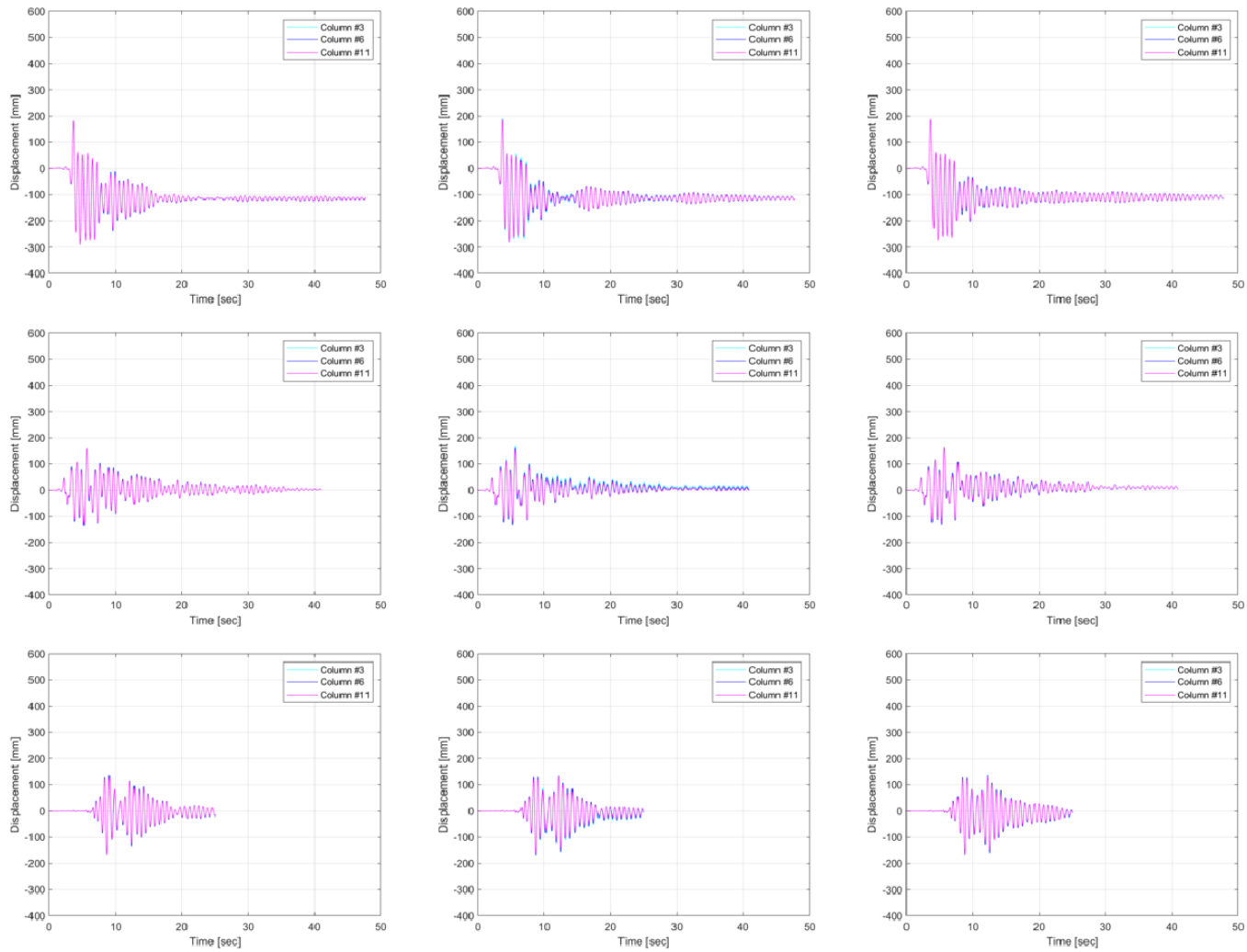
Figure 4.67. Transverse displacement time-history for columns #3, #6, and #11 at 100% – (Row: (1) Northridge, (2) Kobe, and (3) Loma Prieta, Column: (1) Load Case 1, (2) Load Case 6, and (3) Load Case 9).
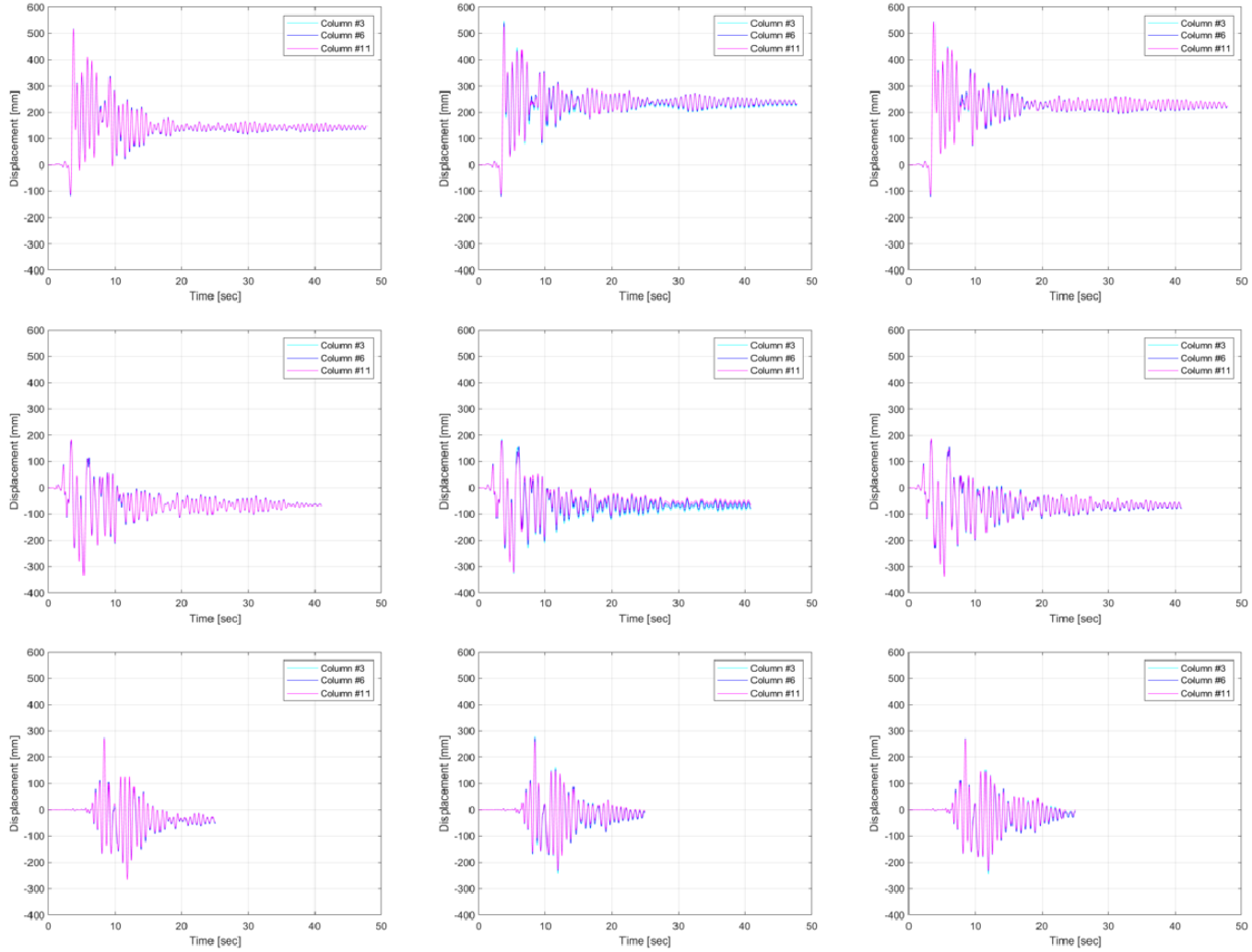
Figure 4.68. Transverse displacement time-history for columns #3, #6, and #11 at 200% – (Row: (1) Northridge, (2) Kobe, and (3) Loma Prieta, Column: (1) Load Case 1, (2) Load Case 6, and (3) Load Case 9).
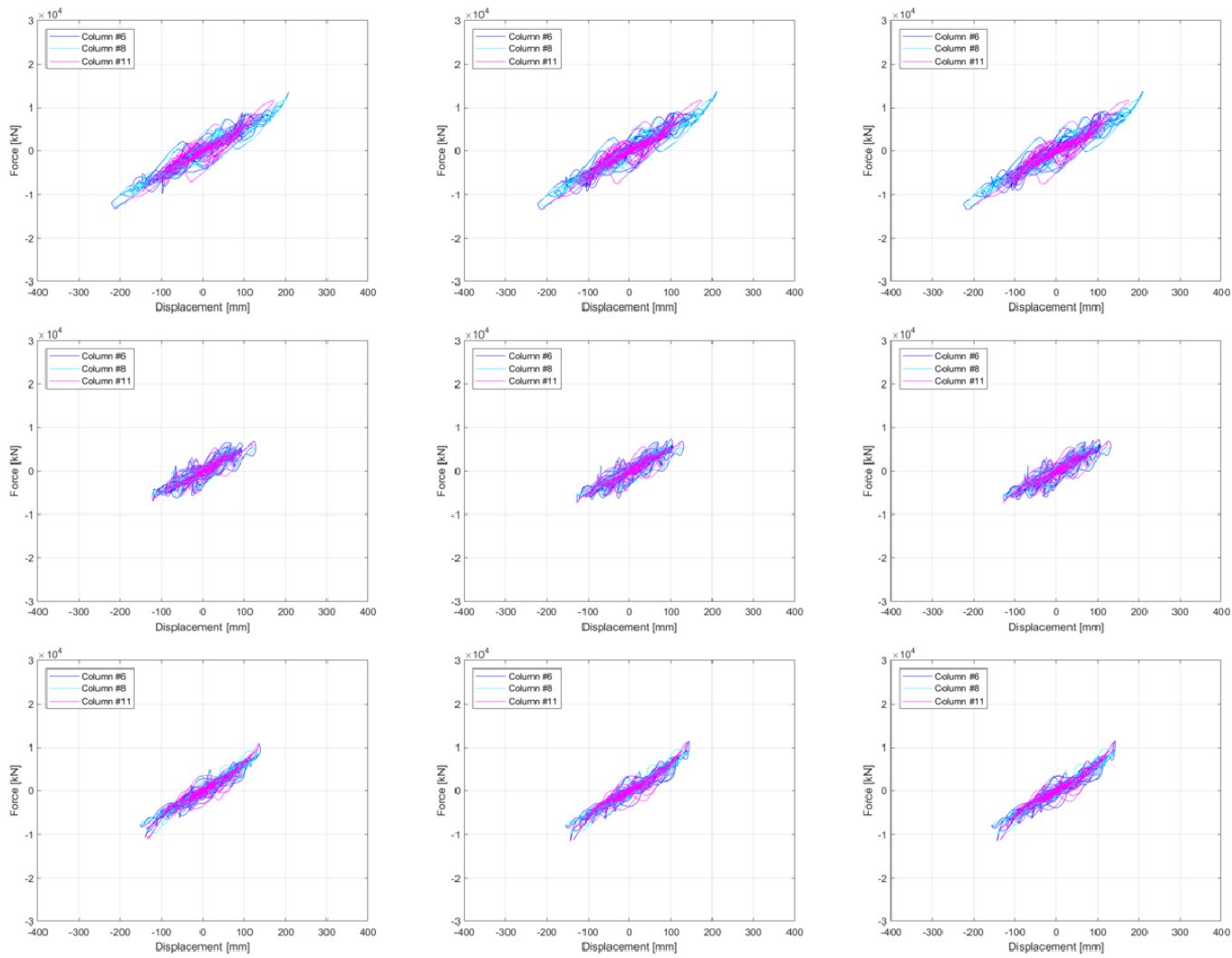
Figure 4.69. Longitudinal force-displacement relationship for columns #6, #8, and #11 at 100% – (Row: (1) Northridge, (2) Kobe, and (3) Loma Prieta, Column: (1) Load Case 1, (2) Load Case 6, and (3) Load Case 9).
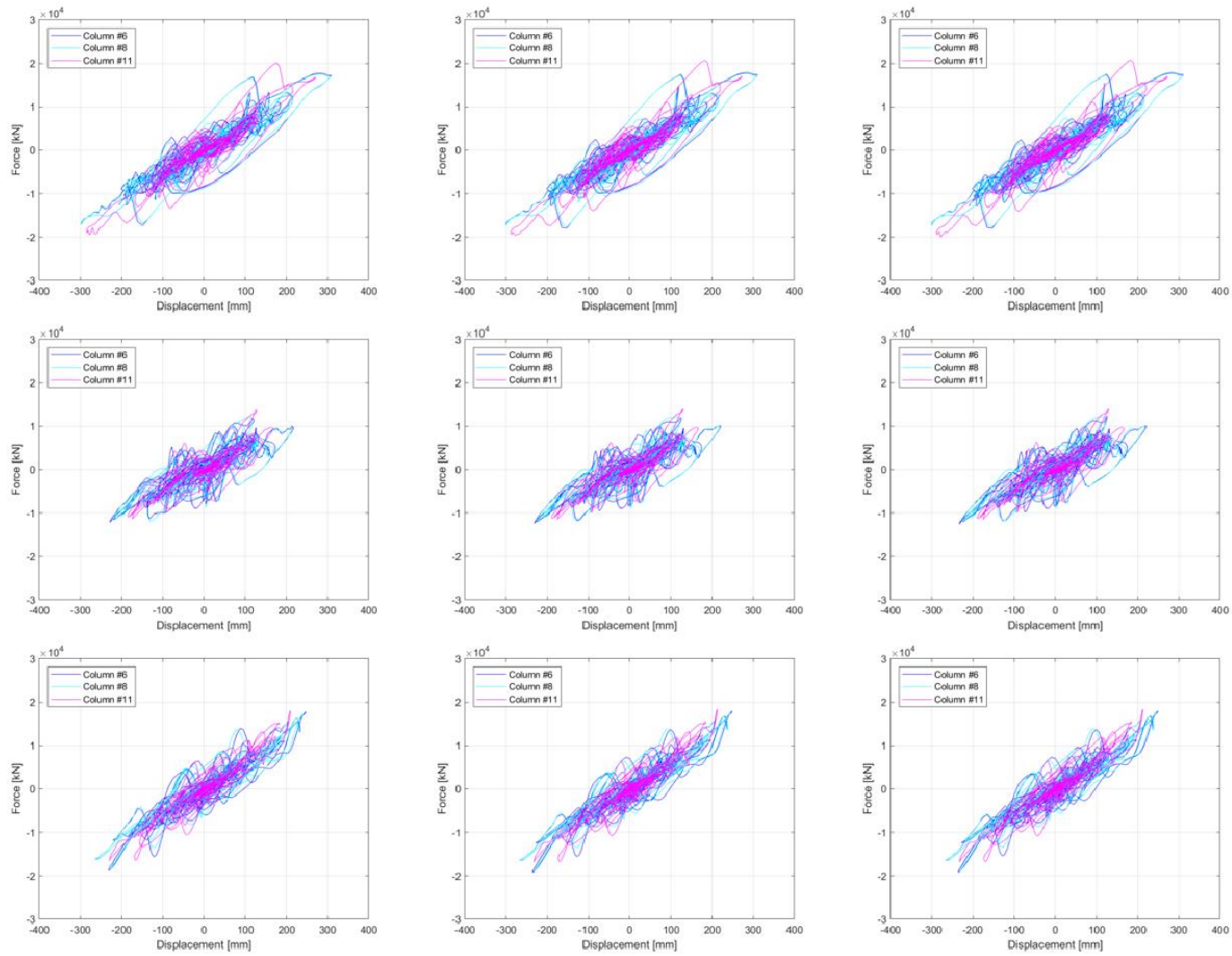
Figure 4.70. Longitudinal force-displacement relationship for columns #6, #8, and #11 at 200% – (Row: (1) Northridge, (2) Kobe, and (3) Loma Prieta, Column: (1) Load Case 1, (2) Load Case 6, and (3) Load Case 9).
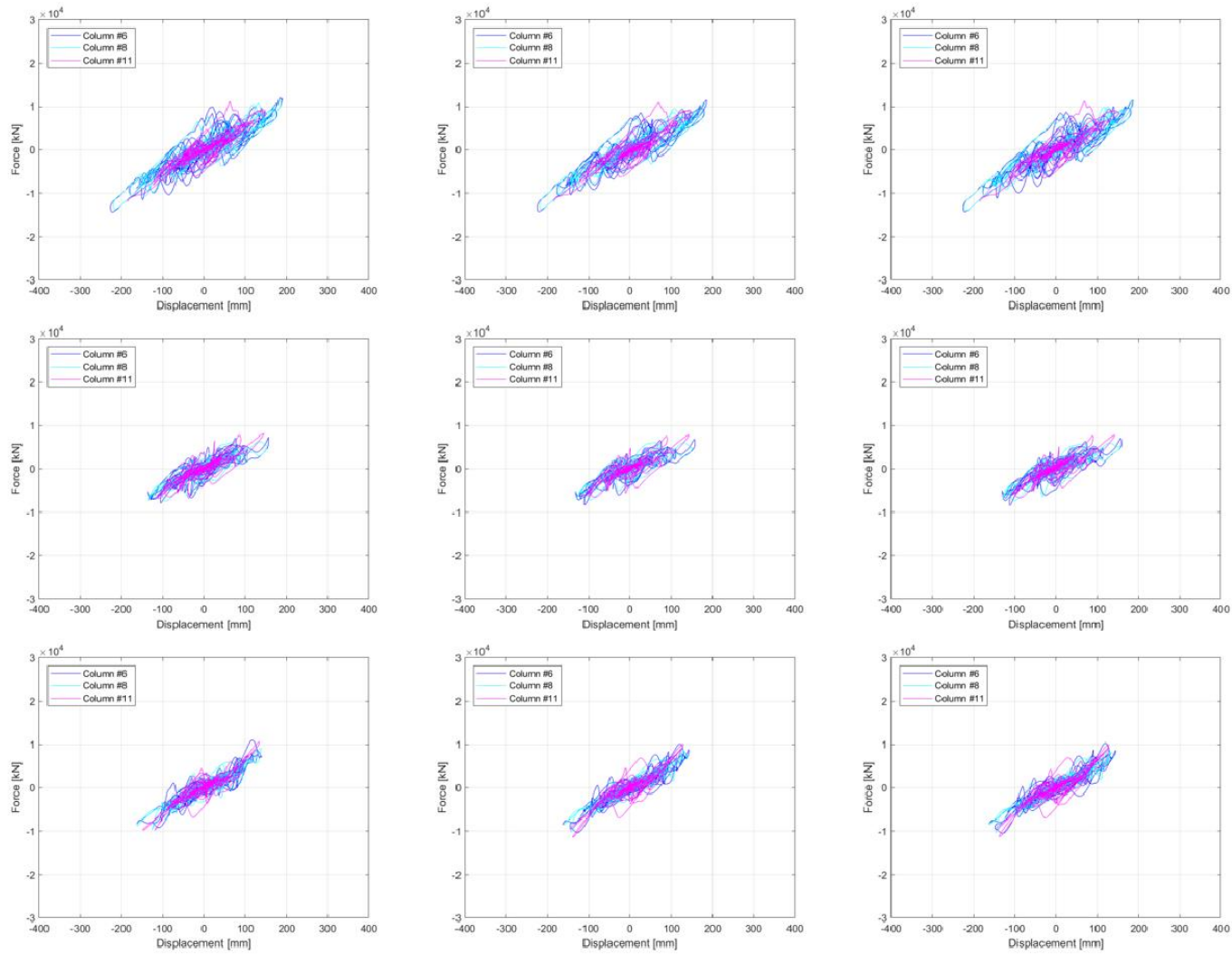
Figure 4.71. Transverse force-displacement relationship for columns #6, #8, and #11 at 100% – (Row: (1) Northridge, (2) Kobe, and (3) Loma Prieta, Column: (1) Load Case 1, (2) Load Case 6, and (3) Load Case 9).
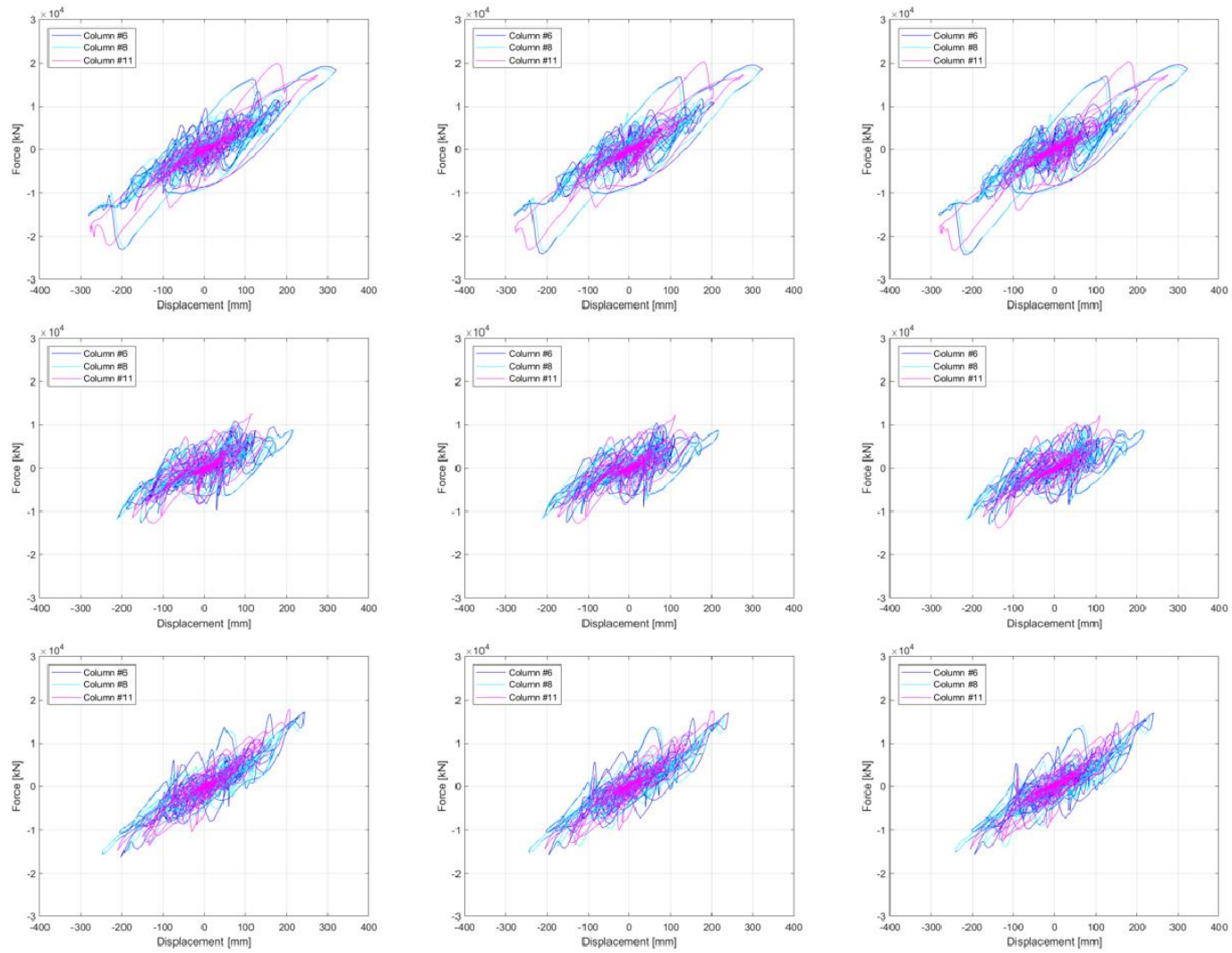
Figure 4.72. Transverse force-displacement relationship for columns #6, #8, and #11 at 200% – (Row: (1) Northridge, (2) Kobe, and (3) Loma Prieta, Column: (1) Load Case 1, (2) Load Case 6, and (3) Load Case 9).
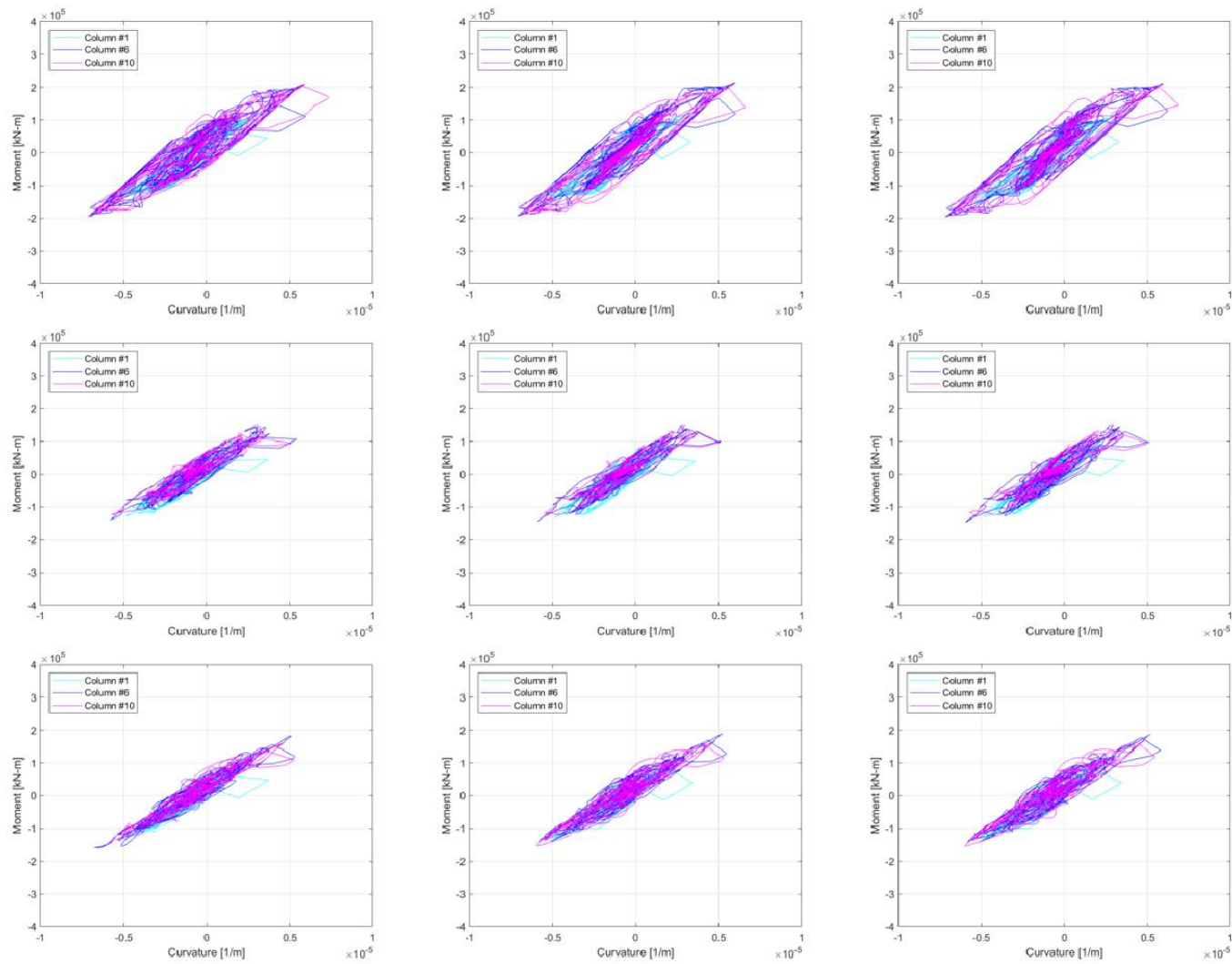
Figure 4.73. Longitudinal moment-curvature relationship for columns #1, #6, and #10 at 100% – (Row: (1) Northridge, (2) Kobe, and (3) Loma Prieta, Column: (1) Load Case 1, (2) Load Case 6, and (3) Load Case 9).
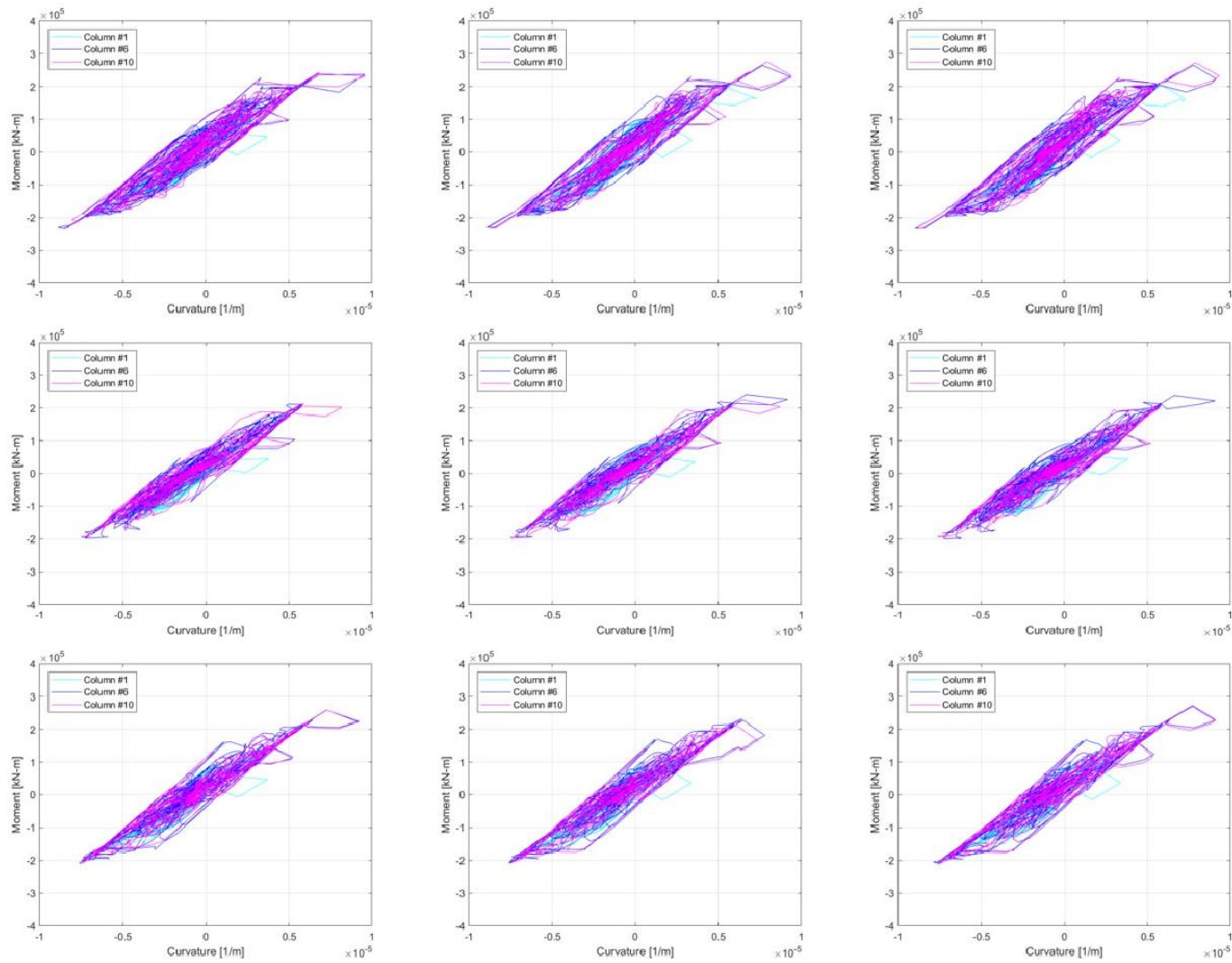
Figure 4.74. Longitudinal moment-curvature relationship for columns #1, #6, and #10 at 200% – (Row: (1) Northridge, (2) Kobe, and (3) Loma Prieta, Column: (1) Load Case 1, (2) Load Case 6, and (3) Load Case 9).
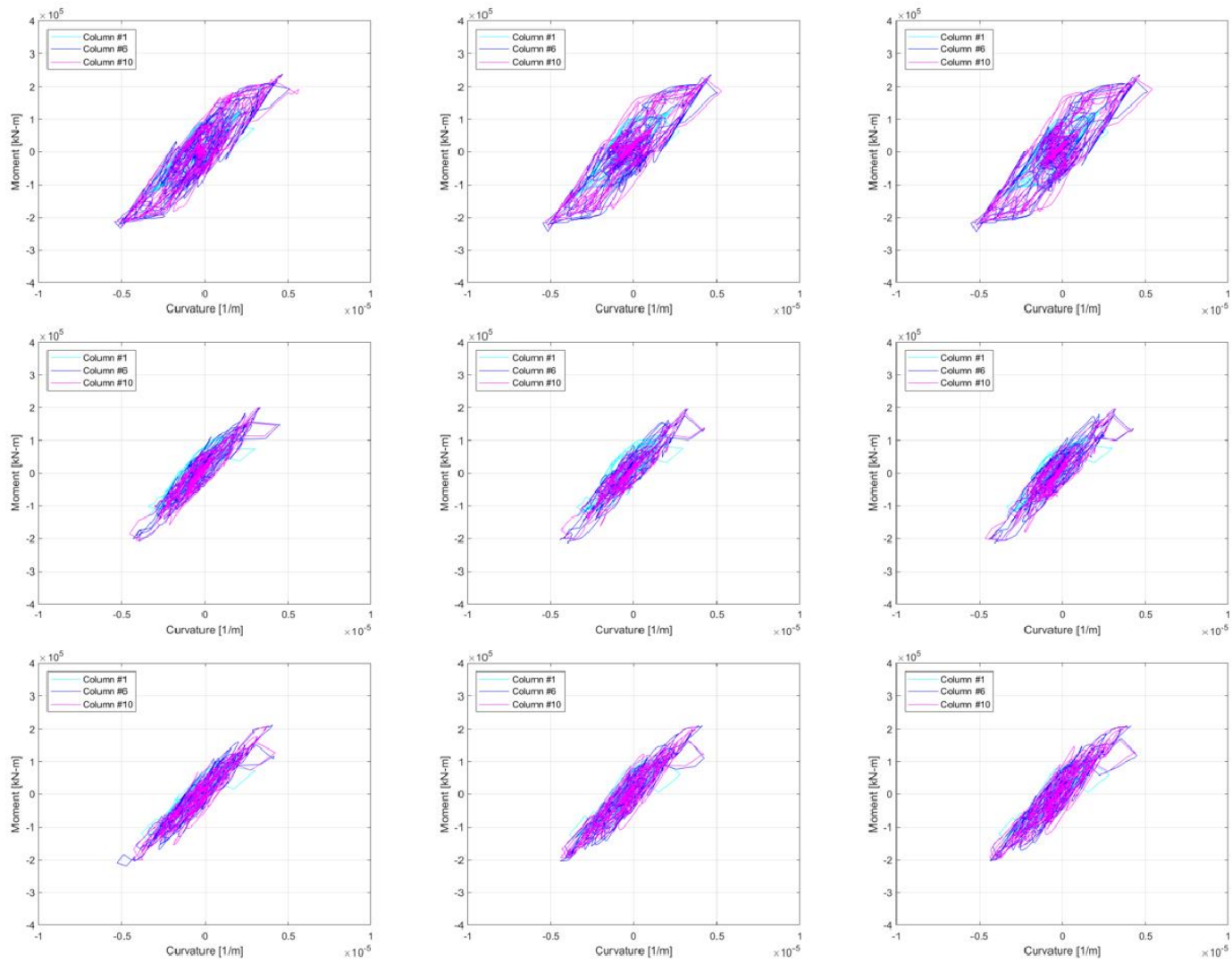
Figure 4.75. Transverse moment-curvature relationship for columns #1, #6, and #10 at 100% – (Row: (1) Northridge, (2) Kobe, and (3) Loma Prieta, Column: (1) Load Case 1, (2) Load Case 6, and (3) Load Case 9).
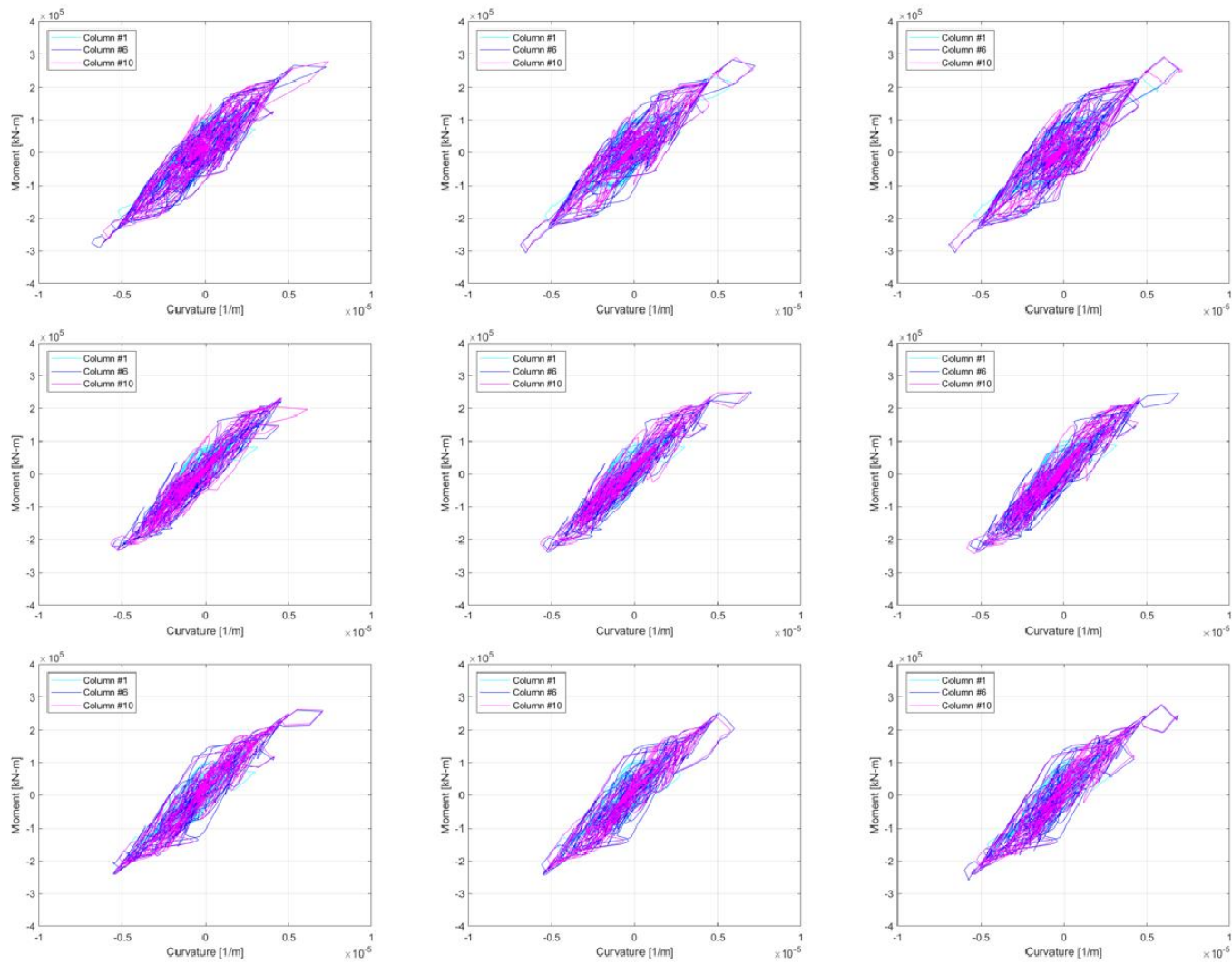
Figure 4.76. Transverse moment-curvature relationship for columns #1, #6, and #10 at 200% – (Row: (1) Northridge, (2) Kobe, and (3) Loma Prieta, Column: (1) Load Case 1, (2) Load Case 6, and (3) Load Case 9).
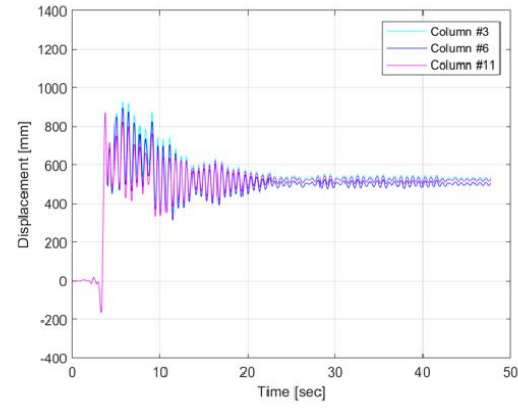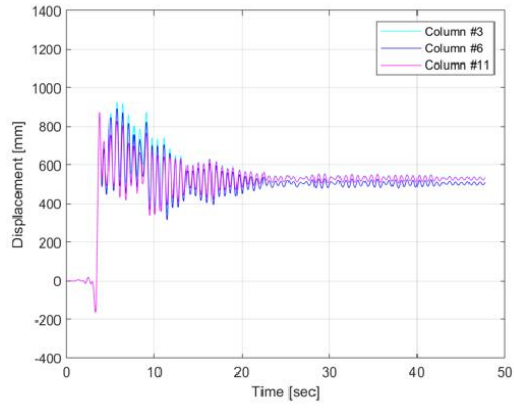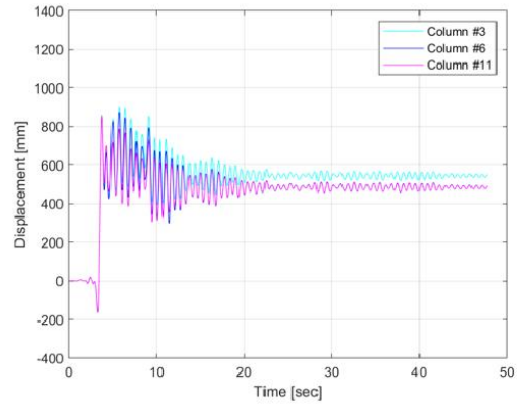
Figure 4.77. Longitudinal displacement time-history for columns #3, #6, and #11 at Northridge 300% – (Left: Load Case 1, Middle: Load Case 6, Right: Load Case 9).
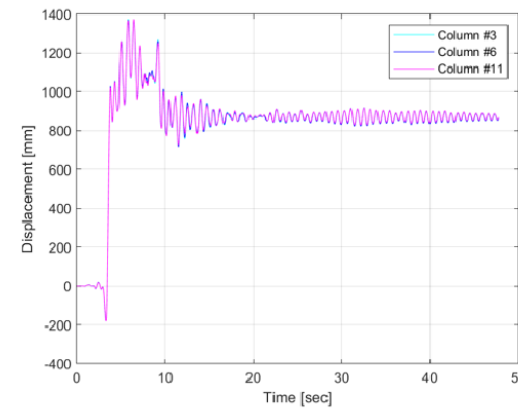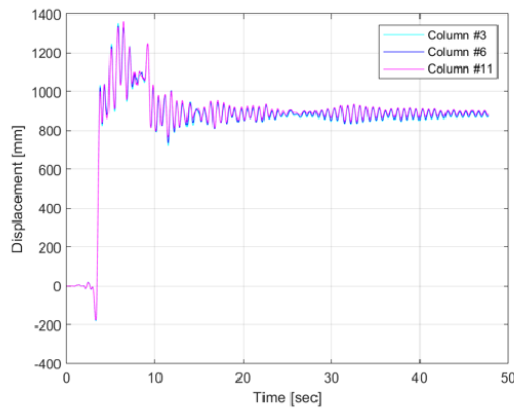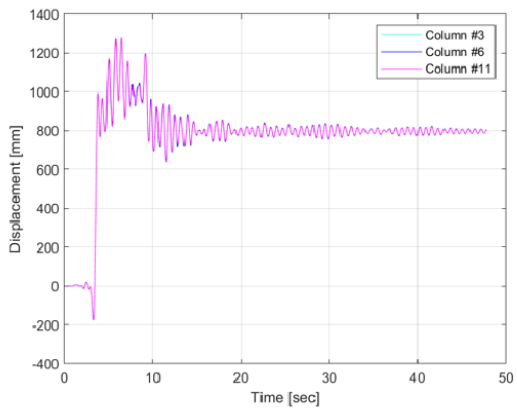
Figure 4.78. Transverse displacement time-history for columns #3, #6, and #11 at Northridge 300% – (Left: Load Case 1, Middle: Load Case 6, Right: Load Case 9).
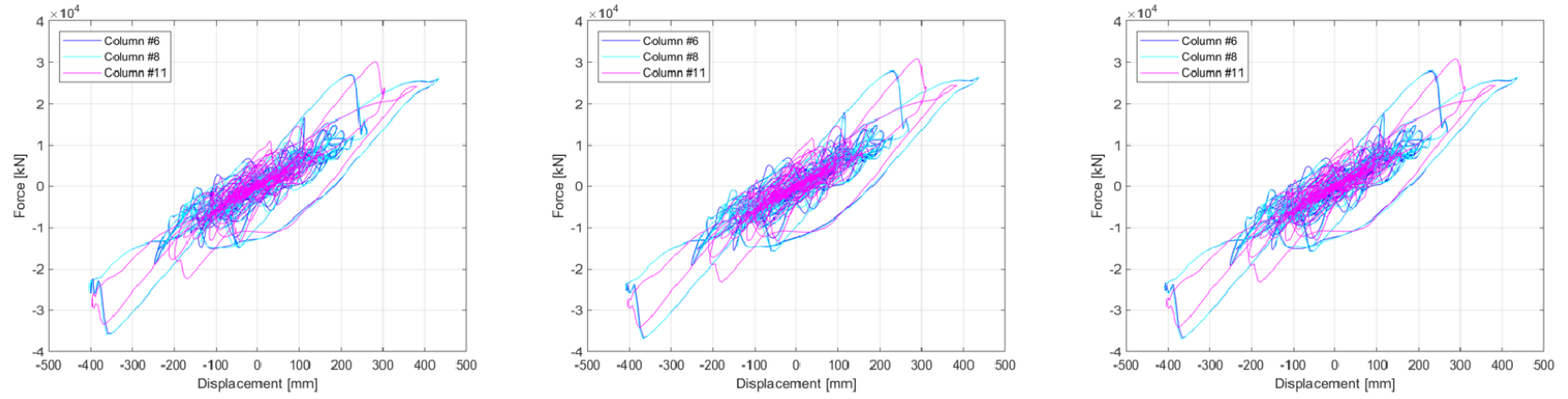
Figure 4.79. Longitudinal force-displacement relationship for columns #6, #8, and #11 at Northridge 300% – (Left: Load Case 1, Middle: Load Case 6, Right: Load Case 9).
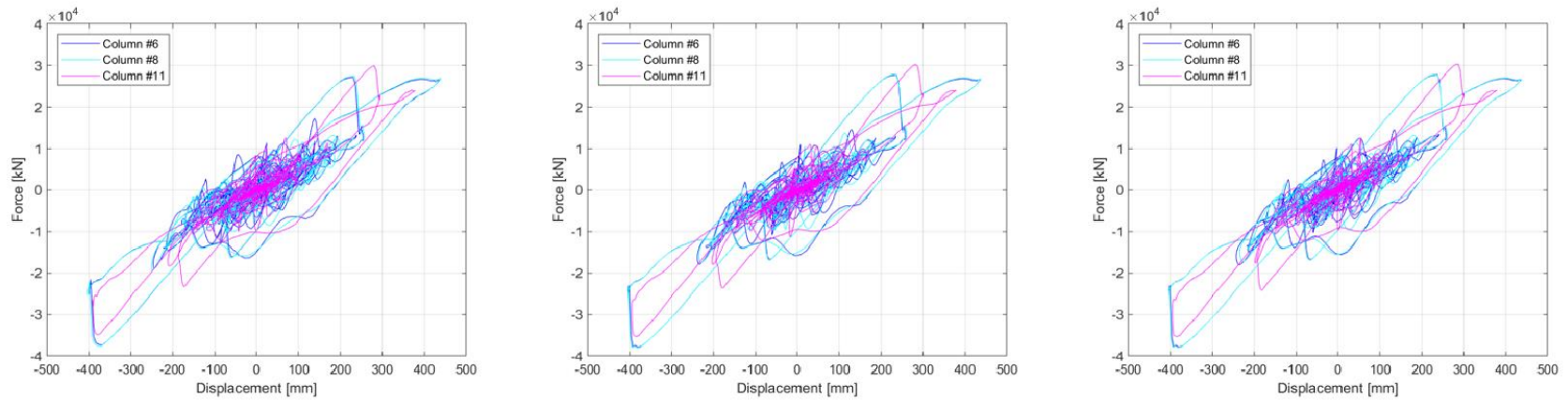
Figure 4.80. Transverse force-displacement relationship for columns #6, #8, and #11 at Northridge 300% – (Left: Load Case 1, Middle: Load Case 6, Right: Load Case 9).

183
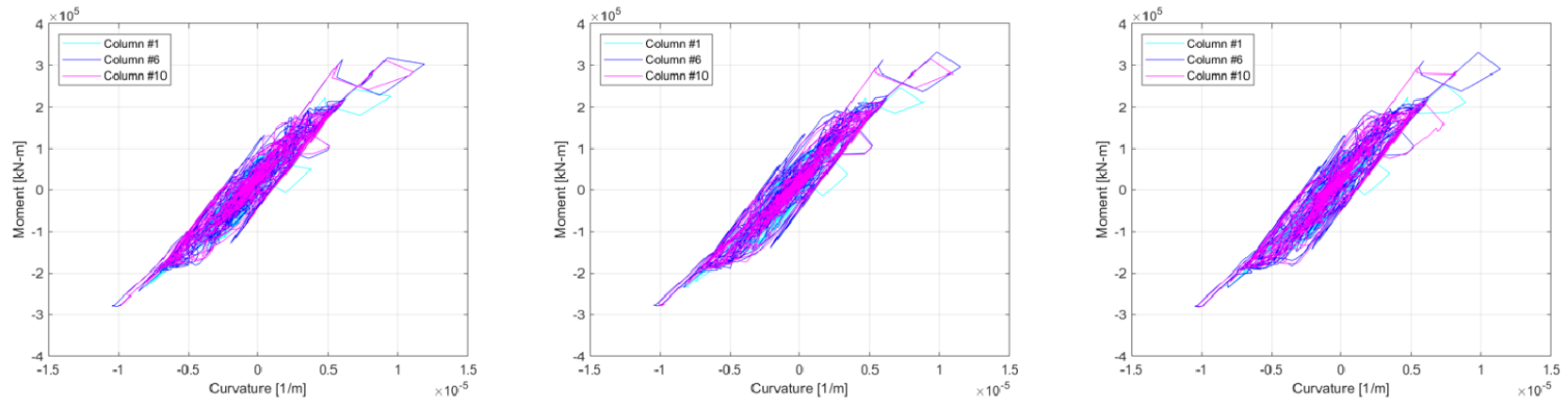
Figure 4.81. Longitudinal moment-curvature relationship for columns #1, #6, and #10 at Northridge 300% – (Left: Load Case 1, Middle: Load Case 6, Right: Load Case 9).
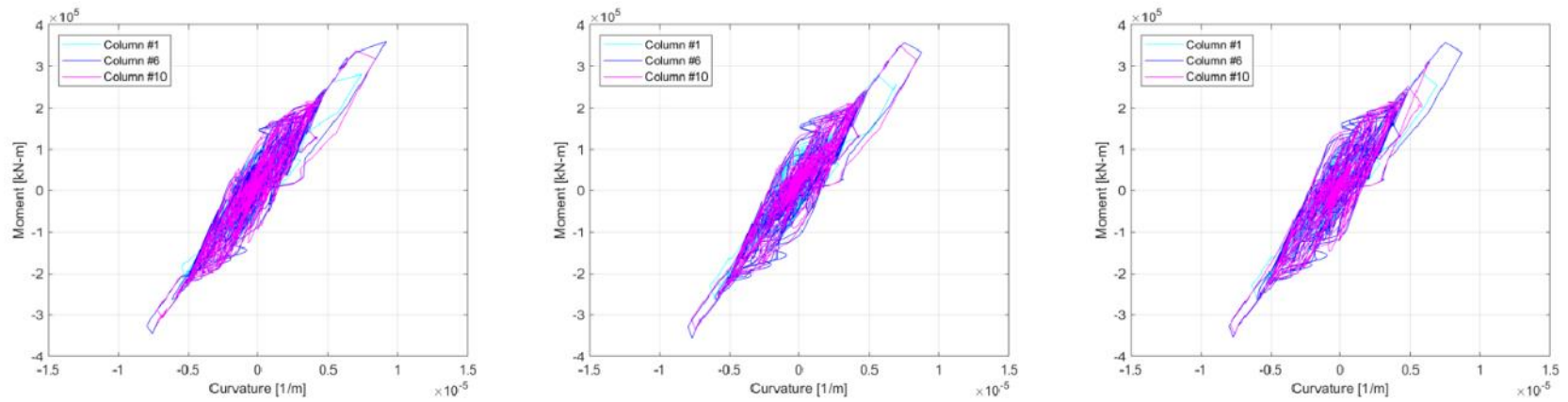
Figure 4.82. Transverse moment-curvature relationship for columns #1, #6, and #10 at Northridge 300% – (Left: Load Case 1, Middle: Load Case 6, Right: Load Case 9).
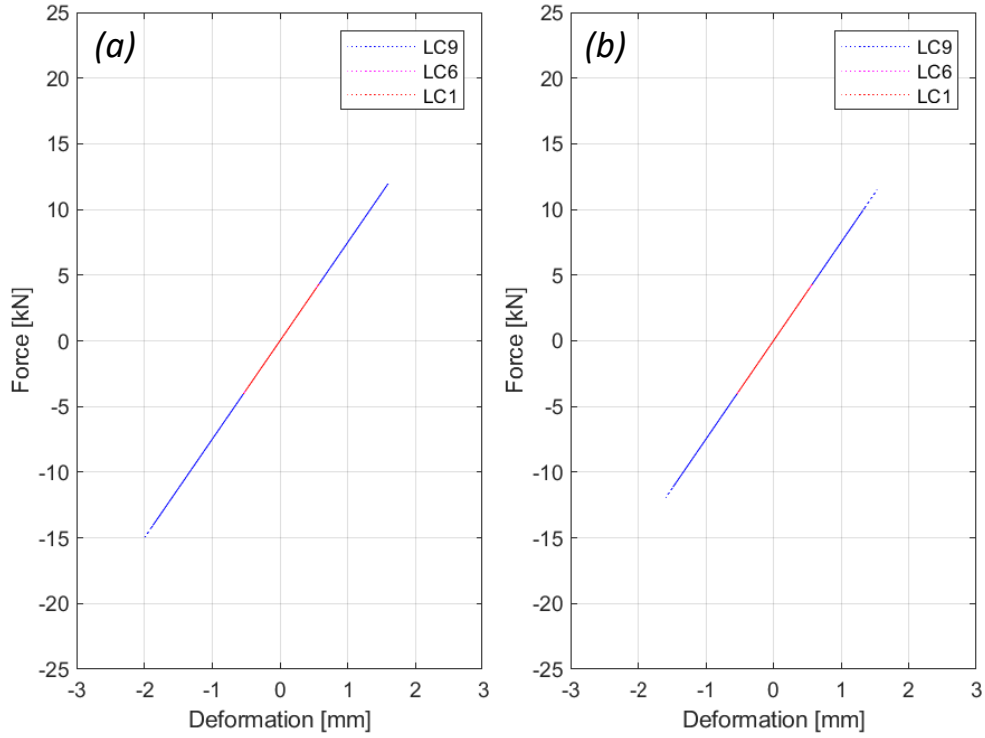
Figure 4.83. Force-deformation relationship of fasteners supporting rail 1 under Northridge 300%: (a) Above column #4, (b) Above column #6.
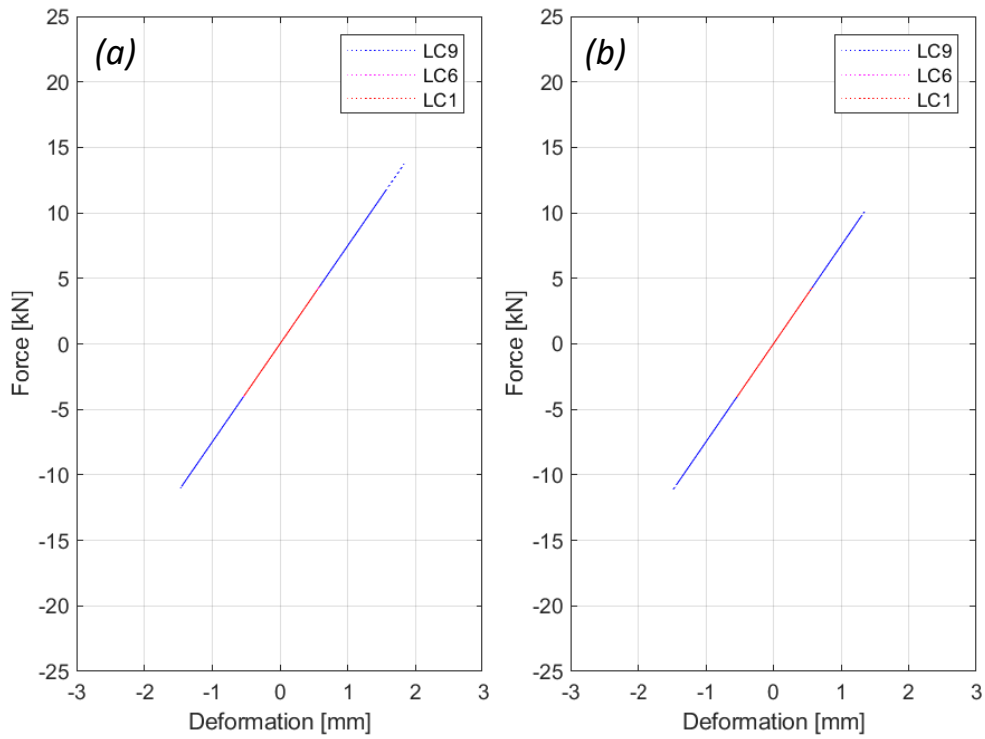
Figure 4.84. Force-deformation relationship of fasteners supporting rail 2 under Northridge 300%: (a) Above column #4, (b) Above column #6.
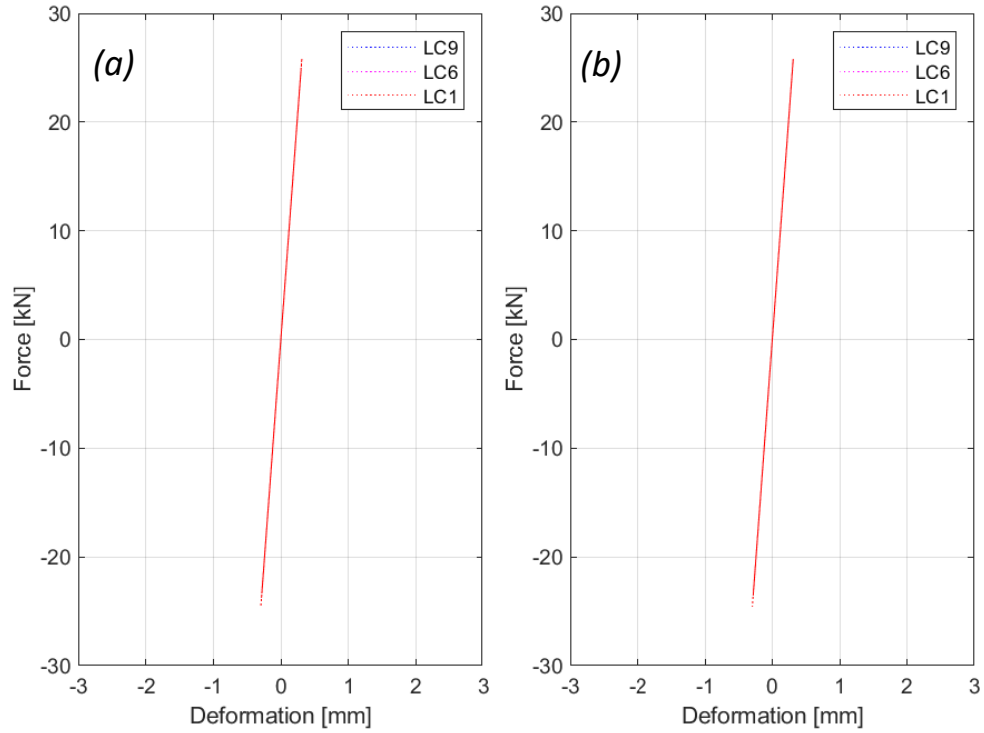
Figure 4.85. Force-deformation relationship of CA mortar layers supporting track 1 under Northridge 300%: (a) Above column #4, (b) Above column #6.
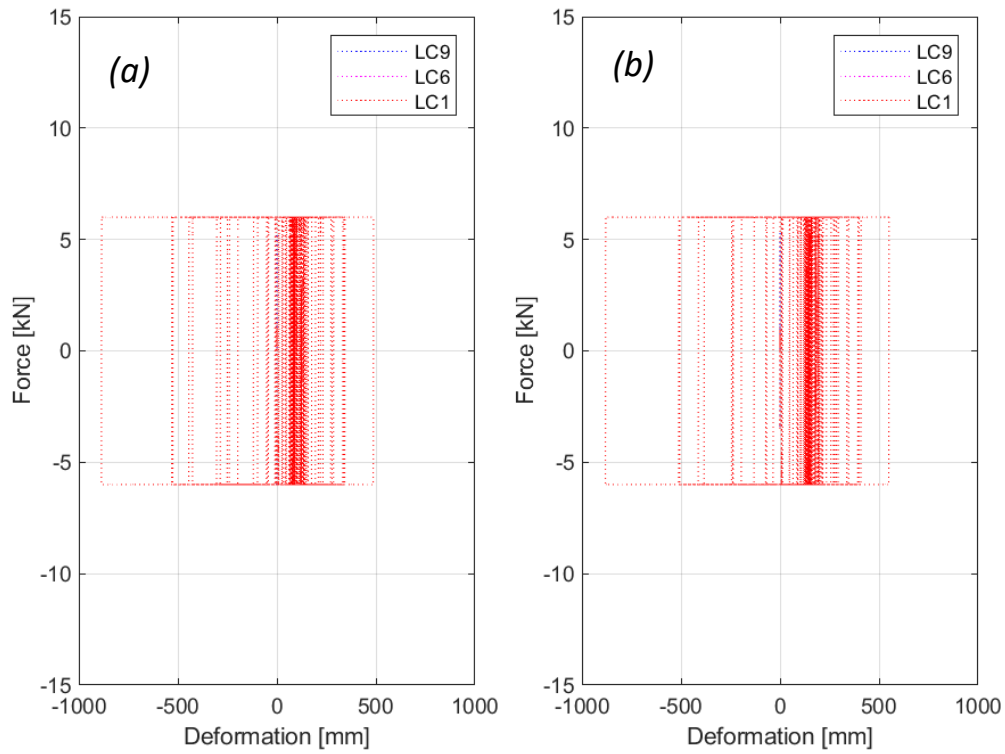
Figure 4.86. Force-deformation relationship of sliding layers supporting track 1 under Northridge 300%: (a) Above column #4, (b) Above column #6.

4.5. CONCLUDING REMARKS

The objective of this study is to present numerical modeling methods of HSR bridge systems including train-track-structure interaction. The modeling details provided in the previous sections along with the complementary step-by-step procedure and scripts provided from an example OpenSees input file in Appendix B are presented. Nonetheless, the study provided a demonstration of the seismic response of HSR bridges through a prototype HSR model created based off previous studies. The analysis results presented in that part of the study are based on a prototype HSR bridge system assumption. However, general conclusions can be still drawn from the performance of the prototype HSR bridge from a broad perspective, which at least could serve as a foundation for future research, as provided next.

Based on the seismic performance of the model in-place, the location of train loading for Load Case 6 and 9 did increase the local and global response within the bridge girders and columns. The maximum longitudinal moment response in the bridge columns under train loading experienced an average 10% and 13% increase throughout the three ground motions scaled to a 100% and 200% for Load Case 6 and Load Case 9, respectively. Column curvature also increased in the longitudinal and transverse directions by 4% and 6% on average for Load Case 6 and Load Case 9, respectively, and the maximum transverse moments in the columns showed an average increase of 5% for both of the load cases with train loading. The columns did not experience a significant increase in maximum shear forces due to additional train loading with less than 2% increase on average due to train loading. As for the global responses, bridge girders under Load Case 6 and Load Case 9 had an average increase of 4% for the maximum longitudinal displacement. Acceleration at the girder level for either direction experienced insignificant effects, even decreasing by 3% for the acceleration under Load Case 9 in the transverse direction.

Although the maximum response of the HSR bridge experienced variation due to the addition of train loading, the behavioral trends documented in the force-displacement and moment-curvature graphs were nearly identical with and without train loading for the original scale of the ground motions and showed slight instances of increased nonlinear loading-unloading loops for the 200% scale. Increase in displacements throughout the course of the ground motion were observed at the bridge girder level in the transverse displacement time-histories. Exceptionally large nonlinearities were not observed until analyzing the HSR bridge under the Northridge earthquake at 300% scale where apparent inelastic behavior was observed in all of the behavioral graphs plotted for Load Case 9.

The similarities in the seismic performance of the HSR columns between the load cases may be attributed to the intrinsic design, where force and moment capacities are much higher compared to typical railway or highway bridges; a by-product of the desired excessively large stiffness for HSR systems. In other words, the HSR bridge started to show response variation due to static train loading when the linear elastic limit had been breached. However, the inherent design complications for HSR bridges may be influenced largely by the dynamic loading of the train system which was not included in this study. To fully understand and design for the operation of HSR systems under the paramount safety, future studies are recommended to analyze the seismic performance of HSR bridges under the dual loading of dynamic train loading and dynamic seismic loading.

The overall performance of the prototype HSR bridge was well as it showed its ability to behave within its linear capacity. The performance was particularly good under the original scale of the ground motions. The HSR bridge columns were able to behave within its elastic capacity and showed slight nonlinearities when analyzed under the 200% scaled ground motions. Thus, at moderate ground motion intensities, it is safe to say the HSR bridge columns behaved essentially linearly or at least did not get into a large range of nonlinearities and were not at their force and moment capacities as well.

5. CONCLUDING REMARKS

The overall goal of this study is to synthesize the existing and ongoing efforts for HSR bridge systems through extensive review and understand the approaches to provide potential solutions to new design and construction. A focus is given to the modeling and numerical simulation techniques for various HSR systems and identify common modeling practices. The work presented in this study is critical and timely as the implementation of HSR as a major mode of transportation in the United States is coming into fruition. Due to the recent advances in HSR research, national studies regarding this topic are still very limited and heavily rely on the publications from researchers abroad in Europe and East Asia where HSR systems are widely used as a major method of transportation. Sub-systems of HSR have evolved over the years as technological advancements continue to improve the safety and efficiency of HSR. The extensive literature search presented in this study synthesizes the modeling methods that have been used by national and international researchers to idealize variety of train, track, and bridge systems. Future researchers can access this study to understand how specific HSR sub-systems are modeled and can pursue the publications referenced within this study for further details since.

Modeling techniques from literature published by researchers around the world are analyzed and discussed to understand the dynamic train-track-bridge interactions. Studies modeling different types of high-speed train systems, track systems, and bridge systems were explicitly researched to offer a comprehensive literature search that will allow the reader to gain insight on the modeling techniques of various HSR systems. This study identifies critical modeling features needed to develop a detailed numerical model, based on synthesized literature, that can capture HSR train-track-structure interaction under service and extreme loads including seismic excitations. A prototype train, track, and bridge system are selected based on available information that can be incorporated into a prototype model. The selections were then used to create a detailed HSR model in OpenSees using the modeling techniques synthesized in the extensive literature search to achieve the second objective. The model is then created to demonstrate the functionality of the modeling techniques. This study provides a step-by-step walk-through of the processes of modeling a prototype HSR system including the train-track-bridge system in detail. The nonlinear seismic response of the prototype HSR bridge is also presented to show the performance under various train loading scenarios and ground motions. This guide will allow future students and researchers with minimal experience in numerical modeling or modeling in OpenSees to formulate their own HSR model. This guide can also be of benefit to researchers or designers who may need some guidance, as existing publications regarding this topic focus mainly on the analysis and results rather than the specific methods used to model each sub-system.

The design and analysis of HSR bridges presents many challenges in comparison to the design of highway bridges and conventional railway bridges. Consequently, this study demonstrates a variety of potential methods for analyzing the seismic performance of an HSR bridge through post-processing OpenSees output which would allow the verification of design. Although the seismic performance assessment demonstrated in this study is not meant to prove the soundness of the prototype HSR bridge modeled, future work can be built off of the research presented to formulate a national code and design guideline for HSR bridges.

For completeness, a statement on the validities and limitations of this study are presented here and discussed to provide points of future recommendations and improvements. Due to the recent emphasis on implementing HSR systems as a mode of transportation in the United States, the literature available is heavily limited to a few national studies and foreign studies that have been translated to English and published to journals. This results in limitation of reference studies that can be researched for the purpose of understanding the methods of numerical modeling of HSR systems.

Another issue is the validity of the prototype model analysis results due to the lack of available design information regarding the prototype train, track, or bridge system that have been selected from the reference studies. This is mainly due to the limitation of content that can be included in such journal papers which could lead to the omission of detail that is not the emphasis of the respective study. To address this, many assumptions were made when formulating the prototype model as discussed in Section 4.2. A design assumption example being the cross-sectional design and strength of concrete and reinforcing steel of the pier columns for the prototype bridge from the Beijing to Xuzhou section of the Beijing-Shanghai high-speed railway. Although the cross-sectional area and height of the pier columns were specified, the reinforcement layout and strength design were omitted so generic assumptions were made regarding reinforcement ratio and strength of core concrete.

For this study, the train-track-structure interaction was the focus of the model. Accordingly, soil-structure interaction was simplified to a few springs between the column bases and the fixed boundaries of the model as discussed in Section 4.2. Future studies should elaborate on the modeling of soil-structure interaction by creating a sophisticated footing model with pile-soil interaction and abutments at bridge ends. In addition, elements were not discretized as precisely as recommended for a study focusing on analysis results, since the focus is to demonstrate the process of modeling and analyzing a prototype model. The prototype HSR bridge model in place is a primitive design combining a train system from Korea, a track-bridge system from China, and general soil properties from California under the assumption that they are all compatible for the sake of demonstrating a model.

A proper seismic analysis of any structural system requires a design guideline and code that acts a standard for the performance of the structural design. Since there is no such standards in-place for HSR bridges in the United States as of yet, the performance of the prototype HSR bridge was based on engineering judgement and preexisting knowledge based on highway bridges. The analysis presented should not be taken as a recommendation for design, but as a demonstration of potential seismic analysis that can be conducted with a formal design guideline and code.

The seismic analysis presented was performed under earthquakes applied biaxially in the longitudinal and transverse directions and applied as identical support excitations. Although this is a common assumption when conducting seismic analysis of structures, there are limitations to the validity of the analysis. Vertical excitations can impact the response of girders with large spans, and multi-support excitations might be considered to accurately analyze the response of multi-support structures under incoherent ground motions. Future research is recommended to consider such limitations to expand the comprehensive understanding of HSR bridge performance.

6. REFERENCES

Abbasi, M. (2018). "Seismic Vulnerability Assessment of As-Built and Retrofitted Multi-Frame Box-Girder Bridges." University of Nevada, Reno.

Abé, M., and Shimamura, M. (2014). "Performance of Railway Bridges during the 2011 Tōhoku Earthquake." Journal of Performance of Constructed Facilities, 28(1), 13–23.

Akiyama, M., Frangopol, D. M., and Mizuno, K. (2014). "Performance analysis of Tohoku-Shinkansen viaducts affected by the 2011 Great East Japan earthquake." Structure and Infrastructure Engineering, 10(9), 1228–1247.

Alfach, M. T. (2019). "Reinforcement of the seismic interaction of soil-damaged piles-bridge by using micropiles." Jordan Journal of Civil Engineering, University of Wolverhampton, UK.

American Galvanizers Association. (2012). "Galvanized Steel Pile Cap for Micropile Transmission Tower Foundations." galvanizeit.org, San Diego, California.

Andersson, A., and Karoumi, R. (2015). "Dynamics of railway bridges, analysis and verification by field tests." MATEC Web of Conferences, (G. Feltrin, ed.), 24(January), 12.

California High-speed Rail Authority. (2015). California High-Speed Rail Authority Request for Proposals for Design-Build Services for Construction Package 4 Book III , Part A . 1 Design Criteria Manual.

California High-Speed Rail Authority. (2018). 2018 Business Plan.

California High-Speed Rail Authority. (2019). California High-Speed Train Project Design Criteria, Rev. 3. Sacramento, CA.

California High-Speed Rail Project. (2016). High-Speed Rail Project Design-Build Contract for California.

California High Speed Rail Authority. (2021). "Design-Build Construction Packages."

Carlos, G.-M., and Miranda, E. (2013). "Performance-Based Seismic Assessment of a Recently Built High-Speed Rail Viaduct in Spain. The Archidona Viaduct." Proceeding of the 7th National Seismic Conference on Bridges and Highways, ResearchGate, Oakland, CA, 1–12.

Chen, Z., and Han, Z. (2018). "Dynamic Analysis of High-Speed Train-Track-Bridge Coupled System Considering Concrete Shrinkage and Creep." ICRT 2017, W. Zhai and K. C. P. Wang, eds., American Society of Civil Engineers, Reston, VA, 181–188.

Chin, C.-T., and Chen, J.-R. (2007). "Foundation engineering practice in Taiwan – High Speed Rail Experiences." Proc., Seminar on the State-of-the-Practice of Geotechnical Engineering in Taiwan and Hong Kong, 28–51.

China Communication Press, B. (2012). "JTG D62-2004 Code for Design of Highway Reinforced Concrete and Prestressed Concrete Bridges and Culverts."

Combault, J. (2013). "Design and construction of segmental bridges for high speed rail."

Aspire, *7(4), 18–21.*

Connolly, D., Giannopoulos, A., and Forde, M. C. (2013). "Numerical modelling of ground borne vibrations from high speed rail lines on embankments." Soil Dynamics and Earthquake Engineering*, 46, 13–19.*

Connor, P. (2019). "The Railway Technical." http://www.railway-technical.com/.

Dong Kang, K., and Suh, S. D. (2003). "Experience with the Precast Span Method on the Korean High-Speed Rail Project." Transportation Research Record: Journal of the Transportation Research Board*, 1825(1), 15–21.*

Du, X. T., Xu, Y. L., and Xia, H. (2012). "Dynamic interaction of bridge-train system under non-uniform seismic ground motion." Earthquake Engineering & Structural Dynamics*, 41(1), 139–157.*

Ed Kay. (2009). "Yichang-Wanzhou Railway Yangtze River Bridge." Wikimedia Commons*.*

ENR. (2019). "Opinion: With Merced-to-Bakersfield Route, a High-Speed Rail Reset in California." ENR California*.*

Evangelista, L., and Vedova, M. (2009). "The Italian high speed network: Design and construction of the reinforced concrete bridges." Bridges for High-speed Railways*, R. Calcada, R. Delgado, and A. C. e Matos, eds., CRC Press, 47–59.*

Federal Railroad Administration. (2016). High-Speed Intercity Passenger Rail Program Federal Investment Highlights*. FRA eLibrary, Washington, DC.*

Gingery, J., O'Neill, B., Hilton, B., Jong, K., and Winkle, H. Van. (2011). Geotechnical Analysis and Design Guidelines*.*

Gong-lian, D., Peng-fei, Z., Bin, Y., and Xiang-nan, X. (2013). "Longitudinal force of CWR on box girder under solar radiation." Journal Of Zhejiang University*, 47.*

González, A., OBrien, E. J., and McGetrick, P. J. (2012). "Identification of damping in a bridge using a moving instrumented vehicle." Journal of Sound and Vibration*, 331(18), 4115–4131.*

Gregory L. Fenves et al. (2020a). OpenSeesWiki*.*

Gregory L. Fenves et al. (2020b). Opensees User Manual*. Berkeley, CA.*

Guo, W., Hu, Y., Gou, H., Du, Q., Fang, W., Jiang, L., and Yu, Z. (2020). "Simplified seismic model of CRTS II ballastless track structure on high-speed railway bridges in China." Engineering Structures*, 211, 110453.*

Guo, W. W., Xia, H., De Roeck, G., and Liu, K. (2012). "Integral model for train-track-bridge interaction on the Sesia viaduct: Dynamic simulation and critical assessment." Computers & Structures*, 112–113, 205–216.*

He, X., Kawatani, M., Hayashikawa, T., and Matsumoto, T. (2011). "Numerical analysis on seismic response of Shinkansen bridge-train interaction system under moderate earthquakes." Earthquake Engineering and Engineering Vibration*, 10(1), 85–97.*

He, X., Wu, T., Zou, Y., Chen, Y. F., Guo, H., and Yu, Z. (2017). "Recent developments

of high-speed railway bridges in China." Structure and Infrastructure Engineering*, 13(12), 1584–1595.*

Herbst, T. . (1994). "The GEWI-PILE, a micropile for retrofitting, seismic upgrading and difficult installation." International Conference on Design and Construction of Deep Foundations*, Federal Highway Administration (FHWA), 913–930.*

Hidema, T., Energy, A., Sussman, J. M., Systems, E., Supervisor, T., Dahleh, M., Science, C., and Program, P. (2017). "Competitive Strategy for the Proposed Texas High Speed Rail Project : A System Dynamics / CLIOS Process Approach." (2010), 1–202.

Hu, N., Dai, G.-L., Yan, B., and Liu, K. (2014). "Recent development of design and construction of medium and long span high-speed railway bridges in China." Engineering Structures*, Elsevier Ltd, 74, 233–241.*

Hurty, W. C., and Rubinstein, M. F. (1964). Dynamics of structures*. Prentice-Hall, Englewood Cliffs, NJ.*

Hutton, S. G., and Cheung, Y. K. (1979). "Dynamic response of single span highway bridges." Earthquake Engineering & Structural Dynamics*, 7(6), 543–553.*

Institute of Railway Comprehensive Technology of Japan (IRCT-J). (2000). Design standards for railway structures*.*

International Code Council. (2015). International Building Code*.*

International Union of Railways. (2006). UIC Code Leaflet 776-1R - Loads to be considered in railway bridge design*.*

International Union of Railways. (2008). UIC Code R 719*.*

International Union of Railways. (2015). "High-speed rail history." UIC, the worldwide railway organisation*.*

Janberg, N. (2020). "structurae.net." Structurae - The Largest Database for Civil and Structural Engineers*.*

Kang, C., Schneider, S., Wenner, M., and Marx, S. (2018). "Development of design and construction of high-speed railway bridges in Germany." Engineering Structures*, 163(December 2017), 184–196.*

Kaviani, P., Zareian, F., and Taciroglu, E. (2012). "Seismic behavior of reinforced concrete bridges with skew-angled seat-type abutments." Engineering Structures*, 45, 137–150.*

Kim, C. W., Kawatani, M., and Kim, K. B. (2005). "Three-dimensional dynamic analysis for bridge–vehicle interaction with roadway roughness." Computers & Structures*, 83(19–20), 1627–1645.*

Kim, M. (2014). "KTX-Sancheon."

Kimmerling, R. E. (2002). Geotechnical Engineering Circular No. 6 - Shallow Foundations*. Seattle, Washington.*

Kwark, J. W., Choi, E. S., Kim, Y. J., Kim, B. S., and Kim, S. I. (2004). "Dynamic behavior

of two-span continuous concrete bridges under moving high-speed train." Computers & Structures, *82(4–5), 463–474.*

Lawrence, M., Bullock, R., and Liu, Z. (2019). China's High-Speed Rail Development.

Lee, C. H., Kawatani, M., Kim, C. W., Nishimura, N., and Kobayashi, Y. (2006). "Dynamic response of a monorail steel bridge under a moving train." Journal of Sound and Vibration, *294(3), 562–579.*

Lee, C. H., Kim, C. W., Kawatani, M., Nishimura, N., and Kamizono, T. (2005). "Dynamic response analysis of monorail bridges under moving trains and riding comfort of trains." Engineering Structures, *27(14), 1999–2013.*

Li, H., Xu, D., and Liu, C. (2008). "Precast segmental design and construction in China." Tailor Made Concrete Structures, *CRC Press, 172–172.*

Li, H., Yu, Z., Mao, J., and Jiang, L. (2020). "Nonlinear random seismic analysis of 3D high-speed railway track-bridge system based on OpenSEES." Structures, *24, 87–98.*

Li, Y., and Conte, J. P. (2016). "Effects of seismic isolation on the seismic response of a California high-speed rail prototype bridge with soil-structure and track-structure interactions." Earthquake Engineering & Structural Dynamics, *45(15), 2415–2434.*

Liu, K., Reynders, E., De Roeck, G., and Lombaert, G. (2009). "Experimental and numerical analysis of a composite bridge for high-speed trains." Journal of Sound and Vibration, *320(1–2), 201–220.*

Long, G., Liu, H., Ma, K., Xie, Y., and Li, W. (2018). "Development of High-Performance Self-Compacting Concrete Applied as the Filling Layer of High-Speed Railway." Journal of Materials in Civil Engineering, *30(2), 04017268.*

Lu, D., Wang, F., and Chang, S. (2015). "The Research of Irregularity Power Spectral Density of Beijing Subway." Urban Rail Transit, *1(3), 159–163.*

Manterola, J., and Escamilla, M. (2014). "Steel and composite bridges for high speed rail: Advanced solutions for challenging designs." American Institute of Steel Construction (AISC) Symposium, *Toronto, CA, 6.*

Mao, J., Yu, Z., Xiao, Y., Jin, C., and Bai, Y. (2016). "Random dynamic analysis of a train-bridge coupled system involving random system parameters based on probability density evolution method." Probabilistic Engineering Mechanics, *46, 48–61.*

Marshall, J., Cañete, A., and Keating, M. (2019). "California High-Speed Rail – Construction Package 4: an analysis of the technical design challenges, design evolution and collaborative solutions developed for the next phase of high-speed rail construction that is underway." AREMA Annual Conference, *AREMA, Minneapolis, MN.*

Marshall, J., and Keating, M. (2016). "COLLABORATIVE SOLUTIONS DEVELOPED FOR THE NEXT PHASE OF HIGH-SPEED RAIL." (November 2008).

Marx, S., and Schlaich, J. (2009). "Gestalten von Eisenbahnbrücken." Stahlbau, *78(3), 197–202.*

Mason, J. A. (1993). CALTRANS full scale lateral load test of a driven pile foundation in soft bay mud. *Sacramento, CA.*

Matsuura, A. (1976). "A study of dynamic behavior of bridge girder for high speed railway." Proceedings of the Japan Society of Civil Engineers, *1976(256).*

Memon, S. A., Smith, T., Kelly, T., and Ishiyama, J. (2014). "High-Speed Rail - New corridor design challenges and alternate analysis (shared and/or greenfield corridors)." AREMA Annual Conference, *AREMA (American Railway Engineering and Maintenance-of-Way Association), Chicago, Illinois, 1–16.*

Millanes, F., Bujalance, E. B., Domínguez, J. L. M., and Suárez, J. M. (2014). "Archidona Viaduct: Composite Steel–Concrete Deck for a Long Railway Bridge." Structural Engineering International, *24(1), 122–126.*

Minami, K., and Shimizu, K. (2011). "Design of Steel Bridges for Shinkansen, Japan, High-Speed Rail." Transportation Research Record: Journal of the Transportation Research Board, *2228(1), 131–138.*

Mizuno, M., and Nozawa, S. (2011). "Seismic damage and restoration in railway facilities of East Japan Railway Company." JSCE (Japan Society of Civil Engineers) Magazine, *96(7), 13–16.*

Momenzadeh, M., Nguyen, T., Lutz, P., Pokrywka, T., and Risen, C. (2013). "Seismic Retrofit of 92/280 I/C Foundations by Micropile Groups in San Francisco Bay Area, California." International Conference on Case Histories in Geotechnical Engineering, *Missouri University of Science and Technology, Chicago, Illinois.*

Montenegro, P. A., Calçada, R., Vila Pouca, N., and Tanabe, M. (2016). "Running safety assessment of trains moving over bridges subjected to moderate earthquakes." Earthquake Engineering & Structural Dynamics, *45(3), 483–504.*

Muncke, M. (2008). "The effects on the interoperability of the European Railway Traffic of European Standards." Bridges for High-Speed Railways, *R. Calcada, R. Delgado, and A. C. e Matos, eds., CRC Press, 15–22.*

Nguyen, D.-V., Kim, K.-D., and Warnitchai, P. (2009). "Simulation procedure for vehicle–substructure dynamic interactions and wheel movements using linearized wheel–rail interfaces." Finite Elements in Analysis and Design, *45(5), 341–356.*

Nishimura, A. (2004). "Damage Analysis and Seismic Design of Railway Structures for Hyogoken-Nanbu (Kobe) Earthquake." Journal of JAEE, *4(3), 184–194.*

Parmantier, D. M., Armour, T. A., Perkins, B. J., and Sexton, J. A. (2004). "Foundation Seismic Retrofit of Boeing Field Control Tower." GeoSupport 2004, *American Society of Civil Engineers, Reston, VA, 278–288.*

Parsons Brinckerhoff. (2009). Design Guidelines for High-Speed Train Aerial Structures: 2.3.3 (Technical Memorandum).

Pearlman, S. L., Wolosick, J. R., and Gronek, P. B. (1993). "Pin piles for seismic rehabilitation of bridges." the 10th International Bridge Conference, *Pittsburgh.*

Plasser American. (2020). "Plasser American - Machines & Systems - Ballast Bed

Cleaning.” www.plasseramerican.com.

Qin, S., and Gao, Z. (2017). “Developments and Prospects of Long-Span High-Speed Railway Bridge Technologies in China.” Engineering, *3(6), 787–794.*

Queiroz, F. D., Vellasco, P. C. G. S., and Nethercot, D. A. (2007). “Finite element modelling of composite beams with full and partial shear connection.” Journal of Constructional Steel Research, *63(4), 505–521.*

Rocha, J. M., Henriques, A. A., and Calçada, R. (2014). “Probabilistic safety assessment of a short span high-speed railway bridge.” Engineering Structures, *71, 99–111.*

Rosignoli, M. (2016). “Full-Span Precasting of High-Speed Railway Bridges.” Bridge Tech, *The Bridge Engineering eManuals.*

Shu, S., and Muhunthan, B. (2010). Influence of Sand State on Network effect of Micropiles.

Skyscraper City. (2019). “High Speed Rail.”

Sobrino, J. (2008). “Bridges for the high speed railway lines in Spain. Design criteria and case studies.” Bridges for High-Speed Railways, *R. Calcada, R. Delgado, and A. C. e Matos, eds., CRC Press, 71–91.*

Song, M.-K., Noh, H.-C., and Choi, C.-K. (2003). “A new three-dimensional finite element analysis model of high-speed train–bridge interactions.” Engineering Structures, *25(13), 1611–1626.*

Su, M., Dai, G., Marx, S., Liu, W., and Zhang, S. (2019). “A Brief Review of Developments and Challenges for High-speed Rail Bridges in China and Germany.” Structural Engineering International, *Taylor & Francis, 29(1), 160–166.*

Sweet, R. (2014). “Why China can build high-speed rail so cheaply.” Global Construction Review, *London, UK.*

Tai, J. C., Jang, D., Gaffney, H., and Flint, J. (2010). “Full Span Precast and Launching Construction in Taiwan’s High Speed Rail Project.” 2010 Joint Rail Conference, Volume 1, *ASMEDC, 167–173.*

Takuma, K. (2019). “Shinkansen Route Map.” nippon.com.

Tamai, S., and Shimizu, K. (2011). “The long spanned bridge for deflection-restricted high speed rail.” 9th World Congress on Railway Research, *International union of railways, Lille, France.*

Tanabe, M., Yamada, Y., and Hajime, W. (1987). “Modal method for interaction of train and bridge.” Computers & Structures, *27(1), 119–127.*

Tayabji, S. D., and Bilow, D. (2001). “Concrete Slab Track State of the Practice.” Transportation Research Record: Journal of the Transportation Research Board, *1742(1), 87–96.*

Tom Armour, Groneck, P., Keeley, J., and Sharma, S. (2000). Micropile Design and Construction Guidelines Implementation Manual Priority Technologies Program Project. *Federal Way, WA.*

Vijay K. Garg, and Dukkipati, R. V. (1984). Dynamics of Railway Vehicle Systems. *Elsevier.*

Wang, J., Zhou, Y., Wu, T., and Wu, X. (2019). "Performance of Cement Asphalt Mortar in Ballastless Slab Track over High-Speed Railway under Extreme Climate Conditions." International Journal of Geomechanics*, 19(5), 04019037.*

Wu, Y.-S., and Yang, Y.-B. (2003). "Steady-state response and riding comfort of trains moving over a series of simply supported bridges." Engineering Structures*, 25(2), 251–265.*

Xia, H., and Zhang, N. (2005). "Dynamic analysis of railway bridge under high-speed trains." Computers & Structures*, 83(23–24), 1891–1901.*

Xia, H., Zhang, N., and De Roeck, G. (2003). "Dynamic analysis of high speed railway bridge under articulated trains." Computers & Structures*, 81(26–27), 2467–2478.*

Yan, B., Dai, G. L., and Hu, N. (2015). "Recent development of design and construction of short span high-speed railway bridges in China." Engineering Structures*, Elsevier Ltd, 100, 707–717.*

Yang, Y.-B., and Lin, B.-H. (1995). "Vehicle-Bridge Interaction Analysis by Dynamic Condensation Method." Journal of Structural Engineering*, 121(11), 1636–1643.*

Yang, Y.-B., and Yau, J.-D. (1997). "Vehicle-Bridge Interaction Element for Dynamic Analysis." Journal of Structural Engineering*, 123(11), 1512–1518.*

Yu, Z., and Mao, J. (2017). "Probability analysis of train-track-bridge interactions using a random wheel/rail contact model." Engineering Structures*, 144, 120–138.*

Yu, Z., and Mao, J. (2018). "A stochastic dynamic model of train-track-bridge coupled system based on probability density evolution method." Applied Mathematical Modelling*, 59, 205–232.*

Yu, Z., Mao, J., Guo, F., and Guo, W. (2016). "Non-stationary random vibration analysis of a 3D train–bridge system using the probability density evolution method." Journal of Sound and Vibration*, 366, 173–189.*

Zeng, Z.-P., Zhao, Y.-G., Xu, W.-T., Yu, Z.-W., Chen, L.-K., and Lou, P. (2015). "Random vibration analysis of train–bridge under track irregularities and traveling seismic waves using train–slab track–bridge interaction model." Journal of Sound and Vibration*, 342, 22–43.*

Zenitaka. (2010). "Sannaimaruyama Overbridge for Tohoku Shinkansen." Zenitaka Major Works*.*

Zhaohua, F., and Cook, R. D. (1983). "Beam Elements on Two-Parameter Elastic Foundations." Journal of Engineering Mechanics*, 109(6), 1390–1402.*

Zhou, Y. E., Drive, N. P., Valley, H., and Niu, B. (2012). "Considerations for Development - High-Speed Rail Bridge Design Standards." Proc., AREMA 2012 Annual Conference*, Chicago, Illinois, 47.*

For the convenience of the reader, this Appendix provides the syntax and input parameter definition (in form of screenshots as obtained from OpenSeesWiki (Gregory L. Fenves et al. 2020a) for the key OpenSees commands used in creating the HSR bridge model.

model BasicBuilder -ndm $ndm <-ndf $ndf>	
$ndm	spatial dimension of problem (1,2, or 3)
$ndf	number of degrees of freedom at node (optional)
	default value depends on value of ndm:
	ndm=1 -> ndf=1
	ndm=2 -> ndf=3
	ndm=3 -> ndf=6

Figure A-1. `model` command parameters.

node $nodeTag (ndm $coords) <-mass (ndf $massValues)>	
$nodeTag	integer tag identifying node
$coords	nodal coordinates (ndm arguments)
$massValues	nodal mass corresponding to each DOF (ndf arguments) (optional))
The optional -mass string allows analyst the option of associating nodal mass with the node	

Figure A-2. `node` command parameters.

fix $nodeTag (ndf $constrValues)	
$nodeTag	integer tag identifying the node to be constrained
$constrValues	ndf constraint values (0 or 1) corresponding to the ndf degrees-of-freedom.
	0 unconstrained (or free)
	1 constrained (or fixed)

Figure A-3. `fix` constraint command parameters.

equalDOF $rNodeTag $cNodeTag $dof1 $dof2 ...	
$rNodeTag	integer tag identifying the retained node (rNode)
$cNodeTag	integer tag identifying the constrained node (cNode)
$dof1 $dof2 ...	nodal degrees-of-freedom that are constrained at the cNode to be the same as those at the rNode
	Valid range is from 1 through ndf, the number of nodal degrees-of-freedom.

Figure A-4. `equalDOF` constraint command parameters.

For a two-dimensional problem:	
geomTransf Linear $transfTag <-jntOffset $dXi $dYi $dXj $dYj>	
For a three-dimensional problem:	
geomTransf Linear $transfTag $vecxzX $vecxzY $vecxzZ <-jntOffset $dXi $dYi $dZi $dXj $dYj $dZj>	
$transfTag	integer tag identifying transformation
	X, Y, and Z components of vecxz, the vector used to define the local x-z plane of the local-coordinate system. The local y-axis is defined by taking the cross product of the vecxz vector and the x-axis.
$vecxzX $vecxzY $vecxzZ	These components are specified in the global-coordinate system X,Y,Z and define a vector that is in a plane parallel to the x-z plane of the local-coordinate system.
	These items need to be specified for the three-dimensional problem.
$dXi $dYi $dZi	joint offset values -- offsets specified with respect to the global coordinate system for element-end node i (the number of arguments depends on the dimensions of the current model). The offset vector is oriented from node i to node j as shown in a figure below. (optional)
$dXj $dYj $dZj	joint offset values -- offsets specified with respect to the global coordinate system for element-end node j (the number of arguments depends on the dimensions of the current model). The offset vector is oriented from node i to node j as shown in a figure below. (optional)

Figure A-5. `geomTransf` *Linear transformation command parameters.*

uniaxialMaterial Steel01 $matTag $Fy $E0 $b <$a1 $a2 $a3 $a4>	
$matTag	integer tag identifying material
$Fy	yield strength
$E0	initial elastic tangent
$b	strain-hardening ratio (ratio between post-yield tangent and initial elastic tangent)
$a1	isotropic hardening parameter, increase of compression yield envelope as proportion of yield strength after a plastic strain of $a2*($Fy/E0). (optional)
$a2	isotropic hardening parameter (see explanation under $a1). (optional).
$a3	isotropic hardening parameter, increase of tension yield envelope as proportion of yield strength after a plastic strain of $a4*($Fy/E0). (optional)
$a4	isotropic hardening parameter (see explanation under $a3). (optional)

Figure A-6. `Steel01` *material command parameters.*

uniaxialMaterial Steel02 $matTag $Fy $E $b $R0 $cR1 $cR2 <$a1 $a2 $a3 $a4 $sigInit>	
$matTag	integer tag identifying material
$Fy	yield strength
$E0	initial elastic tangent
$b	strain-hardening ratio (ratio between post-yield tangent and initial elastic tangent)
$R0 $CR1 $CR2	parameters to control the transition from elastic to plastic branches. Recommended values: $R0=between 10 and 20, $cR1=0.925, $cR2=0.15
$a1	isotropic hardening parameter, increase of compression yield envelope as proportion of yield strength after a plastic strain of $a2*($Fy/E0). (optional)
$a2	isotropic hardening parameter (see explanation under $a1). (optional default = 1.0).
$a3	isotropic hardening parameter, increase of tension yield envelope as proportion of yield strength after a plastic strain of $a4*($Fy/E0). (optional default = 0.0)
$a4	isotropic hardening parameter (see explanation under $a3). (optional default = 1.0)
$sigInit	Initial Stress Value (optional, default: 0.0) the strain is calculated from epsP=$sigInit/$E if (sigInit!= 0.0) { double epsInit = sigInit/E; eps = trialStrain+epsInit; } else eps = trialStrain;

Figure A-7. `Steel02` *material command parameters.*

uniaxialMaterial Concrete02 $matTag $fpc $epsc0 $fpcu $epsU $lambda $ft $Ets	
$matTag	integer tag identifying material
$fpc	concrete compressive strength at 28 days (compression is negative)*
$epsc0	concrete strain at maximum strength*
$fpcu	concrete crushing strength *
$epsU	concrete strain at crushing strength*
$lambda	ratio between unloading slope at $epscu and initial slope
$ft	tensile strength
$Ets	tension softening stiffness (absolute value) (slope of the linear tension softening branch)

Figure A-8. `Concrete02` *material command parameters.*

uniaxialMaterial ViscousDamper $matTag $K $Cd $alpha <$LGap> < $NM $RelTol $AbsTol $MaxHalf>	
$matTag	integer tag identifying material
$K	Elastic stiffness of linear spring to model the axial flexibility of a viscous damper (e.g. combined stiffness of the supporting brace and internal damper portion)
$Cd	Damping coefficient
$alpha	Velocity exponent
$LGap	Gap length to simulate the gap length due to the pin tolerance
$NM	Employed adaptive numerical algorithm (default value NM = 1; 1 = Dormand-Prince54, 2=6th order Adams-Bashforth-Moulton, 3=modified Rosenbrock Triple)
$RelTol	Tolerance for absolute relative error control of the adaptive iterative algorithm (default value 10^-6)
$AbsTol	Tolerance for absolute error control of adaptive iterative algorithm (default value 10^-10)
$MaxHalf	Maximum number of sub-step iterations within an integration step (default value 15)

Figure A-9. `ViscousDamper` *material command parameters.*

uniaxialMaterial Elastic $matTag $E <$eta> <$Eneg>	
$matTag	integer tag identifying material
$E	tangent
$eta	damping tangent (optional, default=0.0)
$Eneg	tangent in compression (optional, default=E)

Figure A-10. `Elastic` *material command parameters.*

For a three-dimensional problem:

element elasticBeamColumn $eleTag $iNode $jNode $A $E $G $J $Iy $Iz $transfTag <-mass $massDens> <-cMass>	
$eleTag	unique element object tag
$iNode $jNode	end nodes
$A	cross-sectional area of element
$E	Young's Modulus
$G	Shear Modulus
$J	torsional moment of inertia of cross section
$Iz	second moment of area about the local z-axis
$Iy	second moment of area about the local y-axis
$transfTag	identifier for previously-defined coordinate-transformation (CrdTransf) object
$massDens	element mass per unit length (optional, default = 0.0)
-cMass	to form consistent mass matrix (optional, default = lumped mass matrix)

Figure A-11. `elasticBeamColumn` *element command parameters.*

```
element dispBeamColumn $eleTag $iNode $jNode $numIntgrPts $secTag $transfTag <-mass $massDens> <-integration
$intType>
```

To change the sections along the element length, the following form of command may be used:

```
element dispBeamColumn $eleTag $iNode $jNode $numIntgrPts -sections $secTag1 $secTag2 ... $transfTag <-mass $massDens> <-
cMass> <-integration $intType>
```

$eleTag	unique element object tag
$iNode $jNode	end nodes
$numIntgrPts	number of integration points along the element.
$secTag	identifier for previously-defined section object
$secTag1 $secTag2 ...	$numIntgrPts identifiers of previously-defined section object
$transfTag	identifier for previously-defined coordinate-transformation (CrdTransf) object
$massDens	element mass density (per unit length), from which a lumped-mass matrix is formed (optional, default = 0.0)
-cMass	to form consistent mass matrix (optional, default = lumped mass matrix)
$intType	numerical integration type, options are Lobotto, Legendre, Radau, NewtonCotes, Trapezoidal (optional, default = Legendre)

Figure A-12. `dispBeamColumn` *element command parameters.*

```
element zeroLength $eleTag $iNode $jNode -mat $matTag1 $matTag2 ... -dir $dir1 $dir2 ...<-doRayleigh $rFlag> <-orient $x1 $x2 $x3
$yp1 $yp2 $yp3>
```

$eleTag	unique element object tag
$iNode $jNode	end nodes
$matTag1 $matTag2 ...	tags associated with previously-defined UniaxialMaterials
$dir1 $dir2 ...	material directions:
	1,2,3 - translation along local x,y,z axes, respectively;
	4,5,6 - rotation about local x,y,z axes, respectively
$x1 $x2 $x3	vector components in global coordinates defining local x-axis (optional)
$yp1 $yp2 $yp3	vector components in global coordinates defining vector yp which lies in the local x-y plane for the element. (optional)
$rFlag	optional, default = 0
	rFlag = 0 NO RAYLEIGH DAMPING (default)
	rFlag = 1 include rayleigh damping

Figure A-13. `zeroLength` *element command parameters.*

```
element twoNodeLink $eleTag $iNode $jNode -mat $matTags -dir $dirs <-orient <$x1 $x2 $x3> $y1 $y2 $y3> <-pDelta (4 $Mratio)> <-
shearDist (2 $sDratios)> <-doRayleigh> <-mass $m>
```

$eleTag	unique element object tag
$iNode $jNode	end nodes
$matTags	tags associated with previously-defined UniaxialMaterial objects
$dirs	material directions:
	2D-case: 1,2 - translations along local x,y axes; 3 - rotation about local z axis
	3D-case: 1,2,3 - translations along local x,y,z axes; 4,5,6 - rotations about local x,y,z axes
$x1 $x2 $x3	vector components in global coordinates defining local x-axis (optional)
$y1 $y2 $y3	vector components in global coordinates defining local y-axis (optional)
$Mratios	P-Delta moment contribution ratios, size of ratio vector is 2 for 2D-case and 4 for 3D-case
	(entries: [My_iNode, My_jNode, Mz_iNode, Mz_jNode]) My_iNode + My_jNode <= 1.0, Mz_iNode + Mz_jNode <= 1.0.
	Remaining P-Delta moments are resisted by shear couples. (optional)
$sDratios	shear distances from iNode as a fraction of the element length, size of ratio vector is 1 for 2D-case and 2 for 3D-case
	(entries: [dy_iNode, dz_iNode] (optional, default = [0.5 0.5])
-doRayleigh	to include Rayleigh damping from the element (optional, default = no Rayleigh damping contribution)
$m	element mass (optional, default = 0.0)

Figure A-14. `twoNodeLink` element command parameters.

```
section Fiber $secTag <-GJ $GJ> {
fiber...
patch...
layer...
...
}
```

$secTag	unique tag among sections
$GJ	linear-elastic torsional stiffness assigned to the section (optional, default = no torsional stiffness)
fiber...	command to generate a single fiber
patch...	command to generate a number of fibers over a geometric cross-section
layer...	command to generate a row of fibers along a geometric-arc

Figure A-15. `section` fiber command parameters.

patch rect $matTag $numSubdivY $numSubdivZ $yI $zI $yJ $zJ

$matTag	tag of previously defined material (UniaxialMaterial tag for a FiberSection or NDMaterial tag for use in an NDFiberSection)
$numSubdivY	number of subdivisions (fibers) in the local y direction.
$numSubdivZ	number of subdivisions (fibers) in the local z direction.
$yI $zI	y & z-coordinates of vertex I (local coordinate system)
$yJ $zJ	y & z-coordinates of vertex J (local coordinate system)

Figure A-16. `patch rect` *command parameters.*

layer straight $matTag $numFiber $areaFiber $yStart $zStart $yEnd $zEnd

$matTag	material tag of previously created material (UniaxialMaterial tag for a FiberSection or NDMaterial tag for use in an NDFiberSection)
$numFibers	number of fibers along line
$areaFiber	area of each fiber
$yStart $zEnd	y and z-coordinates of first fiber in line (local coordinate system)
$$yEnd $zEnd	y and z-coordinates of last fiber in line (local coordinate system)

Figure A-17. `layer straight` *command parameters.*

section Aggregator $secTag $matTag1 $dof1 $matTag2 $dof2 .... <-section $sectionTag>

$secTag	unique section tag
$matTag1 $matTag2 ...	tag of previously-defined UniaxialMaterial objects
$dof1 $dof2 ...	the force-deformation quantity to be modeled by this section object. One of the following section dof may be used:
	P Axial force-deformation
	Mz Moment-curvature about section local z-axis
	Vy Shear force-deformation along section local y-axis
	My Moment-curvature about section local y-axis
	Vz Shear force-deformation along section local z-axis
	T Torsion Force-Deformation
$sectionTag	tag of previously-defined Section object to which the UniaxialMaterial objects are aggregated as additional force-deformation relationships

Figure A-18. `section aggregator` *command parameters.*

mass $nodeTag (ndf $massValues)	
$nodeTag	integer tag identifying node whose mass is set
$massValues	ndf nodal mass values corresponding to each DOF

Figure A-19. `mass` command parameters.

eigen <$solver> $numEigenvalues	
$numEigenvalues	number of eigenvalues required
$solver	optional string detailing type of solver: -genBandArpack, -symmBandLapack, -fullGenLapack (default: -genBandArpack)
RETURNS:	
a tcl string containing eigenvalues.	

Figure A-20. `eigen` analysis command parameters.

D = $alphaM * M + $betaK * Kcurrent +$betaKinit * Kinit + $betaKcomm * KlastCommit

rayleigh $alphaM $betaK $betaKinit $betaKcomm

$alphaM	factor applied to elements or nodes mass matrix
$betaK	factor applied to elements current stiffness matrix.
$betaKinit	factor applied to elements initial stiffness matrix.
$betaKcomm	factor applied to elements committed stiffness matrix.

Figure A-21. `Rayleigh` damping command parameters.

For a load path where the factors are specified in a tcl list with a constant time interval between points:

timeSeries Path $tag -dt $dt -values {list_of_values} <-factor $cFactor> <-useLast> <-prependZero> <-startTime $tStart>

For a load path where the factors are specified in a file for a constant time interval between points:

timeSeries Path $tag -dt $dt -filePath $filePath <-factor $cFactor> <-useLast> <-prependZero> <-startTime $tStart>

For a load path where the values are specified at non-constant time intervals:

timeSeries Path $tag -time {list_of_times} -values {list_of_values} <-factor $cFactor> <-useLast>

For a load path where both time and values are specified in a list included in the command

timeSeries Path $tag -fileTime $fileTime -filePath $filePath <-factor $cFactor> <-useLast>

$tag	unique tag among TimeSeries objects.
$filePath	file containing the load factors values
$fileTime	file containing the time values for corresponding load factors
$dT	time interval between specified points.
{list_of_times}	time values in a tcl list
{list_of_values}	load factor values in a tcl list
$cFactor	optional, a factor to multiply load factors by (default = 1.0)
-useLast	optional, to use last value after the end of the series (default = 0.0)
-prependZero	optional, to prepend a zero value to the series of load factors (default = false). See NOTES.
$tStart	optional, to provide a start time for provided load factors (default = 0.0)

Figure A-22. `timeSeries` path command parameters.

pattern UniformExcitation $patternTag $dir -accel $tsTag <-vel0 $vel0> <-fact $cFactor>
$patternTag	unique tag among load patterns
$dir	direction in which ground motion acts
	1 - corresponds to translation along the global X axis
	2 - corresponds to translation along the global Y axis
	3 - corresponds to translation along the global Z axis
	4 - corresponds to rotation about the global X axis
	5 - corresponds to rotation about the global Y axis
	6 - corresponds to rotation about the global Z axis
$tsTag	tag of the TimeSeries series defining the acceleration history.
$vel0	the initial velocity (optional, default=0.0)
$cFactor	constant factor (optional, default=1.0)

Figure A-23. `UniformExcitation` *pattern command parameters.*

This Appendix provides selected, but detailed, scripts from a sample OpenSees TCL file for modeling and analyzing a full HSR bridge system. The input files for a given bridge configuration and various train positions over the bridge vary from 17,000 to 18,000 lines and could be provided upon request from the author. Nonetheless, the provided scripts herein should be sufficient to reproduce or generate full input files.

```tcl
# Right Track and Left Track Center Line (Looking in the positive x-direction)
set R  3; # Track 1 (Right)
set L -3; # Track 2 (Left)

# Distance between train wheels in the y-direction
set wr 2

# Train Wheel Distance, Wheels are 2 m apart
set R1 [expr $R + $wr/2]; # Rail 1 (Right) in the Track 1
set R2 [expr $R - $wr/2]; # Rail 2 (Left)  in the Track 1
set R3 [expr $L + $wr/2]; # Rail 3 (Right) in the Track 2
set R4 [expr $L - $wr/2]; # Rail 4 (Left)  in the Track 2

# Rail Height
set hr 16.59; # Column height of 13.5 m + Girder depth of 3.09 m
```

```tcl
# Train Vertical Dimensions
set hpm   1.720;    # Height of centroid: Power car
set hcm   1.627;    # Height of centroid: Passenger car
set hb    0.560;    # Height of bogie COM assumption
set hp    0.605;    # Vertical distance from top of primary suspension to power car-body COM (Given in reference study)
set hm    0.420;    # Vertical distance from top of primary suspension to extreme passenger car-body COM (Given in reference study)
set hc    0.508;    # Vertical distance from top of primary suspension to intermediate passenger car-body COM (Given in reference study)

# Train Longitudinal Dimensions
set Lp   14.000;    # Length of power car (Given in reference study)
set Lm   18.700;    # Length of extreme passenger car (Given in reference study)
set Lc   18.700;    # Length of intermediate passenger car (Given in reference study)
set LT  193.150;    # Total length of train system

set w     3.000;    # Distance between same bogie axle wheels in the x-direction (Given in reference study)
set wp    3.275;    # Distance between the power car axle wheel and extreme passenger car axle wheel (Given in reference study)
set x    30.815;    # Location of last axle wheel node relative to start of bridge, depends on load case
```

Figure B-1. Predefined geometric locations for train nodes.

```
# Power Car
#       NodeTag            (X)                  (Y)    (Z)
node    70011      $x                           $R1    $hr;                              # Wheel for bogie 1
node    70012      [expr $x + $w]               $R1    $hr;                              # Wheel for bogie 1
node    80011      $x                           $R2    $hr;                              # Wheel for bogie 1
node    80012      [expr $x + $w]               $R2    $hr;                              # Wheel for bogie 1

node    71011      $x                           $R1    [expr $hr + $hb];                 # Bogie 1
node    71012      [expr $x + $w/2]             $R1    [expr $hr + $hb];                 # Bogie 1
node    71013      [expr $x + $w]               $R1    [expr $hr + $hb];                 # Bogie 1

node    610012     [expr $x + $w/2]             $R     [expr $hr + $hb];                 # Bogie 1

node    81011      $x                           $R2    [expr $hr + $hb];                 # Bogie 1
node    81012      [expr $x + $w/2]             $R2    [expr $hr + $hb];                 # Bogie 1
node    81013      [expr $x + $w]               $R2    [expr $hr + $hb];                 # Bogie 1

node    620012     [expr $x + $w/2]             $R     [expr $hr + $hpm - $hp];          # Primary Suspension for bogie 1
node    720012     [expr $x + $w/2]             $R1    [expr $hr + $hpm - $hp];          # Primary Suspension for bogie 1
node    820012     [expr $x + $w/2]             $R2    [expr $hr + $hpm - $hp];          # Primary Suspension for bogie 1

node    70021      [expr $x + $Lp]              $R1    $hr;                              # Wheel for bogie 2
node    70022      [expr $x + ($Lp + $w)]       $R1    $hr;                              # Wheel for bogie 2
node    80021      [expr $x + $Lp]              $R2    $hr;                              # Wheel for bogie 2
node    80022      [expr $x + ($Lp + $w)]       $R2    $hr;                              # Wheel for bogie 2

node    71021      [expr $x + $Lp]              $R1    [expr $hr + $hb];                 # Bogie 2
node    71022      [expr $x + $Lp + $w/2]       $R1    [expr $hr + $hb];                 # Bogie 2
node    71023      [expr $x + ($Lp + $w)]       $R1    [expr $hr + $hb];                 # Bogie 2

node    610022     [expr $x + $Lp + $w/2]       $R     [expr $hr + $hb];                 # Bogie 2

node    81021      [expr $x + $Lp]              $R2    [expr $hr + $hb];                 # Bogie 2
node    81022      [expr $x + $Lp + $w/2]       $R2    [expr $hr + $hb];                 # Bogie 2
node    81023      [expr $x + ($Lp + $w)]       $R2    [expr $hr + $hb];                 # Bogie 2

node    620022     [expr $x + $Lp + $w/2]       $R     [expr $hr + $hpm - $hp];          # Primary Suspension for bogie 2
node    720022     [expr $x + $Lp + $w/2]       $R1    [expr $hr + $hpm - $hp];          # Primary Suspension for bogie 2
node    820022     [expr $x + $Lp + $w/2]       $R2    [expr $hr + $hpm - $hp];          # Primary Suspension for bogie 2

node    63001      [expr $x + $w/2]             $R     [expr $hr + $hpm];                # Car Body 1
node    63002      [expr $x + $w/2 + $Lp/2]     $R     [expr $hr + $hpm];                # Car Body 1 (COM)
node    63003      [expr $x + $Lp + $w/2]       $R     [expr $hr + $hpm];                # Car Body 1
```

Figure B-2. Node set up for rear power car.

```
# Extreme Passenger Car
#       NodeTag            (X)                               (Y)    (Z)
node    70031      [expr $x + ($Lp + $w + $wp)]             $R1    $hr;                  # Wheel for bogie 3
node    70032      [expr $x + ($Lp + 2*$w + $wp)]          $R1    $hr;                  # Wheel for bogie 3

node    80031      [expr $x + ($Lp + $w + $wp)]             $R2    $hr;                  # Wheel for bogie 3
node    80032      [expr $x + ($Lp + 2*$w + $wp)]          $R2    $hr;                  # Wheel for bogie 3

node    71031      [expr $x + ($Lp + $w + $wp)]             $R1    [expr $hr + $hb];     # Bogie 3
node    71032      [expr $x + ($Lp + $w + $wp) + $w/2]      $R1    [expr $hr + $hb];     # Bogie 3
node    71033      [expr $x + ($Lp + 2*$w + $wp)]          $R1    [expr $hr + $hb];     # Bogie 3

node    610032     [expr $x + ($Lp + $w + $wp) + $w/2]      $R     [expr $hr + $hb];     # Bogie 3

node    81031      [expr $x + ($Lp + $w + $wp)]             $R2    [expr $hr + $hb];     # Bogie 3
node    81032      [expr $x + ($Lp + $w + $wp) + $w/2]      $R2    [expr $hr + $hb];     # Bogie 3
node    81033      [expr $x + ($Lp + 2*$w + $wp)]          $R2    [expr $hr + $hb];     # Bogie 3

node    70041      [expr $x + ($Lp + $w + $wp + $Lm)]       $R1    $hr;                  # Wheel for bogie 4
node    80041      [expr $x + ($Lp + $w + $wp + $Lm)]       $R2    $hr;                  # Wheel for bogie 4

node    71041      [expr $x + ($Lp + $w + $wp + $Lm)]       $R1    [expr $hr + $hb];     # Bogie 4
node    81041      [expr $x + ($Lp + $w + $wp + $Lm)]       $R2    [expr $hr + $hb];     # Bogie 4

node    620032     [expr $x + ($Lp + $w + $wp) + $w/2]      $R     [expr $hr + $hcm - $hm];  # Primary Suspension for bogie 3
node    720032     [expr $x + ($Lp + $w + $wp) + $w/2]      $R1    [expr $hr + $hcm - $hm];  # Primary Suspension for bogie 3
node    820032     [expr $x + ($Lp + $w + $wp) + $w/2]      $R2    [expr $hr + $hcm - $hm];  # Primary Suspension for bogie 3

node    63004      [expr $x + ($Lp + $w + $wp) + $w/2]      $R     [expr $hr + $hcm];    # Car Body 2
node    63005      [expr $x + ($Lp + $w + $wp) + $Lm/2]     $R     [expr $hr + $hcm];    # Car Body 2 (COM)
```

Figure B-3. Node set up for rear intermediate passenger car.

```
# Intermediate Passenger Cars
set n    1
#     NodeTag         (X)                                                          (Y)    (Z)
node   70042   [expr $x + ($Lp + $w + $wp + $Lm) + ($n)*3 + ($n-1)*($Lc - $w)]     $R1    $hr;               # Wheel for bogie 4
node   70051   [expr $x + ($Lp + $w + $wp + $Lm) + ($n)*3 + ($n)*($Lc - $w)]       $R1    $hr;               # Wheel for bogie 5

node   80042   [expr $x + ($Lp + $w + $wp + $Lm) + ($n)*3 + ($n-1)*($Lc - $w)]     $R2    $hr;               # Wheel for bogie 4
node   80051   [expr $x + ($Lp + $w + $wp + $Lm) + ($n)*3 + ($n)*($Lc - $w)]       $R2    $hr;               # Wheel for bogie 5

node   71042   [expr $x + ($Lp + $w + $wp + $Lm) + ($n)*3 + ($n-1)*($Lc - $w) - $w/2]   $R1    [expr $hr + $hb];   # Bogie 4
node   71043   [expr $x + ($Lp + $w + $wp + $Lm) + ($n)*3 + ($n-1)*($Lc - $w)]         $R1    [expr $hr + $hb];   # Bogie 4

node   610042  [expr $x + ($Lp + $w + $wp + $Lm) + ($n)*3 + ($n-1)*($Lc - $w) - $w/2]   $R     [expr $hr + $hb];   # Bogie 4

node   81042   [expr $x + ($Lp + $w + $wp + $Lm) + ($n)*3 + ($n-1)*($Lc - $w) - $w/2]   $R2    [expr $hr + $hb];   # Bogie 4
node   81043   [expr $x + ($Lp + $w + $wp + $Lm) + ($n)*3 + ($n-1)*($Lc - $w)]         $R2    [expr $hr + $hb];   # Bogie 4

node   71051   [expr $x + ($Lp + $w + $wp + $Lm) + ($n)*3 + ($n)*($Lc - $w)]       $R1    [expr $hr + $hb];   # Bogie 5
node   81051   [expr $x + ($Lp + $w + $wp + $Lm) + ($n)*3 + ($n)*($Lc - $w)]       $R2    [expr $hr + $hb];   # Bogie 5

node   620042  [expr $x + ($Lp + $w + $wp + $Lm) + ($n)*3 + ($n-1)*($Lc - $w) - $w/2]   $R     [expr $hr + $hcm - $hc];   # Primary Suspension for bogie 4
node   720042  [expr $x + ($Lp + $w + $wp + $Lm) + ($n)*3 + ($n-1)*($Lc - $w) - $w/2]   $R1    [expr $hr + $hcm - $hc];   # Primary Suspension for bogie 4
node   820042  [expr $x + ($Lp + $w + $wp + $Lm) + ($n)*3 + ($n-1)*($Lc - $w) - $w/2]   $R2    [expr $hr + $hcm - $hc];   # Primary Suspension for bogie 4

node   63006   [expr $x + ($Lp + $w + $wp + $Lm) + ($n)*3 + ($n-1)*($Lc - $w) - $w/2]         $R     [expr $hr + $hcm];   # Car Body 2 & 3 (Articulated)
node   63007   [expr $x + ($Lp + $w + $wp + $Lm) + ($n)*3 + ($n-1)*($Lc - $w) - $w/2 + $Lc/2]  $R     [expr $hr + $hcm];   # Car Body 3 (COM)
```

Figure B-4. Node set up for first intermediate passenger car.

```
set Ar     1e3
set Ir     1e5
set Er     1e8
set Gr     1e8
set Jr     1e6

# Bogie arms in the x-direction
#                              eleTag   iNode   jNode    A      E      G      J      Iy     Iz     transfTag
element elasticBeamColumn      30001    71011   71012   $Ar    $Er    $Gr    $Jr    $Ir    $Ir    $geomTransf
element elasticBeamColumn      30002    71012   71013   $Ar    $Er    $Gr    $Jr    $Ir    $Ir    $geomTransf
```

Figure B-5. Rigid elastic beam-column element for bogie arms in the x-direction.

```
# Bogie arms in the y-direction
#                              eleTag   iNode   jNode    A      E      G      J      Iy     Iz     transfTag
element elasticBeamColumn      30087    71012   610012  $Ar    $Er    $Gr    $Jr    $Ir    $Ir    $geomTransf
element elasticBeamColumn      30088    610012  81012   $Ar    $Er    $Gr    $Jr    $Ir    $Ir    $geomTransf
```

Figure B-6. Rigid elastic beam-column element for bogie arms in the y-direction.

```
# Primary Suspension arms in the y-direction
#                              eleTag   iNode   jNode    A      E      G      J      Iy     Iz     transfTag
element elasticBeamColumn      30122    620012  720012  $Ar    $Er    $Gr    $Jr    $Ir    $Ir    $geomTransf
element elasticBeamColumn      30123    620012  820012  $Ar    $Er    $Gr    $Jr    $Ir    $Ir    $geomTransf
```

Figure B-7. Rigid elastic beam-column element for primary suspension arms in the y-direction.

```
# Connection for car-body ends to Primary Suspension system in the z-direction
#                              eleTag   iNode   jNode    A      E      G      J      Iy     Iz     transfTag
element elasticBeamColumn      30074    620012  63001   $Ar    $Er    $Gr    $Jr    $Ir    $Ir    $geomTransf
element elasticBeamColumn      30075    620022  63003   $Ar    $Er    $Gr    $Jr    $Ir    $Ir    $geomTransf
```

Figure B-8. Rigid elastic beam-column element for primary suspension arms in the z-direction.

```
# Connecting car-bodies in the x-direction
# All car-bodies except the power cars are connected due to the articulated bogie system
#                        eleTag    iNode    jNode     A      E      G      J      Iy     Iz     transfTag
element elasticBeamColumn  30053    63001    63002   $Ar    $Er    $Gr    $Jr    $Ir    $Ir    $geomTransf
element elasticBeamColumn  30054    63002    63003   $Ar    $Er    $Gr    $Jr    $Ir    $Ir    $geomTransf
element elasticBeamColumn  30055    63004    63005   $Ar    $Er    $Gr    $Jr    $Ir    $Ir    $geomTransf
element elasticBeamColumn  30056    63005    63006   $Ar    $Er    $Gr    $Jr    $Ir    $Ir    $geomTransf
element elasticBeamColumn  30057    63006    63007   $Ar    $Er    $Gr    $Jr    $Ir    $Ir    $geomTransf
```

Figure B-9. Rigid elastic beam-column element for car-bodies.

```
# Power Car
set Kapx    40000
set Kapy     9000
set Kapz     1250

set Capz       10

# Stiffness
uniaxialMaterial Elastic        40    $Kapx;                  # x-direction
uniaxialMaterial Elastic        41    $Kapy;                  # y-direction
uniaxialMaterial Elastic        42    $Kapz;                  # z-direction
# Damping
uniaxialMaterial ViscousDamper  43    0    $Capz    0.01;  # z-direction
# Combined
uniaxialMaterial Parallel       44    42    43;              # z-direction

#                     eleTag   iNode     jNode     matTag...         dir...        orient...
element twoNodeLink    301262   71011    70011    -mat 40 41 44    -dir 1 2 3    -orient 1 0 0 0 1 0
element twoNodeLink    301263   71013    70012    -mat 40 41 44    -dir 1 2 3    -orient 1 0 0 0 1 0
element twoNodeLink    301264   71021    70021    -mat 40 41 44    -dir 1 2 3    -orient 1 0 0 0 1 0
element twoNodeLink    301265   71023    70022    -mat 40 41 44    -dir 1 2 3    -orient 1 0 0 0 1 0

element twoNodeLink    301370   81011    80011    -mat 40 41 44    -dir 1 2 3    -orient 1 0 0 0 1 0
element twoNodeLink    301371   81013    80012    -mat 40 41 44    -dir 1 2 3    -orient 1 0 0 0 1 0
element twoNodeLink    301372   81021    80021    -mat 40 41 44    -dir 1 2 3    -orient 1 0 0 0 1 0
element twoNodeLink    301373   81023    80022    -mat 40 41 44    -dir 1 2 3    -orient 1 0 0 0 1 0

element twoNodeLink    301366   71121    70121    -mat 40 41 44    -dir 1 2 3    -orient 1 0 0 0 1 0
element twoNodeLink    301367   71123    70122    -mat 40 41 44    -dir 1 2 3    -orient 1 0 0 0 1 0
element twoNodeLink    301368   71131    70131    -mat 40 41 44    -dir 1 2 3    -orient 1 0 0 0 1 0
element twoNodeLink    301369   71133    70132    -mat 40 41 44    -dir 1 2 3    -orient 1 0 0 0 1 0

element twoNodeLink    301374   81121    80121    -mat 40 41 44    -dir 1 2 3    -orient 1 0 0 0 1 0
element twoNodeLink    301375   81123    80122    -mat 40 41 44    -dir 1 2 3    -orient 1 0 0 0 1 0
element twoNodeLink    301476   81131    80131    -mat 40 41 44    -dir 1 2 3    -orient 1 0 0 0 1 0
element twoNodeLink    301477   81133    80132    -mat 40 41 44    -dir 1 2 3    -orient 1 0 0 0 1 0
```

Figure B-10. Primary suspension system model for the power cars.

```
# Constraining the other DOFs
#               iNode         jNode          DOFs...
equalDOF        71011         70011          4 5 6
equalDOF        71013         70012          4 5 6
equalDOF        71021         70021          4 5 6
equalDOF        71023         70022          4 5 6

equalDOF        81011         80011          4 5 6
equalDOF        81013         80012          4 5 6
equalDOF        81021         80021          4 5 6
equalDOF        81023         80022          4 5 6

equalDOF        71121         70121          4 5 6
equalDOF        71123         70122          4 5 6
equalDOF        71131         70131          4 5 6
equalDOF        71133         70132          4 5 6

equalDOF        81121         80121          4 5 6
equalDOF        81123         80122          4 5 6
equalDOF        81131         80131          4 5 6
equalDOF        81133         80132          4 5 6
```

Figure B-11. Power car primary suspension node MP-constraints with `equalDOF`.

```
# Power Car
set Kpx       303
set Kpy       303
set Kpz      1270

set Cpy       100
set Cpz        20
set Cpphi    4230

# Stiffness
uniaxialMaterial Elastic          10      $Kpx;                    # x-direction
uniaxialMaterial Elastic          11      $Kpy;                    # y-direction
uniaxialMaterial Elastic          12      $Kpz;                    # z-direction
uniaxialMaterial Elastic          13        1;                     # rz-direction
# Damping
uniaxialMaterial ViscousDamper    14      0      $Cpy    0.01;    # y-direction
uniaxialMaterial ViscousDamper    15      0      $Cpz    0.01;    # z-direction
uniaxialMaterial ViscousDamper    16      0      $Cpphi  0.01;    # rz-direction
# Combined
uniaxialMaterial Parallel         17      11     14;              # y-direction
uniaxialMaterial Parallel         18      12     15;              # z-direction
uniaxialMaterial Parallel         19      13     16;              # rz-direction

#                   eleTag   iNode      jNode      matTag...        dir...          orient...
element twoNodeLink  300002  71012      720012     -mat 10 17 18    -dir 1 2 3      -orient 1 0 0 0 1 0
element twoNodeLink  300001  610012     620012     -mat 19          -dir 6          -orient 1 0 0 0 1 0
element twoNodeLink  300003  81012      820012     -mat 10 17 18    -dir 1 2 3      -orient 1 0 0 0 1 0

element twoNodeLink  300005  71022      720022     -mat 10 17 18    -dir 1 2 3      -orient 1 0 0 0 1 0
element twoNodeLink  300004  610022     620022     -mat 19          -dir 6          -orient 1 0 0 0 1 0
element twoNodeLink  300006  81022      820022     -mat 10 17 18    -dir 1 2 3      -orient 1 0 0 0 1 0

element twoNodeLink  300008  71122      720122     -mat 10 17 18    -dir 1 2 3      -orient 1 0 0 0 1 0
element twoNodeLink  300007  610122     620122     -mat 19          -dir 6          -orient 1 0 0 0 1 0
element twoNodeLink  300009  81122      820122     -mat 10 17 18    -dir 1 2 3      -orient 1 0 0 0 1 0

element twoNodeLink  300011  71132      720132     -mat 10 17 18    -dir 1 2 3      -orient 1 0 0 0 1 0
element twoNodeLink  300010  610132     620132     -mat 19          -dir 6          -orient 1 0 0 0 1 0
element twoNodeLink  300012  81132      820132     -mat 10 17 18    -dir 1 2 3      -orient 1 0 0 0 1 0
```

Figure B-12. Secondary suspension system model for the power cars.

```
# Constraining the other DOFs
#                iNode        jNode        DOFs...
equalDOF         71012        720012       4 5 6
equalDOF         610012       620012       1 2 3 4 5
equalDOF         81012        820012       4 5 6

equalDOF         71022        720022       4 5 6
equalDOF         610022       620022       1 2 3 4 5
equalDOF         81022        820022       4 5 6

equalDOF         71122        720122       4 5 6
equalDOF         610122       620122       1 2 3 4 5
equalDOF         81122        820122       4 5 6

equalDOF         71132        720132       4 5 6
equalDOF         610132       620132       1 2 3 4 5
equalDOF         81132        820132       4 5 6
```

Figure B-13. Power car secondary suspension node MP-constraints with `equalDOF`.

```
# Car Body

# Power Car
set mass    54.960
set massxx 59.4
set massyy 1132.8
set masszz 1112.9

#       nodeTag  ndf1    ndf2    ndf3    ndf4      ndf5      ndf6
mass    63002    $mass   $mass   $mass   $massxx   $massyy   $masszz
mass    63022    $mass   $mass   $mass   $massxx   $massyy   $masszz

# Extreme Passenger Car
set mass    26.000
set massxx 33.94
set massyy 971.81
set masszz 971.81

#       nodeTag  ndf1    ndf2    ndf3    ndf4      ndf5      ndf6
mass    63005    $mass   $mass   $mass   $massxx   $massyy   $masszz
mass    63019    $mass   $mass   $mass   $massxx   $massyy   $masszz

# Intermediate Passenger Car
#       nodeTag  ndf1    ndf2    ndf3    ndf4      ndf5      ndf6
mass    63007    $mass   $mass   $mass   $massxx   $massyy   $masszz
mass    63009    $mass   $mass   $mass   $massxx   $massyy   $masszz
mass    63011    $mass   $mass   $mass   $massxx   $massyy   $masszz
mass    63013    $mass   $mass   $mass   $massxx   $massyy   $masszz
mass    63015    $mass   $mass   $mass   $massxx   $massyy   $masszz
mass    63017    $mass   $mass   $mass   $massxx   $massyy   $masszz
```

Figure B-14. Mass assignment for train car-bodies.

```
# Bogie

# Power Car
set mass    2.420
set massxx 1.645
set massyy 2.593
set masszz 3.068

#         nodeTag   ndf1    ndf2    ndf3     ndf4      ndf5      ndf6
mass      610012  $mass   $mass   $mass   $massxx   $massyy   $masszz
mass      610022  $mass   $mass   $mass   $massxx   $massyy   $masszz
mass      610122  $mass   $mass   $mass   $massxx   $massyy   $masszz
mass      610132  $mass   $mass   $mass   $massxx   $massyy   $masszz

# Extreme Passenger Car
set mass    2.514
set massxx 2.07
set massyy 3.26
set masszz 3.86

#         nodeTag   ndf1    ndf2    ndf3     ndf4      ndf5      ndf6
mass      610032  $mass   $mass   $mass   $massxx   $massyy   $masszz
mass      610112  $mass   $mass   $mass   $massxx   $massyy   $masszz

# Intermediate Passenger Car
set mass    3.050
set massxx 2.03
set massyy 3.20
set masszz 3.79

#         nodeTag   ndf1    ndf2    ndf3     ndf4      ndf5      ndf6
mass      610042  $mass   $mass   $mass   $massxx   $massyy   $masszz
mass      610052  $mass   $mass   $mass   $massxx   $massyy   $masszz
mass      610062  $mass   $mass   $mass   $massxx   $massyy   $masszz
mass      610072  $mass   $mass   $mass   $massxx   $massyy   $masszz
mass      610082  $mass   $mass   $mass   $massxx   $massyy   $masszz
mass      610092  $mass   $mass   $mass   $massxx   $massyy   $masszz
mass      610102  $mass   $mass   $mass   $massxx   $massyy   $masszz
```

Figure B-15. Mass assignment for train bogies.

```
# Wheel

# Power and Extreme Passenger Car
set mass    1.025
set massxx 1.03
set massyy 0.0008
set masszz 1.03

#         nodeTag   ndf1    ndf2    ndf3     ndf4      ndf5      ndf6
mass      70011   $mass   $mass   $mass   $massxx   $massyy   $masszz
mass      70012   $mass   $mass   $mass   $massxx   $massyy   $masszz
mass      70021   $mass   $mass   $mass   $massxx   $massyy   $masszz
mass      70022   $mass   $mass   $mass   $massxx   $massyy   $masszz
mass      70031   $mass   $mass   $mass   $massxx   $massyy   $masszz
mass      70032   $mass   $mass   $mass   $massxx   $massyy   $masszz
mass      70111   $mass   $mass   $mass   $massxx   $massyy   $masszz
mass      70112   $mass   $mass   $mass   $massxx   $massyy   $masszz
mass      70121   $mass   $mass   $mass   $massxx   $massyy   $masszz
mass      70122   $mass   $mass   $mass   $massxx   $massyy   $masszz
mass      70131   $mass   $mass   $mass   $massxx   $massyy   $masszz
mass      70132   $mass   $mass   $mass   $massxx   $massyy   $masszz

mass      80011   $mass   $mass   $mass   $massxx   $massyy   $masszz
mass      80012   $mass   $mass   $mass   $massxx   $massyy   $masszz
mass      80021   $mass   $mass   $mass   $massxx   $massyy   $masszz
mass      80022   $mass   $mass   $mass   $massxx   $massyy   $masszz
mass      80031   $mass   $mass   $mass   $massxx   $massyy   $masszz
mass      80032   $mass   $mass   $mass   $massxx   $massyy   $masszz
mass      80111   $mass   $mass   $mass   $massxx   $massyy   $masszz
mass      80112   $mass   $mass   $mass   $massxx   $massyy   $masszz
mass      80121   $mass   $mass   $mass   $massxx   $massyy   $masszz
mass      80122   $mass   $mass   $mass   $massxx   $massyy   $masszz
mass      80131   $mass   $mass   $mass   $massxx   $massyy   $masszz
mass      80132   $mass   $mass   $mass   $massxx   $massyy   $masszz
```

Figure B-16. Mass assignment for power and exterior passenger car axle wheels.

```
# Intermediate Passenger Car
set mass   1.000
set massxx 1.03
set massyy 0.0008
set masszz 1.03

#      nodeTag   ndf1    ndf2    ndf3    ndf4     ndf5     ndf6
mass    70041   $mass   $mass   $mass   $massxx  $massyy  $masszz
mass    70042   $mass   $mass   $mass   $massxx  $massyy  $masszz
mass    70051   $mass   $mass   $mass   $massxx  $massyy  $masszz
mass    70052   $mass   $mass   $mass   $massxx  $massyy  $masszz
mass    70061   $mass   $mass   $mass   $massxx  $massyy  $masszz
mass    70062   $mass   $mass   $mass   $massxx  $massyy  $masszz
mass    70071   $mass   $mass   $mass   $massxx  $massyy  $masszz
mass    70072   $mass   $mass   $mass   $massxx  $massyy  $masszz
mass    70081   $mass   $mass   $mass   $massxx  $massyy  $masszz
mass    70082   $mass   $mass   $mass   $massxx  $massyy  $masszz
mass    70091   $mass   $mass   $mass   $massxx  $massyy  $masszz
mass    70092   $mass   $mass   $mass   $massxx  $massyy  $masszz
mass    70101   $mass   $mass   $mass   $massxx  $massyy  $masszz
mass    70102   $mass   $mass   $mass   $massxx  $massyy  $masszz


mass    80041   $mass   $mass   $mass   $massxx  $massyy  $masszz
mass    80042   $mass   $mass   $mass   $massxx  $massyy  $masszz
mass    80051   $mass   $mass   $mass   $massxx  $massyy  $masszz
mass    80052   $mass   $mass   $mass   $massxx  $massyy  $masszz
mass    80061   $mass   $mass   $mass   $massxx  $massyy  $masszz
mass    80062   $mass   $mass   $mass   $massxx  $massyy  $masszz
mass    80071   $mass   $mass   $mass   $massxx  $massyy  $masszz
mass    80072   $mass   $mass   $mass   $massxx  $massyy  $masszz
mass    80081   $mass   $mass   $mass   $massxx  $massyy  $masszz
mass    80082   $mass   $mass   $mass   $massxx  $massyy  $masszz
mass    80091   $mass   $mass   $mass   $massxx  $massyy  $masszz
mass    80092   $mass   $mass   $mass   $massxx  $massyy  $masszz
mass    80101   $mass   $mass   $mass   $massxx  $massyy  $masszz
mass    80102   $mass   $mass   $mass   $massxx  $massyy  $masszz
```

Figure B-17. Mass assignment for intermediate passenger car axle wheels.

```
# Rail 1
#      nodeTag        (x)       (y)       (z)
node    10001        0.000     $R1       $hr
node    10002        3.195     $R1       $hr
node    10003        6.390     $R1       $hr
```

Figure B-18. Node set up for rail 1 of track 1.

```
# Track 1 Base Plate
#      nodeTag        (x)       (y)       (z)
node    51001        0.000     $R        $hr
node    51002        3.195     $R        $hr
```

Figure B-19. Node set up for base plate of track 1.

```
# Track 1 Track Plate
#      nodeTag        (x)       (y)       (z)
node    52001        0.000     $R        $hr
node    52002        3.195     $R        $hr
```

Figure B-20. Node set up for track plate of track 1.

```
set Ar    7.75e-3;   # Cross-Sectional Area (m2)
set Iyr   5e-6;      # Moment of Inertia 1 (m4)
set Izr   3.20e-5;   # Moment of Inertia 2 (m4)
set Jr    2e-6;      # Torque (kN-m)
set Gr    8.05e6;    # Shear Modulus (kN/m2)
set Er    2.06e8;    # Modulus of Elasticity (kN/m2)


#                         eleTag    iNode    jNode     A     E     G     J     Iy     Iz     transfTag
element elasticBeamColumn   9000    31001    31002    $Ar   $Er   $Gr   $Jr   $Iyr   $Izr   $geomTransf
element elasticBeamColumn   9001    31002    31003    $Ar   $Er   $Gr   $Jr   $Iyr   $Izr   $geomTransf
```

Figure B-21. Elastic beam-column element for rail 3 of track 2.

```
set Atp    5.10e-1;  # Cross-Sectional Area (m2)
set Iztp   1.70e3;   # Moment of Inertia 1 (m4)
set Iytp   2.76e-1;  # Moment of Inertia 2 (m4)
set Jtp    6.8e-3;   # Torque (kN-m)
set Gtp    1.48e7;   # Shear Modulus (kN/m2)
set Etp    3.55e7;   # Modulus of Elasticity (kN/m2)


#                         eleTag    iNode    jNode     A      E      G      J      Iy      Iz      transfTag
element elasticBeamColumn   659    52001    52002    $Atp   $Etp   $Gtp   $Jtp   $Iytp   $Iztp   $geomTransf
element elasticBeamColumn   660    52002    52003    $Atp   $Etp   $Gtp   $Jtp   $Iytp   $Iztp   $geomTransf
```

Figure B-22. Elastic beam-column element for track plates of track 1.

```
set Abp    5.61e-1;  # Cross-Sectional Area (m2)
set Izbp   1.69e-3;  # Moment of Inertia 1 (m4)
set Iybp   4.06e-1;  # Moment of Inertia 2 (m4)
set Jbp    6.74e-3;  # Torque (kN-m)
set Gbp    1.25e7;   # Shear Modulus (kN/m2)
set Ebp    3.00e7;   # Modulus of Elasticity (kN/m2)


#                         eleTag    iNode    jNode     A      E      G      J      Iy      Iz      transfTag
element elasticBeamColumn   441    51001    51002    $Abp   $Ebp   $Gbp   $Jbp   $Iybp   $Izbp   $geomTransf
element elasticBeamColumn   442    51002    51003    $Abp   $Ebp   $Gbp   $Jbp   $Iybp   $Izbp   $geomTransf
```

Figure B-23. Elastic beam-column element for base plates of track 1.

```
# Fastener
set Fyf   15
set dyf   0.002
set K1f   [expr $Fyf/$dyf]

uniaxialMaterial Steel01 600 $Fyf $K1f 0.0

#                     eleTag    iNode    jNode     -mat matTag1...    -dir dir1...
element zeroLength     1317    10001    11001     -mat   600         -dir   1
element zeroLength     1318    10002    11002     -mat   600         -dir   1
```

Figure B-24. Zero-length element for fastener

```
# Lateral Blocking
set Fyl   453
set dyl   0.002
set K1l   [expr $Fyl/$dyl]

uniaxialMaterial Steel01 900 $Fyl $K1l 0.0

#                       eleTag   iNode   jNode   -mat matTag1...   -dir dir1...
element zeroLength      1757     10001   11001   -mat  900         -dir  2
element zeroLength      1758     10002   11002   -mat  900         -dir  2
```

Figure B-25. Zero-length element for lateral blocking.

```
# CA Mortar Layer
set Fyca   41.5
set dyca   0.0005
set K1ca   [expr $Fyca/$dyca]

uniaxialMaterial Steel01 500 $Fyca $K1ca 0.0

#                       eleTag   iNode   jNode   -mat matTag1...   -dir dir1...
element zeroLength      1097     51001   52001   -mat  500         -dir  1
element zeroLength      1098     51002   52002   -mat  500         -dir  1
```

Figure B-26. Zero-length element for CA layer.

```
# Sliding Layer
set Fys   6
set dys   0.0005
set K1s   [expr $Fys/$dys]

uniaxialMaterial Steel01 700 $Fys $K1s 0.0

#                       eleTag   iNode   jNode   -mat matTag1...   -dir dir1...
element zeroLength      877      50001   51001   -mat  700         -dir  1
element zeroLength      878      50002   51002   -mat  700         -dir  1
```

Figure B-27. Zero-length element for sliding layer.

```
# Shear Reinforcement
set Fysr   22.5
set dysr   0.000075
set K1sr   [expr $Fysr/$dysr]

uniaxialMaterial Steel01 800 $Fysr $K1sr 0.0

#                       eleTag   iNode   jNode   -mat matTag1...   -dir dir1...
element zeroLength      2197     50001   51001   -mat 800 800      -dir 1 2
element zeroLength      2198     50011   51011   -mat 800 800      -dir 1 2
```

Figure B-28. Zero-length element for shear reinforcement.

```
equalDOF    51001   52001   2   3   4   5   6
equalDOF    51002   52002   2   3   4   5   6
```

Figure B-29. CA layer node MP-constraints with `equalDOF`.

```
# Rail
set mass    0.1693
set massxx 0.0025
set massyy 0.1459
set masszz 0.1446


#       nodeTag    ndf1      ndf2      ndf3      ndf4      ndf5      ndf6
mass     11001    $mass     $mass     $mass     $massxx   $massyy   $masszz
mass     11002    $mass     $mass     $mass     $massxx   $massyy   $masszz
```

Figure B-30. Mass assignment for first two rail 1 nodes.

```
#       nodeTag      (x)      (y)      (z)
node     90001       0        0        $yg; # Span 1
node     90002       3.195    0        $yg
node     90003       6.390    0        $yg
node     90004       9.585    0        $yg
node     90005       12.780   0        $yg
node     90006       15.975   0        $yg
node     90007       19.170   0        $yg
node     90008       22.365   0        $yg
node     90009       25.560   0        $yg
node     90010       28.755   0        $yg
node     90011       31.950   0        $yg
node     90012       32.000   0        $yg; # 0.05 m gap
```

Figure B-31. Node set up for the first bridge girder span.

```
set Ad    9.06;            # As given in Li et al.'s study
set Ed    2.45e7;          # Decreased from 3.45e7 to be conservative
set Gd    1.44e7;          # As given in Li et al.'s study
set Jd    22.6;            # As given in Li et al.'s study
set Iyd   [expr 0.7*11.0]; # Decreased by 30% to be conservative
set Izd   [expr 0.7*94.8]; # Decreased by 30% to be conservative

# 1                        eleTag    iNode     jNode     A      E     G     J     Iy      Iz      transfTag
element elasticBeamColumn    3311     90001     90002    $Ad    $Ed   $Gd   $Jd   $Iyd    $Izd    $geomTransf
element elasticBeamColumn    3312     90002     90003    $Ad    $Ed   $Gd   $Jd   $Iyd    $Izd    $geomTransf
element elasticBeamColumn    3313     90003     90004    $Ad    $Ed   $Gd   $Jd   $Iyd    $Izd    $geomTransf
element elasticBeamColumn    3314     90004     90005    $Ad    $Ed   $Gd   $Jd   $Iyd    $Izd    $geomTransf
element elasticBeamColumn    3315     90005     90006    $Ad    $Ed   $Gd   $Jd   $Iyd    $Izd    $geomTransf
element elasticBeamColumn    3316     90006     90007    $Ad    $Ed   $Gd   $Jd   $Iyd    $Izd    $geomTransf
element elasticBeamColumn    3317     90007     90008    $Ad    $Ed   $Gd   $Jd   $Iyd    $Izd    $geomTransf
element elasticBeamColumn    3318     90008     90009    $Ad    $Ed   $Gd   $Jd   $Iyd    $Izd    $geomTransf
element elasticBeamColumn    3319     90009     90010    $Ad    $Ed   $Gd   $Jd   $Iyd    $Izd    $geomTransf
element elasticBeamColumn    3320     90010     90011    $Ad    $Ed   $Gd   $Jd   $Iyd    $Izd    $geomTransf
# 2                        eleTag    iNode     jNode     A      E     G     J     Iy      Iz      transfTag
element elasticBeamColumn    3322     90012     90013    $Ad    $Ed   $Gd   $Jd   $Iyd    $Izd    $geomTransf
element elasticBeamColumn    3323     90013     90014    $Ad    $Ed   $Gd   $Jd   $Iyd    $Izd    $geomTransf
element elasticBeamColumn    3324     90014     90015    $Ad    $Ed   $Gd   $Jd   $Iyd    $Izd    $geomTransf
element elasticBeamColumn    3325     90015     90016    $Ad    $Ed   $Gd   $Jd   $Iyd    $Izd    $geomTransf
element elasticBeamColumn    3326     90016     90017    $Ad    $Ed   $Gd   $Jd   $Iyd    $Izd    $geomTransf
element elasticBeamColumn    3327     90017     90018    $Ad    $Ed   $Gd   $Jd   $Iyd    $Izd    $geomTransf
element elasticBeamColumn    3328     90018     90019    $Ad    $Ed   $Gd   $Jd   $Iyd    $Izd    $geomTransf
element elasticBeamColumn    3329     90019     90020    $Ad    $Ed   $Gd   $Jd   $Iyd    $Izd    $geomTransf
element elasticBeamColumn    3330     90020     90021    $Ad    $Ed   $Gd   $Jd   $Iyd    $Izd    $geomTransf
element elasticBeamColumn    3331     90021     90022    $Ad    $Ed   $Gd   $Jd   $Iyd    $Izd    $geomTransf
```

Figure B-32. Example elastic beam-column elements for bridge girder.

```
# Nodes for Bridge Bearing
set Rb   2; # Right Side
set Lb  -2; # Left Side
# Assume bearing distance 3.3m
#       nodeTag         (x)         (y)         (z)
node    1101          0.000       $Lb        13.500
node    1102          0.000       $Rb        13.500
node    1103         31.950       $Lb        13.500
node    1104         31.950       $Rb        13.500
node    2101          0.000       $Lb        13.500
node    2102          0.000       $Rb        13.500
node    2103         31.950       $Lb        13.500
node    2104         31.950       $Rb        13.500
```

Figure B-33. Node set up for bearings supporting the first span of the bridge.

```
# Fixed Bearing
set Fybear1   5000
set dybear1   0.002
set K1bear1   [expr $Fybear1/$dybear1]
uniaxialMaterial Steel01 300 $Fybear1 $K1bear1 0.0

#                        eleTag   iNode   jNode    -mat matTag1...   -dir dir1...
element    zeroLength     3475    1101    2101     -mat 300 300      -dir 1 2
element    zeroLength     3476    1103    2103     -mat 300 300      -dir 1 2
element    zeroLength     3477    1106    2106     -mat 300 300      -dir 1 2
element    zeroLength     3478    1108    2108     -mat 300 300      -dir 1 2
```

Figure B-34. Zero-length elements for fixed bearings supporting the first span of the bridge.

```
# Sliding Bearing
set Fybear2   470
set dybear2   0.002
set K1bear2   [expr $Fybear2/$dybear2]
uniaxialMaterial Steel01 400 $Fybear2 $K1bear2 0.0

#                        eleTag    iNode    jNode    -mat matTag1...   -dir dir1...
element   zeroLength      3495     1102     2102     -mat 400 400      -dir 1 2
element   zeroLength      3496     1104     2104     -mat 400 400      -dir 1 2
element   zeroLength      3497     1105     2105     -mat 400 400      -dir 1 2
element   zeroLength      3498     1107     2107     -mat 400 400      -dir 1 2
```

Figure B-35. Zero-length elements for sliding bearings supporting the first span of the bridge.

```
# Constraining DOF for bearing nodes
equalDOF     1101     2101     3    4    5    6
equalDOF     1102     2102     3    4    5    6
equalDOF     1103     2103     3    4    5    6
equalDOF     1104     2104     3    4    5    6
```

Figure B-36. Bearing node MP-constraints with `equalDOF`*.*

```
# Nominal concrete compressive strength
set fc      28890;                         # Concrete compressive strength(KN/m2)
set nu      0.2;                           # Concrete Poisson's ratio
set Ec   [expr 4700*sqrt($fc/1e3)*1e3];    # Concrete elastic modulus(KN/m2)
set Gc   [expr $Ec/(2*(1+$nu))];           # Concrete shear modulus(KN/m2)

# Cover concrete (un-confined)
set fc1U    $fc;                           # Unconfined concrete, maximum stress
set eps1U  -0.003;                         # Strain at maximum strength of unconfined concrete
set fc2U    [expr 0.2*$fc1U];              # Ultimate stress(KN/m2)
set eps2U  -0.01;                          # Strain at ultimate stress
set lambda  0.1;                           # Ratio between unloading slope at $eps2 and initial slope $Ec

# Core concrete (confined)
set Kfc     1.3;                           # Ratio of confined to unconfined concrete strength
set fc1C    [expr $Kfc*$fc]     ;          # Confined concrete (Mander model), maximum stress(KN/m2)
set eps1C   [expr 2.*$fc1C/$Ec];           # Strain at maximum stress
set fc2C    [expr 0.2*$fc1C]    ;          # Ultimate stress(KN/m2)
set eps2C   [expr 5*$eps1C]     ;          # Strain at ultimate stress

# Tensile-strength properties
set ftC     [expr -0.14*$fc1C];            # Tensile strength + tension confined concrete(KN/m2)
set ftU     [expr -0.14*$fc1U];            # Tensile strength + tension unconfined concrete(KN/m2)
set Ets     [expr $ftU/0.002];             # Tension softening stiffness(KN/m2)

# Reinforcing steel
set fys     483510;                        # Reinforcing steel yield strength(KN/m2)
set fsu     725266;                        # Reinforcing steel ultimate strength(KN/m2)
set Es      200000000;                     # Reinforcing steel elastic modulus(KN/m2)
set b       0.005;                         # Strain-hardening ratio
set R0      15;                            # Parameters to control the transition from elastic to plastic branches
set cR1     0.925;                         # Parameters to control the transition from elastic to plastic branches
set cR2     0.15;                          # Parameters to control the transition from elastic to plastic branches
```

```
# General Cross-Section      matTag    E
uniaxialMaterial Elastic        5      1e10

# Cover Concrete             matTag   fpc      epsc     fpcu     epsU      lambda     ft     Ets
uniaxialMaterial Concrete02    1     $fc1C    $eps1C   $fc2C   $eps2C    $lambda   $ftC   $Ets

# Core Concrete              matTag   fpc      epsc     fpcu     epsU      lambda     ft     Ets
uniaxialMaterial Concrete02    2     $fc1U    $eps1U   $fc2U   $eps2U    $lambda   $ftU   $Ets

# Reinforcing Steel          matTag   Fy       E        b        R0       cR1      cR2
uniaxialMaterial Steel02       3     $fys     $Es      $b       $R0      $cR1     $cR2
```

Figure B-37. Material properties for pier columns.

```
# Cross-Section of Column

section Fiber 1 -GJ 0 {

# Cover concrete      tag    divY      divZ        yI              zI              yJ              zJ
patch rect             1    $divy     $divz    [expr -$ycol/2]  [expr -$zcol/2]  [expr $ycol/2]  [expr $zcol/2]

# Core concrete       tag      divY            divZ           yI       zI      yJ      zJ
patch rect             2   [expr (2*$divy)]  [expr (2*$divz)]  $yy1    $zz1    $yy2    $zz2

# Reinforcing Steel   tag    Nbar     Abar    yStart    zStart    yEnd     zEnd
layer straight         3    $Nbar1   $Abar    $y1       $z1       $y5      $y5

layer straight         3    $Nbar1   $Abar    $y4       $z4       $y8      $y8

layer straight         3    $Nbar2   $Abar    $y2       $z2       $y3      $y3

layer straight         3    $Nbar2   $Abar    $y6       $z6       $y7      $y7
}

#                    secTag   matTag   dofl    sectionTag
section Aggregator    100       5       T      -section 1
```

Figure B-38. Section designer for pier cross-section.

```
set Dtran 12.7e-3;   # Transverse reinforcement diameter (m)
set Abar  1006e-3;   # Longitudinal reinforcement area (m2)
set Dbar  35.81e-3;  # Longitudinal reinforcement diameter (m)
set Nbar1  28;       # Number of bars on short end
set Nbar2  60;       # Number of bars on long end
set cc    0.04;      # Assumption of clear cover (m)
set ycol  5.434;     # Y dimension of column (m)
set zcol  2.50;      # Z dimension of column (m)
set divy  6;         # Number of subdivisions in the local y-direction
set divz  3;         # Number of subdivisions in the local z-direction
set s [expr (($ycol - 2*($cc + $Dtran) - $Dbar)/($Nbar2))]; # Spacing of bars in the y-direction (m)


# --------------------------------------------------------------------------

# Coordinates within the column cross-section to define section
set yy1 [expr -($ycol/2 - ($cc + $Dtran))]
set zz1 [expr -($zcol/2 - ($cc + $Dtran))]
set yy2 [expr ($ycol/2 - ($cc + $Dtran))]
set zz2 [expr ($zcol/2 - ($cc + $Dtran))]

set y1 [expr -($ycol/2 - ($cc + $Dtran + 0.5*$Dbar))]
set z1 [expr -($zcol/2 - ($cc + $Dtran + 0.5*$Dbar))]
set y2 [expr -($ycol/2 - ($cc + $Dtran + 0.5*$Dbar-$s))]
set z2 $z1
set y3 [expr ($ycol/2 - ($cc + $Dtran + 0.5*$Dbar-$s))]
set z3 $z1
set y4 [expr ($ycol/2 - ($cc + $Dtran + 0.5*$Dbar))]
set z4 $z1
set y5 $y1
set z5 [expr ($zcol/2 - ($cc + $Dtran + 0.5*$Dbar))]
set y6 $y2
set z6 $z5
set y7 $y3
set z7 $z5
set y8 $y4
set z8 $z5
```

Figure B-39. Predefined geometric values for pier columns.

```
# Column 1
#        nodeTag       (x)      (y)    (z)
node     111       1.5975      0      0
node     112       1.5975      0      3.375
node     113       1.5975      0      6.75
node     114       1.5975      0      10.125
node     115       1.5975      0      13.5

# Column 2
#        nodeTag       (x)      (y)    (z)
node     211       33.5975     0      0
node     212       33.5975     0      3.375
node     213       33.5975     0      6.75
node     214       33.5975     0      10.125
node     215       33.5975     0      13.5
```

Figure B-40. Node set up for first two columns.

```
#                              eleTag   iNode    jNode   numIntgrPts   secTag    transfTag
element dispBeamColumn   3420    111      112         $n          100       $geomTransf
element dispBeamColumn   3421    112      113         $n          100       $geomTransf
element dispBeamColumn   3422    113      114         $n          100       $geomTransf
element dispBeamColumn   3423    114      115         $n          100       $geomTransf
```

Figure B-41. Displacement-based fiber-section beam-column elements for first pier column.

```
# Footing Center-of-Mass
#        nodeTag        (x)        (y)        (z)
node        1       -0.025        0         $hf
node        2        31.975       0         $hf
node        3        63.975       0         $hf
node        4        95.975       0         $hf
node        5       127.975       0         $hf
node        6       159.975       0         $hf
node        7       191.975       0         $hf
node        8       223.975       0         $hf
node        9       255.975       0         $hf
node       10       287.975       0         $hf
node       11       319.975       0         $hf

# Ground (Fixed)
#        nodeTag        (x)        (y)        (z)
node       12       -0.025        0         $hf
node       13        31.975       0         $hf
node       14        63.975       0         $hf
node       15        95.975       0         $hf
node       16       127.975       0         $hf
node       17       159.975       0         $hf
node       18       191.975       0         $hf
node       19       223.975       0         $hf
node       20       255.975       0         $hf
node       21       287.975       0         $hf
node       22       319.975       0         $hf
```

Figure B-42. Node set up for column footings and ground.

```
fix 1         0    0    1    1    1    1
fix 2         0    0    1    1    1    1
fix 3         0    0    1    1    1    1
fix 4         0    0    1    1    1    1
fix 5         0    0    1    1    1    1
fix 6         0    0    1    1    1    1
fix 7         0    0    1    1    1    1
fix 8         0    0    1    1    1    1
fix 9         0    0    1    1    1    1
fix 10        0    0    1    1    1    1
fix 11        0    0    1    1    1    1

fix 12        1    1    1    1    1    1
fix 13        1    1    1    1    1    1
fix 14        1    1    1    1    1    1
fix 15        1    1    1    1    1    1
fix 16        1    1    1    1    1    1
fix 17        1    1    1    1    1    1
fix 18        1    1    1    1    1    1
fix 19        1    1    1    1    1    1
fix 20        1    1    1    1    1    1
fix 21        1    1    1    1    1    1
fix 22        1    1    1    1    1    1
```

Figure B-43. Column footings and ground node SP-constraints using `fix`*.*

```
set KGh  155440.00
uniaxialMaterial Elastic 9 $KGh

set KGr  0.000000
uniaxialMaterial Elastic 8 $KGr

#                       eleTag    iNode   jNode      -mat matTag1...    -dir dir1...
element   zeroLength     3464      12       1       -mat 9 9 8 8        -dir 1 2
element   zeroLength     3465      13       2       -mat 9 9 8 8        -dir 1 2
element   zeroLength     3466      14       3       -mat 9 9 8 8        -dir 1 2
element   zeroLength     3467      15       4       -mat 9 9 8 8        -dir 1 2
element   zeroLength     3468      16       5       -mat 9 9 8 8        -dir 1 2
element   zeroLength     3469      17       6       -mat 9 9 8 8        -dir 1 2
element   zeroLength     3470      18       7       -mat 9 9 8 8        -dir 1 2
element   zeroLength     3471      19       8       -mat 9 9 8 8        -dir 1 2
element   zeroLength     3472      20       9       -mat 9 9 8 8        -dir 1 2
element   zeroLength     3473      21      10       -mat 9 9 8 8        -dir 1 2
element   zeroLength     3474      22      11       -mat 9 9 8 8        -dir 1 2
```

Figure B-44. Zero-length element for bridge-soil interaction.

```
# Footing Elements
#                             eleTag    iNode    jNode    A      E      G      J      Iy     Iz    transfTag
element elasticBeamColumn      3000       1       111     $Ar    $Er    $Gr    $Jr    $Ir    $Ir   $geomTransf
element elasticBeamColumn      3001       2       211     $Ar    $Er    $Gr    $Jr    $Ir    $Ir   $geomTransf
```

Figure B-45. Rigid elastic beam-column element for footings of columns #1 and #2.

```
# Column-Bearing Connecting Elements
#                             eleTag    iNode    jNode    A      E      G      J      Iy     Iz    transfTag
element elasticBeamColumn      3011      115      1101    $Ar    $Er    $Gr    $Jr    $Ir    $Ir   $geomTransf
element elasticBeamColumn      3012      1102     115     $Ar    $Er    $Gr    $Jr    $Ir    $Ir   $geomTransf
```

Figure B-46. Rigid elastic beam-column element for column-bearing connections at column #1.

```
# Girder-Bearing Connecting Elements
#                             eleTag    iNode    jNode    A      E      G      J      Iy     Iz    transfTag
element elasticBeamColumn      3051     90001     2101    $Ar    $Er    $Gr    $Jr    $Ir    $Ir   $geomTransf
element elasticBeamColumn      3052     2102     90001    $Ar    $Er    $Gr    $Jr    $Ir    $Ir   $geomTransf
```

Figure B-47. Rigid elastic beam-column element for girder-bearing connections above column #1.

```
# Girder-Track System Connecting Elements
#                             eleTag    iNode    jNode    A      E      G      J      Iy     Iz    transfTag
element elasticBeamColumn      3091     90001    50001    $Ar    $Er    $Gr    $Jr    $Ir    $Ir   $geomTransf
element elasticBeamColumn      3092     90002    50002    $Ar    $Er    $Gr    $Jr    $Ir    $Ir   $geomTransf
```

Figure B-48. Rigid elastic beam-column element for first two girder-track system connections.

```
# Girder
set mass    63.7359
set massxx 159.1817
set massyy  61.1692
set masszz 189.1868


#       nodeTag    ndf1     ndf2     ndf3     ndf4     ndf5     ndf6
mass     90001    $mass    $mass    $mass    $massxx  $massyy  $masszz
mass     90002    $mass    $mass    $mass    $massxx  $massyy  $masszz
```

Figure B-49. Mass assignment for first two nodes of bridge girder.

```
# Column
set mass    88.0308
set massxx 300.1776
set massyy 129.4099
set masszz 262.4664


#       nodeTag    ndf1     ndf2     ndf3     ndf4     ndf5     ndf6
mass     111     $mass    $mass    $mass    $massxx  $massyy  $masszz
mass     112     $mass    $mass    $mass    $massxx  $massyy  $masszz
```

Figure B-50. Mass assignment for first two nodes of column #1.

```
# Footing
set mass      629.7408
set massxx   7859.6900
set massyy   7859.6900
set masszz  14122.9870


#      nodeTag    ndf1     ndf2     ndf3      ndf4       ndf5       ndf6
mass     1        $mass    $mass    $mass    $massxx    $massyy    $masszz
mass     2        $mass    $mass    $mass    $massxx    $massyy    $masszz
```

Figure B-51. Mass assignment for footings of column #1 and #2.

```
# Power Car Body Loads
#      Node       X        Y         Z          Mx        My        Mz
load    63002    0.000    0.000    -539.158    0.000    0.000    0.000
load    63022    0.000    0.000    -539.158    0.000    0.000    0.000

# Extreme Passenger Car Body Loads
#      Node       X        Y         Z          Mx        My        Mz
load    63005    0.000    0.000    -255.060    0.000    0.000    0.000
load    63019    0.000    0.000    -255.060    0.000    0.000    0.000

# Intermediate Passenger Car Body Loads
#      Node       X        Y         Z          Mx        My        Mz
load    63007    0.000    0.000    -255.060    0.000    0.000    0.000
load    63009    0.000    0.000    -255.060    0.000    0.000    0.000
load    63011    0.000    0.000    -255.060    0.000    0.000    0.000
load    63013    0.000    0.000    -255.060    0.000    0.000    0.000
load    63015    0.000    0.000    -255.060    0.000    0.000    0.000
load    63017    0.000    0.000    -255.060    0.000    0.000    0.000

# Power Car Bogie Loads
#      Node       X        Y         Z          Mx        My        Mz
load    610012   0.000    0.000    -23.740     0.000    0.000    0.000
load    610022   0.000    0.000    -23.740     0.000    0.000    0.000
load    610122   0.000    0.000    -23.740     0.000    0.000    0.000
load    610132   0.000    0.000    -23.740     0.000    0.000    0.000

# Extreme Passenger Car Bogie Loads
#      Node       X        Y         Z          Mx        My        Mz
load    610032   0.000    0.000    -24.662     0.000    0.000    0.000
load    610112   0.000    0.000    -24.662     0.000    0.000    0.000
```

Figure B-52. Dead loads for train car-bodies and bogies.

```
# Intermediate Passenger Car Bogie Loads
#       Node     X       Y       Z        Mx      My      Mz
load    610042  0.000   0.000  -29.921   0.000   0.000   0.000
load    610052  0.000   0.000  -29.921   0.000   0.000   0.000
load    610062  0.000   0.000  -29.921   0.000   0.000   0.000
load    610072  0.000   0.000  -29.921   0.000   0.000   0.000
load    610082  0.000   0.000  -29.921   0.000   0.000   0.000
load    610092  0.000   0.000  -29.921   0.000   0.000   0.000
load    610102  0.000   0.000  -29.921   0.000   0.000   0.000

# Power and  Extreme Passenger Car Wheel Loads
#       Node     X       Y       Z        Mx      My      Mz
load    70011   0.000   0.000  -10.055   0.000   0.000   0.000
load    70012   0.000   0.000  -10.055   0.000   0.000   0.000
load    70021   0.000   0.000  -10.055   0.000   0.000   0.000
load    70022   0.000   0.000  -10.055   0.000   0.000   0.000
load    70031   0.000   0.000  -10.055   0.000   0.000   0.000
load    70032   0.000   0.000  -10.055   0.000   0.000   0.000
load    80011   0.000   0.000  -10.055   0.000   0.000   0.000
load    80012   0.000   0.000  -10.055   0.000   0.000   0.000
load    80021   0.000   0.000  -10.055   0.000   0.000   0.000
load    80022   0.000   0.000  -10.055   0.000   0.000   0.000
load    80031   0.000   0.000  -10.055   0.000   0.000   0.000
load    80032   0.000   0.000  -10.055   0.000   0.000   0.000

load    70111   0.000   0.000  -10.055   0.000   0.000   0.000
load    70112   0.000   0.000  -10.055   0.000   0.000   0.000
load    70121   0.000   0.000  -10.055   0.000   0.000   0.000
load    70122   0.000   0.000  -10.055   0.000   0.000   0.000
load    70131   0.000   0.000  -10.055   0.000   0.000   0.000
load    70132   0.000   0.000  -10.055   0.000   0.000   0.000
load    80111   0.000   0.000  -10.055   0.000   0.000   0.000
load    80112   0.000   0.000  -10.055   0.000   0.000   0.000
load    80121   0.000   0.000  -10.055   0.000   0.000   0.000
load    80122   0.000   0.000  -10.055   0.000   0.000   0.000
load    80131   0.000   0.000  -10.055   0.000   0.000   0.000
load    80132   0.000   0.000  -10.055   0.000   0.000   0.000
```

Figure B-53. Dead loads for power and extreme passenger car axle-wheels.

```
# Intermediate Passenger Car Wheel Loads
#       Node      X        Y         Z          Mx       My       Mz
load    70041    0.000    0.000    -9.810     0.000    0.000    0.000
load    70042    0.000    0.000    -9.810     0.000    0.000    0.000
load    70051    0.000    0.000    -9.810     0.000    0.000    0.000
load    70052    0.000    0.000    -9.810     0.000    0.000    0.000
load    70061    0.000    0.000    -9.810     0.000    0.000    0.000
load    70062    0.000    0.000    -9.810     0.000    0.000    0.000
load    70071    0.000    0.000    -9.810     0.000    0.000    0.000
load    70072    0.000    0.000    -9.810     0.000    0.000    0.000
load    70081    0.000    0.000    -9.810     0.000    0.000    0.000
load    70082    0.000    0.000    -9.810     0.000    0.000    0.000
load    70091    0.000    0.000    -9.810     0.000    0.000    0.000
load    70092    0.000    0.000    -9.810     0.000    0.000    0.000
load    70101    0.000    0.000    -9.810     0.000    0.000    0.000
load    70102    0.000    0.000    -9.810     0.000    0.000    0.000

load    80041    0.000    0.000    -9.810     0.000    0.000    0.000
load    80042    0.000    0.000    -9.810     0.000    0.000    0.000
load    80051    0.000    0.000    -9.810     0.000    0.000    0.000
load    80052    0.000    0.000    -9.810     0.000    0.000    0.000
load    80061    0.000    0.000    -9.810     0.000    0.000    0.000
load    80062    0.000    0.000    -9.810     0.000    0.000    0.000
load    80071    0.000    0.000    -9.810     0.000    0.000    0.000
load    80072    0.000    0.000    -9.810     0.000    0.000    0.000
load    80081    0.000    0.000    -9.810     0.000    0.000    0.000
load    80082    0.000    0.000    -9.810     0.000    0.000    0.000
load    80091    0.000    0.000    -9.810     0.000    0.000    0.000
load    80092    0.000    0.000    -9.810     0.000    0.000    0.000
load    80101    0.000    0.000    -9.810     0.000    0.000    0.000
load    80102    0.000    0.000    -9.810     0.000    0.000    0.000
```

Figure B-54. Dead loads for intermediate passenger car axle-wheels.

```
# Rail Self Weight
#       Node      X        Y         Z          Mx       My       Mz
load    11001    0.000    0.000    -1.661     0.000    0.000    0.000
load    11002    0.000    0.000    -1.661     0.000    0.000    0.000
load    11003    0.000    0.000    -1.661     0.000    0.000    0.000
load    11004    0.000    0.000    -1.661     0.000    0.000    0.000
```

Figure B-55. Dead loads for rail 1 (first four nodes).

```
# Track Plate Self Weight
#       Node      X        Y         Z          Mx       My       Mz
load    52001    0.000    0.000    -35.196    0.000    0.000    0.000
load    52002    0.000    0.000    -35.196    0.000    0.000    0.000
load    52003    0.000    0.000    -35.196    0.000    0.000    0.000
load    52004    0.000    0.000    -35.196    0.000    0.000    0.000
```

Figure B-56. Dead loads for track plate for track 1 (first four nodes).

```
# Base Plate Self Weight
#        Node        X         Y         Z         Mx        My        Mz
load     51001     0.000     0.000    -38.716     0.000     0.000     0.000
load     51002     0.000     0.000    -38.716     0.000     0.000     0.000
load     51003     0.000     0.000    -38.716     0.000     0.000     0.000
load     51004     0.000     0.000    -38.716     0.000     0.000     0.000
```

Figure B-57. Dead loads for base plate for track 1 (first four nodes).

```
# Bridge Girder Self Weight
#        Node        X         Y         Z         Mx        My        Mz
load     90001     0.000     0.000   -625.249     0.000     0.000     0.000
load     90002     0.000     0.000   -625.249     0.000     0.000     0.000
load     90003     0.000     0.000   -625.249     0.000     0.000     0.000
load     90004     0.000     0.000   -625.249     0.000     0.000     0.000
load     90005     0.000     0.000   -625.249     0.000     0.000     0.000
load     90006     0.000     0.000   -625.249     0.000     0.000     0.000
load     90007     0.000     0.000   -625.249     0.000     0.000     0.000
load     90008     0.000     0.000   -625.249     0.000     0.000     0.000
load     90009     0.000     0.000   -625.249     0.000     0.000     0.000
load     90010     0.000     0.000   -625.249     0.000     0.000     0.000
load     90011     0.000     0.000   -625.249     0.000     0.000     0.000
```

Figure B-58. Dead loads for first bridge girder span.

```
# Pier Column Self Weight
#        Node        X         Y         Z         Mx        My        Mz
load     111       0.000     0.000   -863.582     0.000     0.000     0.000
load     112       0.000     0.000   -863.582     0.000     0.000     0.000
load     113       0.000     0.000   -863.582     0.000     0.000     0.000
load     114       0.000     0.000   -863.582     0.000     0.000     0.000
load     115       0.000     0.000   -863.582     0.000     0.000     0.000
```

Figure B-59. Dead loads for first pier column.

```
# Foundation Self Weight
#        Node        X         Y         Z         Mx        My        Mz
load     1         0.000     0.000  -6177.757     0.000     0.000     0.000
load     2         0.000     0.000  -6177.757     0.000     0.000     0.000
load     3         0.000     0.000  -6177.757     0.000     0.000     0.000
load     4         0.000     0.000  -6177.757     0.000     0.000     0.000
load     5         0.000     0.000  -6177.757     0.000     0.000     0.000
load     6         0.000     0.000  -6177.757     0.000     0.000     0.000
load     7         0.000     0.000  -6177.757     0.000     0.000     0.000
load     8         0.000     0.000  -6177.757     0.000     0.000     0.000
load     9         0.000     0.000  -6177.757     0.000     0.000     0.000
load     10        0.000     0.000  -6177.757     0.000     0.000     0.000
load     11        0.000     0.000  -6177.757     0.000     0.000     0.000
```

Figure B-60. Dead loads for foundations.

```
# Define Gravity Analysis Parameters

# CONSTRAINTS handler-- Determines how the constraint equations are enforced in the analysis
constraints Penalty 1e15 1e15;            # Penalty Method: Uses penalty numbers to enforce constraints

# DOF NUMBERER -- Numbers the degrees of freedom in the domain
numberer RCM;                             # RCM: Renumbers the DOF to minimize the matrix band-width using the Reverse Cuthill-McKee algorithm

# Solution ALGORITHM -- Iterates from the last time step to the current
set algorithmTypeGravity Newton;          # Newton's solution algorithm: Updates tangent stiffness at every iteration
algorithm $algorithmTypeGravity;

# CONVERGENCE test -- Determines if convergence has been achieved at the end of an iteration step
set Tol 1.0e-6;                           # Tolerance
set maxNumIterGravity 100;                # Max number of iterations
set printFlagGravity 1;                   # Flag used to print information on convergence (optional)
set TestTypeGravity NormDispIncr;         # NormDispIncr: Specifies a tolerance on the norm of the displacement increments at the current iteration
test $TestTypeGravity   $Tol  $maxNumIterGravity  $printFlagGravity;

# SYSTEM -- Linear Equation Solvers (how to store and solve the system of equations in the analysis, solves Ku = P)
system UmfPack;                           # UmfPack: Direct UmfPack solver for unsymmetric matrices

# Static INTEGRATOR: -- Determines the next time step for an analysis
set NstepGravity 10;                      # Apply gravity in 10 steps
set DGravity [expr 1.0/$NstepGravity];    # First load increment
integrator LoadControl  $DGravity;        # LoadControl: Specifies the incremental load factor to be applied to the loads in the domain

# ANALYSIS  -- Defines what type of analysis is to be performed
analysis Static;                          # Static Analysis: Solves the KU = R problem, without the mass or damping matrices
```

Figure B-61. Definition of gravity load analysis parameters.

```
# Perform Gravity Analysis

analyze $NstepGravity;            # Perform gravity analysis with the amount of steps defined
loadConst -time 0.0;             # Sets loads constant and resets time to be 0.0

puts "###############################################"
puts            "Gravity Analysis Complete"
puts "###############################################"
```

Figure B-62. Performance of gravity load analysis.

```
# Perform Modal Analysis

set numModes 10;                     # Number of eigenvalues desired
set lambda [eigen $numModes];        # Eigenvalues

set T {};                            # Create an empty vector of T (Period)
set pi 3.141593

# Solve for periods using T=2*pi/sqrt(lambda)
foreach lam $lambda {
    lappend T [expr (2*$pi)/sqrt($lam)]
}

# Open output file
set period "DataLC8/Periods.txt"
set Periods [open $period "w"]

# Input data into the T vector
foreach t $T {
    puts $Periods "$t"
}

#Close the file
close $Periods
```

Figure B-63. Set up for modal analysis.

```
# Select two modes for Rayleigh Damping
set wi          [expr sqrt([lindex $ww 0])];        # Natural frequency of mode 1
set wj          [expr sqrt([lindex $ww 6])];        # Natural frequency of mode 6

# Define damping coefficient
set xi          0.02;                               # Damping Coefficient MIGHT CHANGE (2 or 5%)

# Define parameters for damping equation
set alphaM      [expr $xi*(2*$wi*$wj)/($wi+$wj)];   # M-prop. damping; D = alphaM*M
set betaKcurr   0.;                                 # K-proportional damping; +betaKcurr*KCurrent
set betaKinit   [expr $xi*(2)/($wi+$wj)];           # Initial stiffness proportional damping; +betaKinit*Kini
set betaKcomm   0.;                                 # K-prop. damping parameter; +betaKcomm*KlastCommitt

rayleigh $alphaM $betaKcurr $betaKinit $betaKcomm;  # Apply Rayleigh Damping
```

Figure B-64. Set up for Rayleigh damping.

```
# Define Dynamic Analysis Parameters

# CONSTRAINTS handler-- Determines how the constraint equations are enforced in the analysis
constraints Transformation;          # Transformation Method: Performs a condensation of constrained degrees of freedom

# DOF NUMBERER -- Numbers the degrees of freedom in the domain
numberer RCM;                        # RCM: Renumbers the DOF to minimize the matrix band-width using the Reverse Cuthill-McKee algorithm

# Solution ALGORITHM: -- Iterates from the last time step to the current
algorithmTypeDynamic Newton;         # Newton: Uses the tangent at the current iteration to iterate to convergence
algorithm $algorithmTypeDynamic

# CONVERGENCE test -- Determines if convergence has been achieved at the end of an iteration step
set TolDynamic 1.e-8;                # Tolerance
set maxNumIterDynamic 1000;          # Maximum number of iterations that will be performed before "failure to converge" is returned
set printFlagDynamic 1;              # Flag used to print information on convergence (optional)
set testTypeDynamic EnergyIncr;      # EnergyIncr: Specifies a tolerance on the inner product of the unbalanced load and displacement increments at the current iteration
test $testTypeDynamic $TolDynamic $maxNumIterDynamic $printFlagDynamic

# SYSTEM -- Linear Equation Solvers (how to store and solve the system of equations in the analysis, solves Ku = P)
systemTypeDynamic UmfPack;           # UmfPack: Direct UmfPack solver for unsymmetric matrices
system  $systemTypeDynamic

# Dynamic INTEGRATOR: -- Determines the next time step for an analysis
set NewmarkGamma 0.5;                # Newmark-integrator gamma parameter
set NewmarkBeta 0.25;                # Newmark-integrator beta parameter
set integratorTypeDynamic Newmark;
integrator $integratorTypeDynamic $NewmarkGamma $NewmarkBeta

# ANALYSIS  -- Defines what type of analysis is to be performed
analysis Transient;                  # Transient Analysis: Solves the time-dependent analysis. The time step in this type of analysis is constant.
```

Figure B-65. Definition of seismic load analysis parameters.

```
# Define Ground Motion Parameters

set GMfile "RSN1004_NORTHR_SPV270";  # Ground-motion file from PEER
source ReadSMDFile.tcl;              # Converts PEER ground-motion to an OpenSees readable format
set inFilename $GMfile.AT2;          # Original filename and extension (AT2)
set outFilename $GMfile.g3;          # Set variable holding new filename (PEER files have .at2/dt2 extension)
ReadSMDFile $inFilename $outFilename dt;  # Call procedure to convert the ground-motion file

set DT          0.005;               # Time-step used in dynamic analysis
set Nstep       9557;                # Number of steps in dynamic analysis

set GMfact      $g;                  # Convert GM acceleration from "g" to m/s2
```

Figure B-66. Definition of ground motion parameters.

```
# Apply Ground Motion to Model

set IDloadTagx 400;          # For uniformSupport excitation
set GMdirection_x 1;         # Ground-motion x-direction
set xacc "Series -dt $DT -filePath $outFilename -factor $GMfact";  # Time series information
pattern UniformExcitation $IDloadTagx $GMdirection_x -accel $xacc;  # Create uniform excitation

set IDloadTagy 500;          # For uniformSupport excitation
set GMdirection_y 2;         # Ground-motion y-direction
set yacc "Series -dt $DT -filePath $outFilename -factor $GMfact";  # Time series information
pattern UniformExcitation $IDloadTagy $GMdirection_y -accel $yacc;  # Create uniform excitation
```

Figure B-67. Application of ground motion in both directions.

```tcl
# Perform Dynamic Load Analysis

set ok [analyze $Nstep $DT];              # Perform analysis; returns ok = 0 if analysis was successful

# Create a Loop to Try Other Algorithms and Convergence Test Types if Initial Analysis Fails

set TmaxAnalysis  [expr $Nstep*$DT];      # Maximum duration of ground-motion analysis

if {$ok != 0} {
set ok 0;
set controlTime [getTime];
while {$controlTime < $TmaxAnalysis && $ok == 0} {
set controlTime [getTime]
set ok [analyze 1 $DT]
if {$ok != 0} {
puts "Trying Newton with Initial Tangent .."
test NormDispIncr $Tol 1000 1
algorithm Newton -initial
set ok [analyze 1 $DT]
test $testTypeDynamic $TolDynamic $maxNumIterDynamic 0
algorithm $algorithmTypeDynamic
}
if {$ok != 0} {
puts "Trying Broyden .."
algorithm Broyden 8
set ok [analyze 1 $DT]
algorithm $algorithmTypeDynamic
}
if {$ok != 0} {
puts "Trying NewtonWithLineSearch .."
algorithm NewtonLineSearch .8
set ok [analyze 1 $DT]
algorithm $algorithmTypeDynamic
}
}; # end while loop
}; # end if ok !0


puts "#############################################"
puts    "Ground Motion Done. End Time: [getTime]"
puts "#############################################"
```

Figure B-68. Performance of seismic load analysis